Study of Beam Dynamics in NS-FFAG EMMA with Dynamical Map

A thesis submitted for the degree of Doctor of Philosophy

by Yoel Giboudot

School of Engineering and Design, Brunel University

July 2011

Abstract

Dynamical maps for magnetic components are fundamental to studies of beam dynamics in accelerators. However, it is usually not possible to write down maps in closed form for anything other than simplified models of standard accelerator magnets. In the work presented here, the magnetic field is expressed in analytical form obtained from fitting Fourier series to a 3D numerical solution of Maxwell's equations. Dynamical maps are computed for a particle moving through this field by applying a second order (with the paraxial approximation) explicit symplectic integrator. These techniques are used to study the beam dynamics in the first non-scaling FFAG ever built, EMMA, especially challenging regarding the validity of the paraxial approximation for the large excursion of particle trajectories. The EMMA lattice has four degrees of freedom (strength and transverse position of each of the two quadrupoles in each periodic cell). Dynamical maps, computed for a set of lattice configurations, may be efficiently used to predict the dynamics in any lattice configuration. We interpolate the coefficients of the generating function for the given configuration, ensuring the symplecticity of the solution. An optimisation routine uses this tool to look for a lattice defined by four constraints on the time of flight at different beam energies. This provides a way to determine the tuning of the lattice required to produce a desired variation of time of flight with energy, which is one of the key characteristics for beam acceleration in EMMA. These tools are then benchmarked against data from the recent EMMA commissioning.

Contents

Acknowledgements

I am heartily thankful to Andy Wolski, whose encouragement, supervision and support from the preliminary to the concluding level enabled me to develop an understanding of the subject. I am deeply grateful for his infinite patience explaining concepts again and again over these three years. I cannot remember a single time when knocking at his office door for another question, he did not tell me to come in and spent time helping me.

It is a pleasure to thank those who made this thesis possible Akram Khan and Rajagopal Nilavalan. I would like to thank them for always responding to my needs in a kind and considerate way.

I would like to show my gratitude to Rob Edgecock, Neil Marks and John Dainton for their advices and their guidance at the beginning of this PhD.

I warmly thank my colleagues Ben Shepherd, Bruno Muratori, James Jones and Peter Williams for their support and their smiles and jokes (not always funny) creating a very precious atmosphere in the Cockcroft Institute.

I wish to express my warm gratitude to the EMMA commissioning team and especially to Shinji Machida and David Kelliher for their incredible dedication to the experiment and for the friendliness in our conversations in the control room and in many other occasions.

Finally, I am sincerely thankful to my family including my adopted brothers David and Thomas, being the ear that listens, the heart that supports and the muse that inspires.

List of Figures

List of Tables

1

Introduction

1.1 Perspective for new accelerators

1.1.1 Accelerators in various fields of science

The whole scientific community has its eyes turned toward the Large Hadron Collider (LHC) at CERN in Switzerland; it is about to deliver experimental results from two beams colliding at energies never achieved before. Similarly other projects like ILC and CLIC [1, 2], aim at pushing further this "frontier of energy" and test the particle physics models. In terms of beam dynamics this type of accelerators requires small size beams to optimise the collision of particles. In the past they have always been source of technological development for the rest of accelerators.

Another main type of accelerator is dedicated to photon science and aim for the highest brightness of light that can be induced by a beam of particles. It includes Synchrotron light sources such as ESRF and DIAMOND [3, 4] and the relatively new technology of Free Electron Lasers (FEL) [5]. An important goal for these machines is a tiny beam size such that the light source is point-like; thus great efforts are made to minimise the beam size and the divergence of the beam.

A third field of science uses accelerators as high power sources in which the beam

carries a large amount of power such as the Spallation Neutron Source (SNS) and the 590 MeV cyclotron at the Paul Sherrer Institute [6, 7]. This power is the product of three factors: the energy of each particle, the number of particle per beam and the repetition rate of the acceleration cycle.

The first factor is increased by using the technology of the high energy frontier accelerators. It is limited by the price and the size of the machine involved.

The second factor is related to the aperture available for a large number of particle in a ring. Large aperture requires large accelerator components that are potentially expensive and difficult to built.

The third factor refers to the time it takes to bring a bunch of particles from the initial energy to the nominal energy and then set the machine back to the configuration suitable for injecting a new bunch at low energy. The repetition rate is maximum if the accelerator handles continuous acceleration (bunches at initial and final energy are in the ring at the same time). We shall now explain the technological solutions that optimise these factors.

1.1.2 High beam power accelerators

In most accelerator rings, particles are guided by magnetic fields. The higher is the energy of the particle, the stronger has to be the magnetic field to bend its trajectory. In a synchrotron, the magnet strengths are increased during acceleration; the beam stays on the same orbit even when gaining energy. However the modulation of magnetic field is slow and is a strong limitation to obtain a high repetition rate in the kHz range; Synchrotron repetition rate is usually limited to a few tens of Hz. Therefore high power machines tend to use fixed (in time) magnetic field; As a result particles spiral outward through acceleration and a larger beam chamber is required. Note that linear accelerator can also be used to create high power beam; they are generally the most expensive solution.

Historically high power beam were produced by cyclotrons composed of simple magnets only bending the beam [8]. Synchrotron accelerators generally contain focusing magnets to control the divergence of the beam and also decrease the beam size at the collision point for instance. The more challenging requirements on the beam extracted from cyclotrons made necessary the use of focusing magnetic field. Moreover increasing the number of particles in the beam, particles are more subject to repulsive forces. A magnet field focusing the beam in the transverse horizontal (vertical) plane is always defocusing in the transverse vertical (horizontal) plane. Therefore in order to control the beam size in both planes, rings were composed of a sequence of magnetic gradient alternatively focusing and defocusing the beam (also insuring the bend of the trajectory).

High power machine logically evolved to use Fixed Field and Alternating Gradient (FFAG). Cyclotrons are still seen today as the most suitable machine for high power beam. For instance researches have been done on sector-focused cyclotron [9]; Cyclotrons enthusiasts pretend that FFAG are only a particular type of cyclotron. FFAG enthusiasts reply that cyclotrons are an old-fashioned version of their machine. However the accelerator community sometimes struggles to define clearly the frontier between cyclotrons and FFAGs.

1.1.3 Evolution and applications of FFAG accelerators

The concept of FFAG accelerator was developed in the 1950's at MURA [10] but technical issues (such as manufacturing of magnets with complex geometries) and lack of funding stopped its evolution until its rebirth in the 1990's with the construction of the Proof of Principle at KEK in Japan [11]. Nowadays four main fields are interested in the applications of FFAG accelerators:

- The Neutrino factory project in which a proton beam with high power is directed at a target and creates muons, decaying later in neutrinos [13].

- Accelerator Driven Subcritical nuclear Reactor (ADSR); these are nuclear reactors in which the fission process is initiated by neutrons created by the collision of a proton beam on a spallation target [14].

- Hadrons therapy which launches hadrons in the body to destroy tumours; this technique limits the degradation of healthy tissues surrounding the tumour. Here FFAG accelerators are suitable for their capacity to deliver high intensity pulsed beam allowing a short irradiation time compared to respiratory motion. In addition, FFAG accelerators may be significantly smaller and cheaper than synchrotron accelerators and be therefore more suitable for hospitals environment.

- Muons accelerator; Fast acceleration in FFAG is thought to be useful for unstable particles decaying rapidly such as muons. The original name for the prototype EMMA was Electron Model for Muons Acceleration, a reduced size prototype accelerating lighter and more stable lepton: electrons.

1.1.4 Non scaling and scaling FFAG accelerators

Generally FFAG accelerators are separated in two families defined according to the properties of their magnets. A "Scaling" FFAG accelerator contains large magnets whose magnetic field enforces the scaling law [12]. By inducing a highly nonlinear magnetic field, magnets are designed such that when particles gain energy (see figure 1.1), they spiral outwards experimenting the same focusing strength, keeping the value of the tune constant. The magnetic field is therefore scaled up from low to high energy giving its name to the accelerator. According to the value of the tune, a beam can be sensitive to errors in the lattice and become unstable. With the scaling law, once a stable shape for the orbit has been found, the beam stays stable through acceleration. This is explained in more details in section 1.3.3 of this chapter. The main drawback of this type of machine is the complexity of the magnets. Since particles are moving

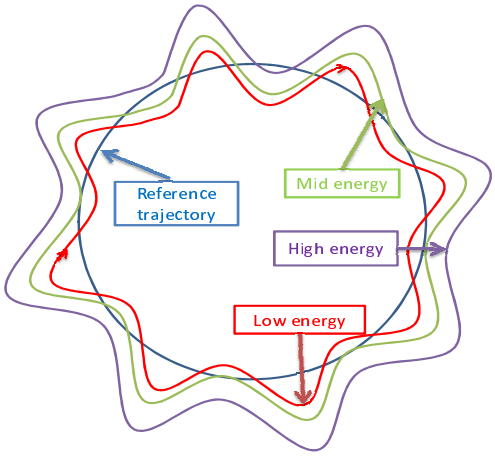

Figure 1.1: Closed orbit for various momenta in a scaling FFAG. The orbits keep the same shape when the energy is increased. The reference trajectory is the blue circle used to align the magnet around the ring.

outwards when gaining energy, magnets are generally large radially to accommodate particles from low energy to high energy. Moreover, the non-linearity of the field is created by complex geometries requiring extensive 3D modelling of the magnetic fields.

More recently beam dynamics simulations suggested that acceleration in a FFAG machine could be achieved without following the scaling law in the magnets. The beam becomes sensitive to errors in the ring; however an acceleration within a few turns only should not let enough time to the beam to be unstable. Without the scaling law, magnets can be kept simple and linear. Since orbits at various energies do not conserve the same shape, they can be compressed to fit in a smaller aperture. Magnets are therefore smaller and cheaper; also the beam only need to be bent and focused; therefore in theory the lattice can be composed of dipole magnets (magnetic field constant across the transverse aperture) and quadrupole magnets (magnetic field varying linearly across the transverse aperture).

A scaling FFAG accelerator had been successfully built in Japan and proved the validity of the concept. A prototype of Non-Scaling needed to be built to test the

evolution of the concept. That is why the construction of the Non Scaling FFAG Electron Model for Many Applications (EMMA) was proposed in 2005.

1.2 The EMMA project

The design and construction of the non scaling FFAG EMMA is part of the Construction Of an Non-scaling FFAG For Oncology, Radiation and Medicine (CONFORM project). CONFORM is sponsored by the British Accelerator Science and Radiation Oncology Consortium (BASROC) and has been awarded a multi-million pound grant from the RCUK Basic Technology programme to pursue this research. It includes the design and the construction of two prototypes of FFAG accelerators [15, 16], EMMA and PAMELA. EMMA - the Electron Model for Many Application [20] will demonstrate the principle of non-scaling FFAGs and be used to study the features of this type of accelerator in detail. Although a model of the muon accelerators in a Neutrino Factory, EMMA will have sufficient flexibility to study a variety of applications including hadrons machines. PAMELA is a prototype of an Non Scaling FFAG accelerator for proton used for cancer therapy [17]. Being still at the design stage, positive results from the EMMA experiment will be an important step towards the start of its construction.

The EMMA machine is being commissioned at Daresbury in the UK since July 2010. Since it is the first machine of this type ever built, extensive simulations had to be performed for the design. Particle tracking simulations are also relevant during the commissioning to analyse measurements and predict which tuning of machine will achieve stable acceleration. Moreover the experimental results will be used to benchmark the various codes that simulated the machine; future FFAG accelerators can then be designed with the most reliable codes.

At the design stage, agreements between tracking results of different codes evaluated the validity of a given configuration of the ring. Important characteristics for which

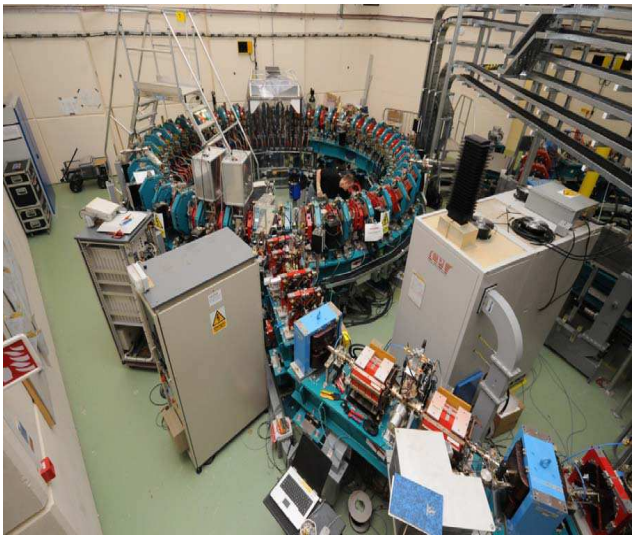

Figure 1.2: EMMA in June 2010.

codes were compared had to be defined. In the next section, we will describe the main properties of the linear beam dynamics in the EMMA ring.

1.3 Linear transverse dynamics in a non-scaling FFAG

1.3.1 A reference trajectory : the closed orbit

Particle dynamics are generally described with respect to a reference trajectory. In a ring this can be defined by the trajectory of an ideal particle travelling at fixed energy without dissipative forces. Often the reference trajectory is chosen such that the trajectory closes itself after one turn by coming back at the same position. Magnets are usually aligned with respect to this trajectory called the reference closed orbit. In a synchrotron, when a particle is accelerated, the strengths of the magnet are increased in order to keep the beam on the same reference trajectory.

In an FFAG, since the magnetic field in the magnets is fixed, the orbit of a particle will be displaced toward the outside of the ring when it gains energy. After one turn, the accelerated particle does not come back to the same transverse position; this means

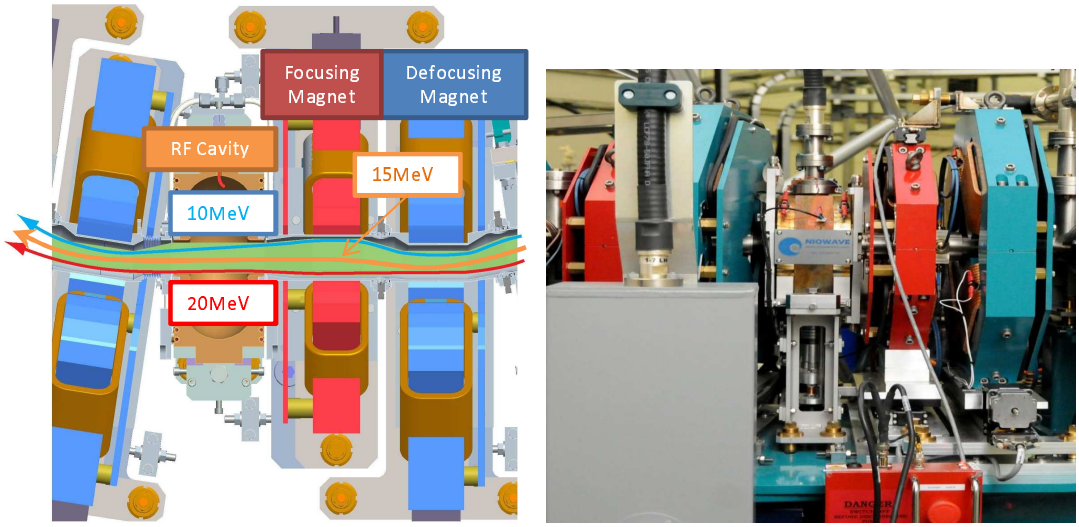

(a) (b)

Figure 1.3: (a) Schematic top view of one EMMA cell.(b) Picture of one cell in the EMMA ring. Particles travel through a defocusing magnet (blue), a focusing magnet (red) and a cavity (every other cell). The trajectories at 10 MeV, 15 MeV and 20 MeV are also represented. We observe that the most important bending occurs at 10 MeV

that the orbit is not closed. However it is possible to study the trajectory of a particle in an FFAG without acceleration; then the orbit is closed. For an FFAG accelerator there will be a different closed orbit for each energy.

Accelerators structures called "lattices" are composed of repeated patterns of magnetic elements. For instance the EMMA ring is built of 42 identical cells, each cell containing one defocusing quadrupole and one focusing quadrupole. Ideally, cells are exactly identical (same magnet strengths, same magnet positions with respect to the reference) and hence the lattice has a $2\pi/42$ periodicity; beam dynamics in a single cell characterise the entire ring. However the frame of reference within this cell in which the dynamics are derived must be chosen with care to represents dynamics in the entire ring.

One could use an absolute frame of reference defined with respect to the centre of the ring. The trajectory of a particle over the whole ring could then be derived in the

same frame. This solution has two main drawbacks:

- Since the radius of the EMMA ring is of about 2.5 meters, the transverse position of the closed orbit will be defined with value of the same order. However beam dynamics studies usually deals with millimetre-scale variation of particle trajectory with respect to the reference trajectory. It is rather non practical to evaluate millimetre-scales variations on meter-scales values.

- In this study, the magnetic field induced by the magnets is derived by solving numerically Maxwell's equation for a 3D model of a single cell. To compute the trajectory of a particle through the magnetic field in a global frame of reference, this numerical solution (also called "field map") for one cell must be adapted for each of the 42 cells to the corresponding global location of that cell. For instance even if the magnetic field in cell 1 and cell 34 are identical because their magnets are identical, their field maps will be different because the two cells have different locations. In fact, field maps must be rotated by an angle $2\pi/42$ between two following cells, taking into account the overlapping and the hole introduced by the rotation. This process is rather cumbersome.

Instead, we chose to compute the beam dynamics in one cell, with a frame of reference defined within this cell. From the initial design of the EMMA ring [21], the reference is a straight line across one cell. The reference straight line of the following cell is rotated by an angle $2\pi/42$ around the vertical axis. Therefore the coordinates of the particle at the end of a cell must be rotated by this angle before being tracked in the next cell, defined by the same field map.

In the baseline lattice configuration in figure 1.4, the magnetic axes of the defocusing (D) magnet (blue) and the focusing (F) magnet (red) are distant from the reference polygon (orange) by 34.048 mm and 7.514 mm respectively. THe rotation of the reference system is performed at the entrance face of the D magnet.

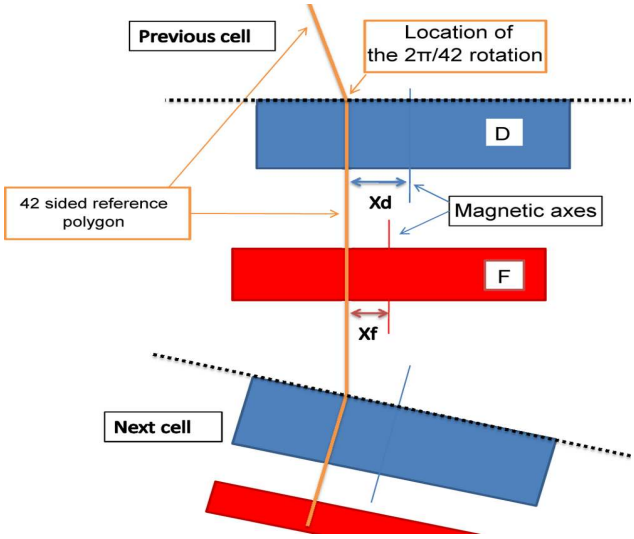

Figure 1.4: Schematic of the EMMA cell. In the baseline configuration (not up to scale here), the magnetic axes of the defocusing (D) magnet (blue) and the focusing (F) magnet (red) are distant from the reference polygon (orange) by X_d= 34.048 mm and X_f=7.514 mm respectively. The rotation of the reference system is performed at the entrance face of the D magnet.

Figure 1.5 shows the closed orbits for six energies in one EMMA cell. The transverse coordinates at the exit face would be equal to those at the entrance face after rotation of $2\pi/42$ not represented in this figure.

1.3.2 Synchronising the transverse dynamics with the acceleration device: the time of flight (tof)

We observe in figure 1.5 that closed orbits vary with energy. A important characteristic to evaluate is the change in path length of the trajectory with changes in energy. In EMMA, particles are accelerated in resonating radio frequency (rf) cavities in which an electromagnetic field oscillates in time.

There is one cavity every two cells in EMMA and all cavities are tuned with the same rf frequency. A particle gets the optimal acceleration if it enters a cavity when the field is maximum. Therefore the time it takes to travel from one cavity to another must be equal to an integer number of oscillation of the accelerating field. In that case

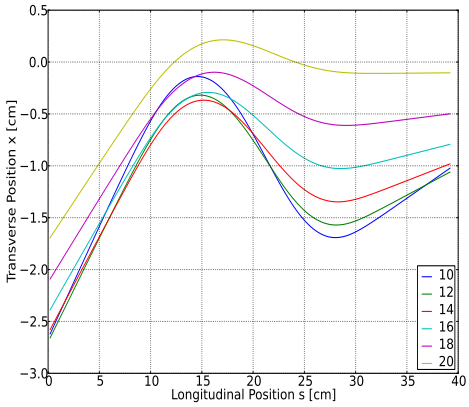

Figure 1.5: closed orbits for six energies in one EMMA cell. The transverse coordinates at the exit face would be equal to those at the entrance face after rotation of $2\pi/42$ not represented in this figure. We observe as in figure 1.3 (a) that the most important bending occurs at 10 MeV

particles can experience the maximum accelerating voltage in all the cavities.

In the case of EMMA, particles are electrons with kinetic energy between 10 MeV and 20 MeV. They are relativistic and do not tend to travel faster when they gain energy. Hence, the path length evolution with energy reflects the time of flight evolution with energy.

A 20 MeV particle travels on the outside of the ring. We expect therefore its path length to be larger than those of a 10 MeV particle. If the path length (or time of flight) shift with energy is larger than half a period of the field in the cavity, while a particle at 10 MeV experiences an accelerating field, at 20 MeV it is decelerated.

To overcome this problem, the lattice was design such that a particle at 10 MeV experiences stronger fields in the magnets and thus follows a larger bend than a rather straight trajectory at 20 MeV (see figure 1.5). Figure 1.6(a) shows the values of the time of flight for various energies obtained from two simulation techniques (dynamical maps and PyZgoubi). We observe that two behaviours compete to form a parabola. From 10 MeV to 16.5 MeV (minimum of the curve) trajectories are less bended and their time of flight decreases. From 16.5 MeV to 20 MeV the orbit moves significantly

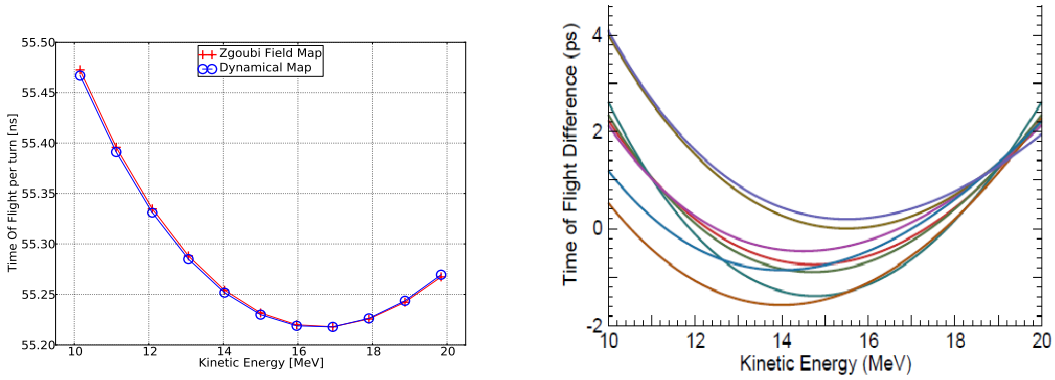

(a) (b)

Figure 1.6: (a) Values of the time of flight for various energies obtained from two simulation techniques (dynamical maps and PyZgoubi). We observe that two behaviours compete to form a parabola. From 10 MeV to 16.5 MeV trajectories are less bended and their time of flight decreases. From 16.5 MeV to 20 MeV the orbit moves significantly outside the ring, hence the time of flight increases with energy. (b) Figure produced by Berg in the EMMA design report [21] shows the difference in time of flight between the closed obit at various energy and a particle synchronised with the rf frequency. Each curve represents a different configuration of the lattice (i.e. different strengths and transverse positions of the magnets).

outside the ring, hence the time of flight increases with energy.

In this design the time of flight is not constant but is kept within a small range. By adjusting the cavity frequency to the average time of flight of this parabola, particles at all energy can experience a positive (accelerating) voltage in the cavity.

The time of flight variation with energy depends on the magnet strengths responsible for the bend of the trajectories. It depends also on the transverse positions of the magnets since by moving one magnet with respect to the other, the magnetic field in the cell is changed and the closed orbits are different. The lattice in EMMA has therefore four parameters in each cell than can be adjusted: the focusing and defocusing quadrupoles strengths and their horizontal transverse positions. To conserve the periodicity of the lattice, all the cells are always kept with the same values of these four parameters. The entire EMMA ring has therefore four parameters that can be adjusted.

The nominal lattice configuration was designed such that the time of flight parabola was exactly symmetrical, with its minimum at 15 MeV; this was shown to be a stable configuration to accelerate successfully. Figure 1.6(b) produced by Berg in the EMMA design report [21] shows the difference in time of flight between the closed obit at various energy and a particle synchronised with the rf frequency. Each curve represents a different configuration of the lattice (i.e. different strengths and transverse positions of the magnets). Because of manufacturing errors and misalignments of the magnets, the design nominal strengths and positions of the magnets will probably not correspond to a symmetrical time of flight curve in the real machine. Obtaining the real nominal configuration of the lattice in terms of time of flight is one of the main criteria to achieve acceleration in the EMMA FFAG. It is important to be able to model the time of flight curve for given lattice configurations, taking into account realistic field profiles in the magnets. Being able to determine the changes in the lattice configuration needed to achieve desired changes in the time of flight curve is also important. The development of tools and techniques to provide these capabilities is one of the main objectives of this study.

1.3.3 Studying instabilities of the beam: the tune

Once a closed orbit has been found for a given energy, it is interesting to study how particles behave if they are injected with the same energy but off this closed orbit. We will see in the section 3.1.1.5 of chapter 3 that in the linear approximation beam dynamics in a quadrupole are equivalent to the harmonic oscillator. A particle with a given energy E oscillates around the corresponding closed orbit. The amplitude of the oscillations depends on the initial coordinates of the particle and on the strengths of the magnet. In accelerator terminology, it is called "betatron oscillations" because it was first observed in an accelerator called the betatron [22].

To understand the importance of the study of these oscillations, let us imagine

that a magnetic field error is introduced in the ring at a given longitudinal location z_e. Each time a particles passes by this location z_e (once per turn), whatever is its transverse position, it is slightly kicked towards the outside of the ring. In other words its transverse angle is increased at each turn. This type of error is called a dipole error since it has the effect a dipole field added to the lattice. As shown in figure 1.7, a particle that performs an integer number of oscillation within one turn will see its amplitude increase turn after turn until it hits the wall of the beam pipe.

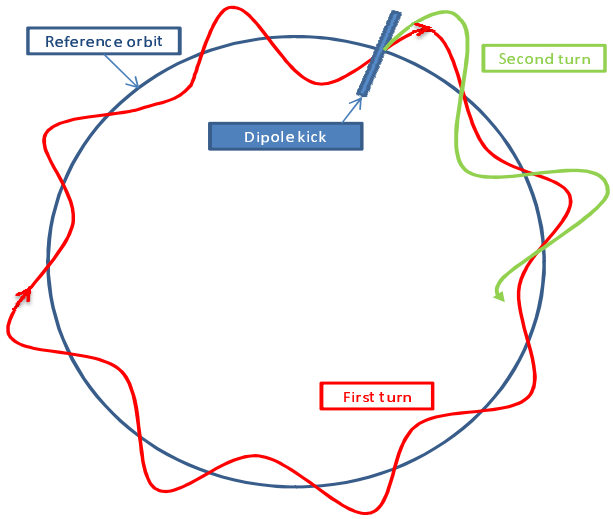

Figure 1.7: Description of a first order resonance. A magnetic field error is introduced in the ring at a given longitudinal location z_e. Each time a particles passes by this location z_e (once per turn), whatever is its transverse position, it is slightly kicked towards the outside of the ring. In other words its transverse angle is increased at each turn. This type of error is called a dipole error since it has the effect a dipole field added to the lattice. A particle that performs an integer number of oscillation within one turn will see its amplitude increase turn after turn until it hits the wall of the beam pipe.

This example illustrates the principle of optical resonance. We observe that if the particle does not come back to the dipole error with the same transverse position and

angle then the effect is not cumulative. The resonance effect occurs if the particle performs an integer number of oscillations (8 in figure 1.7) around the reference orbit in one turn. This is a first order resonance. Quadrupole errors for which the strength of the kick increases with the transverse excursion of the particle are second order resonances. In that case a resonance occurs for half integer number of oscillations (for instance $8+\frac{1}{2}$ oscillations). More complex types of error lead to higher order resonances. Note that resonances can occur in the horizontal transverse plane and also in the vertical transverse plane since a particle generally oscillates in both planes.

The number of oscillations around the closed orbit over one turn is called the tune. The fractional part of the tune tells which resonance could be excited and therefore which kind of field error the beam is sensitive to. It is an important parameter of the beam dynamics. Since we consider that cells are all identical, we will be considering the fractional part of the number of oscillation performed in a single cell, referenced as ν_x for the horizontal tune per cell and ν_y for the vertical tune per cell. Note that in theory an error in the quadrupole field identical in all the cells will excite a resonance not every turn but every cell. The beam can therefore be lost rapidly. In reality manufacturing errors and misalignments of the magnets make each cell slightly different from the other cells.

Since the focusing strength changes with energy in a non-scaling FFAG, the tune also varies with energy. This variation is called chromaticity. Therefore through acceleration resonances may be excited. In practise, accelerator lattices are designed such that nominal dynamics are far from resonance and the chromaticity is kept as small as possible by using nonlinear magnetic field [32]. Since the EMMA ring is composed of linear magnets only (quadrupole magnets), the tune variation with energy is large. Despite the fact that in an FFAG, the accelerated orbit is not closed, we evaluate the tune for closed orbits found at given energies, as shown in figure 1.5. Even if the ideal trajectory of an accelerated orbit will not involve a jump from one closed orbit

to another (but a continuous spiral), we assume that this evaluation of the tune is a relevant characterisation of a lattice configuration. Figure 1.8(a) shows the values of the horizontal and vertical fractional part of tune for one cell for various energies.

The (ν_x,ν_y)-space, called the tune diagram is covered with resonances appearing as lines described by $a\nu_x + b\nu_y = p$. The resonance order is given by $a + |b|$. One can plot the evolution of the tune in EMMA in a tune diagram to visualise values of the tunes that can excite a resonance. Through the commissioning of the machine, the strengths of both families of quadrupole magnets will be used in order to change the tune variation of the machine and therefore find a lattice configuration in which the beam can be accelerated. The four parameters of the EMMA lattice can be adjusted to study resonance crossing. Several reference lattices have been studied at the design stage by Berg [21]. The variation with energy of the horizontal and vertical (dashed line) fractional part of the cell tune for some of the reference lattice configuration ("b" to "e") is shown in figure 1.8(b).

The challenge of the FFAG accelerator EMMA is therefore to accelerate particles going through resonances without losing the beam. Simulations have shown that it is possible [23] with the condition that the resonances are crossed quickly. In other words, if the acceleration is performed in a few turns, the effect of field errors do not accumulate enough to destroy the beam.

1.4 From the 3D numerical solution to Maxwell's equations to the computation of a dynamical map

In EMMA, a highly compact doublet cell is achieved using short quadrupole magnets. A large aperture requirement compare to the length of the magnets leads to potentially significant effect of fields at the edges of the magnets, also called fringe fields. Accurate simulations of the beam dynamics in EMMA may require a dense description of the

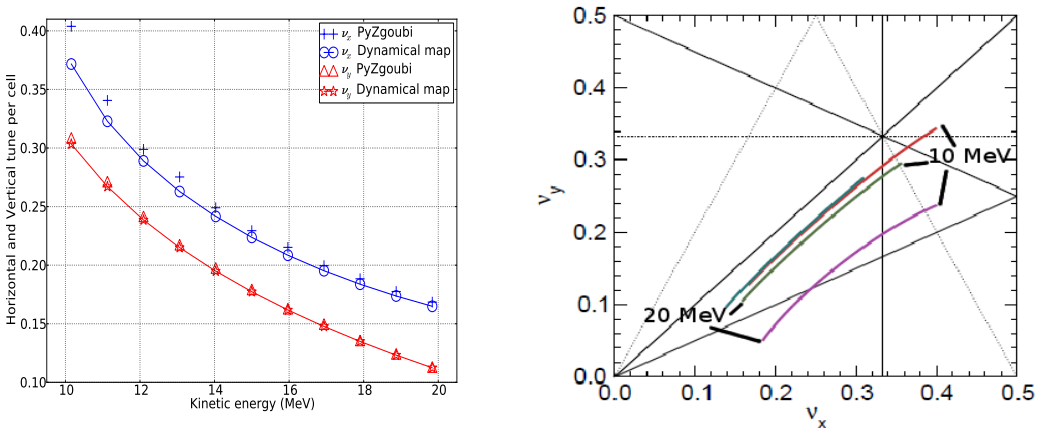

(a) (b)

Figure 1.8: (a) Value of the horizontal (ν_x) and vertical (ν_y) fractional part of tune for one EMMA cell for various energies; simulations were carried out with PyZgoubi and dynamical maps. (b) Variation of the horizontal and vertical tune per cell with energy from 10 MeV to 20 MeV in the tune diagram ((ν_x,ν_y)-space) for some of the reference lattice configuration ("b" to "e") designed by Berg [21]. The four parameters of the EMMA lattice can be adjusted to study resonance crossing.

magnetic field in 3D.

We generated a 3D numerical representation of the magnetic field by solving Maxwell's equations in one EMMA cell using the Finite Element Method implemented in the software OPERA [25]. This representation can be used for numerical tracking in EMMA with PyZgoubi [48, 56, 68]. Numerical tracking means that the position of a particle is computed throughout the EMMA cell, step by step, by solving numerically the equations of motion, knowing the numerical value of the magnetic field at each step.

In most cases, PyZgoubi routines are fast and reliable. However, an alternative approach based on dynamical maps could provide some benefits, particularly where speed is important; for example, when tracking many particles through many cells. Dynamical maps also provide the possibility of reading significant quantities (such as tune and chromaticity) directly from the map, giving an insight into the dynamics that is not provided directly by purely numerical methods.

To generate a dynamical map, the coordinates of a particle are computed step

by step in the EMMA cell not as numerical values but as functions of the starting coordinates. Generally a particle is defined by six coordinates: the horizontal and vertical positions x, y and their associated momenta p_x, p_y, the longitudinal position z and the energy deviation δ. A dynamical map is expressed as a function of these coordinates and the magnetic field also must be expressed in analytical form.

The second chapter of this thesis (following the introduction) will be dedicated to the construction of the analytical representation of a magnetic system. First we will present the 3D model of the EMMA magnetic elements in the numerical solver OPERA. We will describe the numerical solution to Maxwell's equations obtained by Finite Element Method. We will discuss the possibility of constructing a 3D representation of the EMMA cell by adding two numerical solutions computed separately for each magnetic element. Results will be compared to some measurements of the magnetic field in real magnets. An analytical representation will then be extracted from the numerical solution. We will look at the basis functions and coordinate system most adapted to the geometry of the system and to beam simulations. Having chosen truncated Fourier series expressed in Cartesian coordinates as an appropriate analytical representation, we will optimise the chosen truncation order and the adaptation of the periodicity of this function to the real geometry.

In chapter 3, the theoretical background of the construction of dynamical maps will be presented. Starting from the general Hamiltonian formalism, we will define sets of canonical variables relevant for beam simulations and express the Hamiltonian for an accelerator in a straight coordinate system without dissipative forces. We will show that solutions to Hamilton's equations have the common property of being symplectic resulting in the existence of an invariant of motion for particles in an accelerator. This invariant called the "action" is a canonical variable conjugate to the "angle" variable; this pair of canonical variables is particularly appropriate to express beam dynamics in periodic structures. In the second part of this chapter, in order to solve Hamilton's

equations for nonlinear systems, we will express the Hamiltonian as a sum of terms using the paraxial approximation. We will then introduce the Lie transformation and use its properties to express the solution to Hamilton's equations in a form known as Yoshida Factorisation, in which each factor corresponds to a simple operation on the dynamical variables. This will result in the definition of an explicit symplectic integrator developed by Wu, Forest, and Robin [39] which computes a symplectic dynamical map with the paraxial approximation for particles moving in a magnetic field expressed in analytical form. We will eventually describe the Differential Algebra code COSY infinity in which we have implemented the explicit symplectic integrator. We will then take the example of a dynamical map expressed as a truncated Taylor series and discuss its symplecticity and the implication of the paraxial approximation.

In chapter 4, we will present the beam dynamics simulations performed with dynamical maps for the non-scaling FFAG EMMA. The time of flight, horizontal tune and vertical tune evolution with energy will be compared to simulations with simplified models of the magnets and with simulations tracking particles through the numerical field map. These two types of simulations will be performed with the numerical tracking code PyZgoubi. Also, since the dynamical maps are defined with a reference trajectory and a reference energy, we will study the validity of this dynamical map when tracked particles have a large energy deviation with respect to the reference energy and large transverse excursions with respect to the reference trajectory. The next section of this chapter will present a comparison between two methods to study a non linear effect: the tune shift with amplitude. One method will require the numerical tracking of numerous particles whereas the second method will make use of the information directly contained in the dynamical map.

We will then describe the longitudinal dynamics in EMMA. It will be shown qualitatively that the fast acceleration scheme in EMMA, called serpentine acceleration, can be simulated with dynamical maps. We will also see that a bunch of particles starting

with different energies loses its structure (in other words "decoheres") within a few turns in EMMA without acceleration.

Eventually in chapter 5, we will investigate how dynamical maps can be efficiently used to predict the beam dynamics in any configuration of the EMMA lattice. The EMMA lattice having four degrees of freedom (strengths and transverse position of both magnets), it would be highly time consuming to compute a 3D field model for each new configuration of the lattice. Thus we will compute the dynamical map for a set of configurations and then directly interpolate the coefficients of the dynamical map for a given configuration. Since the symplecticity is not conserved in this process, we will instead interpolate the coefficients of the generating function corresponding to the given configuration, ensuring the symplecticity of the solution. This procedure will be included in an optimisation routine that looks for the lattice configuration respecting four constraints on the variation of the time of flight with energy.

The experimental procedure developed to measure the time of flight will then be presented; the optimisation routine will be applied to the real machine and we will assess the accuracy of the prediction obtained from beam simulations with dynamical maps.

The last chapter of this study will be dedicated to a summary of the results and conclusions obtained in the study. We then finally discuss the achievement of the original aims and define further objectives to apply this study to other types of FFAG accelerators, particularly non-linear machines.

1.5 Aims and objectives

Before going into the details of the study, it is important to clarify the overall aims of this study and the more detailed objectives. The structure of this thesis is such that each chapter deals with one of the main aims of the study. We listed below the main

aims and their corresponding objectives:

- Obtain an accurate 3D representation of a magnetic element.
  - create a 3D numerical solution of Maxwell's equations
  - optimise the fit of an analytical representation for this 3D model
- Derive the equations of motion of a particle in this magnetic element to obtain a dynamical map.
  - develop the Hamiltonian formalism for particle accelerators.
  - construct an explicit symplectic integrator
  - apply the integrator to integrate the dynamical variables in the form of Taylor series (dynamical map) through the analytical representation of the magnetic element.
- Study the validity of the beam dynamics simulations of FFAG accelerators with dynamical maps.
  - benchmark the dynamical map tracking results against the tracking code PyZgoubi for the EMMA accelerator for linear dynamics, studying in particular closed orbit, time of flight, tune per cell.
  - study a nonlinear effect of the dynamics
  - test the capability of the dynamical map to simulate the longitudinal beam dynamics in EMMA, especially during fast acceleration.
- Make use of the specificity of this method to analyse the experimental results.
  - develop computational tools for constructing a dynamical map for any derived machine configuration by interpolation between maps for a selected set of standard configurations.

- discuss the experimental procedure to measure the time of flight in the machine
- apply the new computational tools to predict the behaviour of the real machine starting from the measured configuration.

2

Representation of the magnetic field

2.1 Introduction

For systems described by a simple geometry a representation of the magnetic field can be obtained by solving analytically Maxwell's equations. However modern accelerator beamlines are often composed of magnets with complex geometries. Therefore deriving an analytical description of the magnetic field by solving directly Maxwell's equation in such complex geometries is often cumbersome. A general approach consists in using the Finite Element Method (FEM) to obtain a numerical solution to Maxwell's equations. Since analytical representation of the magnetic field is needed for the calculation of Dynamical Map for particle tracking, the objective of this chapter is to compute an accurate analytical description of the magnetic field from an arbitrary geometry of a magnetic element for which Maxwell's equations are solved numerically.

In the first section of this chapter, we will describe the construction of a numerical field map expressed in the form of a table containing the numerical values of the components of the magnetic field vector at various positions in a magnetic element.

This will be illustrated by the case study of the FFAG accelerator EMMA; however the technique can be generalised to any accelerator magneto-static element. First, the geometry of the magnetic element will be presented along with the hypotheses that will optimise the numerical computation of the magnetic field. We will then describe the Finite Element Method (FEM) used for this numerical solution to Maxwell's equations. FEM implies the creation of a mesh mapping the studied geometry. We will discuss the influence of the mesh configuration and compare the computed magnetic field with measurements of the real EMMA magnets.

In the second part we will derive an analytical description of the field from the previously created numerical field map. This analytical representation will be used in the next chapter to compute dynamical maps. Since dynamical maps are created by integrating the analytical description of the dynamical variables through the magnetic field, this latter must also be expressed analytically. To start with we will derive an analytical form in polar cylindrical coordinates by performing a 2D Fourier transform on the numerical data. Since in general, beam dynamics studies are performed in Cartesian coordinates, we will present a mathematical transformation of the analytical description from cylindrical to Cartesian coordinates. Finally we will outline the geometrical limitations of this transformation.

2.2 Description of the OPERA model of the EMMA magnets

The short lengths and wide apertures of magnets in the EMMA FFAG mean that the variations of the magnetic field in the longitudinal direction may be significant for beam dynamics. A 3D numerical solution of Maxwell's equation may be required to describe accurately the magnetic field. The EMMA magnets were designed with the software OPERA-3D [25, 29], solving Maxwell's equations numerically using the Finite Element

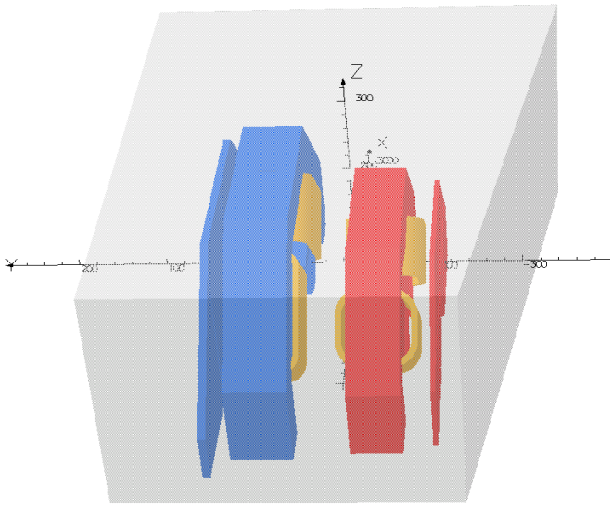

Figure 2.1: 3D view of the OPERA model of the EMMA cell.A particle travelling from left to right passes through a horizontally defocusing (D) quadrupole magnet (in blue), and then a horizontally focusing (F) quadrupole magnet (in red). Only the top half of the magnets are present in the model for symmetry reasons explained further in this section. Metallic plates (also called clamp plates) are located before the D magnet (in blue) and after the F magnet (in red). They limit the influence of the magnetic field induced by the magnets of the cell on the previous and following cell. No clamp plates could be inserted between the two magnets of a same cell because of a lack of space. The magnetic field is induced by circulating current in conducting coils wounded around the poles. These coils can be seen in yellow colour.

Method (FEM). For a given current distribution and a given geometry of the magnet yokes, the software computes the numerical values of the field at the nodes of a mesh mapping the whole geometry. The value of the field for positions in between these nodes must be interpolated.

In this section we will begin with defining the framework of the model, including the geometrical conventions chosen and the symmetries of the model. We will then briefly describe the Finite Element Method and the output format of the solution obtained. We will study how this solution differs when changing the mesh configuration used in the FEM. Finally, we will focus on the difference between solving Maxwell's equations in a system containing various magnetic elements. Either a field map is extracted from a model including simultaneously all the elements, or field maps are extracted for

individual elements and then superposed to represent the entire system. Field maps from these two approaches will also be compared to magnet measurements.

2.2.1 Geometrical conventions and symmetries of the model

We worked in a Cartesian coordinate frame $(\vec{x}, \vec{y}, \vec{z})$ where $\vec{x}$ and $\vec{y}$ are the horizontal and vertical transverse directions respectively and $\vec{z}$ is the longitudinal direction, oriented in the direction of the beam. This coordinate frame is not following the curvature of the beam. In each cell, its axes are straight. The EMMA ring is composed of 42 cells therefore the frame is rotated by an angle $2\pi/42$ around the $\vec{y}$ axis when passing from one cell to the next. B_x, B_y and B_z are the components of the magnetic field flux density vector **B** along these axes.

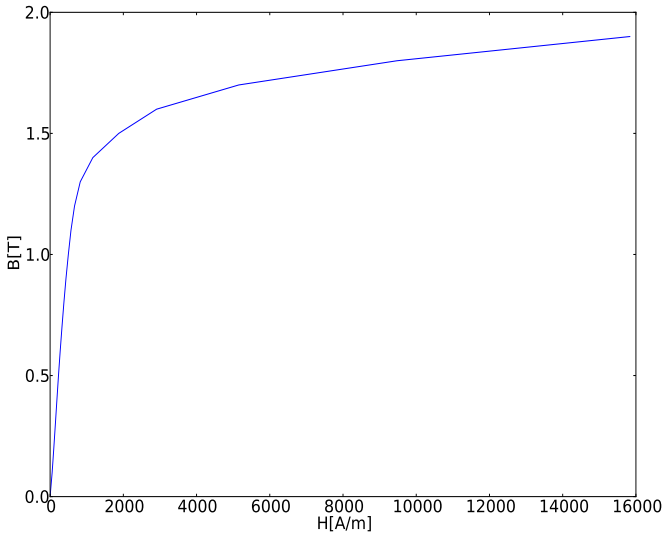

Figure 2.2: Evolution of the magnetic field **B** with respect to the magnetic intensity **H**.The data are given by the manufacturer of the EMMA magnet [26] and correspond to a yoke made of 1006 grade steel. The hysteresis effect is not taken into account here; in other words, figure 2.2 shows the curve of first magnetisation . We observe a sharp increase of B from 0 T to 1.5 T for H up to 2000 A/m, further increases in magnetic field intensity will result in no further change in magnetic field. This condition is called magnetic saturation.

The geometry of the EMMA cell used as case study is represented in figure 2.1.

Four distinct elements can be seen. The two thin plates on each side of the cell are clamp plates. They limit the influence of the magnetic field induced by the magnets of the cell on the previous and following cell. No clamp plates could be inserted between the two magnets in the same cell because of the lack of space.

In between the clamp plates, a particle travelling from left to right passes through a horizontally defocusing (D) quadrupole magnet (in blue), and then a horizontally focusing (F) quadrupole magnet (in red). Only the top half of the magnets are present in the model for symmetry reasons explained further in this section.

Each magnet is composed of a yoke joining four poles made of the same magnetic material around which are wound the conductive coils (in orange). In the case of EMMA, the magnets are made of magnetic alloy [28]. An important feature of any magnetic material is its response to an external field. The response of a material to an external magnetic field $\mathbf{B}$ is measured by the magnetic intensity $\mathbf{H}$:

$$\mathbf{B} = \mu_0 \mu_r \mathbf{H} \tag{2.1}$$

where μ_0 is a fundamental physical constant, the permeability of free space and μ_r is the relative permeability of the material. Often, the relative permeability of a given material is approximated by a constant; in reality, it is itself function of the fields that are present, and function also of the frequency of oscillation of the external field (hysteresis effect). Figure 2.2 shows the evolution of the magnetic field $\mathbf{B}$ with respect to the magnetic intensity $\mathbf{H}$. The data are given by the manufacturer of the EMMA magnet [26] and correspond to a yoke made of 1006 grade steel. The hysteresis effect is not taken into account here; in other words, figure 2.2 shows the curve of first magnetisation before any variation of the field strength. We observe a sharp increase of B from 0 T to 1.5 T for H up to 2000 A/m, followed by a slow evolution where further increases in magnetic field intensity will result in no further change in magnetic field.

Figure 2.3: Front view of the full quadrupole magnets. Focusing quadrupole magnet in red and defocusing quadrupole magnet in blue. Yellow coils are wounded around the poles. We observe that the magnetic axes are not aligned. The only symmetry of the system is a two fold symmetry with respect to the median plane $(\vec{x}, \vec{z})$.

This condition is called magnetic saturation.

In accelerator magnets, the magnetic field is induced by circulating current in conducting coils. Considering only magneto-static fields, the magnetic intensity $\mathbf{H}$ is related to current density $\mathbf{J}$ by Maxwell's equation:

$$\nabla \times \mathbf{H} = \mathbf{J} \tag{2.2}$$

We deduce that because of magnetic saturation, increasing current in the coils does not indefinitely raise the magnetic field in the yoke and therefore in the gap between the poles. For the magnetic field to follow linearly the current in the coil, we have to operate the magnet below the saturation threshold.

A quadrupole magnet has a four-fold symmetry and only the description of the magnetic field in a fourth of the magnet is sufficient to characterise the whole space. The intersection of the planes of symmetry is the magnetic axis (see figure 2.3). This axis is used as a reference to position the magnet in the ring. In EMMA, the magnetic axes of the F and D quadruples are not aligned, so when including both magnets in the OPERA model, the usual four-fold symmetry of a quadrupole is broken. The symmetry

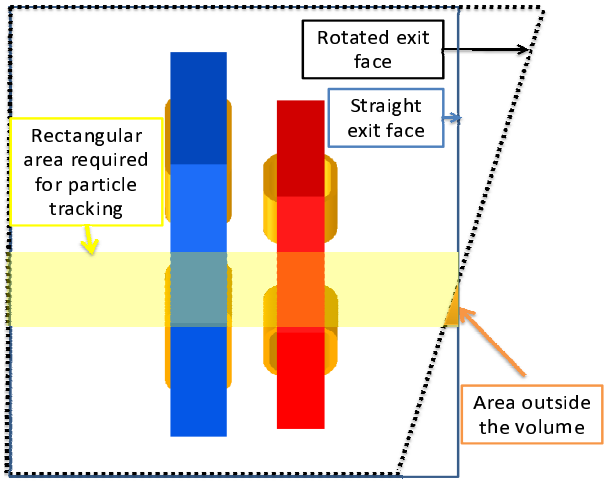

Figure 2.4: Upper view of the OPERA model of the EMMA cell with area of interest for beam dynamics. Most beam dynamics integrators or tracking codes requires a regular and rectangular numerical field map (corresponding to the yellow rectangular area. The rotation of the exit face prevents the extraction of a rectangular grid covering the full cell length because some points (orange area) are out of the solved volume delimited by the black dashed line. We therefore chose to solve the model with parallel faces with periodic boundary conditions.

with respect to the median plane $(\vec{x}, \vec{z})$ is conserved; thus, computing the upper half of the model as seen in figure 2.1 is necessary and sufficient.

The median plane is a boundary of our model but does not have any physical reality. The characteristic of the field in the plane should therefore conserve the symmetry of the full system expressed as:

$$B_y(y) = B_y(-y) \tag{2.3}$$
$$B_x(y) = -B_x(-y)$$
$$B_z(y) = -B_z(-y)$$

where positive sign for y corresponds to position above the median plane.

Longitudinally, an effort was made to respect the actual configuration of the EMMA

ring. At the edges of the cell, the magnetic field created by the magnets of the previous and following cells should be taken into account. In OPERA the periodic condition forces the field on a boundary to be the same as the field on a chosen twin boundary. By linking the entrance face to the exit face of the cell with the periodic condition, we simulate in reality the effect of the previous cell and the next cell on the field of the studied cell.

The EMMA ring is composed of 42 cells, each cell having a straight line as reference. Magnetic axes of the quadruples in each cell are parallel to that line. The angle between the reference lines of two adjacent cells is $2\pi/42$. Therefore to match the following entrance face, the exit face of a cell must also be rotated by that angle. This solution turned out to be inadequate for two reasons: first, in order to associate two twin boundaries, OPERA needed to construct exactly the same mesh on both 2D surfaces and fill up the 3D volume of the cell. The routine did not succeed when faces were not parallel. Further studies on OPERA routine could certainly solve this issue. Secondly most beam dynamics integrator or tracking codes requires a regular and rectangular numerical field map (corresponding to the yellow rectangular area on figure 2.4). The rotation of the exit face prevents the extraction of a rectangular grid covering the full cell length because a surface (orange area) remains outside the solved volume delimited by the black dashed line. We therefore chose to solve the model with parallel faces with periodic boundary conditions. This periodic boundary condition is thus an approximation since the straight exit face does not match exactly the entrance face of the following cell.

The assumption was made that the magnetic field was small enough close to the exit faces and that its effect on the beam dynamics would therefore be negligible.

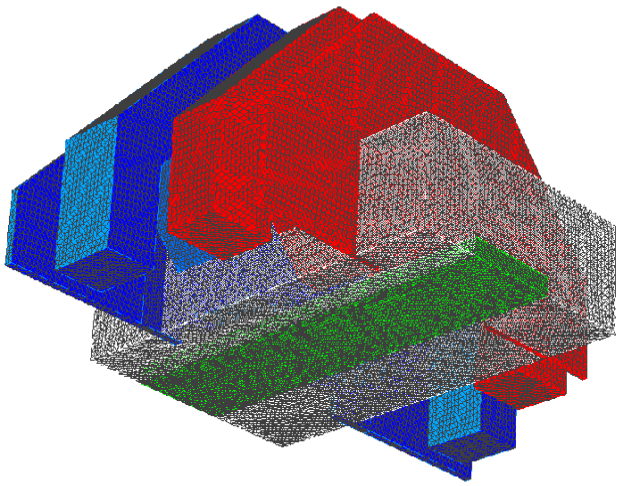

Figure 2.5: 3D view of OPERA meshed volumes in the EMMA cell. The OPERA model are divided into three volumes with different mesh sizes. This allow higher precision of the calculation in the regions close to the beam avoiding unnecessary precision on the far edges of the model. This figure shows the two inner air regions located in the gap of the magnets. The volume in green corresponds to the allowed excursion of the beam.

2.2.2 Finite Element Method (FEM)

The Finite Element Method (FEM) is based on the principle that by solving a set of equations for a given variable on a finite number of points (defining a mesh), the numerical value of this variable can be determined everywhere by interpolation [27]. The finer the mesh, the more accurate is the field description, but the longer it takes to compute a solution. In this study, the equations solved are Maxwell's equations in the magneto-static case.

When computing the solution, the non linearity of the magnetic permeability of the materials is taken into account. Indeed as explained in section 2.2.1, the magnetic permeability is a function of the external field. Thus it must be calculated after initially deriving the magnetic field distribution for a constant permeability. Once the actual permeability is computed, the new distribution of the magnetic field can be derived.

The process is therefore iterative and goes on until the change in **B** after another iteration is less than a given tolerance value. This value represents the numerical error tolerated in the solution at each node of the mesh. In this study we chose the OPERA default value: $10^{-6}\,T$, also used for the original design of the magnets. Further investigations could be useful to optimise this value, limiting computational time.

From the numerical solution of Maxwell's equations for a given mesh, the value of each component of the magnetic field **B** on a regular grid of points covering the beam path is interpolated. In general, this grid does not correspond to the mesh used by FEM, this latter being composed of tetrahedral elements that does not suit the rectangular grid required for particle tracking.

2.2.3 Mesh convergence study

The non material regions (neither yoke nor coil) in the OPERA model are divided into three volumes with different mesh element sizes. This allow higher precision of the calculation in the regions close to the beam while avoiding unnecessary precision on the far edges of the model. Figure 2.5 shows the two inner air regions located in the gap of the magnets. The volume in green corresponds to the allowed excursion of the beam. The third volume (not represented in figure 2.5) surrounds the whole system; it corresponds to the grey external box in figure 2.1. Since the volume of the model is constant, increasing the number of mesh elements means decreasing the size of these elements.

By steadily increasing the mesh density and computing the effect on a particle trajectory, one can determine the mesh density required to give a convergent tracking behaviour.

First, we looked at the value of the vertical component of the magnetic field in the median plane (**x**, **z**) while increasing the number of mesh elements. This gives a qualitative estimation of the convergence behaviour. Figure 2.6 shows the difference ΔB_y

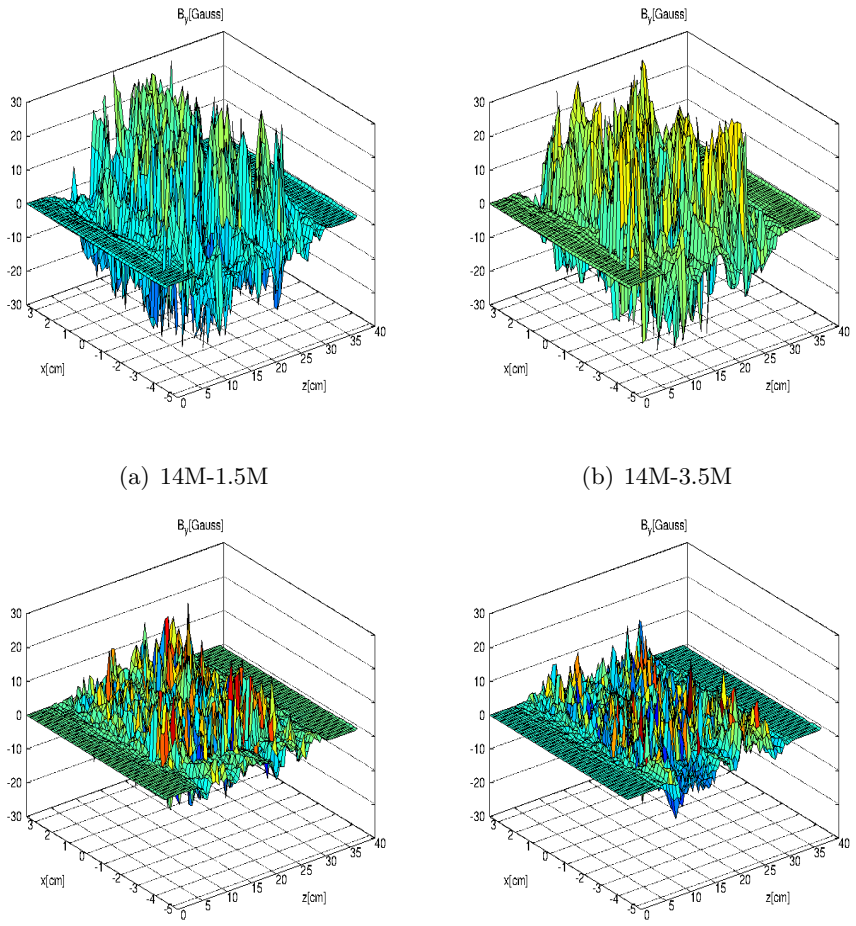

(a) 14M-1.5M

(b) 14M-3.5M

(c) 14M-6.7M

(d) 14M-9.1M

Figure 2.6: Difference in the vertical component of magnetic field (B_y) between 14 million mesh elements and 1.5 million mesh elements (top left hand side), 3.5 million mesh elements (top right hand side), 6.7 million mesh elements (bottom left hand side) and 9.1 million mesh elements (bottom right hand side) . Data are on the median plane (left).

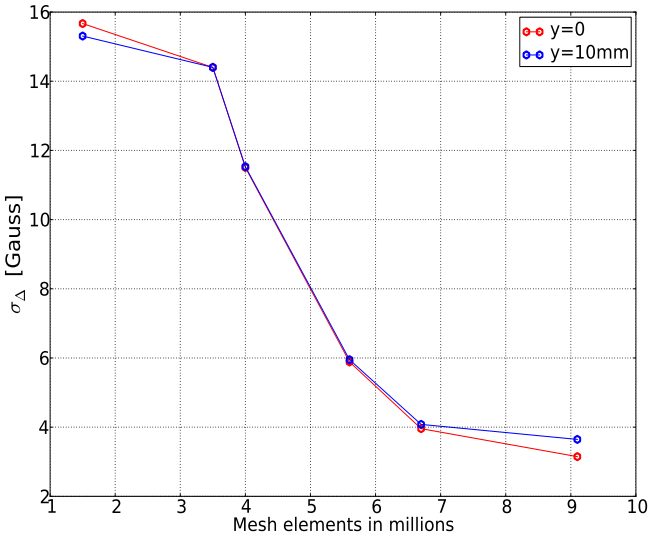

Figure 2.7: Standard deviation of the difference ΔB_y between a model with 14 million mesh elements and models with fewer mesh elements. The standard deviation is calculated over the median plane (y=0) and over the horizontal plane for y=1 cm. The standard deviation drops rapidly from 16 G to 4 G when increasing the number of element from 4 million to 6.5 million. Then increasing the number of elements above 7 million decreases the standard deviation by less than 1 G for both planes y=0 and y=1. A sensible choice for the number of element would therefore be between 7 million and 14 million.

between a model with 14 million mesh elements and models with smaller number of mesh elements. The smaller is ΔB_y, the closer to convergence is the solution, since increasing the number of mesh elements does not change the magnetic field configuration anymore.

Figure 2.7 shows the corresponding standard deviation of the error ΔB_y over the median plane (y=0) and over the horizontal plane for y=1 cm. The standard deviation drops rapidly from 16 G to 4 G when increasing the number of element from 4 million to 6.5 million. Then increasing the number of elements above 7 million decreases the standard deviation by less than 1 G for both planes y=0 and y=1. A sensible choice for the number of element would therefore be between 7 million and 14 million. To refine this estimation, beam dynamics obtained from field maps have to be compared

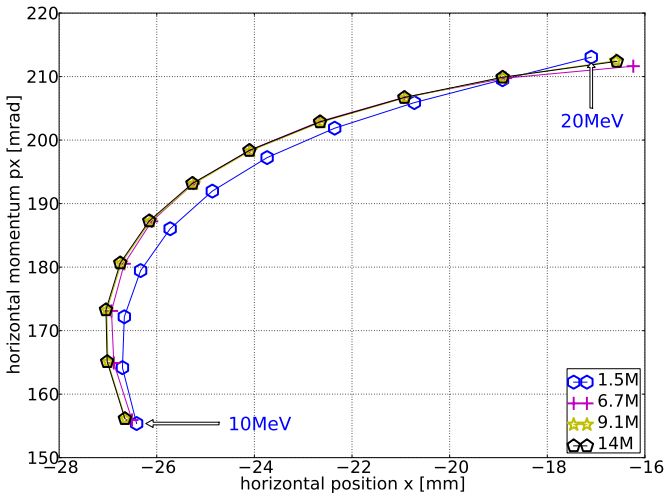

Figure 2.8: Closed orbit positions from 10 MeV to 20 MeV computed with field map obtained using different mesh densities. The yellow and black curves for 9.1 million and 14 million elements are overlapped. At 20 MeV the difference between the 6.7 million element curve and the 9.1 million element is still significant (about 300 μm). We conclude that the changes in the closed orbit introduced by increasing the number of mesh elements above 9.1 million would not be measurable in the machine since variations are smaller than the measurement precision of 50 μm.

for these several mesh configurations.

As explained in the first chapter, the main characteristic of the beam dynamics in EMMA are the closed orbit positions, time of flight and tunes for energies from 10 MeV to 20 MeV. The influence of the mesh configuration on these factors is shown in figures 2.8 to 2.11. These results have been processed in a pragmatic approach. A discrepancy is considered as relevant only if its magnitude is greater than the precision of the measurements in the real machine.

In an optimistic estimation, the tune per cell and the time of flight can be measured in the real machine to a precision of the order of 5×10^{-3} and 10 ps respectively. The horizontal position is estimated with a precision of 50 μm. We observe that increasing the number of mesh elements above 9.1 million would not be measurable in the machine since variations are below the measurement precision.

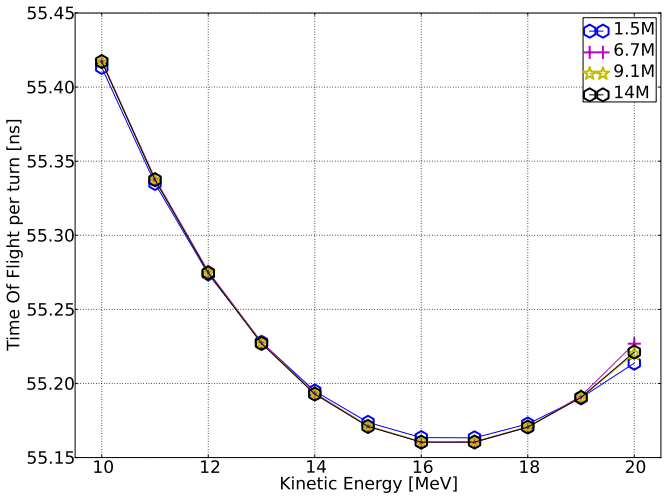

Figure 2.9: Time of Flight for one turn computed with field map obtained using different mesh densities. The four curves are overlapped for all energies except 20 MeV. The measurement precision being 10 ps, increasing the number of mesh element above 6.7 M varies the time of flight by amounts smaller than the measurement precision.

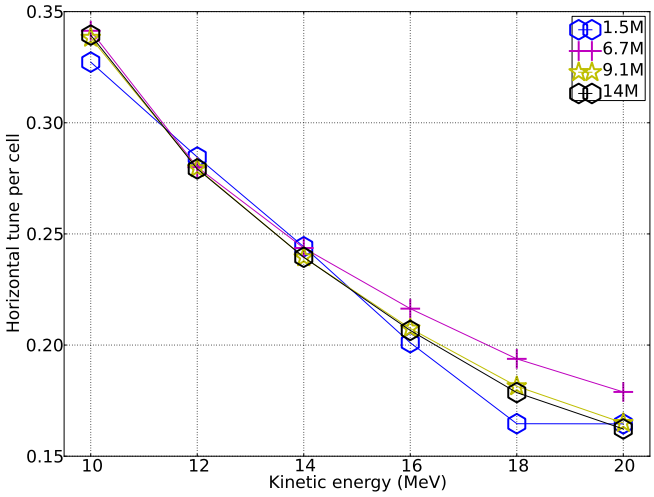

Figure 2.10: Horizontal tune per cell computed with field maps obtained using different mesh densities. The yellow and black curves for 9.1 million and 14 million elements are overlapped. At high energy, for instance 20 MeV, the model with 6.7 million mesh elements differs from the 9.1 million by about 0.01. This value being larger than the measurement precision, we conclude that a configuration with 9.1 million element is required for convergent beam dynamics.

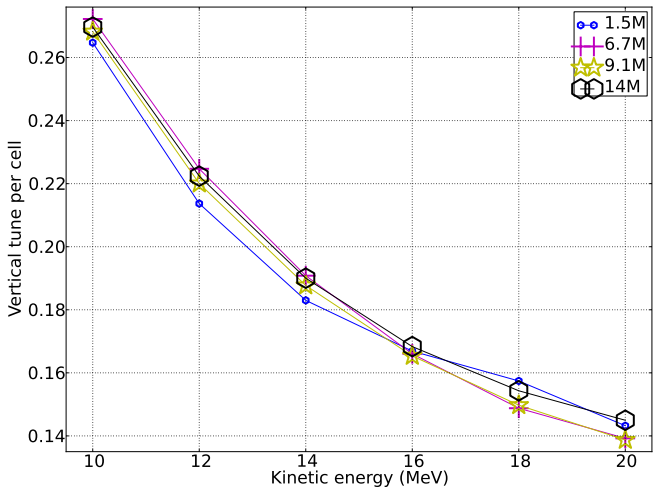

Figure 2.11: Vertical tune per cell computed with field maps obtained using different mesh densities. The discrepancy in vertical tune is of the order of 5×10^{-3} for high energies. It may be due to the variation of the mesh structure in the second volume (around the small volume representing the vacuum chamber in figure 2.5) having an effect vertically on the magnetic field distribution.

The discrepancy in vertical tune between the 9.1 million model and the 14 million model is of the order of 5×10^{-3} for high energies. It may be due to the variation of the mesh structure in the second volume (around the small volume representing the vacuum chamber in figure 2.5) having an effect vertically on the magnetic field distribution. To increase the number of mesh elements in the model, only the mesh density in the smaller volume is increased. The discontinuity in the mesh element size at the boundary between the smaller volume and the surrounding volume is therefore getting larger when increasing the number of mesh elements to 14 million. Since the volumes are rectangular with the narrow side in the vertical direction, the discontinuity in the mesh size over the border may affect more significantly the vertical dynamics. In order to confirm this hypothesis, the increase in mesh size should be carried on in both volumes, keeping the variation of the mesh size at the boundary at a constant ratio.

The final argument in favour of a 9.1 million mesh element model is the fact that

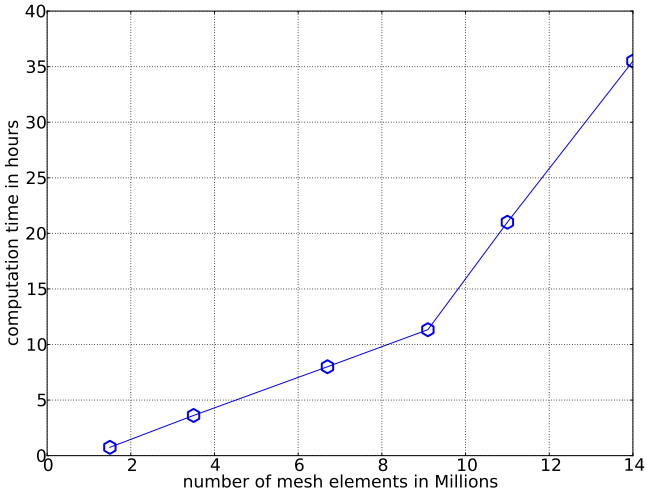

Figure 2.12: Evolution of computation time for an OPERA model with number of mesh elements. We chose to solve model with 9.1 million mesh elements because the computation time is about 10 hours allowing an overnight solving of the model. The gain in terms of beam dynamics simulations of a 14 million elements model that needs 35 hours to be solved is certainly not measurable in the real machine.

the computation time is about 10 hours allowing an overnight solving of the model (see figure 2.12). The gain in terms of beam dynamics simulation of a 14 million elements model of the EMMA cell, which needs 35 hours to be solved is not measurable in the real machine.

2.2.4 Field map construction

In this section, we will study the validity of the construction of a field map by superposition of two different field maps, one for each magnet. The process can be useful when modelling the entire EMMA cell with different gradient strengths. The magnets strengths can be varied in two ways: either the current in the coil in the OPERA model is increased and a new numerical solution is computed for each current configuration, or the field map produced for a given current is multiplied by a given factor. Choosing the first option means that a new model must be solved for each new current configuration;

the flexibility of the simulation is then highly reduced. We opted for the construction of field maps from separated model because it made possible the study of a larger range of lattice configurations.

The second option is valid if the magnetic strength increases linearly with the current in the coil; the magnet must not be in the saturation regime explained in section 2.2.1. Magnet measurements have shown [28] that for the range of current used in EMMA the excitation of the magnets with current was linear to within 2% . This means that the simulation results to the measured results should be compared in terms of magnet strengths, taking into account the 2% error in linearity when converting the current circulating in the real magnet and the corresponding magnetic strength induced.

To vary independently the two magnet strengths, one need a field map for each magnet. The field map of the entire EMMA cell is then created by superposition of the two adjusted field maps for each magnets. However it is not obvious that the arithmetical addition of the two field maps represents accurately the real configuration.

In a first approximation, one can compute a field map by superposing the field maps generated by powering each magnet separately and with the magnet powered far from the other magnet ("D only" + "F only"). In reality the yoke of one magnet may influence the field created by the other magnet; so we also computed a field map for the case when one magnet is powered and the yoke of the other magnet is present but not powered ("D + F"). Finally the results can be compared with field maps extracted from models including both magnets powered at the same time ("D&F").

We studied the difference in magnetic field in the median plane $(\vec{x}, \vec{z})$ between the two OPERA solutions: F magnet "on" only and F magnet "on" close the yoke of the D magnet "off". The result is shown in figure 2.13 on the left hand side. The blue and red rectangles represent the poles of the D magnet and F magnets respectively. The main effect occurs at the edge of the D magnet facing the F magnet for z=6 cm and

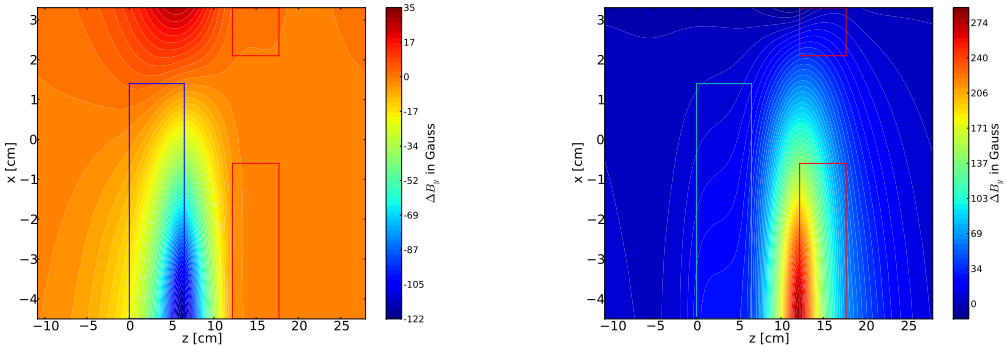

(a) "F only" - "F with D yoke"

(b) "D only" - "D with F yoke"

Figure 2.13: Difference in B_y in Gauss between D only and D with F yoke (b) and F only and F with D yoke (a) configurations. The blue and red rectangles represent the poles of the D magnet and F magnets respectively. The main effect occurs at the edge of the D magnet facing the F magnet for z= 6 cm and x= -4 cm where the difference in magnetic field is -122 G. The maximum corresponds to the transverse position where the pole of the D magnet ("off") is the closest to the median plane. On the path of particles (between x=-1 cm and x=+1 cm)) the maximum discrepancy is about 40 G. Similarly, on the right hand side of figure 2.13, we see the comparison between D magnet "on" only and D magnet "on" close the yoke of the F magnet 'off'. The largest discrepancy of 270 G is located at the edge of the F pole facing the D magnet for z=12.5 cm and x=-4.5 cm. The influence on the beam path is larger than for the previous comparison: about 200 G.

x=-4 cm where the difference in magnetic field is -122 G. The maximum corresponds to the transverse position where the pole of the D magnet ("off") is the closest to the median plane. This can be understood by observing the shape of the poles in figure 2.3. On the path of particles (between x=-1 cm and x=+1 cm) the maximum discrepancy is about 40 G. Similarly, on the right hand side in figure 2.13, we see the comparison between D magnet "on" only and D magnet "on" close the yoke of the F magnet "off". The largest discrepancy of 270 G is located at the edge of the F pole facing the D magnet for z=12.5 cm and x=-4.5 cm. The influence on the beam path is larger than for the previous comparison: about 200 G. We conclude that some magnetic field lines are "captured" by the non powered yoke and as a result the magnetic field in the gap changes. Hence a quantitative study in terms of beam dynamics is required to conclude whether the model must always include both magnets yokes.

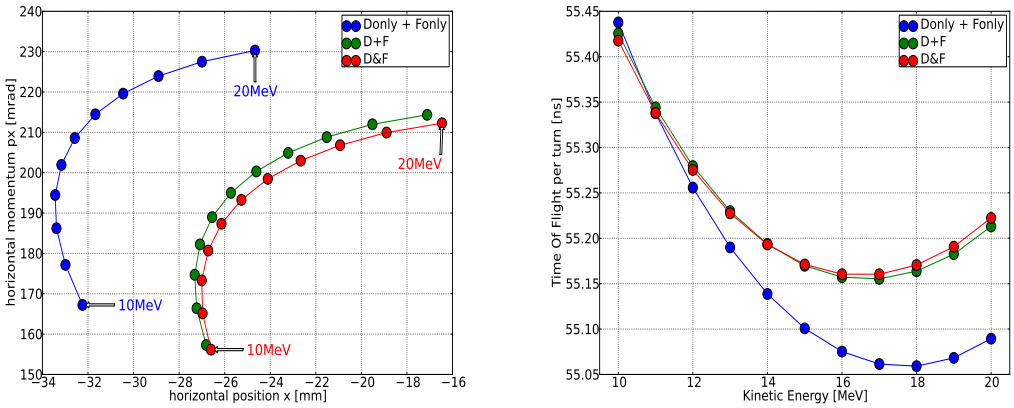

(a) Closed orbit position

(b) Time of flight

Figure 2.14: (a): Closed orbit position from 10 to 20 MeV computed for "Donly + Fonly", "D+F" and "D&F" configurations.(b): Time of Flight for one turn versus energy computed for "Donly + Fonly", "D+F" and "D&F" configurations. Tracking results in the "Donly+Fonly" configuration are significantly different from the others configurations. At 10 MeV, the closed orbit is shifted by about 5 mm and 10 mrad - from (-27, 155) for the "D+F" configuration to (-32, 165) for the "Donly+Fonly" configuration. Regarding the time of flight evolution with energy (figure 2.14(b)) a difference of 140 ps occurs at 20 MeV. This difference is significant (larger than the estimated measurement precision of 10 ps). Since the time of flight is crucial parameter for the dynamics in EMMA, we conclude that the unpowered yoke must be included in the OPERA model.

Figures 2.14(a), 2.14(b) and 2.15 show the difference between different configurations of the OPERA model in terms of positions of the closed orbit in transverse phase space (x, p_x) at different energies, in terms of time of flight evolution with energy and in terms of horizontal and vertical tunes per cell evolution with energy respectively. Particles were tracked in field maps constructed in the three configurations of the model explained at the beginning of this section. Tracking results in the "D only" + "F only" configuration are significantly different from the others configurations. At 10 MeV, the closed orbit is shifted by about 5 mm and 10 mrad —from (-27, 155) for the "D+F" configuration to (-32, 165) for the"Donly+Fonly" configuration. Regarding the time of flight evolution with energy (figure 2.14(b)) a difference of 140 ps occurs at 20 MeV. This difference is significant (larger than the estimated measurement precision of 10 ps). Since the time of flight is crucial parameter for the dynamics in EMMA, we conclude that the unpowered yoke must be included in the OPERA model. As a remark, in figure 2.15, we can observe a 0.05 difference in vertical tune between these two configurations. However the presence of the unpowered yoke does not significantly affect the horizontal tune.

We observe in figure 2.14(a) a 0.5 mm shift of the closed orbit at 20 MeV from "D&F" to "D+F" configuration. Such a difference may be measurable but will not affect significantly the main beam dynamics parameters in EMMA that are the time of flight and the tune. The maximum discrepancy for the time of flight evolution with energy differs is 10 ps at 20 MeV (see figure 2.14(b)) and the discrepancy for the horizontal and vertical tune is smaller than 0.001 over the entire range of energy (see figure 2.15). The difference between the two configurations does not significantly affect the main parameters of the beam dynamics.

It is now interesting to evaluate the discrepancy between the "D+F" and "D&F" configurations in terms integrated magnetic gradient along the entire cell. The gradient $\frac{\partial B_y}{\partial x}$ integrated along straight lines in the median plane through the entire cell for

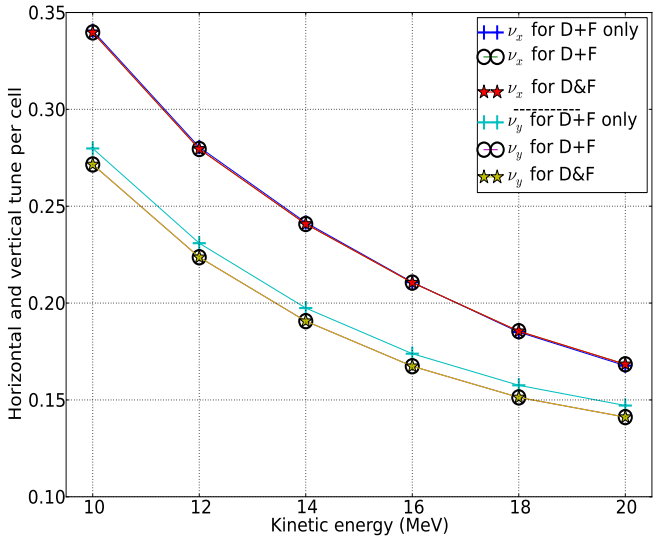

Figure 2.15: Horizontal and vertical tune per cell computed for "Donly + Fonly", "D+F" and "D&F" configurations. We can observe a 0.05 difference only in vertical tune between these two configurations. The presence of the unpowered yoke does not significantly affect the horizontal tune. The discrepancy between "D&F" and "D+F" configurations for the horizontal and vertical tune is smaller than 0.001 over the entire range of energy

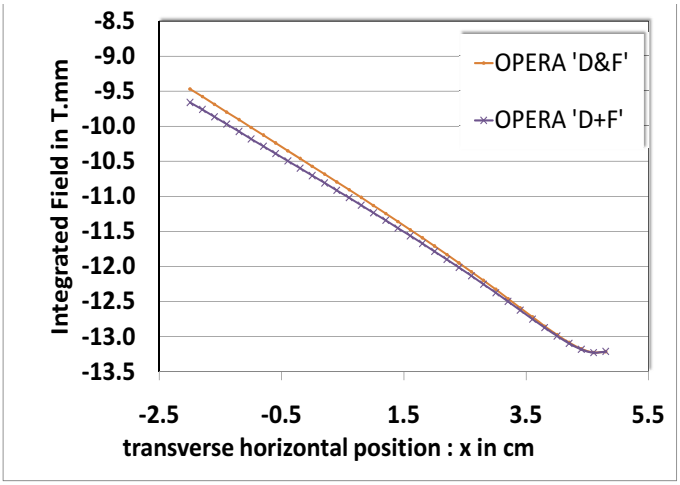

Figure 2.16: Integrated field along the EMMA cell computed for "D+F" and "D&F" configurations with simulated data.

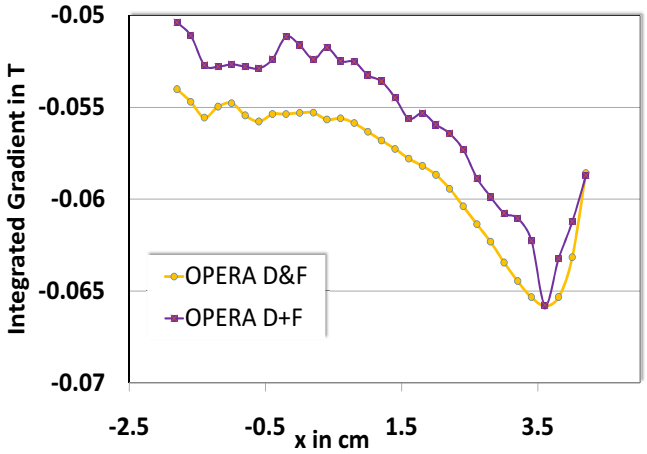

Figure 2.17: Integrated gradient along the EMMA cell computed for "D+F" and "D&F" configurations with simulated data.

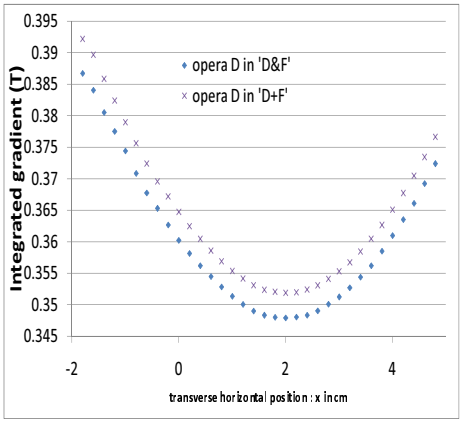

(a) D in "D+F" and "D&F"

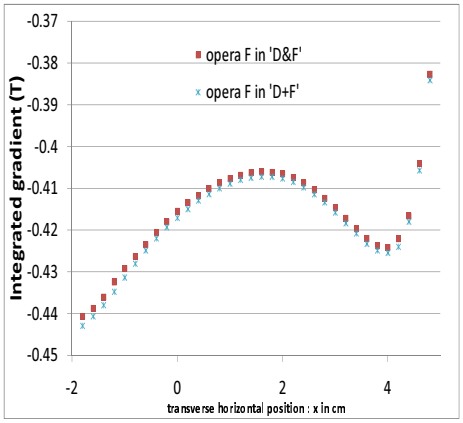

(b) F in "D+F" and "D&F"

Figure 2.18: Integrated gradient along the EMMA cell computed for individual magnets in "D+F" and "D&F" configurations with simulated data.

various horizontal positions. We observe in figure 2.17 that in both configurations, the integrated field gradient is not constant across the transverse excursion. This outlines the fact that because of the physical limitations, magnets do not create an ideal quadrupolar field, for which the field gradient $\frac{\partial B_y}{\partial x}$ should be constant in the horizontal transverse direction. For the "D&F" configuration, the relative variation on the beam path i.e. for $x < +10\,mm$ from -0.056 T at x=10 mm to -0.054 T at x=-20 mm is 3.8%. This result is within the tolerance for the magnet design [28].

Comparing "D+F" and "D&F" configurations, the integrated gradient is about 0.003 T larger (in absolute value) for the "D&F" configuration which corresponds to a 5% discrepancy between the two configurations. We observed in figures 2.14(a), 2.14(b) and 2.15 that this discrepancy did not affect significantly the linear beam dynamics.

To summarise, the presence of the unpowered magnet yoke has an influence on the beam dynamics when using the field map of individually powered magnet. We observed a large shift of the closed orbit positions over the entire range of energy and more important a difference in time of flight evolution with energy, greater than 100 ps for high energies. We concluded that when powering only one magnet, the solved OPERA model must also included the unpowered magnet.

According to the OPERA model, there is a small difference (5%) in the integrated gradient for field maps with both magnets on ("D&F") and the sum of the magnetic field from each magnet powered individually ("D+F") including the unpowered magnet. As a result the discrepancy in terms of beam dynamics is smaller than the measurement precision on the real machine. This suggests that the fields of the two magnets can indeed be computed independently, and the total field can be obtained by superposition.

The strength of individual magnet is adjusted by varying the entire numerical field map by a given factor. This is not valid for large currents where nonlinear features of the magnets (related to the "B-H curve in figure 2.2") may appear. A further study must be dedicated to evaluate the range of validity of the linear increase of the magnetic

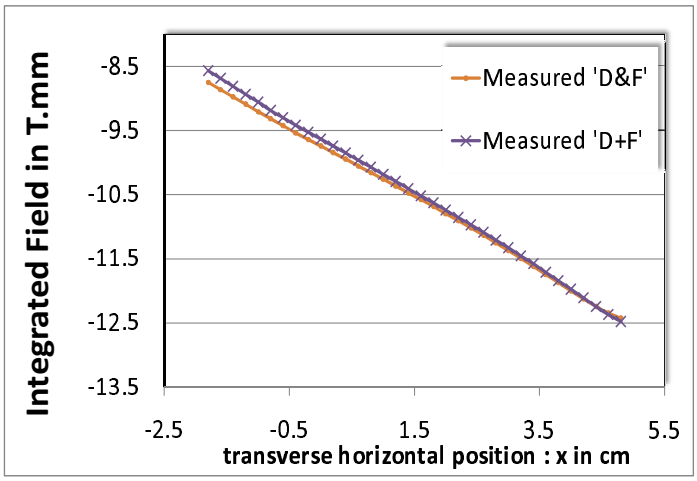

Figure 2.19: Integrated field along the EMMA cell computed for "D+F" and "D&F" configurations with measured data. The difference in integrated fields along the EMMA cell increases when going towards large negative value for x. The allowed transverse excursion for particles is (-1.5 cm, 1.5 cm). In that range the maximum discrepancy is about 0.1 T.mm. The relative difference is then of about 1% as in the same study in section 2.2.4 with OPERA field map in figure 2.16.

strength with the current.

In addition, we studied the validity of the superposition by processing data from the magnetic field measurement performed on prototype magnets.

2.2.5 Magnetic field measurements in the prototype magnets

The D and F magnets prototypes have been mounted on a measurement bench at Daresbury Laboratory. The magnetic field in the median plane of the prototype magnets has been measured using a Hall probe. A Cartesian grid of measurements has been used since the reference axis of a cell is a straight line. For mechanical reason, the measurement arm did not allow measurements to be made through the entire cell longitudinally. Thus, the measurements only provide an indication of the agreement between simulation and reality. Field maps have been measured for each individually powered magnet, including the unpowered yoke and for both magnets simultaneously powered. Figure 2.20 shows that the integrated gradients along the EMMA cell differ by about 0.05 T between "D+F" (purple) and "D&F" (green) configurations for

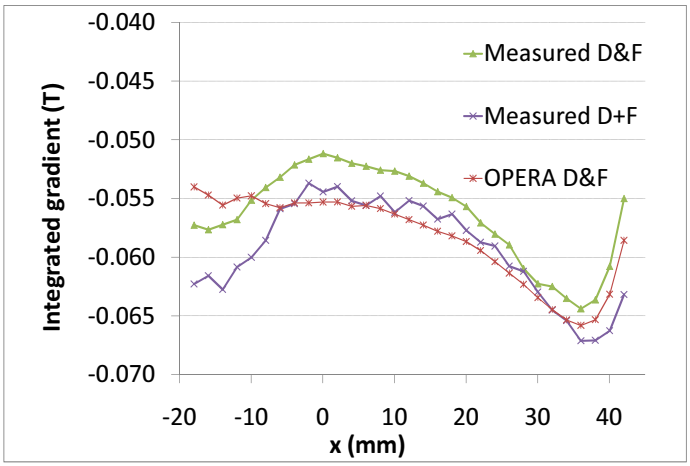

Figure 2.20: Integrated gradient along the EMMA cell computed for "D+F" and "D&F" configurations with measured data. The integrated gradients along the EMMA cell differ by about 0.05 T between "D+F" (purple) and "D&F" (green) configurations for measured fields. The relative difference is then of about 5% similarly to the same study in section 2.2.4 with OPERA field map in figure 2.17. Moreover, we observe that the discrepancy between the measured field and the OPERA field is again of the same order of magnitude.

measured fields. The relative difference is then about 5% similar to the result from the same study in section 2.2.4 with the OPERA field map in figure 2.17. No beam dynamics results could be derived from the measurements because beam dynamics simulations requires a three dimensional field map and field measurements had only been performed in the median plane. However with OPERA field maps, a 5% difference in the integrated field did not affect significantly the beam dynamics. We can therefore assume that the agreement between "D+F" and "D&F" configurations for measured fields can validate the superposition of field map.

We notice also that the integrated gradient for measured field for the "D+F" configuration is larger in absolute value than for the "D&F" configuration. It was the opposite when studying the field derived from the OPERA model. In addition, for x $<$ -10 mm the discrepancy between OPERA and the measured integrated gradient increases to about 0.01 T; the measured integrated gradient decreases when moving inward in the ring (negative value of x) whereas the OPERA integrated gradient in 2.17 increases. We conclude that the OPERA model does not match perfectly the real mag-

netic field. This is likely due to manufacturing errors of the real magnets not taken into account in the OPERA model. Also numerical approximations in the Finite Element Method may induce discrepancies. More detailed measurements may be necessary to identify the origin of the discrepancy. Increasing the precision of the FEM solution is also the subject for a further study. However, beam dynamics in the measured and simulated field maps should first be compared. A conclusion could then be drawn on the relevance of the integrated gradient.

The ultimate test to validate a simulation technique is to compare the simulated dynamics to the real machine dynamics where the discrepancy in integrated gradient is likely to have a significant effect.

2.2.6 Summary and conclusions

In the first section of this chapter we focused on the construction of a numerical field map from a given geometry of a magnetic element. To illustrate the process, we used the EMMA doublet composed of a defocusing quadrupole and a focusing quadrupole. The Maxwell's equations are solved numerically by Finite Element Method. We minimised the volume in which the equations are solved by considering the two-fold symmetry of the system. The four fold symmetries of each individual magnet were broken by the fact that their magnetic axes are not coincident.

An optimum number of mesh element of 9 million was chosen as a result of a compromise between the convergence of the beam dynamics results and the computing time required.

Then, we compared three ways to construct the field map of the entire EMMA cell. First we realised that when computing the field distribution for a single magnet powered, the magnetic field was affected by the presence of the unpowered yoke of the other magnet. The time of flight evolution with energy and the positions of the closed orbit at different energies were significantly affected. To be accurate magnets should

therefore be modelled taking into account the presence of the other magnet.

Eventually, we compared the field map created from the superposition of individual magnet (including the unpowered magnet) to the field map with both magnet powered simultaneously. The integrated gradients along the EMMA cell differed by 5% which resulted in a discrepancy in the beam dynamics smaller than the expected measurement precision in the machine. A similar result was obtained from measured field maps. We concluded that the superposition of field maps could give sufficiently accurate results as a first approach to simulation of an FFAG with dynamical maps. The superposition allows the study of the beam dynamics with field maps varying independently each magnet strength without computing a new OPERA model. However tracking simulations with dynamical maps require a further step in the processing of the field map : deriving an analytical representation of the magnetic field.

2.3 Analytical field representation

2.3.1 Introduction

A numerical field map often takes the form of a table of numerical values. A precise description of a magnetic element can lead to large tables, that may be cumbersome to handle. A more compact representation of the field derived from these tables is therefore of interest. Stronger motivations than the practical aspect justify the attempt to derive an analytical representation of the field.

Firstly, the solution to the Maxwell's equation given by FEM is numerical and therefore implies approximations. The solution obtained will not exactly respect Maxwell's equations. By fitting to the numerical data a function or a set of functions that are analytical solution to Maxwell's equations, the representation of the magnetic field is more physical. This does not mean that the analytical representation is more accurate with respect to the real magnets, but non physical features can be detected.

Secondly, with an appropriate choice for the set of functions, characteristics of the field can be outlined. For instance, by using series functions corresponding to the mode decomposition of the field, we can evaluate the higher-order modes in the field. On one hand, measurement or simulation noise can be decreased by filtering out higher-order modes. On the other hand, errors in magnets can be realistically introduced as higher-order terms.

Finally, the objective of this study is the simulation of beam dynamics using dynamical maps. We developed in more detail in chapter 3 that in order to compute the dynamical map of a cell, polynomial functions of the dynamical variables - transverse and longitudinal position and momentum- are propagated through the cell. At each integration step the equations of motion, relating the magnetic field and the dynamical variables are solved. This solution requires an analytical representation of the magnetic field (see chapter 3 section 3.2.3.3).

2.3.2 Analytical solution to Maxwell's equations in cylindrical coordinates

In this section, we will discuss the choice of Fourier series to fit the numerical data. First these functions will be expressed in polar cylindrical coordinates, more appropriate to the symmetry and periodicity of magnetic fields in accelerators. We will present the result of the fit by comparing the magnetic field derived from the Fourier series to the original numerical data.

Since conventional beam dynamics are expressed in Cartesian coordinates and more specifically because the integrator used to compute the dynamical map (see chapter 3) is written in Cartesian coordinates, an analytical formulation of the field in Cartesian coordinates will be derived from the previous fit. The resulting field given by Fourier Series in Cartesian coordinates will be also compared to the original numerical field map. Since the Fourier series are truncated to a chosen order, we will evaluate the

influence of high order terms on the fit quality. We will also investigate the effect of the periodicity imposed by the Fourier Series in Cartesian coordinates not matching the natural periodicity of the field in the transverse directions.

Eventually, we will discuss the range of validity of the analytical representation regarding the transverse excursion of the particles in an FFAG.

In free space and absence of electric field $\mathbf{E}$, the relevant Maxwell's equations are:

$$\nabla \cdot \mathbf{B} = 0, \text{ and } \nabla \times \mathbf{B} = 0\,. \tag{2.4}$$

Multiple fields of the form :

$$B_y + iB_x = |A_m| e^{-im\theta_m} r^{m-1} e^{i(m-1)\theta} \tag{2.5}$$

provide valid solutions of Maxwell's equation in free space [30]. r and θ are the polar coordinates within the magnet and θ_m is the angle by which the magnet is rolled around the z axis.

This multipolar field can be generated by currents flowing in coils around magnet poles as seen in yellow in figure 2.3. The field is a pure $2m$ pole field if the surface of the pole corresponds to a surface of constant scalar potential Φ, given by:

$$\Phi = -|A_m| \frac{r^m}{m} \sin(m\theta - \theta_m) \tag{2.6}$$

In reality magnet poles have limited size and cannot match perfectly this surface. Therefore the field is more generally expressed as a superposition of $2m$-pole field giving a multipole decomposition expressed as:

$$B_y + iB_x = \sum_{m=1}^{\infty} |A_m| e^{-im\theta_m} r^{m-1} e^{i(m-1)\theta} \tag{2.7}$$

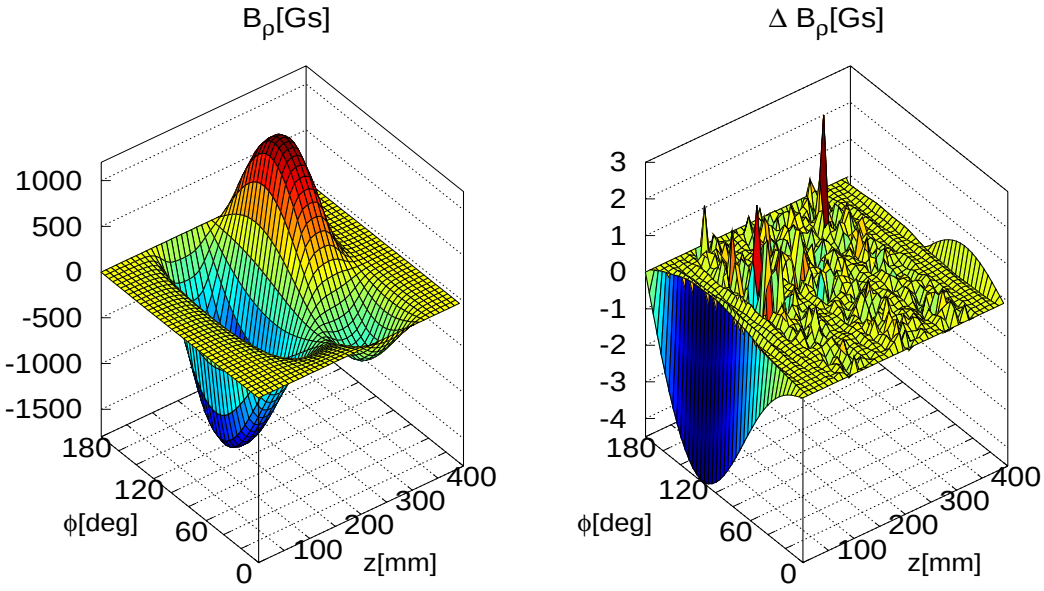

Figure 2.21: Radial component of the magnetic field (left) and residual of the fit (right) on a reference cylinder of radius $\rho_0 = 12\,\text{mm}$ within one EMMA cell. The (relatively) large residuals at the entrance and exit of the cell arise from the non-zero values of the field, which cannot be represented by the Fourier basis functions we have used. It would be possible to extend the basis functions to include these fields, however, with errors of the order of few gauss, this fit is considered good enough for our tracking studies.

and :

$$B_\theta + iB_\rho = (B_y + iB_x)e^{i\theta} = \sum_{m=1}^{\infty} |A_m| e^{-im\theta_m} r^{m-1} e^{im\theta} \tag{2.8}$$

These expressions are directly related to the azimuthal symmetries of a magnetic field, however it is only applicable to a 2D field. The longitudinal dependence of the field is not included in this formulation.

A 3D field representation that satisfies Maxwell's equations (2.4) is given by:

$$B_\rho = \int dkz \sum_m a_m(k_z) I'_m(k_z\rho) \sin(m\phi) \sin(k_z z), \tag{2.9}$$

$$B_\phi = \int dkz \sum_m a_m(k_z) \frac{m}{k_z\rho} I_m(k_z\rho) \cos(m\phi) \sin(k_z z), \tag{2.10}$$

$$B_z = \int dkz \sum_m a_m(k_z) I_m(k_z\rho) \sin(m\phi) \cos(k_z z). \tag{2.11}$$

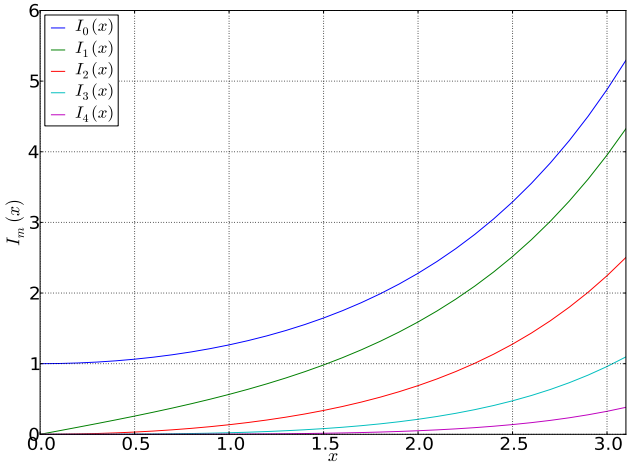

Figure 2.22: Modified Bessel function of the first kind $I_m(x)$ for m = 0,1,...,4

Including other phases in the azimuthal angle ϕ and the longitudinal direction z would fully generalise these equations. The functions $I_m(\rho)$ are modified Bessel functions of the first kind of order m. For small values of the argument ξ, the modified Bessel function of order m has the series expansion:

$$I_m(\xi) = \frac{\xi^m}{2^m \Gamma(1+m)} + O(m+1). \tag{2.12}$$

Functions for order $m = 0$ to $m = 4$ are plotted in figure 2.22. For larger value of ξ, the modified Bessel functions increase exponentially. It means that if we fit the field to data taken on the surface of a cylinder of radius ρ_0, then residual of the fit will increase exponentially outside the cylinder and decrease exponentially towards $\rho = 0$. Accelerator magnets often have a circular aperture, and in such cases, cylindrical coordinates provide an appropriate coordinate system for describing the field; other cases like undulator magnets or wigglers [34, 35] used for synchrotron radiation and free electron laser machines have rectangular aperture and Cartesian coordinate system is then most appropriate.

Performing the fit on a inscribed cylinder within the aperture maximise the "safe" region of the fit. In addition the modes written in polar basis reflect the real periodicity of the field with the angle ϕ given by the azimuthal symmetry $\vec{B}(\phi + 2\pi) = \vec{B}(\phi)$. To give a better understanding of this representation of the magnetic field, we can define a relation between the 2D multipole expansion and these 3D forms. If we consider the coefficients $a_m(k_z)$ given by:

$$a_m(k_z) = 2^m \Gamma(1+m) A_m \frac{\delta(k_z)}{m k_z^{m-1}} \tag{2.13}$$

where δ is the Dirac delta function and A_m a constant, by substituting this expression in equations (2.9-2.11) and integrating over k_z, we obtain:

$$B_\rho = \sum_m A_m \rho^{m-1} \sin(m\phi), \tag{2.14}$$

$$B_\phi = \sum_m A_m \rho^{m-1} \cos(m\phi), \tag{2.15}$$

$$B_z = 0. \tag{2.16}$$

We identify these expressions to a multipole field of order n in equation (2.8). Hence a two-dimensional multipole field is a special case of a three dimensional field expressed in (2.9-2.11) with mode coefficients given by equation (2.13). The mode coefficients $a_m(k_z)$ may be obtained by a 2D Fourier transform of the field on the surface of a cylinder of given radius inscribed in the magnets aperture. Since each coefficient $a_m(k_z)$ is related to a multipole coefficient of a 2D field, its contribution to the field made at any point is the contribution of a multipole of order m (e.g. dipole for m=1, quadrupole for m=2 and so on).

The Fourier Transform is performed using a Python library function for a Discrete Fourier Transform (DFT) [57]. The dependence of the field in the longitudinal direction is included in the coefficients returned by the DFT; hence the coefficients $a_m(k_z)$ are

now written a_{mn}. The field is given by:

$$\begin{aligned} B_\rho &= \sum_{m,n} a_{mn} I'_m(nk_z\rho)\sin(m\phi)\sin(nk_z z), \\ B_\phi &= \sum_{m,n} a_{mn} \frac{m}{nk_z\rho} I_m(nk_z\rho)\cos(m\phi)\sin(nk_z z), \\ B_z &= \sum_{m,n} a_{mn} I_m(nk_z\rho)\sin(m\phi)\cos(nk_z z). \end{aligned} \tag{2.17}$$

In this expression "m" is related to the contribution of multipoles of the two dimensional field and "n" refers to the longitudinal expansion of this contribution.

Note that equation 2.17 implies that for $z = 0$ the radial component of the magnetic field B_ρ must be zero. Therefore the fit on the field data will be accurate if the value for z=0 is close to zero.

Fig. 2.21 shows the radial field component and the residual of the fit on a reference cylinder of radius $\rho_0 = 12$ mm in one EMMA cell. The (relatively) large residuals at the entrance and exit of the cell arise from the non-zero values of the field, which cannot be represented by the Fourier basis functions we have used. It would be possible to extend the basis functions to include these fields; however, with errors of the order of few Gauss, this fit is considered good enough for our tracking studies.

To suppress this entrance residual we should use the general expression of the Fourier Series given by:

$$B_\rho = \sum_{m,n} \tilde{a}_{mn} I'_m(nk_z\rho)e^{im\phi}e^{ink_z z} + \sum_{m,n} \tilde{b}_{mn} I'_m(nk_z\rho)e^{im\phi}e^{-ink_z z} + c.c., \tag{2.18}$$

$$B_\phi = \sum_{m,n} \tilde{a}_{mn} \frac{m}{nk_z\rho} I_m(nk_z\rho)e^{im\phi}e^{ink_z z} + \sum_{m,n} \tilde{b}_{mn} \frac{m}{nk_z\rho} I_m(nk_z\rho)e^{im\phi}e^{-ink_z z} + c.c., \tag{2.19}$$

$$B_z = \sum_{m,n} \tilde{a}_{mn} I_m(nk_z\rho)e^{im\phi}e^{ink_z z} + \sum_{m,n} \tilde{b}_{mn} I_m(nk_z\rho)e^{im\phi}e^{-ink_z z} + c.c.\,. \tag{2.20}$$

"c.c" refers to the complex conjugate of the first part of the expression. These expressions still satisfy Maxwell's equations (2.4).

2.3.3 From cylindrical to Cartesian coordinates

In this section, we will give an analytical description of the magnetic field as Fourier series in Cartesian. For reasons explained later in this section, in the following of this study, we did not perform the Fourier transform directly in Cartesian coordinate as derived here, but instead performed the Fourier transform in cylindrical corrdinate and then convert the coefficients of the Fourier transform from cylindrical to Cartesian coordinates.

2.3.3.1 Field representation in Cartesian basis

Although cylindrical polar coordinates are more appropriate for the field description, beam dynamics studies are more conveniently performed using Cartesian coordinates. In that case, we need to obtain a representation of the field using basis functions in Cartesian coordinates. The field given by:

$$B_x = \iint c_{k_x,k_z} \frac{k_x}{k_y} \cos(k_x x) \sin(k_z z) \sinh(k_y y) dk_z \, dk_x, \tag{2.21}$$

$$B_y = \iint c_{k_x,k_z} \sin(k_x x) \sin(k_z z) \cosh(k_y y) dk_z \, dk_x, \tag{2.22}$$

$$B_z = \iint c_{k_x,k_z} \frac{k_z}{k_y} \sin(k_x x) \cos(k_z z) \sinh(k_y y) dk_z \, dk_x. \tag{2.23}$$

with $k_y^2 = k_x^2 + k_z^2$, satisfies Maxwell's equations (2.4). It is possible to find similar sets of equations but with different phase along each of the coordinate axes, and with the hyperbolic trigonometric function appearing for the dependence on x or z, rather than y.

We see that considering the vertical component B_y in (2.22) on a given plane $y = y_0$, we can derive the coefficients c_{k_x,k_z} from a discrete Fourier transform of field data given on a grid over x and z. In expression (2.22) the factor $\cosh(\mathrm{k_y y_0})$ is constant and can be extracted from the integral over k_x and k_z. The mode amplitude c_{k_x,k_z} are then

given by:

$$c_{k_x,k_z} = \frac{1}{\cosh(k_y y_0)} \iint B_y \sin(k_x x) \sin(k_z z) dk_z \, dk_x, \tag{2.24}$$

Because of the term $\cosh(k_y y)$, any small error in c_{k_x,k_z} will be amplified exponentially in B_y in (2.22) as we move away from y=y_0. On the other hand, any error in c_{k_x,k_z} will be damped exponentially as we move towards y = 0. When performing a discrete Fourier transform, the $\int$ is changed to a summation sign $\sum$. The field is the given by:

$$B_x = \sum_{m,n} c_{mn} \frac{mk_x}{k_y} \cos(mk_x x) \sinh(k_y y) \sin(nk_z z) \tag{2.25}$$

$$B_y = \sum_{m,n} c_{mn} \sin(mk_x x) \cosh(k_y y) \sin(nk_z z) \tag{2.26}$$

$$B_z = \sum_{m,n} c_{mn} \frac{nk_z}{k_y} \cos(mk_x x) \sinh(k_y y) \cos(nk_z z)\,, \tag{2.27}$$

now with $k_y^2 = (mk_x)^2 + (nk_z)^2$.

It is best to fit on a plane with y_0 as large as possible. The upper limit is given by the actual position of the magnet poles.

2.3.3.2 Periodicity and symmetry of the field representation

The expressions of the field in equations (2.21) to (2.23) only represent accurately fields that are periodic in x (with k_x kept in finite range). In general in accelerator, fields do not have such a periodicity hence a large number of modes will be necessary to give an accurate description which will be valid only over a limited range in x; generally, a fit to numerical field data based on equations (2.27) is less successful than one using cylindrical polar coordinates, equation (2.9).

However, it is possible to obtain a reasonable description of the field by converting the cylindrical mode coefficients a_{mn} to the Cartesian mode coefficients c_{mn}. A value for k_x needs to be assumed, and can be chosen to minimise the residual in the final field description.

Given a set of coefficients a_{mn}, our objective is to find the corresponding set of coefficients c_{mn}, such that the expressions in polar and Cartesian basis are equivalent. To reach this objective, we need to separate the coefficients in two groups: one group for even values of m and the other for odd values of m. These two groups corresponds in reality to two groups of modes of the magnetic field having different symmetries.

In this section we will derive the relation between a_{mn} and c_{mn} coefficients only for even values of m. The relation between a_{mn} and c_{mn} coefficients for odd values of m has also been derived. Both relations are used when reconstructing the magnetic field in Cartesian basis from the DFT in polar cylindrical basis.

However, in the case of a general magnetic field given in equations 2.18 to 2.20, the coefficients given by the DFT on a cylinder are complex. The imaginary part of a given multipole m gives the skew multipole strength. A m-skew multipole is just obtained by a rotation of the corresponding m normal multipole by $m\Phi/2$ around the longitudinal axis z. Most accelerator magnets are built with symmetries which keep skew multipoles to zero to prevent coupling between horizontal and vertical transverse dynamics [32]. In a real accelerator, skew multipoles are introduced by magnet positioning errors.

Field maps obtained from the OPERA model of the EMMA cell do not contains such errors since they assume an ideal symmetry. Hence in our case study, we did not take them into account and we only transformed the real part of the Fourier Transform coefficients from polar basis to Cartesian basis. If we intentionally add a skew component to the F magnet in the OPERA model (for instance by inverting the sign of the current in only two of the coils), we must be able to detect it in the analytical representation of the field.

Figure 2.23 shows the difference in Gauss between the Cartesian multipole expansion of the field and the initial version of the OPERA field map; this difference is the residual of the fit. At the location of the F magnet (z=250 mm), we observe a linear increase of the residual along the x axis which corresponds to a skew quadrupole (m=2) introduced

in the F magnet. The multipole decomposition method turned out therefore to be useful to outline errors in the OPERA model or in the real magnet measurements.

Further work must be dedicated to generalise this process transforming the representation of the magnetic field in equations 2.18, 2.19 and 2.20 to their Cartesian equivalent.

The multipole expansion was obtained from converting the normal multipoles derived from the Fourier Transform in cylindrical basis. Along the z axis, the defocusing and focusing magnets are located as shown in figure 2.13. Once obtaining the analytical reoresentation of the magnetic field, we derived the corresponding representation for the potential vector A, being the physical magnitude used to solved the equations of motion in particle tracking.

The potential vector and the magnetic field are related by :

$$\mathbf{B} = \nabla \times \mathbf{A} \tag{2.28}$$

From the description of $\mathbf{B}$ in (2.27), we obtain the expression for the components of the potential vector, chossing a gauge in which $A_x = 0$.

$$\begin{aligned} A_x &= 0 \\ A_y &= \sum_{m,n} c_{mn} \frac{nk_z}{mk_x k_y} \cos(mk_x x) \sinh(k_y y) \cos(nk_z z) \\ A_z &= \sum_{m,n} c_{mn} \frac{1}{k_x} \cos(mk_x x) \cosh(k_y y) \sin(nk_z z)\,, \end{aligned} \tag{2.29}$$

Equations 2.29 are used in the symplectic integrator built in chapter 3 to represent the magnetic element in which a particle is tracked. Note that the expression for the potential vector is different for odd and even values of the transverse mode m. Equations 2.29 are written for odd values of m.

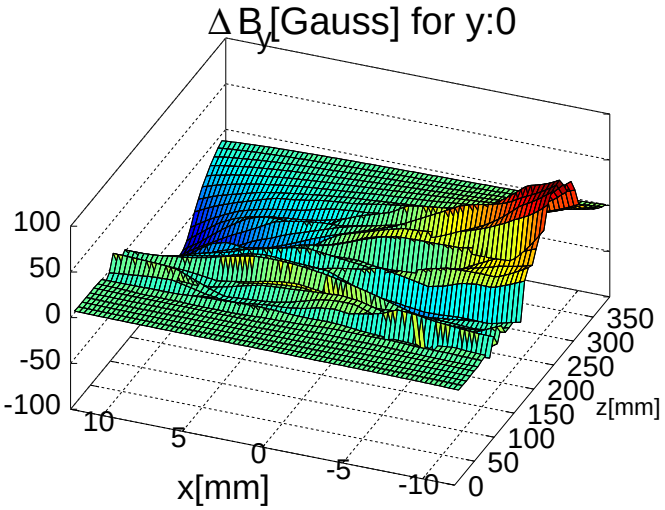

Figure 2.23: Difference in Gauss between the Cartesian multipole expansion of the field and the original OPERA field map (also called residual of the fit). At the location of the F magnet (z=250 mm), we observe a linear increase of the residual along the x axis. After obtaining this result we checked the original OPERA model and found a mistake in the current distribution of the coils of the F magnet introducing a skew quadrupole (m=2) in the field.

2.3.3.3 Mathematical transformation from cylindrical to Cartesian basis

The aim of this section is to derive a relation between the a_{mn} and c_{mn} coefficients. We will develop the case for even values of m and then mention the required change for odd values of m. The skew component of the magnetic field will not be treated here and should be developed in a further study for a more generalised transformation. We start with the expressions for the azimuthal component and vertical component of the magnetic field:

$$B_y = \sum_{m,n} c_{mn} \sin(mk_x x) \cosh(k_y y) \sin(nk_z z) \tag{2.30}$$

$$B_\phi = \sum_{m,n} a_{mn} \frac{m}{nk_z\rho} I_m(nk_z\rho) \cos(m\phi) \sin(nk_z z)\,. \tag{2.31}$$

Since the field in one representation must equal the field in the other representation at all points in space, and both fields are entirely determined by the coefficients, we can

choose any particular point in space to carry out the study. If we can find the relation between the coefficients a_{mn} and c_{mn} by considering the fields at that particular point, then we have solved the problem.

Let us choose the point:

$$x = \rho, \;\; y = 0, \;\; z = \pi/(2nk_z)\,. \tag{2.32}$$

For $y = 0$, i.e in the median plane, the relation between the transverse magnetic field components in cylindrical and Cartesian bases are given by:

$$B_y = B_\phi \;\text{ and }\; B_x = B_\rho \tag{2.33}$$

At that location in space, only considering even values for m, expressions (2.30) and (2.31) become:

$$B_\phi = \sum_{m,n} a_{mn} \frac{m}{nk_z\rho} I_m(nk_z\rho)\,, \tag{2.34}$$

$$B_y = \sum_{m,n} c_{mn} \sin(mk_x\rho)\,. \tag{2.35}$$

Then,

$$\sum_{m,n} a_{mn} \frac{m}{nk_z\rho} I_m(nk_z\rho) = \sum_{m,n} c_{mn} \sin(mk_x\rho) \tag{2.36}$$

Let us assume that a function f exists such that:

$$c_{mn} = f_{mm'} a_{m'n} \tag{2.37}$$

Our goal is to find the components $f_{mm'}$, which will allow us to transform from the cylindrical to the Cartesian basis. We make use of the series expansions for the

derivative of the modified Bessel function:

$$I_m(\rho) = \sum_{l=0}^{\infty} \frac{1}{l!m+l!}(\frac{\rho}{2})^{(2l+m)} \tag{2.38}$$

and for the sine function:

$$\sin(mk_x\rho) = \sum_{l=0}^{\infty}(-1)^l \frac{(mk_x\rho)^{2l+1}}{2l+1!} \tag{2.39}$$

As shown in appendix A, we can rewrite 2.36 in matrix form as:

$$\mathbf{v}_{lm} = \sum_{m'} \mathbf{k}_{lm'} f_{m'm} \tag{2.40}$$

where we define the matrix $\mathbf{v}$ with components:

$$\mathbf{v}^{(n)}_{l'm} = m\frac{(-1)^{l'}(2l'+1)!}{(l'+1-\frac{m}{2})!(l'+\frac{m}{2}+1)!}\frac{(nk_z)^{2l'+1}}{2^{2l'+2}} \tag{2.41}$$

and the matrix $\mathbf{k}$ with components:

$$k_{l'm'} = (m'k_x)^{2l'+1} \tag{2.42}$$

Formally, the matrices have an infinite number of components; however, we can reduce them to finite-sized square matrices by making appropriate truncations in l', m and m'. We can then solve equation 2.42 for the required components $f_{mm'}$:

$$f_{mm'} = \sum_{l'} \mathbf{k}^{-1}_{ml'} v_{l'm'} \tag{2.43}$$

We calculated in a similar way the transformation for odd values of m choosing $x = 0$, $y = \rho$ and $z = \pi/(2nk_z)$ as reference point where the relation between the component of the magnetic field in cylindrical and Cartesian bases are $B_y = B_\rho$ and

$B_x = B_\phi$. At that new location in space, considering only odd values of m, we have:

$$B_\rho = \sum_{m,n} a_{mn} I'_m(nk_z\rho)(-1)^{\frac{m-1}{2}}\,, \tag{2.44}$$

$$B_y = \sum_{m,n} c_{mn}\cosh(k_{y,mn}\rho)\,. \tag{2.45}$$

Eventually we obtain the components $g^{(n)}_{mm'}$ of the g function given by:

$$g^{(n)}_{mm'} = \sum_{l'} k^{-1}_{ml'} v^{(n)}_{l'm'}\,, \tag{2.46}$$

where the coefficient of the matrix $\mathbf{v}^{odd}$ are given by:

$$v^{(n)}_{l'm} = (-1)^{\frac{m-1}{2}} \frac{(2l'+1)!(nk_z)^{2l'}}{2^{2l'+1}(l'-\frac{m-1}{2})!(l'+\frac{m+1}{2})!} \tag{2.47}$$

and the matrix $\mathbf{k}$ with components:

$$k^{(n)}_{l'm'} = (m'^2k_x^2 + n^2k_z^2)^{l'} \tag{2.48}$$

Using equations (2.37), (2.43) and (2.46) one can transform the multipole expansion of the magnetic field from cylindrical to Cartesian basis. The analytical representation in Cartesian coordinate of the magnetic field can then be compared to the original numerical field data.

2.3.4 Cartesian coordinates fit

In EMMA, the excursion of particles in the vertical direction is supposed to be smaller than 1 cm. To simulate accurately the dynamics, the residual of the fit must be small up to vertical excursion of y=1 cm. As explained in section 2.3.2, the residual of a fit of the magnetic field data on a cylinder increases exponentially outside this cylinder. After transforming the fit coefficients from cylindrical basis to Cartesian basis, the range of

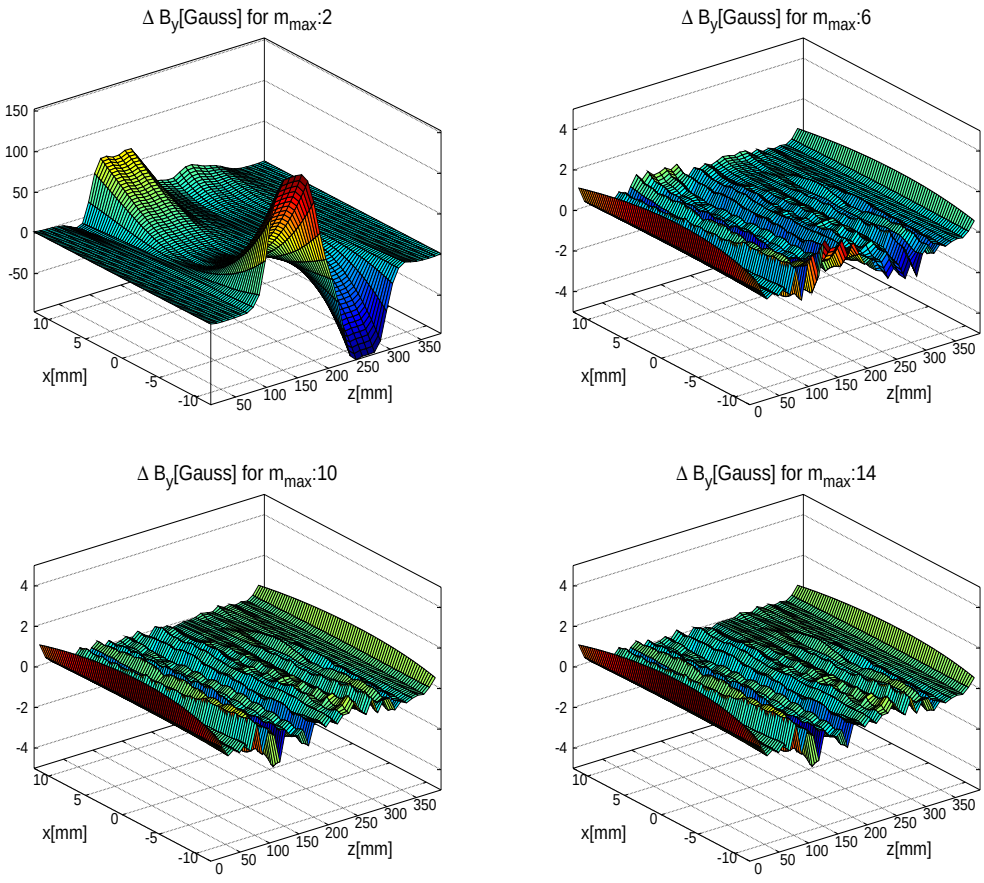

Figure 2.24: Residuals after Cartesian conversion for different transverse truncation order (m_{max}). Data are on the median plane.The Fourier expansion retaining only the quadrupole term $m = 2$ (a) does not include enough higher multipoles to represent accurately the numerical solution given by OPERA. In figure (b), the residual of fit including terms up to the 6^{th} order is plotted. The maximum values for the residual are now down to 2 G and -2 G in the D and F magnets respectively. The main higher harmonic that had to be included was therefore for $m = 6$.

validity of the analytical representation in Cartesian coordinate must be assessed. In addition Fourier Series contains in theory an infinite number of modes. Realistically, they must be truncated to a certain order in m and n. The accuracy of the fit will depend on the strength of the truncated high orders in the original field map. On the other hand, computation of high orders takes computational time. A compromise has to be found between appropriate computing time and an accurate fit. Eventually the physical meaning and the optimal value of the parameter k_x related to the periodicity of the field in the horizontal direction, must be discussed.

2.3.4.1 Truncation order of the Fourier expansion

In theory, Fourier Series solution to Maxwell's equations may contain an infinite number of multipole. In practise, they must be truncated to a certain order in m and n. The accuracy of the fit will depend on the strength of the truncated higher orders in the original field map. On the other hand, computation of high orders takes time. Beyond some point, the higher order coefficients become sensitive to noise (from numerical precision or inaccuracies in the field solution). Also applying the integrator (see chapter 3) takes longer with a Fourier series with many coefficients.

Since the magnets in EMMA are quadrupoles, the quadrupolar multipole $m = 2$ is expected to be the largest coefficient in the Fourier expansion. In theory, the symmetry of a magnetic field is entirely defined by the geometry of the magnet. The symmetry of a $2m$ multipole consists in changing the sign of the field $\mathbf{B} \rightarrow$ -$\mathbf{B}$ under a rotation by π/m about the z axis. However extra harmonics satisfy as well this condition. For instance in a quadrupole magnet geometry ($m = 2$), the symmetry of harmonics $m = 6$, 10, 14 and so on, also inverses the sign of the field under rotation by $\pi/2$ and are therefore allowed by the geometry of the magnets.

The strength of higher harmonics can be studied by increasing gradually the truncation order in m. In the top left corner of figure 2.24, we observe that the residual of

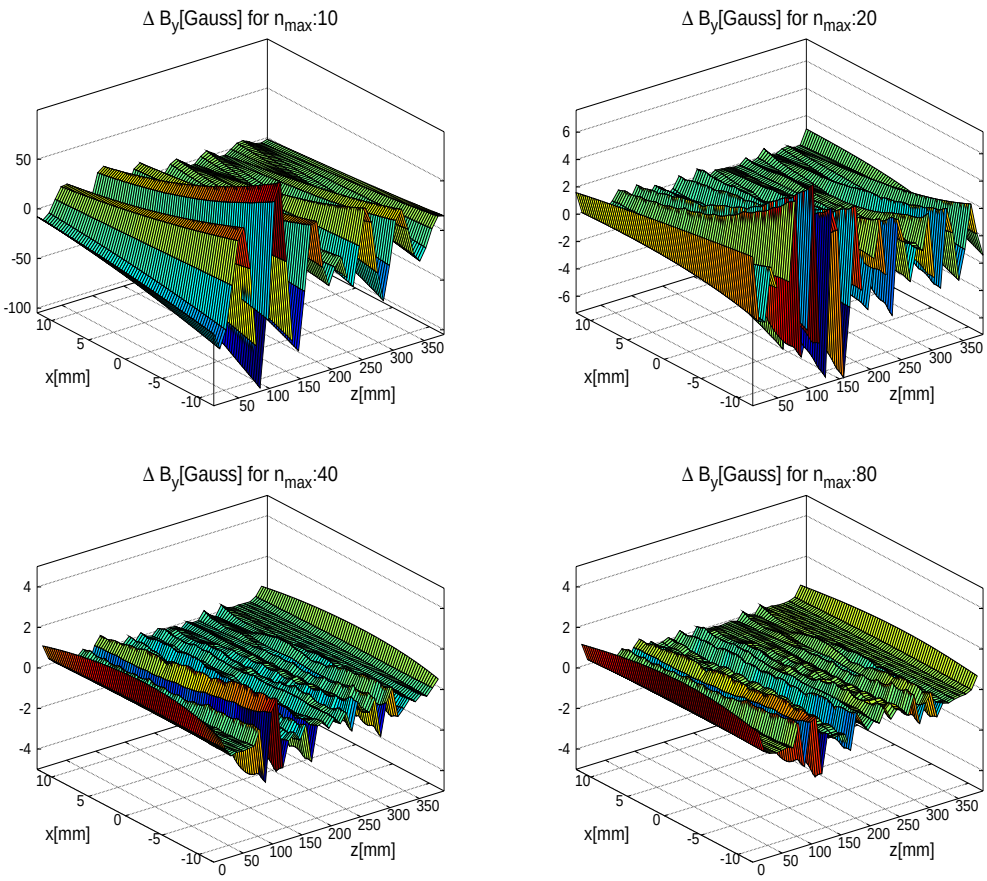

Figure 2.25: Residuals after Cartesian conversion for different longitudinal truncation order (n_{max}). Data are on the median plane. We observe that the maximum value of the residual (for $x = -10\,\text{mm}$ and $z = 100\,\text{mm}$) decreases from 100 G (top left corner) to 2 G (bottom left corner) when increasing the truncation order from $n_{max} = 10$ to $n_{max} = 40$. Then keeping higher modes up $n = 80$ does not have significant effect on the residual. Therefore the longitudinal truncation order chosen is $n_{max} = 40$.

the fit including only terms up to the 2^{nd} order reaches values of the order of 100 G for $x = -10$ mm and $z = 150$ mm (in the D magnet) and values of the order of -100 G for $x = -10$ mm and $z = 250$ mm (in the F magnet). This means the Fourier expansion retaining only the quadrupole term $m = 2$ does not include enough higher multipoles to represent accurately the numerical solution given by OPERA. On the top right corner of the same figure, the residual of fit including terms up to the 6^{th} order is plotted. The maximum values for the residual are now down to 2 G and -2 G in the D and F magnets respectively. The main higher harmonic that had to be included was therefore for $m = 6$. The fact the residual error has opposite sign in the D magnet ($z = 150$ mm) and in the F magnet ($z = 250$ mm) shows that higher transverse harmonics still have a non-zero strength.

Including harmonics up to $m = 10$ in the bottom left corner, we observe that the maximum of the maximum value of the residual is about 1 G for $x = -10$ mm and $z = 150$ mm but this maximum does not seem to be related to the transverse configuration of the magnet since it is not visible in the other magnet. It is more likely to be caused by the truncation of longitudinal modes (studied in figure 2.25). From the bottom right corner plot, we conclude that increasing the truncation order up to $m = 14$ did not have an effect on the accuracy of the fit. We therefore chose $m_{max} = 10$ as transverse truncation order.

Because magnets have finite length in the z direction, the Fourier expansion must include longitudinal variation of the field to accurately match the numerical solution from OPERA. The longitudinal features are decomposed as modes n in the Fourier expansion similarly to transverse mode m. These modes represents the frequency of oscillation of the field along the z direction. Rapid variations (in space) of the field along z (such as magnet edges) requires high order n modes. The residuals of the fit for longitudinal truncation order $n_{max} = 10$, 20, 40, 80 are shown in figure 2.25 (the horizontal truncation order is $m_{max} = 10$). In all plots, the largest value of the residual

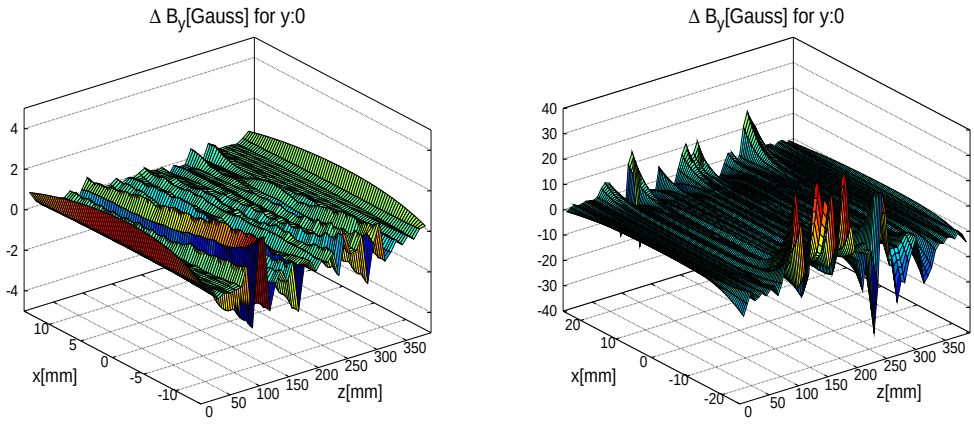

Figure 2.26: Residuals after Cartesian conversion over a large range in x (r.h.s), and over a region contained within the original 12 mm radius reference cylinder (l.h.s). Data are on the median plane. The exponential increase in the residuals for transverse position outside the reference cylinder originally used for obtaining the fit can be seen clearly for large x. Therefore performing a Fourier transform in cylindrical coordinates and then deriving the mathematical equivalent in Cartesian coordinates conserves the "safe zone" in the median plane for the fit within the reference cylinder, adapted for accelerator magnet.

occurs for $z = 100\,\text{mm}$ corresponding to the entrance face of the D magnet. At that location the rate of variation of the field requires high order modes. We observe that the maximum value of the residual (for $x = -10\,\text{mm}$ and $z = 100\,\text{mm}$) decreases from 100 G (top left corner) to 2 G (bottom left corner) when increasing the truncation order from $n_{max} = 10$ to $n_{max} = 40$. Then keeping higher modes up $n = 80$ does not have significant effect on the residual. Therefore the longitudinal truncation order chosen is $n_{max} = 40$.

We will see in section 2.3.4.2 that the residual obtained for that truncation order (bottom left corner of figure 2.25), which is plotted as well in figure 2.27 was good enough to simulate dynamics with an accuracy (with respect to the OPERA model) smaller than the measurement precision of the machine.

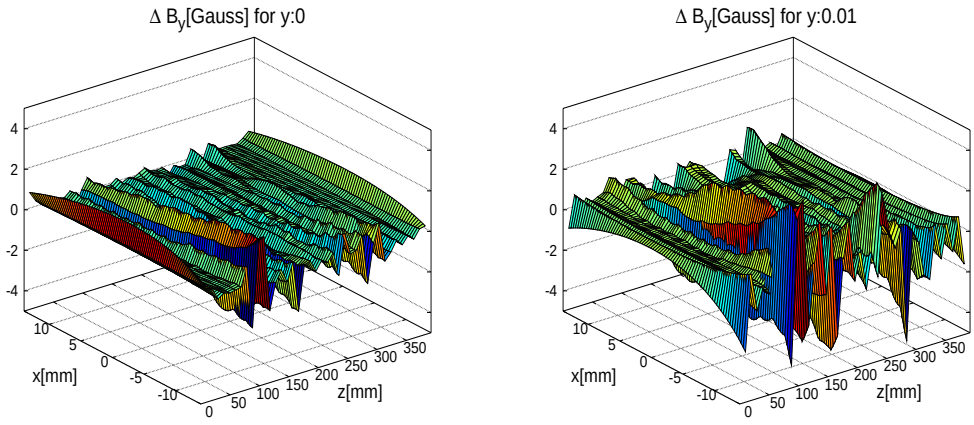

Figure 2.27: Residuals of the fit in the median plane (l.h.s) and in plane with coordinate y=1 cm (r.h.s). In both cases, the residual increases with the transverse excursion x in negative values. On the median plane the residual reaches a maximum of 2 G at the entrance of the D magnet. Since the field at that point is of about 2000 G, the relative error is 0.1%. More importantly the discrepancies have peak shapes in the longitudinal direction corresponds to high order longitudinal mode. It means that their effect on the integrated gradient is negligible. For y=1 cm, the residual has a maximum of 4 G which is also accurate enough.

2.3.4.2 Validation of the analytical description of the field in Cartesian basis

In this section Fourier expansions are truncated to the 10^{th} order in m and 40^{th} order in n meaning that higher orders are not included in the calculation of the magnetic field.

Figure 2.27 shows the residual of the fit in the median plane on the left hand side and in plane with coordinate y=1 cm on the right hand side. In both cases, the residuals increase with the transverse excursion x in negative values. For y=1 cm, the residual reaches a maximum of 4 G for x=-15 mm and z=110 mm. In figure 2.28, we observe that the difference in integrated field is 0.2 T.mm across the entire transverse range. Therefore closed orbit and time of flight evolutions with energy are accurately simulated by the analytical description for vertical coordinates up to y=1 cm. We draw the same conclusion for the tune evolution with energy since the discrepancy in terms

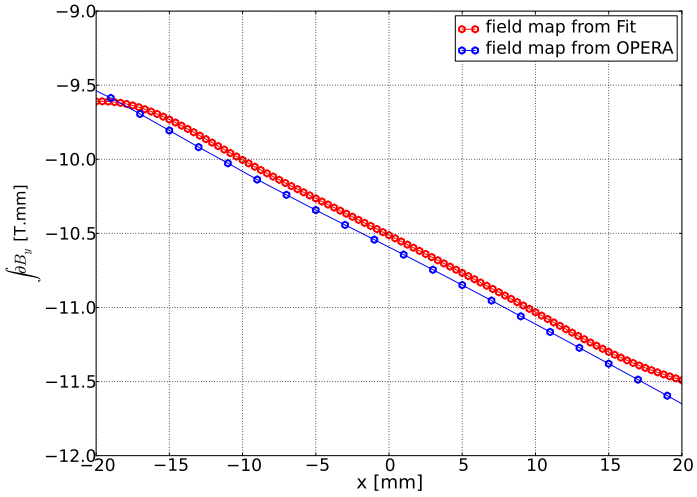

Figure 2.28: Comparison of the integrated field between the numerical field map and the analytical description in Cartesian basis. The field data are in the plane (y=1 cm). The difference in integrated field is 0.2 T.mm across the entire transverse range. The discrepancy is of the same order as that of figure 2.16 which had small impact on the beam dynamics (tune and time of flight).

of integrated gradient reaches a maximum of 0.02 T for x=-5 mm.

Figure 2.26 shows the residuals after Cartesian conversion over a large range in x (right hand side), and over a region contained within the original 12 mm radius reference cylinder (left hand side). Data are on the median plane. The residual increases exponentially for transverse position outside the reference cylinder. On the left hand side the residual reaches a maximum of 2 G at the entrance of the D magnet (z=110 mm). The vertical component of the field at that point is about 2000 G, so the relative error is 0.1%.

In section 2.2.4 we studied the effect of magnetic field discrepancy (between "D+F" and "D&F" configurations) on the linear dynamics (closed orbit, tune and time of flight evolutions with energy) by evaluating the difference in terms of integrated field and integrated gradient $\int \frac{\partial B_y}{\partial x} dz$ along the z axis for various transverse positions x. Closed orbit and time of flight evolutions with energy are linked to the integrated field whereas

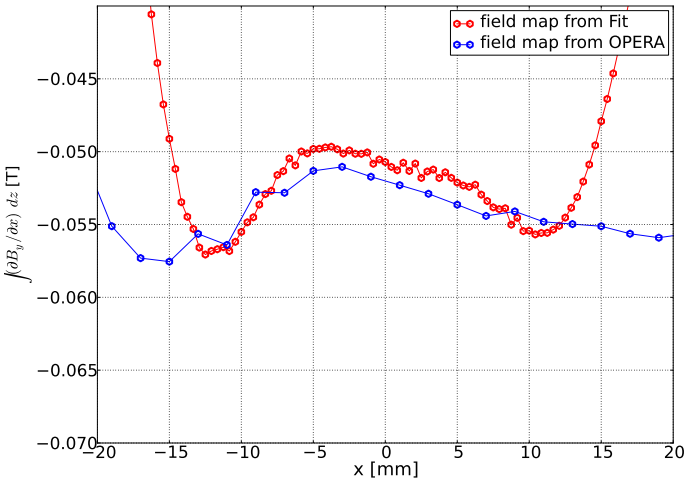

Figure 2.29: Comparison of the integrated gradient between the numerical field map and the analytical description in Cartesian basis.The field data are in the plane (y=1 cm). We observe an exponential increase of the residual of the fit outside the 12 mm radius reference cylinder. Within this cylinder the maximum discrepancy is 0.002 T for x=-9 mm. Since for the field map superposition in 2.17, we saw that such discrepancies of the same order did not affect the dynamics we conclude that the analytical representation of the magnetic field in Cartesian basis is accurate enough.

tune evolution with energy is related to the integrated gradient. The discrepancy in integrated field reached 0.2 T.mm for x=-2.5 cm (see figure 2.16); it resulted in dynamical effects smaller than the precision measurement on the real machine (see figures 2.14(a) and 2.14(b)). The difference in tune evolution with energy was also negligible (see figures 2.15) for a maximum discrepancy of 0.01 T for the integrated gradient (see figure 2.17).

We now compare the numerical field map and the analytical description in Cartesian basis in terms of the integrated field and the integrated gradient respectively. The field data are in the plane y=1 cm, upper limit of the vertical motion of the particles; the residual decreases exponentially for smaller value of y. The difference in integrated field is 0.2 T.mm across the entire transverse range (see figure 2.28). Also figure 2.29 shows the exponential increase of the residual of the fit outside the 12 mm radius reference

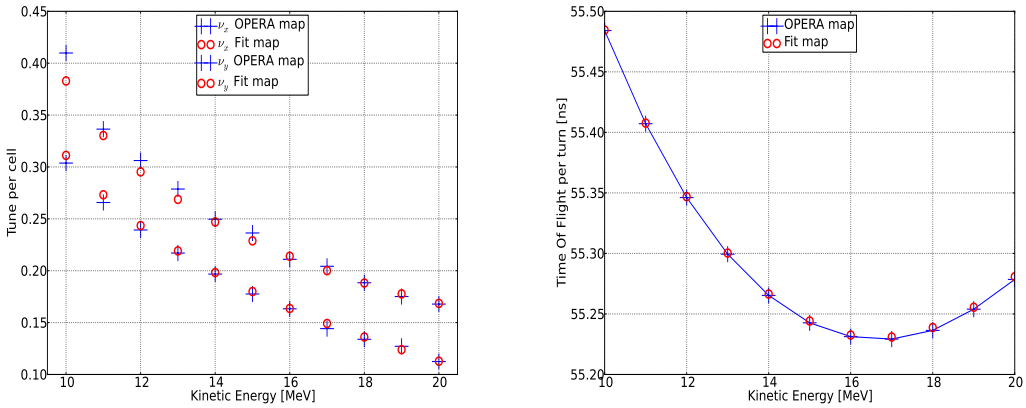

(a) Tune per cell vs. energy

(b) Time of flight vs. energy

Figure 2.30: Comparison of tracking results in the original numerical field map and in a field map from the analytical representation (Fourier series in Cartesian coordinates). Particles are tracked in both maps with PyZgoubi. We observe in (a) that the agreement is almost perfect for the time of flight from 10 MeV to 20 MeV. However in (b), a disagreement in the horizontal tune of about 0.02 occurs at 10 MeV; this is likely to be due to the fact that the 10 MeV orbit has a large excursion and therefore the accuracy of the analytical representation may not be sufficient, and therefore a cylinder with larger radius would be needed.

cylinder. Within this cylinder the maximum discrepancy is 0.002 T for x=-9 mm.

It is possible to create a numerical field map from the analytical representation by interpolation of the field on a grid. We can then track particles in this field map (called "fit map") and compare with tracking result in the original numerical field map for values of the tune and time of flight at various energies. Particles are tracked in both maps with PyZgoubi. We observe in figure 2.30(b) that the agreement is almost perfect for the time of flight from 10 MeV to 20 MeV. However in figure 2.30(a), a disagreement in the horizontal tune of about 0.02 occurs at 10 MeV; this is likely to be due to the fact that the 10 MeV orbit has a large excursion and therefore the accuracy of the analytical representation may not be sufficient; a cylinder with larger radius would be needed. However we will see in section 2.3.5 that the radius is limited and the solution could be to scan the aperture with various reference cylinders.

To sum up, we have studied in this section the accuracy of the analytical description of the magnetic field in terms of magnetic field characteristic. The small differences with respect to the original field map in terms of integrated field $\int B_y dz$ and integrated gradient $\int \frac{\partial B_y}{\partial x} dz$ along the z axis for various transverse positions allowed us to conclude that the linear dynamics can be accurately simulated with this Fourier expansion in Cartesian basis.

2.3.4.3 Interpretation and influence of the periodicity parameter k_x

As explained in the section 2.3.3.2, the functions representing the field in Cartesian basis have an inherent periodicity in the x direction arising from the dependence on a trigonometric function characterised by the parameter $k_x = \pi/x_{max}$ where x_{max} corresponds to the wavelength of the field. In reality the magnetic field is not periodic along the transverse Cartesian axes $\vec{x}$ and $\vec{y}$. Nevertheless an accurate fit may be achieved by choosing an appropriate value for k_x; since the field drops to zero for transverse position $x = \pm x_{max}$ the distance $2x_{max}$ corresponds to one period for which

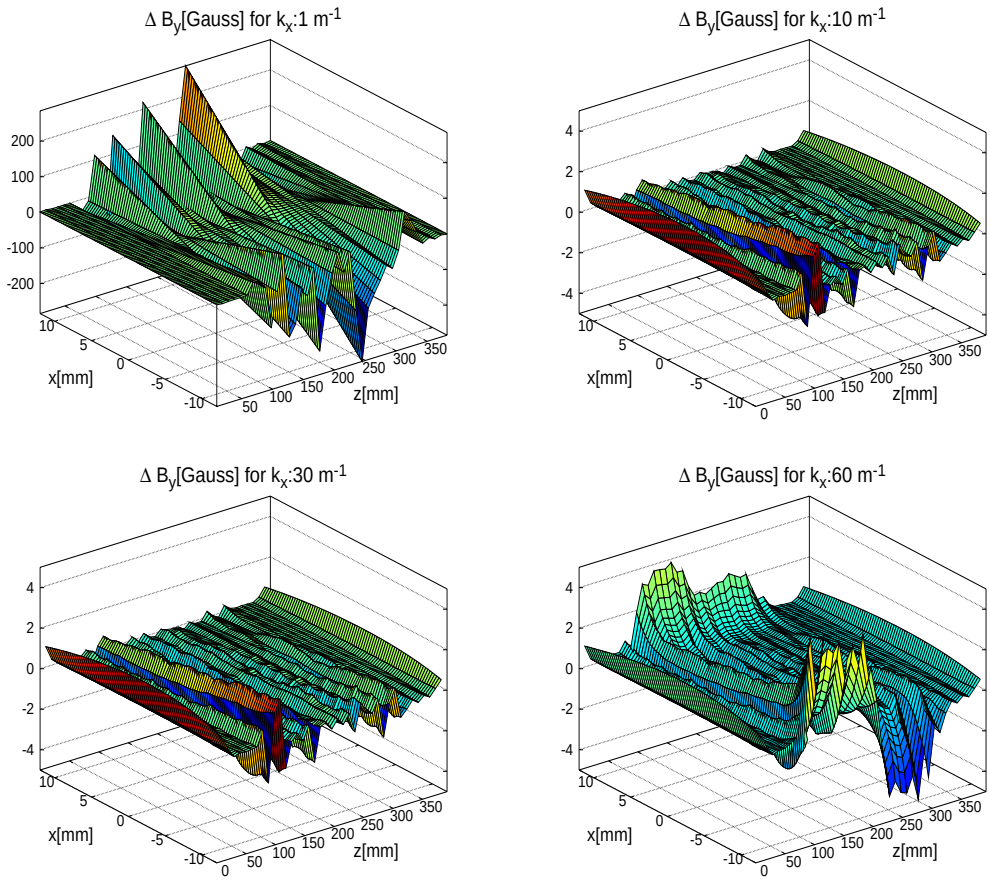

Figure 2.31: Residuals after transformation of the Fourier coefficient from cylindrical basis to Cartesian basis for different periodicity criteria k_x. Data are on the median plane.

k_x can be found. The value of k_x is determined by optimising the fit.

Adjusting this parameter allows an optimisation of the transformation from cylindrical to Cartesian coordinates. The residual of the fit for several values of k_x has been plotted in figure 2.31. For $k_x = 1\,m^{-1}$ (top left corner) the residual reaches values of 300 G, whereas the maximum value of the residual drops down to 2 G for $k_x = 10\,m^{-1}$ (see top right corner). Hence values for x_{max} larger than $\pi/10 = 0.314$ m do not seem to be appropriate in this case. For $k_x = 30\,m^{-1}$ (bottom left corner), the residual remains optimal under 2 G. When k_x is greater than 60 (bottom right corner), the residual increases exponentially in the x direction. The error is of opposite sign in the D magnet ($z = 150$ mm) and in the F magnet ($z = 250$ mm) which tells us that k_x is related to the transverse modes.

2.3.4.4 Summary and conclusions

In this section we have optimised the residual of the fit in Cartesian basis. We have checked that choosing the appropriate truncation orders m_{max} and n_{max}, and the parameter k_x the analytical description of the field as multipole expansion in Cartesian basis could represent the original numerical field map given by the OPERA model. We have shown that with the residual obtain smaller than 2 G, the integrated field and integrated gradient extracted from the analytical representation were close enough to the numerical one to simulate beam dynamics accurately. This statement was true for the median plane (y=0) and for vertical coordinate up to $y = 1$ cm. Transversely modes up to $m = 10$ had to be kept in the expansion to include higher harmonics allowed by the geometry of the magnet. Longitudinally, high rate of change of the magnet field at the entrance face of the magnets required modes up to $n = 40$ to be included in the series. Finally we have optimised the residual by adjusting the parameter k_x related to the periodicity of the field along the x axis. We have found that $10\,m^{-1} < k_x < 30\,m^{-1}$ gives a minimised residual, therefore $k_x = 30\,m^{-1}$ was chosen as the nominal value for

the rest of the study.

As a remark, we should note that the optimisation of the residual was done assuming that the parameters were independent. It might be that the optimal longitudinal truncation order n_{max} depends on the value of k_x and vice-versa. The value of residual we obtained by this method was sufficient for our study but a further study would be needed for more complicated magnetic fields (e.g. highly non-linear scaling FFAG magnets [12]).

In addition, we evaluated the residual for transverse position varying within $x = \pm 15\,\text{mm}$ which does not cover the entire excursion of the particles in the EMMA FFAG. Therefore we shall now study the range of validity of the analytical representation of the magnetic field.

2.3.5 Geometrical limitation and range of validity

An FFAG accelerator allows large transverse excursion of the beam. In section 2.3.2, we explained that the Fourier representation in polar basis was valid only within the reference cylinder. Then in section 2.3.4.2, we concluded that the transformation to the analytical representation in Cartesian basis conserved this range of validity. To obtain an accurate fit on the whole range of the particle in EMMA, one has to start with a cylinder with radius large enough. The radius of the reference cylinder is limited by the geometry of the cell. The D and F magnets inscribed radius, 53 mm and 37 mm respectively, contain the whole beam excursion. The maximum radius for a cylinder going through both magnet without touching the pole should be 37 mm. However in most of lattice configurations, the magnets are not aligned. Therefore the maximum allowed radius of a cylinder going through the whole cell is limited to 20 mm (see figure 2.32) for configuration with large distance between the magnetic axes of both magnets.

A larger horizontal transverse aperture can be scanned by using several cylinders with 12 mm radius (see figure 2.32). Note that the transverse vertical excursion of the

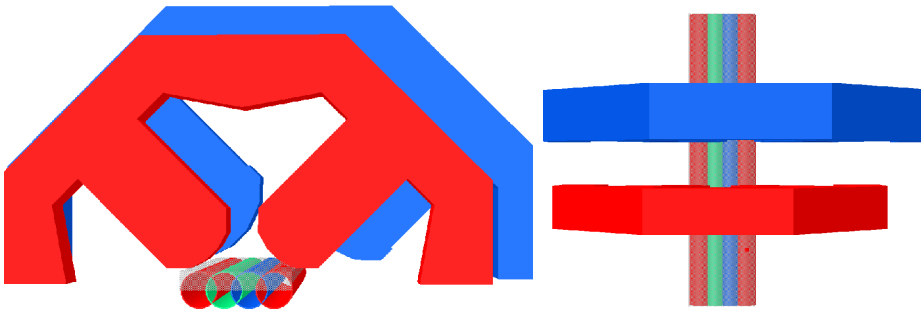

Figure 2.32: Geometry with various small cylinders in the aperture of the EMMA magnets. Front view (l.h.s) and top view (r.h.s).

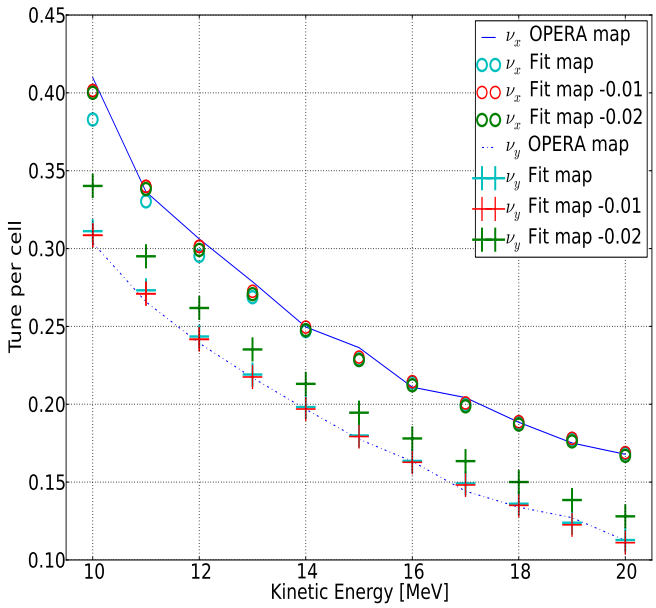

Figure 2.33: Tune variation with energy for various positions of the reference cylinder.

beam is expected to be smaller than 10 mm.

As it was done to create figure 2.30(a), we can create a numerical field map (called "fit map") from the analytical representation with different transverse position of the reference cylinder for the fit. We can then track particles in these field maps with PyZgoubi and compare the simulation results with results for particles tracked in the original numerical map from OPERA. We observe in figure 2.33 that the discrepancy in the horizontal tune at 10 MeV between the OPERA field map (blue line) and the fit map decreases from 0.03 to 0.01 when the axis of the reference cylinder is located at x=0.00 m (light blue circles) and x=-0.01 m (red circles) respectively; x=-0.01 m means that the axis is moved 1 cm towards the centre of the ring with respect to the transverse position (x=0) defined as geometrical reference for the lattice.

When tracking through the fit map with the axis of the reference cylinder located at x=-0.02 m (green circles), the horizontal tune is the same as for x=-0.01 m; however we observe an offset of 0.02 in the vertical tune (green crosses) over the whole energy range. The reason may be that the reference cylinder moved by -0.02 m is close to the pole of the magnet where the rate of change of the magnetic field is large and the interpolation of the field between the nodes of the mesh in the FEM solution requires a higher precision. Although it is not clear why the horizontal tune is not affected. A further study is required to get a deeper understanding of this effect.

An optimal solution for this geometrical limitation would consist in fitting an elliptic cylinder in the aperture. The basis of functions required involves Mathieu functions [33]. The fit and the transformation to Cartesian coordinates are more challenging. A further study could be dedicated to this subject.

2.3.6 Another case study: non-linear magnet for the PAMELA FFAG

To validate this method, we applied the same process to the periodic cell designed for the proton FFAG accelerator PAMELA [17]. The cell is a triplet composed of three

magnets, alternatively focusing, defocusing and focusing. The design of the PAMELA ring was done such that the tune variation is small during acceleration. To do so, the magnetic field is mainly quadrupolar but contains nonlinear components: sextupolar, octupolar and decapolar components [36]. The vertical component of the magnetic field in the median plane is shown in figure 2.34(a). We observe that the maximum value of the magnetic field reaches 1.5 T which is close to the limit of conventional magnets. Hence PAMELA has been designed with superconducting magnets.

Figure 2.34(b) shows the residual of the fit in Cartesian coordinates. The truncation order is m_{max}= 14 and n_{max}= 100. The residual increases at the entrance and exit face of the cell because the magnet field at these points is not exactly zero whereas the basis of functions we used in that case assumed a zero magnetic field. This could be fixed by extending the basis of functions to the equations 2.18, 2.19 and 2.20.

Far from the edges, the residual oscillates along the z direction below 2 G which corresponds to 0.0001% of the maximum magnetic field. We can therefore conclude that the fit can be applied to magnets with some nonlinear components. To generalise this result, a similar study should be applied to a highly nonlinear field of a scaling FFAG magnet.

2.4 Conclusions

In this chapter, the process to create a convenient representation of the magnetic field in the EMMA cell has be developed. The starting element was the study of an already existing OPERA model of the EMMA magnets. We figured out the optimal number of mesh elements (9 million) for the Finite Element Method resolution. This threshold was evaluated by looking at the result of beam dynamics simulations (closed orbit position, time of flight and tune per cell) using different mesh configurations. Discrepancies of greater than the precision of measurement in the real machine have been considered as

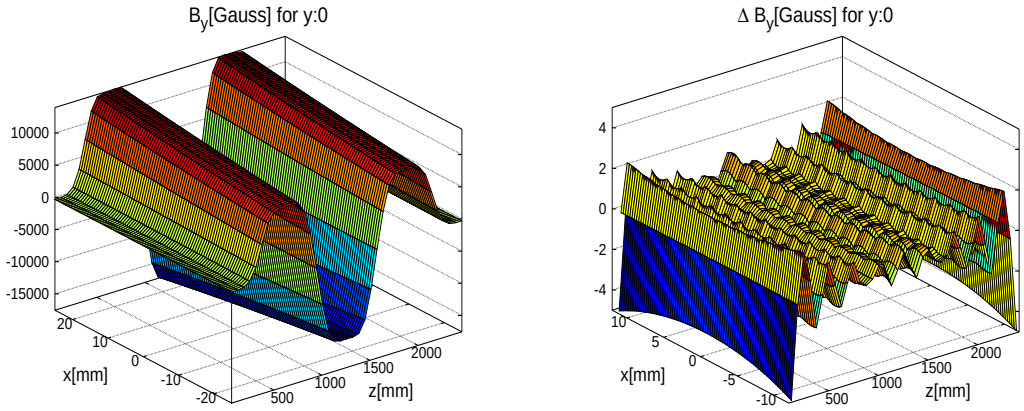

(a) Tune per cell

(b) Time of flight

Figure 2.34: (a):Vertical component of the magnetic field in the median plane of the PAMELA triplet.(b):The residual of the fit in the median plane (y=0 cm). The residual increases with the transverse excursion x in negative values. On the median plane the residual reaches a maximum of 2 G at the entrance of the D magnet. Since the field at that point is of about 2000 G, the relative error is 0.1%. More importantly the discrepancies have peak shapes in the longitudinal direction corresponds to high order longitudinal mode. It means that their effect on the integrated gradient is negligible. For y=1 cm, the residual has a maximum of 4 G which is also accurate enough.

negligible.

The numerical field map representing the EMMA cell could be built in two different ways: either by considering both magnets in the same model or by adding the field created by each magnet independently. When computing a field map created by one magnet, the yoke of the magnet unpowered has to be included in the geometry. Studying the beam dynamics in these configurations, we concluded that the dynamics could be accurately modelled using superposed maps. With the assumption that this is true when varying the strengths of the magnets, many different EMMA lattices can be studied with few field maps of D and F magnets, varying their relative strengths and adding them.

Once the magnetic field has been computed in a numerical format, we developed an algorithm that fits a power series to those data. Considering the symmetries of

the system, the fit was first performed in polar cylindrical coordinates. Since beam dynamics are usually expressed in Cartesian coordinates, a mathematical equivalent of this power series was derived. This analytical solution was then compared with the original numerical field. The power series truncation order has been optimised looking at the magnitude of the residual between analytical and numerical representations. Modes up to the 10^{th} and 40^{th} order have been included considering transverse and longitudinal directions respectively. In addition the parameter k_x representing the "pseudo" periodicity of the field in the transverse horizontal direction have been fixed to $k_x = 30\,m^{-1}$ minimising the residual.

Finally geometrical limitations due to the non alignment of the magnetic axes of the magnets have been addressed. The computation of several sets of coefficients fitting the data with different transverse positions allows coverage of the whole aperture. Small cylinders will be used for lattice configurations where the transverse excursion of the beam is larger that the maximum radius allowed for the reference cylinder.

The next step of our study was to develop an integrator solving the equations of the beam dynamics in the magnetic field obtained in analytical form from our model.

3

Computation of a dynamical map

3.1 The accelerator Hamiltonian

The basic and very first idea in studying particle accelerators is to understand the dynamics of charged particles in an electromagnetic field. This problem has been largely studied in classical mechanics, through three main fundamentally equivalent approaches : Newtonian, Lagrangian and Hamiltonian. In each approach, the physics of the system is contained in a function, respectively the force, the Lagrangian and the Hamiltonian. Figuring out the dynamics of the system consists in deriving these functions and solve the equations of motion. According to Newtonian mechanics, the equation of motion is given by:

$$\frac{d}{dt} m\dot{\mathbf{x}} = \mathbf{F}(\mathbf{x}, \dot{\mathbf{x}}; t)\,, \tag{3.1}$$

where $\mathbf{F}$ is the force, $\mathbf{x} = (x, y, z)$ is the vector position, and $\dot{\mathbf{x}} = (\dot{x}, \dot{y}, \dot{z})$ is the vector velocity. The dot over a variable corresponds to its derivative with respect to time. In an accelerator, the main force for a particle of charge q moving in an electric field $\mathbf{E}(\mathbf{x})$

and magnetic field $\mathbf{B}(\mathbf{x})$ is the Lorentz force defined as:

$$\mathbf{F} = q(\mathbf{E} + \dot{\mathbf{x}} \times \mathbf{B})\,. \tag{3.2}$$

In Lagrangian mechanics, the equations of motion for a dynamical system is given by the "Euler-Lagrange equations":

$$\frac{\partial L}{\partial q_i} - \frac{\partial}{\partial t}(\frac{\partial L}{\partial \dot{q}_i}) = 0 \tag{3.3}$$

where q_i are components of $\mathbf{q}$, vector of the generalised coordinates of the system, and L($\mathbf{q}$,$\dot{q}$;t) is the Lagrangian of the system. In that case physics consists in deriving the Lagrangian of the system. It is often defined as:

$$L = T - V\,, \tag{3.4}$$

where T is the kinetic energy of the system, and V is the potential energy. In the case of motion in one degree of freedom of a particle with kinetic energy T and potential energy V given by:

$$T = \frac{1}{2}m\dot{x}^2 \qquad\qquad V = \frac{1}{2}m\omega^2 x^2 \quad , \tag{3.5}$$

the Lagrangian is then:

$$L = T - V = \frac{1}{2}m\dot{x}^2 - \frac{1}{2}m\omega^2 x^2 \tag{3.6}$$

Using (3.3), we find the equations of motion:

$$\frac{d^2x}{dt^2} = -\omega^2 x\,. \tag{3.7}$$

An advantage of this method is that the equation of motion can be written for any

convenient set of coordinate variable q_i. Note that in the Euler Lagrange equations each variable is treated separately even if by definition they are related by differentiation ($\dot{\mathbf{x}}$ is the rate of change of $\mathbf{x}$). We notice as well that for a motion in n degrees of freedom, we obtain n second order differential equations.

Representing the dynamics using first-order equations has certain advantages concerning linear methods, stability analysis, etc. To transform the second order equation in first order equation, one can derive two quantities from the Lagrangian L as follows:

$$p_i = \frac{\partial L}{\partial \dot{x}_i}\,, \tag{3.8}$$

$$H = \sum_i \dot{x}_i p_i - L\,, \tag{3.9}$$

with as usual

$$\dot{x}_i = \frac{dx_i}{dt}\,. \tag{3.10}$$

The components p_i are the momenta conjugate to the coordinates x_i and H is called the Hamiltonian of the system. Given the Hamiltonian $H(x_i, p_i; t)$, the equations of motion are derived in the following manner:

$$\begin{aligned} \frac{dx_i}{dt} &= \frac{\partial H}{\partial p_i}\,, \\ \frac{dp_i}{dt} &= -\frac{\partial H}{\partial x_i}\,, \end{aligned} \tag{3.11}$$

These equations of motion are then first order differential equations.

In Hamiltonian mechanics, the state of a system at any time is defined by specifying values for the coordinates $\mathbf{x}$ (or more generally $\mathbf{q}$) and the momentum $\mathbf{p}$. Consider the Lagrangian defined in (3.6), the conjugate momentum is :

$$p_i = \frac{\partial L}{\partial \dot{x}_i} = m\dot{x}_i. \tag{3.12}$$

We note that in that case the conjugate momentum is equal to the mechanical momentum $m\dot{\mathbf{x}}$. This is not always the case. Now consider the Lagrangian describing a non-relativistic particle with two components to its potential energy: a scalar function $\Phi(\mathbf{x})$ of position and a vector potential $A(\mathbf{x})$:

$$L = \frac{1}{2}\dot{\mathbf{x}}^2 - \Phi(\mathbf{x}) + A(\mathbf{x}) \cdot \dot{\mathbf{x}} \tag{3.13}$$

Note that in general A and Φ can also be functions of time. From (3.8), the conjugate momentum is:

$$p_i = \frac{\partial L}{\partial \dot{x_i}} = m\dot{x_i} + qA_i, \tag{3.14}$$

and the Hamiltonian is:

$$H = \mathbf{p} \cdot \dot{\mathbf{x}} - L = \frac{(\mathbf{p} - q\mathbf{A})^2}{2m} + q\Phi\,, \tag{3.15}$$

In this case the conjugate momentum is not equal to the mechanical momentum $p_m = m\dot{\mathbf{x}}$, but has an additional contribution, qA.

To summarise, we have seen in the first section that a physical system can be studied in Newtonian, Lagrangian and Hamiltonian approach. We observed that the Hamiltonian approach was the only one keeping the equation of motion as first-order differential equations. We shall now describe the Hamiltonian approach for relativistic particles.

3.1.1 The relativistic Hamiltonian

3.1.1.1 Expression of the Hamiltonian

In Special Relativity, Einstein's equation relating energy E and mechanical momentum p_m of a particle with rest mass m is:

$$E^2 = p_m^2 c^2 + m^2 c^4 \,. \tag{3.16}$$

Note that p_m is the mechanical momentum. The Hamiltonian can often take the form:

$$H = T + V \,, \tag{3.17}$$

where T is the kinetic energy and V is the potential energy. This means that the Hamiltonian corresponds to the total energy of the system expressed in canonical variables. From (3.16) the relativistic Hamiltonian, in the absence of an electromagnetic field, becomes:

$$H = \sqrt{p^2 c^2 + m^2 c^4} \,, \tag{3.18}$$

When considering the electromagnetic field for the non-relativistic case we found that the conjugate momentum was expressed as :

$$\mathbf{p} = m\dot{\mathbf{x}} + q\mathbf{A}, \tag{3.19}$$

By identification, for the relativistic case the Hamiltonian becomes:

$$H = \sqrt{(\mathbf{p} - q\mathbf{A})^2 c^2 + m^2 c^4} + q\Phi \,, \tag{3.20}$$

where $\mathbf{A}$ is the vector potential and Φ a scalar potential. From this Hamiltonian,

Hamilton's first equation, (3.11), will give:

$$\frac{dx}{dt} = \frac{\partial H}{\partial p_x} = \frac{c(p_x - qA_x)}{\sqrt{(\mathbf{p} - q\mathbf{A})^2 + m^2c^2}}\,. \tag{3.21}$$

Rearranging the last equation gives:

$$\mathbf{p} - q\mathbf{A} = \beta\gamma mc\ , \tag{3.22}$$

where β and γ are the relativistic factors. Note that $\beta c = \dot{x} + \dot{y} + \dot{z}$. Equation (3.22) gives the canonical momentum :

$$\mathbf{p} = \beta\gamma mc + q\mathbf{A}\,. \tag{3.23}$$

Hamilton's second equation, gives:

$$\begin{aligned}\frac{dp_x}{dt} \quad = \quad & -\frac{\partial H}{\partial x} = \frac{qc}{\sqrt{(\mathbf{p} - q\mathbf{A})^2 + m^2c^2}} \times \\ & \left[(p_x - qA_x)\frac{\partial A_x}{\partial x} + (p_y - qA_y)\frac{\partial A_y}{\partial x} + (p_z - qA_z)\frac{\partial A_z}{\partial x}\right] \\ & -q\frac{\partial \phi}{\partial x}\,.\end{aligned} \tag{3.24}$$

Using equation (3.23) results in the simpler form:

$$\frac{dp_x}{dt} = q\left(\dot{x}\frac{\partial A_x}{\partial x} + \dot{y}\frac{\partial A_y}{\partial x} + \dot{z}\frac{\partial A_z}{\partial x}\right) - q\frac{\partial \phi}{\partial x}\,, \tag{3.25}$$

where $\dot{x} = \beta\gamma mc$, mechanical momentum. If we define the fields $\mathbf{E}$ and $\mathbf{B}$ given by:

$$\mathbf{E} = -\nabla\Phi - \frac{\partial \mathbf{A}}{\partial t}\,, \quad \text{and} \quad \mathbf{B} = \nabla \times \mathbf{A}\,, \tag{3.26}$$

then equation (3.25) can be rewritten, in the form:

$$\frac{d}{dt}(\mathbf{p} - q\mathbf{A}) \quad = \quad q(\mathbf{E} + \dot{\mathbf{x}} \times \mathbf{B}) \tag{3.27}$$

where $\dot{\mathbf{x}} = (\dot{x}, \dot{y}, \dot{z})$. We identify clearly $\mathbf{E}$ and $\mathbf{B}$ as the electric and magnetic fields respectively. Hence equation (3.27) is equivalent to the Lorentz force equation (3.2). This proves that the dynamics corresponding to the Hamiltonian H derived in this section (see (3.20)) are equivalent to the dynamics in the Newtonian approach.

3.1.1.2 Path length as independent variable

In the Hamiltonian approach, treating independently coordinates and conjugate momenta, equations of motions are kept to first-order differential equations. The dynamics of a particle are described by expressing the dynamical variables as function of the independent variable t. In the present case, t is the time variable. However in accelerators we do not generally know when a particle reaches a particular lattice element but instead we know where each lattice element is situated along the beam line. In an accelerator beamline, the Hamiltonian is a function of the position along the beamline. Therefore choosing the path length s as independent variable is more convenient than the time t. A new Hamiltonian has to be written with s as independent variable and coordinates and canonical momenta as canonical variables. To do so, we use an equation that relates the canonical variables, the Hamiltonian and the independent variable t.

Consider the principle of least action: the Euler-Lagrange equations define a path in a plot of $\dot{q}$ vs q for which the action S is minimum:

$$\delta S = \delta \left[\int_{t_0}^{t_1} L dt \right] = 0 \,. \tag{3.28}$$

From equation (3.15) we can express the action in terms of the Hamiltonian:

$$S = \int_{t_0}^{t_1} (p_x \dot{x} + p_y \dot{y} + p_z \dot{z} - H) dt \,. \tag{3.29}$$

The particles coordinates and momenta are defined with respect to a reference trajectory. We choose our coordinates so that the z axis defines the reference trajectory. The action can be expressed with z as integration variable instead of t:

$$S = \int_{z_0}^{z_1} (p_x x' + p_y y' + p_z - H t') dz \,, \tag{3.30}$$

where the prime indicates derivatives with respect to z. In equation (3.29) the canonical variables were:

$$(x, p_x), \qquad (y, p_y) \qquad (z, p_z) \,, \tag{3.31}$$

We deduce that the canonical variables with z as independent variable (equation (3.30)) should be:

$$(x, p_x), \qquad (y, p_y) \qquad (-t, H) \,, \tag{3.32}$$

and use for the Hamiltonian $H_1 = -p_z$. In this section H was identified as the energy of the system. The canonical momentum conjugate to the variable $-t$ is now the total energy of the particle E.

Rearranging equation (3.20) we can derive an expression for p_z and H_1:

$$H_1 = -p_z = -\sqrt{\frac{(E - q\phi)^2}{c^2} - m^2c^2 - (p_x - qA_x)^2 - (p_y - qA_y)^2} - qA_z \,. \tag{3.33}$$

3.1.1.3 Reference momentum

The description of the dynamics consists in expressing the canonical variables as function of the independent variable (with respect to a chosen reference trajectory). It is convenient to choose the reference trajectory such that values of the variables remain

small. As explained in the next section 3.1.1.5, this allows useful approximations to be made. To start with, we define a reference momentum P_0. The nominal momentum of particles in the accelerator under study is in general a suitable choice for the value of P_0.

We make the substitutions:

$$p_i \to \widetilde{p}_i = \frac{p_i}{P_0}\,, \quad \text{and} \quad H_1 \to \widetilde{H} = \frac{H}{P_0}\,, \tag{3.34}$$

Then the Hamiltonian equations are unchanged and the new Hamiltonian is given by:

$$\widetilde{H} = -\sqrt{\frac{(E-q\phi)^2}{P_0^2c^2} - \frac{m^2c^2}{P_0^2} - (\widetilde{p}_x - a_x)^2 - (\widetilde{p}_y - a_y)^2} - a_z\,, \tag{3.35}$$

where the normalised vector potential $\mathbf{a}$ is defined by:

$$\mathbf{a} = q\frac{\mathbf{A}}{P_0}\,, \tag{3.36}$$

where q is the electric charge of the particle.

The largest contribution to the particle total momentum is the longitudinal momentum since particles are travelling at high speed through accelerators, usually close to speed of light. The transverse normalised momenta $\widetilde{p_x}, \widetilde{p_y}$ will now be small but from Einstein's equation (3.16) the longitudinal normalised momentum E/P_0 will generally be close to the speed of light, c. To overcome this issue we perform a new transformation of canonical variable. A transformation from one set of canonical variables to another is called a canonical transformation. There is a useful recipe (or rather, set of recipes) for constructing canonical transformations. The technique developed in more details in appendix B is based on generating functions [31, 41]. We use a generating function of the second kind, function of the "old" coordinates and the "new" momenta

given by:

$$F_2(x, P_x, y, P_y, -t, \delta, s) = xP_x + yP_y + \left(\frac{s}{\beta_0} - ct\right)\left(\frac{1}{\beta_0} + \delta\right), \tag{3.37}$$

where P_x, P_y and δ are the new momentum variables, and β_0 is the normalised velocity of a particle with the reference momentum P_0. With the help of equations:

$$\widetilde{p}_i = \frac{\partial F_2}{\partial q_i} \quad Q_i = \frac{\partial F_2}{\partial P_i} \quad K = \widetilde{H} + \frac{\partial F_2}{\partial z}, \tag{3.38}$$

we find that the transverse variables remain unchanged,

$$\begin{aligned} \widetilde{p}_x &= P_x \qquad X = x \\ \widetilde{p}_y &= P_y \qquad Y = y\,. \end{aligned} \tag{3.39}$$

The momenta P_x and P_y will therefore remain small (i.e. $P_x << 1$, $P_y << 1$). The old and new longitudinal variables are related by:

$$\frac{E}{P_0 c} = c(\frac{1}{\beta_0} + \delta) \text{ and } Z = \frac{z}{\beta_0} - ct. \tag{3.40}$$

The new Hamiltonian K is then:

$$K = \frac{\delta}{\beta_0} - \sqrt{\left(\frac{1}{\beta_0} + \delta - \frac{q\phi}{P_0 c}\right)^2 - (P_x - a_x)^2 - (P_y - a_y)^2 - \frac{m^2c^2}{P_0^2}} - a_z\,, \tag{3.41}$$

By rearranging equation (3.40) the "energy deviation" δ is expressed as:

$$\delta = \frac{E}{P_0 c} - \frac{1}{\beta_0}\,. \tag{3.42}$$

We see that for a particle travelling with the reference momentum P_0, δ is zero. Therefore if the reference momentum is wisely chosen, this canonical variable will also remain

small. Let us define this accelerator Hamiltonian K using standard notations. For that we rewrite:

$$K \to H, \quad P_i \to p_i = \frac{\gamma m \dot{x} + q\mathbf{A}_i}{P_0}, \quad z \to s\,, \quad Z \to z\,, \tag{3.43}$$

By this we define the variable s as the path length covered by the reference particle and the variable z is related to the longitudinal position relative to the reference particle. We then arrive at the so-called "accelerator Hamiltonian":

$$H = \frac{\delta}{\beta_0} - \sqrt{\left(\frac{1}{\beta_0} + \delta - \frac{q\phi}{P_0 c}\right)^2 - (p_x - a_x)^2 - (p_y - a_y)^2 - \frac{1}{\gamma_0^2 \beta_0^2}} - a_z\,, \tag{3.44}$$

where $\frac{mc}{P_0} = 1/\gamma_0\beta_0$ with $\gamma_0 = \frac{1}{\sqrt{1-\beta_0^2}}$. This Hamiltonian depends on coordinate x, y and z only through the potential vector a_i; To get a sense of the solution of the dynamics given by this accelerator Hamiltonian, we consider the simple example of a field free region.

3.1.1.4 Dynamics in a field free region

In a field free region equation (3.44) becomes

$$H = \frac{\delta}{\beta_0} - \sqrt{\left(\frac{1}{\beta_0} + \delta\right)^2 - p_x^2 - p_y^2 - \frac{1}{\beta_0^2 \gamma_0^2}} \tag{3.45}$$

THe Hamiltonian does not depend on the coordinates therefore from Hamilton equations the momenta are constant (with respect to the independent variable s):

$$\Delta p_x = 0\,, \qquad \Delta p_y = 0\,, \qquad \Delta\delta = 0\,. \tag{3.46}$$

For a field free region of length L, the transverse coordinates then will change as:

$$\Delta x = \frac{p_x L}{\sqrt{\left(\frac{1}{\beta_0}+\delta\right)^2 - p_x^2 - p_y^2 - \frac{1}{\beta_0^2\gamma_0^2}}}, \tag{3.47}$$

$$\Delta y = \frac{p_y L}{\sqrt{\left(\frac{1}{\beta_0}+\delta\right)^2 - p_x^2 - p_y^2 - \frac{1}{\beta_0^2\gamma_0^2}}}. \tag{3.48}$$

The change in the longitudinal coordinates is given by

$$\Delta z = \frac{L}{\beta_0} - \frac{L(\frac{1}{\beta_0}+\delta)}{\sqrt{\left(\frac{1}{\beta_0}+\delta\right)^2 - p_x^2 - p_y^2 - \frac{1}{\beta_0^2\gamma_0^2}}}. \tag{3.49}$$

In these equations (3.47), (3.48) and (3.49), the values of the canonical variables at the exit of the region are expressed as functions of their values at the entrance of the region. Such relations are called the dynamical map of the region.

An interesting result is the fact that even for the simple example of a drift space, the exact solution for the dynamics is not linear since the final value do not vary linearly with the initial values of the variables. However it is possible to describe the dynamics linearly by making Taylor expansions for the changes in coordinates (3.47), (3.48) and (3.49). Taylor expansions are valid for small values of the variables justifying the effort put in choosing the most convenient set of canonical variables in section 3.1.1.3. Because the approximation is made on the exact solutions, these solutions are not exact any more. It will be explained in section 3.1.2 that an important characteristic of a transformation (e.g. change of the canonical variables along a beam line) that satisfies Hamilton's equations is its symplecticity. That is, the volumes of small elements in phase space must be conserved. Conserved quantities are important for an number of reasons; for example they can be used to estimate the accuracy of analytical and computational calculations.

Making an approximation on the solution of the Hamilton's equation violates the

symplecticity of the dynamics. To express the dynamics in a linear form and still conserve symplecticity, we can approximate directly the Hamiltonian such that the solutions are linear. Solutions are still not exact but are symplectic.

The so-called paraxial approximation consists in expanding the relativistic Hamiltonian to second order in canonical variables. Beamline elements whose effect on the beam can be described by this approximation are called linear element. To illustrate this technique, we can derive the linear map of a quadrupolar field.

3.1.1.5 The paraxial approximation for a quadrupolar field

The magnetic field inside a normal quadrupole is given by:

$$B_x = b_2 \frac{y}{\rho_0}\,, \quad B_y = b_2 \frac{x}{\rho_0}\,, \quad B_z = 0\,, \tag{3.50}$$

where the coefficient b_2 describes the strength of the quadrupole field. The above field components can be derived from the potential:

$$A_x = 0\,, \quad A_y = 0\,, \quad A_z = -\frac{1}{2}\frac{b_2}{\rho_0}(x^2 - y^2)\,. \tag{3.51}$$

The longitudinal component of the normalised potential vector a_z is therefore given by:

$$a_z = q\frac{A_z}{P_0} = -\frac{1}{2}\frac{q}{P_0}\frac{b_2}{\rho_0}(x^2 - y^2)\,, \tag{3.52}$$

The Hamiltonian describing the motion inside a quadrupole, using the usual accelerator variables, is:

$$H = \frac{\delta}{\beta_0} - \sqrt{\left(\frac{1}{\beta_0} + \delta\right)^2 - p_x^2 - p_y^2 - \frac{1}{\gamma_0^2\beta_0^2}} - a_z\,, \tag{3.53}$$

with q being the charge of the particle and P_0 the reference momentum. To simplify

this expression we define the normalised quadrupole gradient k_1 given by:

$$k_1 = \frac{q}{P_0}\frac{b_2}{\rho_0}\,, \tag{3.54}$$

then the Hamiltonian can be rewritten as:

$$H = \frac{\delta}{\beta_0} - \sqrt{\left(\frac{1}{\beta_0} + \delta\right)^2 - p_x^2 - p_y^2 - \frac{1}{\gamma_0^2\beta_0^2}} - \frac{1}{2}k_1(x^2 - y^2)\,. \tag{3.55}$$

This Hamiltonian does not have an exact closed form solution; however expanding it to second order in the dynamical variables (making the paraxial approximation) we construct the Hamiltonian:

$$H_2 = \frac{1}{2}p_x^2 + \frac{1}{2}p_y^2 + \frac{1}{2}k_1x^2 - \frac{1}{2}k_1y^2 + \frac{1}{2\gamma_0^2\beta_0^2}\delta^2\,. \tag{3.56}$$

Comparing with the description of the Hamiltonian as $H = T + V$, T and V being the kinetic and potential energy respectively, equation (3.56) resembles the Hamiltonian for an harmonic oscillator; the terms $\frac{1}{2}p_x^2$, $\frac{1}{2}p_y^2$ and $\frac{1}{2\gamma_0^2\beta_0^2}\delta^2$ compose the kinetic energy K and the terms $\frac{1}{2}k_1x^2$ and $\frac{1}{2}k_1y^2$ horizontally focusing potential and vertically defocusing potential respectively. There is no focusing in the longitudinal direction. The solutions to Hamilton's equations in the horizontal plane for the harmonic oscillator are given by:

$$x(L) = x(0)\cos\omega L + p_x(0)\frac{\sin\omega L}{\omega} \tag{3.57}$$

$$p_x(L) = p_x(0)\cos\omega L - \omega\sin\omega L \tag{3.58}$$

where $\omega = \sqrt{kL}$. Solutions in the vertical plane are similar to equations (3.57) and (3.58), using hyperbolic functions *sinh* and *cosh* instead of sine and cosine functions.

In the longitudinal plane solutions are given by:

$$z(L) = z(0) + \delta_0 \frac{L}{2\gamma_0^2\beta_0^2} \tag{3.59}$$

$$\delta(L) = \delta_0 \tag{3.60}$$

The equation of motion in a beamline element can be written using linear algebra. If $\mathbf{x}_{initial}$ and $\mathbf{x}_{final}$ are vectors of initial coordinates and final coordinates respectively, then the dynamics are written as: $\mathbf{x}_{final} = R \cdot \mathbf{x}_{initial}$, where R is a matrix also called the transfer map of a beamline element. In the case of a quadrupole, R is given by:

$$R = \begin{pmatrix} \cos\omega L & \frac{\sin\omega L}{\omega} & 0 & 0 & 0 & 0 \\ -\omega\sin\omega L & \cos\omega L & 0 & 0 & 0 & 0 \\ 0 & 0 & \cosh\omega L & \frac{\sinh\omega L}{\omega} & 0 & 0 \\ 0 & 0 & \omega\sinh\omega L & \cosh\omega L & 0 & 0 \\ 0 & 0 & 0 & 0 & 1 & \frac{L}{\gamma_0^2\beta_0^2} \\ 0 & 0 & 0 & 0 & 0 & 1 \end{pmatrix} \tag{3.61}$$

Note that a direct consequence of constraints from Maxwell's equations is that it is impossible to built a quadrupole focusing (or defocusing) in x and y simultaneously.

3.1.2 Symplectic transport

Conserved quantities are very useful for verifying the accuracy of analytical and computational calculations. We will show in this section that using the property of the symplecticity Hamiltonian systems are conservative systems. That is, areas of phase space elements (areas defined in a plot of the conjugate momentum vs the corresponding coordinate) are conserved for all Hamiltonian systems.

3.1.2.1 Definition of symplecticity

A matrix M is symplectic if it satisfies:

$$M^T \cdot S \cdot M = S\,, \tag{3.62}$$

where S is a $2n \times 2n$ matrix with block diagonals:

$$S_2 = \begin{pmatrix} 0 & 1 \\ -1 & 0 \end{pmatrix}\,. \tag{3.63}$$

S has interesting characteristics such as:

$$S^T = -S \tag{3.64}$$

$$S^2 = -I \tag{3.65}$$

where I is the $2n \times 2n$ identity matrix.

3.1.2.2 Symplecticity in Hamiltonian mechanics

Let us consider a vector $\mathbf{x}$ of canonical (phase space) variables given by:

$$\mathbf{x} = (x, p_x, y, p_y, z, \delta)\,, \tag{3.66}$$

and the values of the canonical variables at any position along the reference trajectory is defined by:

$$\mathbf{X} = \mathbf{X}(\mathbf{x}(s); \Delta s)\,, \tag{3.67}$$

We will prove that the Jacobian of this transformation given by:

$$J_{ij} = \frac{\partial X_i}{\partial x_j}\,, \tag{3.68}$$

satisfies :

$$J^T \cdot S \cdot J = S\,, \tag{3.69}$$

where S is defined in (3.63). In other words, the Jacobian of a transformation of the phase space variables in an Hamiltonian system is symplectic. For short, the transformation (also called map) is itself said to be symplectic. Using the S matrix from (3.63), Hamilton's equation can be rewritten:

$$\frac{d\mathbf{x}}{ds} = S \cdot \frac{\partial H}{\partial \mathbf{x}} \tag{3.70}$$

In this case, we choose s as independent variable for the Hamiltonian H. The transport of variables in the system are linked to the Jacobian by:

$$\frac{d\mathbf{X}}{ds} = \frac{\partial \mathbf{X}}{\partial \mathbf{x}} \cdot \frac{d\mathbf{x}}{ds} = J \cdot S \cdot \frac{\partial H}{\partial \mathbf{x}} \tag{3.71}$$

Also we have:

$$\frac{\partial H}{\partial \mathbf{x}} = J^T \cdot \frac{\partial H}{\partial \mathbf{X}} \tag{3.72}$$

Therefore:

$$\frac{d\mathbf{X}}{ds} = J \cdot S \cdot J^T \cdot \frac{\partial H}{\partial \mathbf{X}} \tag{3.73}$$

The variables $\mathbf{X}$ are also canonical variables and their evolution is determined by the same Hamiltonian H. Therefore as in equation (3.70), we have:

$$\frac{d\mathbf{X}}{ds} = S \cdot \frac{\partial H}{\partial \mathbf{X}} \tag{3.74}$$

Eventually from equations (3.73) and (3.74) it follows that :

$$J \cdot S \cdot J^T = S\,, \tag{3.75}$$

Using the properties:

$$S^{-1} = S^T = -S, \text{ and } (J^{-1})^T = (J^T)^{-1} , \tag{3.76}$$

Equation (3.75) is written as the symplecticity condition:

$$J^T \cdot S \cdot J = S . \tag{3.77}$$

Hence the Jacobian of a map from s to $s + \Delta s$ in an Hamiltonian system is symplectic.

3.1.2.3 Liouville's theorem

To understand the physical meaning of symplecticity, let us consider the area A defined in two-dimensional phase space by the vectors v_1 and v_2 is given by:

$$A = |v_1 \times v_2| = {v_1}^T \cdot S \cdot v_2 . \tag{3.78}$$

As the system evolves the transformation $M(s)$ is applied to the vectors :

$$v_1 \rightarrow {v_1}' = M(s) \cdot v_1 \text{ and } v_2 \rightarrow {v_2}' = M(s) \cdot v_2 \tag{3.79}$$

The area of the new section defined by the vectors v_1' and v_2' is given by:

$$A' = {v_1}'^T \cdot S \cdot {v_2}' \tag{3.80}$$

$$= {v_1}^T \cdot M(s)^T \cdot S \cdot M(s) \cdot v_2 \tag{3.81}$$

It is obvious in equation (3.81) that if $M(s)$ is symplectic the area A' is equal to A.

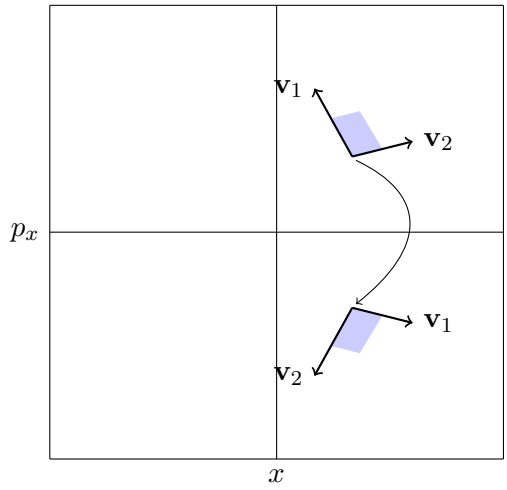

In the case if a linear transformation, the area bounded by the vector $\mathbf{v}_1$ and $\mathbf{v}_2$ of any length is preserved (see figure 3.1.2.3). The argument can be extended to the nonlinear case by considering infinitesimal areas. Also, note that in more than one degree of freedom there is more than one conserved quantity. It is known as Liouville's theorem.

In accelerator physics without dissipative forces (such as synchrotron radiation), Liouville's theorem tells us that the phase space volume occupied by a bunch of particles, called the emittance of a bunch, is conserved with the motion of this bunch through the accelerator. This outlines another interesting reason to use Hamiltonian mechanics: dissipative forces can be quantified by their contribution to the loss of symplecticity.

In this section we gave a main reason for using Hamiltonian mechanics in accelerator. We proved that in a system governed by Hamilton's equations, the Jacobian of a transformation of the phase space variables is symplectic. Applying Liouville's theorem, we concluded that therefore a phase space volume defined by these variables is conserved through that transformation.

In accelerator physics, we use the term "map" to refer to a transformation corresponding to the change of the phase space variables along the reference trajectory. The variables after the change expressed as function of the starting variables are canon-

ical since the transformation is symplectic. This transformation can therefore also be described as a transformation from a set of canonical variables to another set of canonical variables, also called canonical transformation. This tool can be used when Cartesian coordinates are not the most appropriate variables to describe the dynamics. To identify a useful set of canonical variable, we will first develop the consequences of symplecticity on a general beamline element defined by a symplectic transfer matrix.

3.1.3 Linear optics in periodic beamline

In this section we will develop the consequences of symplecticity in the analysis of dynamics in periodic, uncoupled linear beamlines. We will see that the phase space volume conserved through symplectic transformation can be defined by parameters called Twiss parameters. Eventually we will derive a set of canonical variables -action-angle variables- useful for dynamics in periodic beamlines.

In the case of uncoupled linear dynamics, the projection of the conserved volume in each phase space (x,p_x), (y,p_y) and (z,δ) is an ellipse. To prove this, let us consider a symplectic transfer matrix R. Generally the transfer 2×2 matrix for the horizontal motion can be written:

$$R_2 = I_2 \cos \mu_x + S_2 \cdot A_2 \sin \mu_x \tag{3.82}$$

where I_2 is the 2×2 identity matrix, μ_x is a parameter, S_2 is one of the 2×2 block diagonal of S, and A_2 is a 2×2 symmetric matrix. The matrix R_2 has four degrees of freedom and so has the right hand side of equation (3.82) with the parameter μ_x and the three coefficient of A_2. Therefore in periodic lattices, there is a unique set of four parameters at each location in a beamline period. Let us define α_x, β_x and γ_x such that:

$$A_2 = \begin{pmatrix} \gamma_x & \alpha_x \\ \alpha_x & \beta_x \end{pmatrix} . \tag{3.83}$$

R_2 is symplectic:

$$R_2^T \cdot S \cdot R_2 = S\,. \tag{3.84}$$

which applied to the right hand side of (3.82) gives:

$$\beta_x \gamma_x - \alpha_x^2 = 1\,. \tag{3.85}$$

If R_2 is symplectic, applying the result from (3.85) gives:

$$R_2^T \cdot A_2 \cdot R_2 = A_2\,. \tag{3.86}$$

which means that the matrix A_2 is also an invariant of the motion through the period defined by R_2. Moreover if we construct the quantity J_x:

$$J_x = \frac{1}{2}(x \;\; p_x) \cdot A_2 \cdot \begin{pmatrix} x \\ p_x \end{pmatrix}\,. \tag{3.87}$$

Propagating a particle through the cell we also have:

$$\begin{pmatrix} x \\ p_x \end{pmatrix} \rightarrow R_2 \cdot \begin{pmatrix} x \\ p_x \end{pmatrix}\,. \tag{3.88}$$

Therefore propagating J_x through the cell substituting (3.86) into (3.87) and using (3.88):

$$J_x \rightarrow \frac{1}{2}(x \quad p_x) \cdot R_2^T \cdot A_2 \cdot R_2 \cdot \begin{pmatrix} x \\ p_x \end{pmatrix} = J_x\,, \tag{3.89}$$

we observe that J_x is also an invariant of the motion through the symplectic element.

Using the parameter defined in (3.83), J_x is given by:

$$J_x = \frac{1}{2}(\gamma_x x^2 + 2\alpha_x x p_x + \beta_x p_x^2) \tag{3.90}$$

Since we have seen that J_x is constant we identify in (3.90) the equation of an ellipse in phase space (x,p_x) (with β_x and γ_x of same sign). The shape of the ellipse is defined by the parameters α_x, β_x and γ_x known as the Twiss parameters. J_x is usually called the action of a particle. The area of the ellipse is equal to $2\pi J_x$.

For the periodic case, there exists a unique set of Twiss parameters at each location along the beamline. Thus the Twiss parameters characterise the beamline rather than the beam. They are periodic with the lattice and therefore the shape of ellipse also varies periodically with the lattice having the same shape at the corresponding point in each of the cells in the beamline.

To understand the implications of this, let us take a simple example. A particle is launched in a lattice composed of a succession of identical cells, the starting conditions of this particle can be plotted as a point in phase space. The shape of the ellipse and the action are not known at this point yet. The position of this particle is recorded at the entrance of each cell (corresponding to the starting point in the first cell) and plotted in phase space. All the points will then trace out an ellipse from which the Twiss parameter and the action of the particle can be derived. In theory, there is no reason for a particle to perform a complete turn around the ellipse after each cell. This is because the trajectory of a particle is not necessarily periodic with the lattice. We will see in the next section that the increase in angle around the ellipse in phase space is called the phase advance.

It is also interesting to note that if the position of a particle is the same at the entrance of each cell, the phase space representation of its trajectory will be point-like. This point is called a closed orbit since if we consider a complete turn around the

machine, the position of the particle at the end of the turn will be the same as the starting position. The orbit is therefore closed. In a purely periodic lattice a particle travelling on the closed orbit will have the same position in phase space at the entrance of each cell. In reality, successive cells in a lattice are not strictly identical because of errors introduced during manufacturing and installation. Therefore a particle starting on the closed orbit comes back to the same position only after one complete turn.

A particle launched away from the closed orbit will take different position on the ellipse after each turn and therefore perform oscillations around the closed orbit (in coordinate x and in momentum p_x). The oscillations in x are called betatron oscillations and therefore the ellipse is often called the betatron ellipse.

We shall now identify a set of canonical variable that takes advantage of this parametrisation of the beamline.

3.1.4 Action-angle variables

In order to specify the location of a particle in phase-space we need to know the coordinate x and the conjugate momentum p_x. An alternative way for this specification is to give the action J_x and the position (or angle) ϕ_x around the phase-space ellipse. The action J_x and angle ϕ_x can be defined so that:

$$\begin{aligned} x &= \sqrt{2\beta_x J_x}\cos\phi_x\,, \\ p_x &= -\sqrt{\frac{2J_x}{\beta_x}}(\sin\phi_x + \alpha_x\cos\phi_x)\,. \end{aligned} \tag{3.91}$$

We deduce that:

$$\tan\phi_x = -\alpha_x - \beta_x\frac{p_x}{x}\,, \tag{3.92}$$

$$2J_x = \gamma_x x^2 + 2\alpha_x x p_x + \beta_x p_x^2\,. \tag{3.93}$$

It turns out that (ϕ_x, J_x) form a pair of canonical variable, ϕ_x being the coordinate and J_x the conjugate momentum. This can be proved by identifying a transformation that changes (x, p_x) into (ϕ_x, J_x) and which is canonical. We saw in section 3.1.1.3 that generating functions are a useful recipe to construct canonical transformation. It can be shown [31, 37] that (ϕ_x, J_x) can be derived from the generating function of the first kind $F_1(x, \Phi_x)$ given by:

$$F_1 = F_1(x, \phi_x) = -\frac{x^2}{2\beta_x}(\tan\phi_x + \alpha_x)\,. \tag{3.94}$$

The equation of motion expressed in terms of action-angle variables must be derived from an Hamiltonian H that needs to be defined. Since the action J_x is constant, from the first Hamilton's equation:

$$\frac{dJ_x}{ds} = -\frac{\partial H}{\partial \phi_x} = 0 \tag{3.95}$$

we deduce that the Hamiltonian must be independent of ϕ_x. Note that equation (3.95) is true for linear system (and certain special nonlinear cases). In addition, in the paraxial approximation the Hamiltonian is second order in (x, p_x). Since J_x is also second order in (x, p_x), the Hamiltonian must be linear in J_x. Also the Hamiltonian generally involves a momentum term $p_x/2$. From equation (3.91) we deduce:

$$H = \frac{J_x}{\beta_x}\,. \tag{3.96}$$

The Hamiltonian from (3.96) provides a convenient equation of motion derived from Hamiltonian equations:

$$\frac{dJ_x}{ds} = -\frac{\partial H}{\partial \phi_x} = 0 \tag{3.97}$$

$$\frac{d\phi_x}{ds} = \frac{\partial H}{\partial J_x} = \frac{1}{\beta_x} \tag{3.98}$$

We observe from equation (3.98) that the rate of change the angle variable ϕ_x is proportional to the inverse of the function $\beta_x(s)$. The change in angle variable when moving from one point to another along the beamline is often called the phase advance and is given by:

$$\Delta\phi_x = \int_s^{s+\Delta s} \frac{1}{\beta_x}\, ds\,. \tag{3.99}$$

Note that from equation (3.91), Φ_x can be interpreted as the phase related to the betatron oscillation of a particle and β_x as the betatron wavelength. Since in a periodic lattice the beta function is periodic, the phase advance over an entire single cell is the same, no matter what starting point is chosen for the cell. This means that the angle performed on the ellipse over one cell is constant.

The phase advance over one turn in a ring is called the betatron tune ν_x and given by:

$$\nu_x = \frac{\Delta\phi_x}{2\pi} = \int_0^{C_0} \frac{1}{\beta_x}\, ds\,. \tag{3.100}$$

where C_0 is the path length for one complete turn following the reference trajectory. It appears in equation (3.100) that the betatron tune corresponds to the number of oscillation made in one complete turn. ν_x is very important quantity in FFAG because if for instance it is an integer it tells that a particle oscillating around the closed orbit will perform a certain number of entire oscillations and come back at the position in transverse phase space after one turn. Therefore if there is a dipole error in the ring that kick slightly the particle towards the wall of the beam pipe, turn after turns, the particle will see the same kick and the deviation will add up until it is lost. This is the resonance phenomenon seen in section 1.3.3 of the introduction chapter. There exist several orders of resonances having cumulative effect on the beam if the tune is either an integer, half an integer or more generally a "simple" fraction of an integer. The stability of a lattice depends on the distance from a resonance (in tune space) and on

the strength of any effect driving the resonance. To design a stable lattice, the value for the horizontal tune ν_x and the vertical tune ν_y must be carefully set. The strength of the resonance will depend on the accuracy of the construction of the machine.

3.1.5 Summary and conclusions

In this section, we saw that the equation of motion of a particle in an electromagnetic field could be derived from Hamilton's equations. A first advantage of the Hamiltonian approach was the fact that equations of motion were first order differential equations whereas other approaches involved higher orders.

We then derived the accelerator Hamiltonian for relativistic particles choosing the path length as independent variable and defining a reference momentum to keep small values for the canonical variables, allowing us later on to use the paraxial approximation.

We then applied the Hamiltonian approach to the study of the dynamics to a field free region. We observed that even for a simple field free region the dynamics were not linear, raising questions about the accuracy of linear tracking codes. The dynamical map could be linearised by making a Taylor expansion at the cost of losing symplecticity. However taking the example of a quadrupolar field, we derived linear solutions while conserving symplecticity by making a Taylor expansion to second order of the Hamiltonian itself (paraxial approximation) and solving Hamilton's equations.

The symplecticity condition led to Liouville's theorem in accelerator physics stating that volumes in phase space were conserved with motion through a conservative system. In periodic, linear and uncoupled beam line, a particle passing along one period of the beamline maps out an ellipse in phase space when observed at a given point in each successive period. The area of the ellipse is an invariant of the particle motion, equal to $2\pi J$, where J is the action. The action is the conjugate momentum to the angle variable.

From the second Hamilton's equation, the phase advance was defined as the variation of the angle variable from one point to another along the beamline. We could then define the tune (phase advance over a complete turn in a ring), which will be a key characteristics of the dynamics in an accelerator and especially in a non scaling FFAG regarding the stability of the lattice and the effect of resonances introduced by errors.

3.2 Generation of dynamical maps

We shall now explain how to construct a dynamical map for accelerators elements. We have already built the dynamical map for a drift space in section 3.1.1.4 but in that case Hamilton's equations could be solved exactly. We will show in a first section a technique for constructing maps for accelerator elements: Lie transformation.

We will see that the Lie transformation provides a symplectic representation of the map in implicit form (i.e. in a form that requires further algebraic manipulations before the map can be applied by direct substitution of the values for the dynamical variable). Lie transformations can be expressed (explicitly) as power series useful for tracking particles but their truncation makes the map no longer symplectic. Therefore we will describe a possible method for constructing a representation that is both explicit and symplectic. The method develop will be a symplectic integrator based on the Yoshida factorisation generalised by Wu et al. to a general magnetic field.

3.2.1 Example of non-integrable Hamiltonian: a sextuple magnet

The Hamiltonian for a sextuple is given by:

$$H = \frac{\delta}{\beta_0} - \sqrt{\left(\frac{1}{\beta_0} + \delta\right)^2 - p_x^2 - p_y^2 - \frac{1}{\gamma_0^2 \beta_0^2}} - a_z \,, \tag{3.101}$$

where a_z is the potential vector given in this case by:

$$a_z(x,y) = \frac{1}{6}k_2(x^3 - 3xy^2) \tag{3.102}$$

The coordinate variables x and y appear explicitly in the Hamiltonian and therefore the conjugate momenta p_x and p_y are not constant. The equations are non-linear and cumbersome to solve exactly. We cannot find an exact solution in closed form. The Hamiltonian is said to be not integrable.

3.2.2 Lie transformation

To integrate the equations of motion that cannot be solved exactly, numerical method such as the Runge-Kutta algorithm are often used. However they tend to be rather slow for tracking large number of particles for thousands of turns. For the EMMA case study, they are still very useful because particles are not performing thousands of turns in the ring. The aim of this study is more to study the validity of dynamical maps for modelling the beam dynamics in FFAGs, and investigate potential advantages over a more conventional, purely numerical techniques. Approximations that may introduce discrepancies between simulated and experimental results, will be made to write down an approximate map in closed form.

We define the Lie operator $:g:$ for any function g($\mathbf{p}$,$\mathbf{q}$):

$$:g: = \sum_i \frac{\partial g}{\partial q_i}\frac{\partial}{\partial p_i} - \frac{\partial g}{\partial p_i}\frac{\partial}{\partial q_i} \tag{3.103}$$

where p_i and q_i are the components of the vector $\mathbf{p}$ and $\mathbf{q}$ respectively. Consider a function f of the pair of canonical variable ($\mathbf{q}$,$\mathbf{p}$). The time evolution of f is:

$$\frac{df}{dt} = \frac{d\mathbf{q}}{dt}\frac{\partial f}{\partial \mathbf{q}} + \frac{d\mathbf{p}}{dt}\frac{\partial f}{\partial \mathbf{p}} \tag{3.104}$$

and using Hamilton's equations:

$$\frac{df}{dt} = \frac{\partial H}{\partial \mathbf{p}}\frac{\partial f}{\partial \mathbf{q}} - \frac{\partial H}{\partial \mathbf{q}}\frac{\partial f}{\partial \mathbf{p}} \tag{3.105}$$

Therefore applying the definition of the Lie operator in (3.103):

$$\frac{df}{dt} = -:H:f \tag{3.106}$$

This has the form of a first order differential equation. A solution can be written as:

$$f(t) = e^{-:H:t} f(0)\,. \tag{3.107}$$

where the exponential of the Lie operator is defined by the expansion :

$$e^{-:H:t} = 1 - t:H: + \frac{t^2}{2}:H:^2 - \frac{t^3}{3!}:H:^3 + ... \tag{3.108}$$

The operator $e^{:g:}$ is called a Lie transformation. We shall now see how this applies to the dynamics in an sextupolar field.

By considering the case that f is simply equal to any one of the canonical variables, we see that:

$$\mathbf{x}(s) = e^{-:H:s}\mathbf{x}(0)\,. \tag{3.109}$$

where $\mathbf{x}$ is the vector of canonical variables.

3.2.3 An explicit symplectic integrator

In this section, we will develop an approach that makes an approximation of the Hamiltonian in such a way that the resulting Lie transformation can be expressed as a power series with a finite number of terms. By not performing any truncation, symplecticity can be conserved.

Let us consider the case of a simplified Hamiltonian for a sextupole of length L in one degree of freedom ($\delta = 0$ and $y = p_y = 0$). Considering fully relativistic particles ($\beta_0 \to 1$), the Hamiltonian (3.101) becomes:

$$H = -\sqrt{1 - p_x^2} + \frac{1}{6} k_2 x^3. \tag{3.110}$$

Now let us evaluate the Lie transformations of x and p_x. To second order in L we obtain:

$$x(L) = e^{-L:H:} x_0 = x_0 + \frac{p_{x0} L}{\sqrt{1 - p_{x0}^2}} - \frac{k_2 x_0^2 L^2}{4(1 - p_{x0}^2)^{\frac{3}{2}}} + O(L^3), \tag{3.111}$$

$$p_x(L) = e^{-L:H:} p_{x0} = p_{x0} + \frac{1}{2} k_2 x_0^2 L - \frac{k_2 x_0 p_{x0} L^2}{2(1 - p_{x0}^2)^{\frac{3}{2}}} + O(L^3), \tag{3.112}$$

The subscript 0 on a dynamical variable means the value of the variable at $s = 0$. We can expect to have a loss of accuracy by ignoring terms of order higher than two. The computation of higher order terms quickly becomes cumbersome.

As explained in section 3.2.1, the Hamiltonian (3.101) is not integrable. However each term in the Hamiltonian is separately integrable. A Lie transformation in closed form is generated for each term:

$$\begin{aligned} e^{-L:H_d:} x &= x + L p_x, \qquad e^{-L:H_d:} p_x = p_x, \\ e^{-L:H_k:} x &= x, \qquad e^{-L:H_k:} p_x = p_x - \frac{1}{2} k_2 L x^2, \end{aligned} \tag{3.113}$$

where $H_d = \frac{1}{2} p_x^2$ and $H_k = \frac{1}{6} k_2 x^3$. So if we can find a relation between the maps $e^{-L:H:}$, $e^{-L:H_d:}$ and $e^{-L:H_k:}$, we could find a solution for the sextupole in closed form.

3.2.3.1 The Baker-Campbell-Hausdorff formula

To derive the relation between $e^{-L:(H_d+H_k):}$, $e^{-L:H_d:}$ and $e^{-L:H_d:}$, we use the Baker-Campbell-Hausdorff formula (BCH) [38]:

$$e^{:A:}e^{:B:} = e^{:C:} \tag{3.114}$$

where

$$C = A + B + \frac{1}{2}[A,B] + \frac{1}{12}[A,[A,B]] + \frac{1}{12}[B,[B,A]] + \frac{1}{24}[[[A,B],A],B]] + ... \tag{3.115}$$

In equation (3.115) the notation $[\cdot,\cdot]$ stands for the Poisson bracket given by:

$$[A,B] = \frac{\partial A}{\partial \mathbf{p}}\frac{\partial B}{\partial \mathbf{q}} - \frac{\partial A}{\partial \mathbf{q}}\frac{\partial B}{\partial \mathbf{p}} \tag{3.116}$$

Clearly we have:

$$[A,B] =: A : B \tag{3.117}$$

3.2.3.2 Explicit symplectic integrator for a sextupole

Using BCH formula (3.115), we can write:

$$e^{-L:H_d:}e^{-L:H_k:} = e^{-L:H-\frac{L}{2}[H_d,H_k]+O(L^2):}. \tag{3.118}$$

Therefore the map for a sextupole can be expressed as a concatenation of Lie Transformations (each of which expressed in explicit closed form in equations (3.113)) with an error of order L^2 in the generator for the complete map contained in the ignored Poisson brackets of higher order in the BCH formula (3.115). Here we are doing a second approximation after the paraxial approximation. Inspecting the left hand side, we observe that the map of the sextupole may be interpreted as a drift (for the length

L of the sextupole) followed by a transverse kick (by the amount of the integrated strength of the sextupole). Moreover using the BCH formula for the concatenation of three maps drift-kick-drift, we obtain:

$$e^{-d_1 L:H_d:} e^{-L:H_k:} e^{-d_2 L:H_d:} = e^{-L:(d_1+d_2)H_d + H_k - \frac{1}{2}(d_1-d_2)L[H_k,H_d] + O(L^2):}. \tag{3.119}$$

If $d_1 = d_2 = \frac{1}{2}$, we find

$$e^{-\frac{1}{2}L:H_d:} e^{-L:H_k:} e^{-\frac{1}{2}L:H_d:} = e^{-L:H+O(L^2):}. \tag{3.120}$$

The term in L^2 in the exponential in the right hand side disappears. For that formulation of the map the error is therefore of order L^3. It can be shown that by concatenating larger numbers of drifts and kicks with optimised length, the error can pushed to higher order. This method is sometimes called "symmetric factorisation" or "Yoshida factorisation" [42].

3.2.3.3 Explicit symplectic integrator for a general magnetic field

In the previous example, we could split the Hamiltonian in two integrable parts. The Hamiltonian for a drift space H_d is given by:

$$H_d = \frac{\delta}{\beta_0} - \sqrt{\left(\frac{1}{\beta_0} + \delta\right)^2 - p_x^2 - p_y^2 - \frac{1}{\gamma_0^2 \beta_0^2}}\,. \tag{3.121}$$

and the Hamiltonian for the kick was given by:

$$H_k = \frac{1}{6} k_2 (x^3 - 3xy^2)\,. \tag{3.122}$$

When comparing these expressions with the general accelerator Hamiltonian:

$$H = \frac{\delta}{\beta_0} - \sqrt{\left(\frac{1}{\beta_0} + \delta - \frac{q\phi}{P_0 c}\right)^2 - (p_x - a_x)^2 - (p_y - a_y)^2 - \frac{1}{\gamma_0^2 \beta_0^2}} - a_s \,, \tag{3.123}$$

we observe that the sextupole case (in fact any magnetic multipole case) is special because the dependence of the Hamiltonian on the coordinates (in $\mathbf{a}$) and on the momenta can be separated into different terms. This is the case when the longitudinal variation of the magnet field across the magnet is not taken into account. We explained in chapter 2 that the EMMA magnets being short with respect to the size of the gap between the poles, this approximation may not be valid to simulate the beam dynamics accurately. Therefore the kick-drift approach in the previous example has to be extended to a general magnetic field. The goal is to develop an explicit symplectic integrator for a general static magnetic field for which the potential vector is known analytically. The technique has been developed by Y.Wu, E.Forest and D.Robin [39].

The general normalised potential vector $\mathbf{a} = (a_x, a_y, a_s)$ is a function of the coordinates:

$$\mathbf{a} = \mathbf{a}(x, y, s) \,. \tag{3.124}$$

Hence the Hamiltonian is not anymore independent of the coordinate s and the expression of the dynamical map:

$$f(t) = e^{-s:H:} f(0) \,. \tag{3.125}$$

is not valid anymore. We must extend the phase space by introducing an additional pair of dynamical variable $(s,\, p_s)$ where p_s is the momentum conjugate to s. Also we define a new independent variable σ which corresponds to the integration step. The evolution of a system of length L is computing by integrating the equation of motion with respect to σ, until $s = L$.

The evolution of s is given by:

$$\frac{ds}{d\sigma} = \frac{\partial H}{\partial p_s} = 1\,. \tag{3.126}$$

Hence if $s = 0$ when $\sigma = 0$, $s = \sigma$.

The new Hamiltonian to be split in integrable terms is given by:

$$H = \frac{\delta}{\beta_0} - \sqrt{\left(\frac{1}{\beta_0} + \delta - \frac{q\phi}{P_0 c}\right)^2 - (p_x - a_x)^2 - (p_y - a_y)^2 - \frac{1}{\gamma_0^2\beta_0^2}} + (p_s - a_s)\,. \tag{3.127}$$

Since a_x and a_y are non-zero and depend on the coordinates, this Hamiltonian cannot directly be expressed as a sum of integrable terms. The paraxial approximation is applied to transform this expression, expressing the square root as a Taylor series. We obtain:

$$H = H_1 + H_2 + H_3\,, \tag{3.128}$$

where

$$H_1 = -\left(\frac{1}{\beta_0} + \delta\right) + \frac{1}{2\gamma_0^2\beta_0^2}\left(\frac{1}{\beta_0} + \delta\right)^{-1} + \frac{\delta}{\beta_0} + \frac{(p_x - a_x)^2}{2(\frac{1}{\beta_0} + \delta)} + p_s \tag{3.129}$$

$$H_2 = \frac{(p_y - a_y)^2}{2(\frac{1}{\beta_0} + \delta)} \tag{3.130}$$

$$H_3 = -a_s\,. \tag{3.131}$$

We can make a gauge transformation to make one component of the potential vector vanish [39]. Choosing the gauge that makes a_x equal to zero, the Hamiltonian H_1 becomes only function of p_x and is therefore integrable. H_3 is independent of the momenta and therefore is integrable; the last step to obtain the integrator involves showing that H_2 is integrable, knowing that a_y is non-zero.

Let us write the map generated by H_2 as a Lie transform:

$$\mathcal{M}_2(\Delta\sigma) = e^{-\Delta\sigma:H_2:} = \exp(-\Delta\sigma : \frac{(p_y - a_y)^2}{2(\frac{1}{\beta_0} + \delta)} :) \,. \tag{3.132}$$

We shall now use two rules of the Lie transformation [40]:

$$e^{:f:}e^{:g:}e^{-:f:} = \exp : e^{:f:}g : , \tag{3.133}$$

$$e^{:f:}g(h) = g\left(e^{:f:}h\right) \,. \tag{3.134}$$

This allow us to write:

$$\mathcal{M}_2(\Delta\sigma) = e^{:I_y:}\exp(-\Delta\sigma : \frac{p_y^2}{2(\frac{1}{\beta_0} + \delta)} :)e^{-:I_y:} \,, \tag{3.135}$$

with:

$$e^{:I_y:}p_y = p_y - a_y \,. \tag{3.136}$$

A generator I_y that satisfies equation (3.136) is given by:

$$I_y = \int_0^y a_y(x, y', s)dy' \,. \tag{3.137}$$

We must now evaluate the effect of the term $e^{:I_y:}$ on the canonical variables. Since I_y is independent of the momenta p_x, p_y and p_s, the coordinates (x, y, s) are unchanged. The changes in the momenta is calculated by solving Hamilton's equation with I_y as

Hamiltonian and σ as the independent variable. We obtain:

$$e^{:I_y:}p_x = p_x - \int_0^y \frac{\partial}{\partial x} a_y(x, y', s)dy' \,, \tag{3.138}$$

$$e^{:I_y:}p_y = p_y - a_y \,, \tag{3.139}$$

$$e^{:I_y:}p_z = p_z - \int_0^y \frac{\partial}{\partial z} a_y(x, y', s)dy' \,, \tag{3.140}$$

$$e^{:I_y:}\delta = \delta \,. \tag{3.141}$$

The effect of $e^{-:I_y:} = (e^{:I_y:})^{-1}$ is the same as equations (3.138) to (3.141) , but replacing minus signs by plus signs. Note that this step is equivalent to a canonical transformation from the canonical variable $(p_y - a_y)$ to p_y^{new}; hence the term $e^{:I_y:}$ is the explicit Lie transformation of the generating function associated to this transformation.

Finally the complete explicit symplectic integrator for the map $\mathcal{M}$ may be written:

$$\mathcal{M}(\Delta\sigma) = e^{-\Delta\sigma:H_1+H_2+H_3:} \,, \tag{3.142}$$

$$\mathcal{M}(\Delta\sigma) \approx e^{-\frac{\Delta\sigma}{2}:H_1+H_3:} e^{-\Delta\sigma:H_2:} e^{-\frac{\Delta\sigma}{2}:H_1+H_3:} \,, \tag{3.143}$$

$$\mathcal{M}(\Delta\sigma) \approx e^{-\frac{\Delta\sigma}{4}:H_1:} e^{-\frac{\Delta\sigma}{2}:H_3:} e^{-\frac{\Delta\sigma}{4}:H_1:} e^{-\Delta\sigma:H_2:} e^{-\frac{\Delta\sigma}{4}:H_1:} e^{-\frac{\Delta\sigma}{2}:H_3:} e^{-\frac{\Delta\sigma}{4}:H_1:} \tag{3.144}$$

where:

$$e^{-\Delta\sigma:H_2:} = e^{:I_y:} e^{-\Delta\sigma:\tilde{H}_2:} e^{-:I_y:} \,, \tag{3.145}$$

and :

$$\tilde{H}_2 = \frac{p_y^2}{2(\frac{1}{\beta_0} + \delta)} \,. \tag{3.146}$$

The Lie maps $e^{-\Delta\sigma:\tilde{H}_2:}$ and $e^{-\frac{\Delta\sigma}{4}:H_1:}$ are independent of the potential. They can be called "drift" maps. The "kick" maps $e^{-\frac{\Delta\sigma}{2}:H_3:}$ and $e^{:I_y:}$ are expressed explicitly by using the analytical representation of the potential vector developed in chapter 2.

Note that expression (3.144) for the integrator is an approximation to the exact

dynamics since the separation of the Hamiltonian in integrable terms has been made possible by the paraxial approximation. The integrator is therefore of second order in the dynamical variables. Moreover a second approximation is applied when using the BCH formula (3.115). An error of order $(\Delta\sigma)^2$ is introduced by applying the BCH formula from the expression (3.142) to the expression (3.143). This error corresponds to a numerical error linked to the size of the integration step. As seen in section 3.2.3.1, including more terms in the BCH formula could increase the order of this error. The explicit symplectic integrator expressed in (3.144) and used for the beam simulations of chapter 4 is of second order in $(\Delta\sigma)$. Each integration step will consist in applying all the terms in equation (3.144) to the dynamical variables.

3.3 Construction of a dynamical map

We shall now describe the computer tools used to apply the symplectic integrator obtained in section 3.2.3.3. Each term of the expression (3.144) corresponds to a finite set of arithmetical operations on the dynamical variables. The map can therefore be expressed algebraically in closed form. Given the representation of the potential vector as a function of the coordinates, the equations of motion can be integrated by a computer code for a particle moving through the magnetic element. We use a differential algebra (DA) code to construct the Taylor series representing the dynamics in a given magnetic element. In this section we will first briefly describe this code. Then we will outline features of the Taylor series obtained from the integration of the equations of motion. We will give the physical meaning of some of the coefficients. Finally, we will study the choice of reference trajectory for the dynamical map and the implications of this choice regarding the paraxial approximation.

3.3.1 Differential Algebra (DA) code

The explicit symplectic integrator consists of a succession of arithmetical operation on the dynamical variables. The vector of dynamical variables can be expressed as a vector of the numerical values of these variables. However this numerical integration has not much advantage over numerical integration in the original field map using numerical tracking codes (e.g. PyZgoubi [56]). Therefore we choose to use the differential algebra code COSY infinity developed by M.Berz [47].

In this study, COSY INFINITY performs all its calculations in the following scaled coordinates:

$$X_1 = x; \qquad X_2 = p_x/p_0; \tag{3.147}$$

$$X_3 = y; \qquad X_4 = p_y/p_0; \tag{3.148}$$

$$X_5 = z = \frac{s}{\beta_0} - ct; \qquad X_6 = \delta = \frac{E}{p_0 c} - \frac{1}{\beta_0}; \tag{3.149}$$

The variables form three canonically conjugate pairs in which the map is symplectic. p_0, K_0 and β_0 are the momentum, kinetic energy and velocity of the reference particle respectively. s is the independent variable and t is the time taken for a particle to travel from $s = 0$ to the position defined by s.

In COSY, variables can be expressed as DA objects that represent the Taylor series to some order in a set of basis variables X(1), X(2), and so on. In our case the basis variables are the six dynamical variables (x, p_x, y, p_y, z, δ). For instance if x and y are DA objects, writing :

$$x := X(1); \tag{3.150}$$

$$y := e^x; \tag{3.151}$$

means that y can be written as:

$$1 + \frac{X(1)}{1!} + \frac{X(1)^2}{2!} + \frac{X(1)^3}{3!} + \cdots \tag{3.152}$$

The code performing the various operations on the DA variables at each step of integration is shown in figure 3.1. The procedures AZFIELD and AYFIELD computed the DA object of the potential vector and its integral at each step of integration from the set of coefficients c_{mn} representing the magnetic field (see chapter 2). A more detailed description of the integrator is presented in appendix C. Each block of command corresponds to the application of one of the Lie maps in expression (3.144) (referenced between "{}" as comments in the script).

Note that the potential vector is evaluated twice in the script. This is due to the fact that in the expression (3.144) Lie maps for H_3 and I_y are evaluated for at longitudinal positions $\frac{\Delta\sigma}{4}$ and $\frac{\Delta\sigma}{2}$ respectively. These different longitudinal positions within one integration step are represented by the variable $X7$ that is progressively increased by $\frac{\Delta\sigma}{4}$ steps (in this code, "DL" corresponds to $\Delta\sigma$).

Special care has to be taken concerning the longitudinal position at which the potential vector is evaluated. The correct physical position is given by the dynamical variable s ($X7$ in the script) and not σ. The variable s was introduced by the phase space extension (see section 3.2.3.3) to the new pair of variables (s,p_s). At each integration step we have $\Delta\sigma = \Delta s$ but only s is the actual longitudinal position of the reference particle in the whole cell. Since only H_1 depends on p_s, $X7$ is changed only when applying the Lie map $e^{-\frac{\Delta\sigma}{4}:H_1:}$.

3.3.2 Features of the Taylor series

The DA integration routine outputs the dynamical map in explicit form as shown in figure 3.2. The final six columns indicate, as exponents for the six dynamical variables,

```
DP   := 1/( 1/BETA0 + X(6) );
   DD:=0;

   X(1) := X(1) + X(2)*DP*DL/4; {H1}
   X(5) := X(5) + (DD - X(2)*X(2)*DP*DP/2 )*DL/4;
   X7   := Z + DL/4;

   AZFIELD;

   X(2) := X(2) - AZDX*DL/2; {H3}
   X(4) := X(4) - AZDY*DL/2;

   X(1) := X(1) + X(2)*DP*DL/4; {H1}
   X(5) := X(5) + (DD - X(2)*X(2)*DP*DP/2 )*DL/4;
   X7   := X7 + DL/4;

   AYFIELD;

   X(2) := X(2) + IADY; {H2(Iy)}
   X(4) := X(4) + AY;

   X(3) := X(3) + X(4)*DP*DL; {H2}
   X(5) := X(5) - X(4)*X(4)*DP*DP*DL/2;

   AYFIELD;

   X(2) := X(2) - IADY; {H2(Iy)}
   X(4) := X(4) - AY;

   X(1) := X(1) + X(2)*DP*DL/4; {H1}
   X(5) := X(5) + (DD - X(2)*X(2)*DP*DP/2 )*DL/4;
   X7   := X7 + DL/4;

   AZFIELD;

   X(2) := X(2) - AZDX*DL/2; {H3}
   X(4) := X(4) - AZDY*DL/2;

   X(1) := X(1) + X(2)*DP*DL/4; {H1}
   X(5) := X(5) + (DD - X(2)*X(2)*DP*DP/2 )*DL/4;
   X7   := X7 + DL/4;
```

Figure 3.1: Code performing the various operations on the DA variables at each step of integration is shown in figure 3.1. The procedures AZFIELD and AYFIELD computed the DA object of the potential vector and its integral at each step of integration from the set of coefficients c_{mn} representing the magnetic field.

```
   I  COEFFICIENT             ORDER EXPONENTS
   1   1.111442201528357       1   1 0  0 0  0 0
   2  0.2920444940195839       1   0 1  0 0  0 0
   3  -.8288397620180908E-02   1   0 0  0 0  0 1
   4   2.621390443812261       2   2 0  0 0  0 0
   5  0.9589399117226007       2   1 1  0 0  0 0
   6  0.1052472136664450       2   0 2  0 0  0 0
   7   2.139818636231494       2   0 0  2 0  0 0
   8  0.6287214831607242       2   0 0  1 1  0 0
   9  0.4315530255088764       2   1 0  0 0  0 1
  10  -.1313320036386119       2   0 1  0 0  0 1
  11  0.5689838828118509E-01   2   0 0  0 2  0 0
  12  0.8677287828463824E-02   2   0 0  0 0  0 2
-----------------------------------------------
   I  COEFFICIENT             ORDER EXPONENTS
   1  -6.098213931760943       1   1 0  0 0  0 0
   2  -.7026454466551645       1   0 1  0 0  0 0
   3  0.1728159261576379       1   0 0  0 0  0 1
   4   18.91670122316419       2   2 0  0 0  0 0
   5   7.994146930331629       2   1 1  0 0  0 0
   6  0.7759293763919728       2   0 2  0 0  0 0
   7  -1.287692099153911       2   0 0  2 0  0 0
   8   1.299401526419163       2   0 0  1 1  0 0
   9   4.417846016082665       2   1 0  0 0  0 1
  10   2.154252397263629       2   0 1  0 0  0 1
  11  0.2871015010002934E-01   2   0 0  0 2  0 0
  12  -.8805578006296640E-01   2   0 0  0 0  0 2
-----------------------------------------------
   I  COEFFICIENT             ORDER EXPONENTS
   1  -.3633645928289083       1   0 0  1 0  0 0
   2  0.3335779793345011       1   0 0  0 1  0 0
   3   9.668878416578217       2   1 0  1 0  0 0
   4   1.050612280095602       2   0 1  1 0  0 0
   5   2.036069704068454       2   1 0  0 1  0 0
   6  0.3090989209723089       2   0 1  0 1  0 0
   7   1.825938770475264       2   0 0  1 0  0 1
   8  -.2242970810900542       2   0 0  0 1  0 1
-----------------------------------------------
   I  COEFFICIENT             ORDER EXPONENTS
   1  -4.518899164061225       1   0 0  1 0  0 0
```

Figure 3.2: Selected terms from the 2nd order dynamical map for the X variable, for one EMMA cell at 15 MeV reference energy.

the term in the map to which the coefficient in second column refers. Thus, each variable is expressed as a power series in the values of the dynamical variables at the entrance of the cell. For instance the expression for the horizontal position (truncating coefficients after the fourth digit) is:

$$\begin{aligned} X(1) &= 1.1114\, X_0 + 0.2920\, P_{X0} - 0.0082\, \delta_0 + \\ & \quad 2.6213\, X_0^2 + 0.9589\, X_0 P_{X0} \cdots + 0.0086\, \delta_0^2. \end{aligned}$$

Once the dynamical map has been obtained, tracking particles in the EMMA cell simply involves calculating the output values for a given set of input values. We observe that there are no zeroth order terms. This means that a particle launched with zero initial values for the dynamical variables will have zero values at the exit face (except for the path length variable which will be increased by the length cell). The entrance coordinates being the same as exit coordinates, the map is said to be computed around the closed orbit. We will see in section 3.3.4 of this chapter that the reference trajectory is a straight line. To obtain a dynamical map with no zeroth order terms, the map is computed with reference straight line starting from the closed orbit position at the entrance of the cell (blue dashed line for 10 MeV in figure 3.8 on the left hand side).

In the EMMA cell, the closed orbit at 10 MeV is located at $x = -1.7$ cm (with respect to the reference polygon where x=0). The transverse offset of the reference straight line must be taken into account when tracking particles in the map. A particle with transverse position of -0.2 cm with respect to the reference trajectory will be sent with an initial transverse coordinate of 1.5 cm in the 10 MeV map (i.e. with respect to the 10 MeV closed orbit). If the exit coordinate for this particle given by the map is 0.7 cm, then the position of the particle with respect to the reference trajectory is -1.0 cm.

3.3.3 Symplectic error

In the expression (3.144), the map $\mathcal{M}_2$ is not exact because the Hamiltonian was transformed by the paraxial approximation and also because the factorisation in Lie map using the BCH formula was truncated to second order in $\Delta\sigma$. But since each factor in the factorisation is itself a symplectic map, the total map must be symplectic.

The integration of the equations of motion is done using DA objects for the dynamical variables. The purpose of an integrator is to solve the equations of motion in the form of an expression in closed form. In general, these closed forms expressed as power series have a very large number of terms. In other words, the integrated solution includes very high order terms. In practise the computer code needs to truncate them at a given order (e.g. second order in the example in figure 3.2). Even though the integration routine is symplectic, this truncation results in a symplectic error. A symplectic transformation satisfies $J^T \cdot S \cdot J = S$, where S is a block diagonal matrix constructed from the 'unit' 2×2 antisymmetric matrix, and J is the Jacobian of the transformation. The symplectic error can be quantified by computing the coefficient of the matrix Δ given by:

$$\Delta = J^T \cdot S \cdot J - S \tag{3.153}$$

Since the variables are expressed as power series, the coefficients of the Jacobian are also power series of the dynamical variables. The coefficients of Δ are therefore calculated for arbitrary numerical values of the dynamical variables. The computation of symplectic error is developed in more detail in section 5.1.3.2 in chapter 5.

If a map is truncated at order N then symplectic error is introduced at order $N+1$. In the Jacobian, defined in equation (3.68), the error will appear at the order N. The matrix Δ will then contain coefficient of order N and higher. Because of numerical precision, non-zero terms appear in Δ for order smaller than N.

The fact that tracking of particles with dynamical map gives results with some

symplectic error may mean that this method does not have great advantage over numerical tracking with standard Runge-Kutta integrator. Since the exact solution of the equation of motion must be symplectic, improving the accuracy of the Runge-Kutta integrator (e.g. decrease the step size) will reduce the symplectic error. However, in the dynamical map approach, the symplectic error up to the order the map comes from the limited numerical precision, regardless to the integration step size. If the map is computed using a symplectic integrator (as it is the case for the results presented here), then the symplectic error depends on the order of truncation, rather than the integration step size.

A symplectic error in a map may be significant if the map is applied iteratively many times, or if small non-symplectic physical effects are being investigated.

3.3.4 Reference trajectory and frame rotation

3.3.4.1 Frame rotation

When tracking particles iteratively in one cell, one needs to perform a rotation of the reference axis before entering the new cell. After one turn, the reference straight line (not corresponding to the path of any real particle) has drawn a n-sided polygon as shown in black and red in figure 3.4 (n being the number of cells considered). The real machine has been built such that the corners of the polygon are situated at the entrance face of the defocusing magnet (D magnet) since bending of the electrons mainly occurs in this magnet. The point can be located just before the entrance of the hard edge model of the magnet.

In the absence of a magnetic field, the equations relating the canonical variables after rotation (written with subscript "new") to those before rotation were taken from [41] and are expressed as followed:

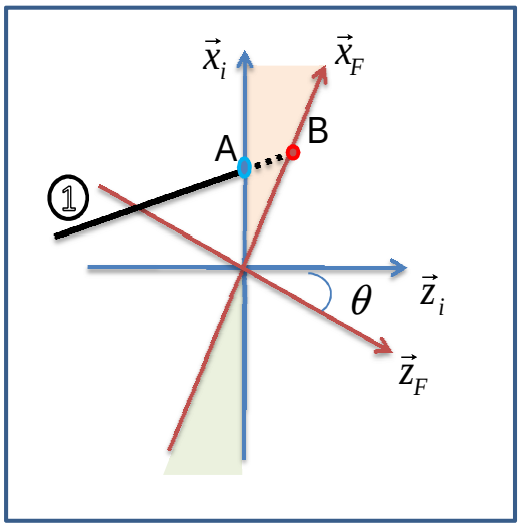

Figure 3.3: Schematic view of the rotation of reference frame by an angle θ. The blue lines and the red lines represent the initial and final (after rotation) frames respectively. The black line represents the trajectory of a particle reaching the end of the cell with a transverse position x_1. The black dashed line corresponds to the effect of the rotation on this particle changing the coordinate from the point A at the exit face of the first cell to the point B at the entrance face of the new cell. We notice that this dash line is a straight extension of the trajectory. The effect of the rotation on the trajectory is equivalent to the effect of a drift space added in the beam line (corresponding to the light red area). This choice is realistic only if the magnetic field is negligible in that area in the real machine.

$$x^{new} = \frac{x}{\cos\theta(1 - \frac{p_x \tan\theta}{p_z})} \tag{3.154}$$

$$p_x^{new} = p_x \cos\theta + p_z \sin\theta \tag{3.155}$$

$$y^{new} = y + \frac{p_y \ x \ \tan\theta}{p_z(1 - \frac{p_x \tan\theta}{p_z})} \tag{3.156}$$

$$p_y^{new} = p_y \tag{3.157}$$

$$l^{new} = l + \frac{(1+\delta) \ x \tan\theta}{p_z(1 - \frac{p_x \tan\theta}{p_z})} \tag{3.158}$$

$$where \ \ p_z = \sqrt{(1+\delta)^2 - p_x^2 - p_y^2} \tag{3.159}$$

In the absence of a magnetic field, the effect of the rotation on the trajectory of a particle is equivalent to the effect of a drift space placed between the exit face of

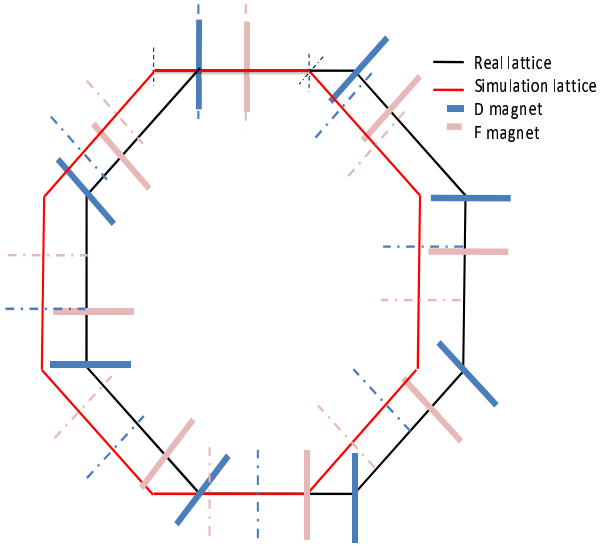

Figure 3.4: Schematic of the EMMA ring showing two descriptions of the lattice: one with rotation at the entrance of the D magnet (black) and the other with rotation in the middle of the long drift (red). In spite of the fact the only 8 cells are present in the figure, the ring is composed in reality of 42 cells. This modification as been made to show that the overall length of the polygon in both configuration remains constant. However we observe that when performing the rotation of the axis of reference far the D magnet (in red) rather than at its entrance face (in black), the absolute position of the magnets in dashed line is different form the real position following the black polygon. Hence the lattice is different.

a cell and the entrance face of the following cell (red area in figure 3.3). In reality, because of the fringe fields for instance, the magnetic field may be non zero at the exit face of a cell. Hence, when applying the transformation to the particle coordinates corresponding to the rotation of the reference axis, this magnetic field should be taken into account.

The vector potential does not appear in equations (3.154) to (3.159). Hence, with these equations, the magnetic field is not taken into account at the location of the rotation. We could therefore either derive more complete equations that include the magnetic field or always perform the rotation where the magnetic field is negligible. Deriving the equations including the vector potential in analytical form in this geometry seemed to be rather cumbersome. It would be an interesting subject for a future study. Instead we reconsidered the positioning of the rotation in two consecutive steps.

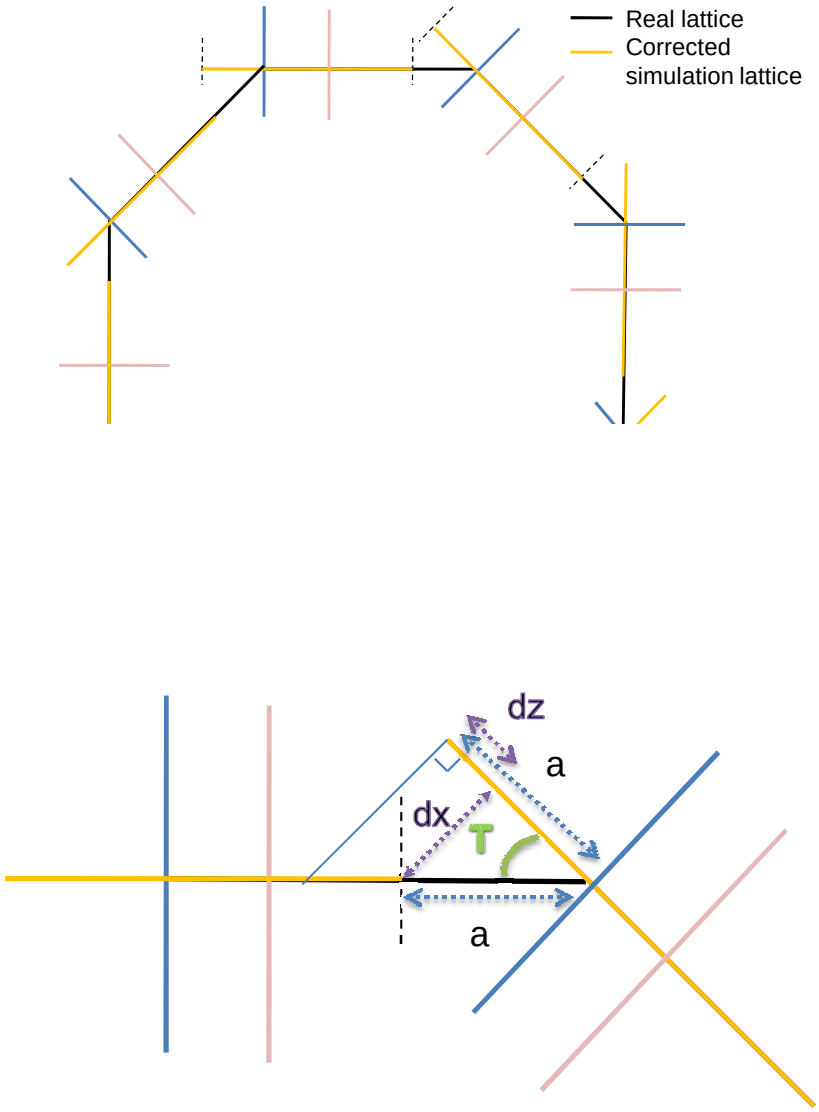

Figure 3.5: Top: Schematic of the EMMA ring showing the configuration with rotation at the entrance of the D magnet (black) and with rotation in the middle of the long drift corrected to match the real lattice (yellow). The black dashed line show the entrance and exit faces of the field maps of two consecutive cells. Hence particles coordinates at an exit face need to be translated to the next cell entrance face. Bottom: a more detailed view of the geometry of this translation is presented. The correction is composed of two translations dx and dz along each of the reference axes after rotation.

First, we shift the location of rotation to the middle of the long drift where the field is negligible. Consequently, the lattice obtained is different from the real lattice (see figure 3.4), hence beam dynamics will be different. However since we wanted at some point to compare the simulation results with the experimental data, we need to be tracking in the real lattice. Therefore we had to correct the effect of the location of the rotation.

Figure 3.5 shows the corrected configuration of the lattice. The idea consisted in applying a transformation to the particle coordinates at the exit of each cell. By applying an additional transformation to the particle's coordinates (after applying the rotation described in (3.154) to (3.159)), i.e a translation by a distance dx along the new $\vec{x}$ axis and dz along the new $\vec{z}$ axis, we obtained a lattice identical to the real one while still performing the rotation far from the magnets.

$$\begin{aligned} dx &= a \times \sin T \\ dz &= a \times (1 - \cos T)\,. \end{aligned} \tag{3.160}$$

a is the distance from the middle of the long drift to the entrance face of the D magnet.

To verify the validity of the correction, we tracked particles in the different configurations with the hard edge model in PyZgoubi. The horizontal tune ν_x is insensitive to the change whereas the vertical tune ν_y and the time of flight are significantly affected by it (see figure 3.6). Changing the reference trajectory mainly affects the closed orbit, therefore the time of flight will vary. Also, with a different closed orbit, particles will experience different fringe fields, which will affect the vertical tune.

When applying the correction to the lattice with the rotation in the drift, the beam dynamics are back to the same values as the real lattice. In the following we assumed

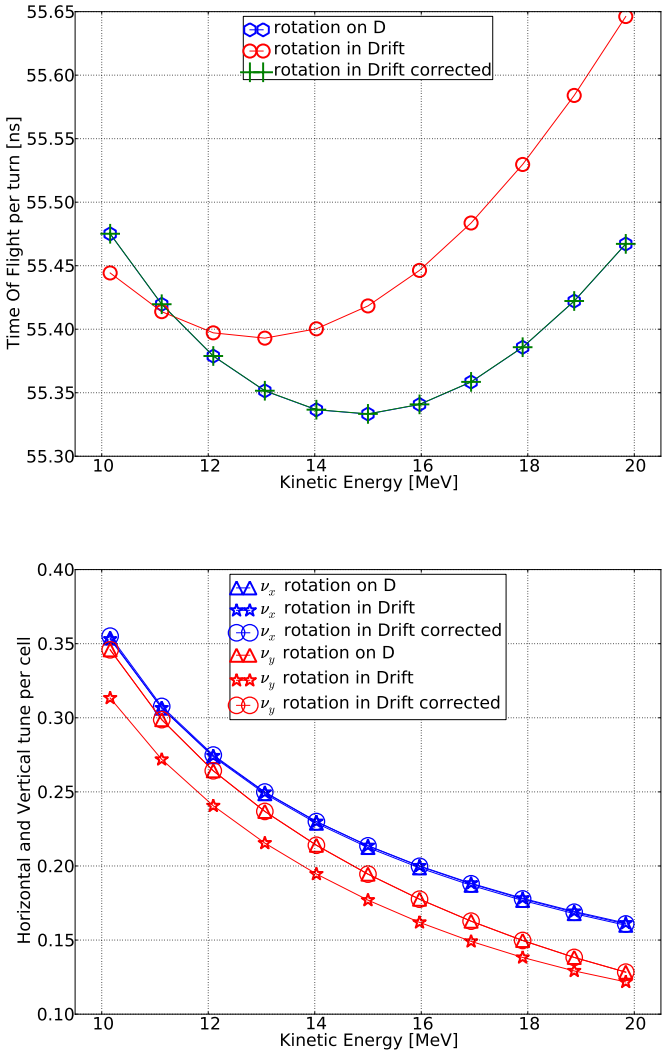

Figure 3.6: Top: variation of time of flight with energy. We observe a large discrepancy between the configuration with rotation performed at the entrance of the D magnet (blue) and the rotation performed in the drift (red). When applying the appropriate correction to the former (green), behaviours of both configurations agree. Bottom: Tune variation with energy.The horizontal tune (blue) is barely affected by the location of the rotation whereas the vertical tune is significantly smaller for low energy (0.03 at 10 MeV) for rotation in the long drift (red stars). The rotation affects closed orbits for low energy having larger excursion in the D magnet. We observe that the correction applied to the rotation in the drift configuration (red circles) agrees with the real lattice (red triangles)

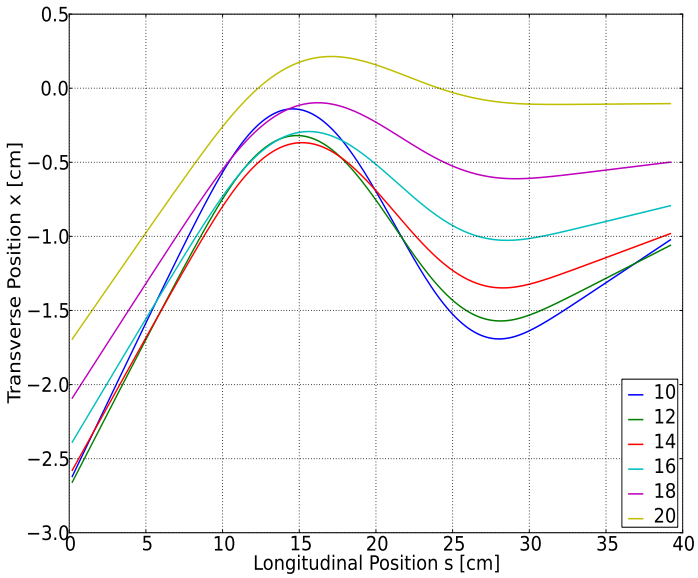

Figure 3.7: Closed orbits in one EMMA cell for energy from 10 MeV to 20 MeV with 2 MeV step.

this correction to be valid with field maps, and therefore avoided the need to make a rotation in a region of non zero magnetic field. We were then able to study the beam dynamics in the field map corresponding to the real baseline lattice as it was designed (see section 1.3) and built.

3.3.4.2 Reference trajectory for a dynamical map

The symplectic integrator that we use requires the paraxial approximation. This must be studied with care, since in an FFAG there is a significant change of trajectory when gaining energy. Different reference energy may be needed for different energies. Several maps are computed for a discrete number of energies (e.g. in EMMA, from 10 MeV to 20 MeV by 2 MeV step); their reference trajectory being as near as possible to the closed orbit at this energy (see figure 3.7). Particle trajectories should then remain close to the reference trajectory, and the paraxial approximation should be valid.

Ideally, the closed orbit itself could be used as the reference trajectory at a given

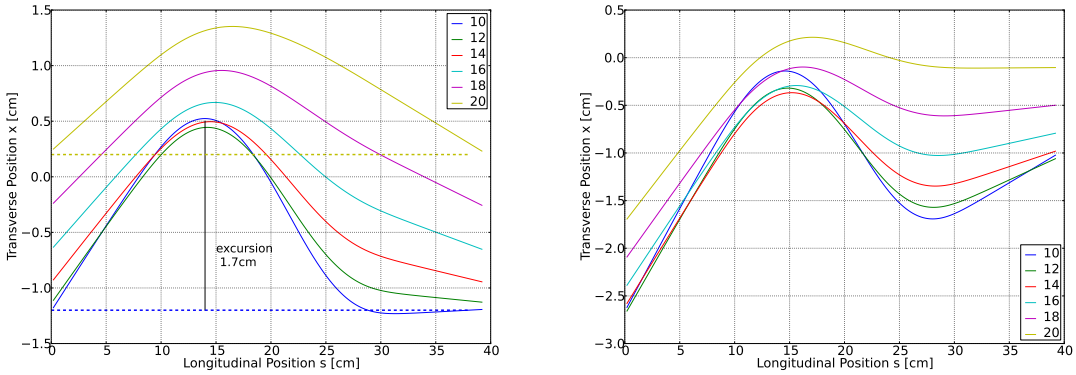

Figure 3.8: Closed orbits in one EMMA cell for energy from 10 MeV to 20 MeV with 2 MeV step.

reference energy. However the accelerator Hamiltonian used for this study (see equation (3.127)) is written for a straight coordinate system. More terms must be added to include a non-zero bending radius to the integrator required to follow the curvature of the closed orbit in EMMA. The generalisation of this integrator to curved system is an interesting topic for further investigation.

In this study, we use instead a straight line starting (and ending) at the middle of a long drift, where the field is close to zero. We chose the horizontal transverse position of the reference straight line for a given energy to correspond to the position of the closed orbit for the same energy. The reference straight line for each dynamical therefore differs from the reference polygon chosen by Berg when designing the EMMA ring [21] (see orange straight line in figure 1.4 in chapter 1). However the reference polygon is still used as the reference transverse location with expressing the tracking results (e.g. a particle with transverse coordinate x=0 is located on the reference polygon and not necesseraly on the reference trajectory of the dynamical map used for tracking).

Figure 3.8 shows the closed orbits for various reference energies in EMMA. On the left hand side, the rotation is performed in the middle of the drift but the "frame correction" is not applied. This configuration is therefore not equivalent to the real

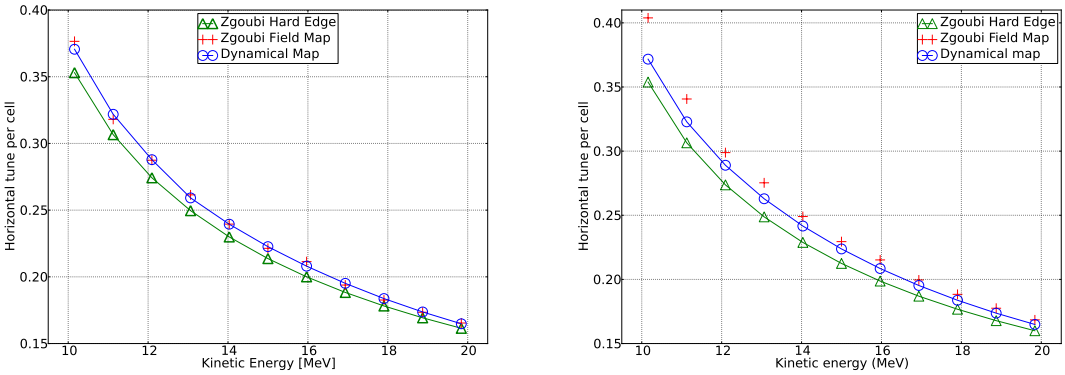

Figure 3.9: Horizontal tune evolution with energy in the EMMA cell. On the left hand side results from numerical tracking in the original field map with PyZgoubi are compared with dynamical maps results. In both codes the rotation is performed in the middle of the drift and the correction frame is not applied. On the right hand side, the same comparison is shown but this time with "frame correction" in both codes. We observe that the agreement between the two codes is better on the left hand side, especially for low energy. For instance at 10 MeV the discrepancy is 0.005 on the left hand side and 0.1 and the right hand side.

EMMA lattice. On the right hand side, the rotation is also performed in the middle of the long drift and the "frame correction" is applied. In both cases a different dynamical map is computed for each reference energy and the analytical representation of the field is performed with a single reference cylinder of radius 25 mm. We observe that in the case of the "frame correction", the closed orbits have a larger transverse excursion. The excursion is defined by the distance between the closed orbit trajectory and the reference straight line transversely located at the position of the closed orbit at the beginning of the cell (blue dashed line for 10 MeV and yellow dashed line for 20 MeV). For instance at 10 MeV in blue in figure 3.8, the excursion without the correction is maximum at $s = 14$ cm (symbolised by the black vertical line in the D magnet) and is equal to $0.5 - (-1.2) = 1.7$ cm whereas it reaches $-0.2 - (-2.6) = 2.4$ cm with the correction.

Figure 3.9 shows the horizontal tune evolution with energy in the EMMA cell. On the left hand side results from numerical tracking in the original field map with PyZgoubi are compared with dynamical maps results. In both codes the rotation is

performed in the middle of the drift and the correction frame is not applied. On the right hand side, the same comparison is shown but this time with "frame correction" in both codes. We observe that the agreement between codes is better on the left hand side, especially for low energy. For instance at 10 MeV the discrepancy is less than 0.01 on the left hand side and about 0.06 and the right hand side.

It is important to note that PyZgoubi does not apply the paraxial approximation. We conclude therefore that when applying the "frame correction", because the excursion of the closed orbits are larger with respect to the reference straight line in the dynamical map, two factors may play a role in this discrepancy: first in this case , the analytical representation was computed only with one reference cylinder. We saw in section 2.3.4.2 of chapter 3 (see figure 2.30(a)) that this could affect the value of the tune. Second, the limit of validity of the paraxial approximation for particle with large excursion could be observed. We will see in chapter 4 that this effect is negligible in terms of time of flight. For the rest of the study, we will work with the realistic model (with "frame correction") and try to estimate the effect of the paraxial approximation on other beam dynamics results.

3.4 Summary and conclusions

In this chapter, the aim was to develop a procedure that solves the equations of motions in an accelerator element defined by an analytical representation of the magnetic field. To do so, we started by deriving the Hamiltonian for an accelerator in a straight coordinate system normalising the dynamical variables and choosing the appropriate set of variables to keep their values small. To solve Hamilton's equations for a quadrupolar field, we applied the paraxial approximation and expressed the Hamiltonian as a sum of integrable terms. We observed that dynamics in a quadrupolar magnet can be described as an harmonic oscillator. We then proved that a transformation in Hamil-

tonian systems is symplectic. This implied Liouville's theorem stating the invariance of the density of particles in phase space for motion in an Hamiltonian system. We studied the implication of symplecticity to beam dynamics in periodic beamlines and derived an invariant quantity J of the motion: the action. This invariant was proportional to the area of the betatron ellipse traced out by a particle in phase space after each period. We defined a set of parameters, the twiss parameters, characterising this ellipse and therefore following the periodicity of the lattice. We showed that the action was the conjugate momentum to a canonical variable called the "angle". The new Hamiltonian was found to be simply expressed as the ratio of the action and the beta function. From the second Hamilton's equation, the phase advance was defined as the variation of the angle variable from one point to another along the beamline, and the tune was defined as the phase advance over a complete turn in a ring divided by 2π.

In the following section, we first observed that Hamilton's equations could not easily be solved for a general magnetic field. We saw that using the BCH formula and useful properties of the Lie transformations, we obtained a symplectic integrator for a sextupolar field. This integrator took the form of the "Yoshida" factorisation equivalent to applying to the dynamical variables a sequence of drift and kicks. We presented the extension of this method to a general magnetic field. By applying the paraxial approximation to express the Hamiltonian as a sum of integrable terms, we derived the second order explicit symplectic integrator developed by Wu, Forest and Robin. This integrator requires the computation of the integral and the differential of the vector potential, justifying the work made in chapter 2 to obtain an analytical representation of the magnetic field.

In the last section of this chapter, we presented the computer tools created to apply this symplectic integrator. The transformations of the dynamical variables were

expressed as Taylor series obtained by integration through the magnetic field using the Differential Algebra code COSY infinity. This code is especially written to perform integration and differentiation (and algebraic manipulation) of Taylor series variables. Since the Taylor series are truncated, we concluded that the symplecticity of the solution was lost in the missing high order terms. However, the advantage of this integrator over a non symplectic integrator (such as the Runge-Kutta algorithm) is that the symplectic error does not depend on the integration step, but only on the truncation order. Finally, we discussed the consequences of the paraxial approximation in an FFAG accelerator. Effects of this approximation are seen when comparing the horizontal tune at low energy obtained from Pyzgoubi not using the paraxial approximation and dynamical maps. The reference straight line for the dynamical map at each energy must be carefully chosen to minimise this effect.

In this chapter, we developed the computer tools that we will use to study beam dynamics in accelerators. The challenge is to apply this technique to beam dynamics in FFAG accelerators where the paraxial approximation may not be valid. The Non-Scaling FFAG EMMA was chosen as case study because simulations and experimental results could be compared. However the use of dynamical map for EMMA is not of large benefit compare to numerical tracking in efficient code such as PyZgoubi. Firstly because the dynamics are expected to be rather linear in the ring; hence conventional linear code may be precise enough. Secondly symplectic errors may not be significant since particles only perform few tens of turns in EMMA. The aim of the following study is therefore not to produce better simulation results than other codes for EMMA but rather to evaluate the validity of this method with respect to large deviations of the dynamical variables. If the results are convincing, this method can then be applied to nonlinear FFAG accelerators with more complex magnetic fields and potentially large number of turns performed; benefits of this type of approach would then be significant.

4

Beam dynamics simulations

4.1 Introduction

So far, we have developed computational tools to extract an analytical representation of the magnetic field in a lattice element and derived an integrator for the equation of motion in order to track particles in the field. The beam dynamics have been expressed in the form of a Taylor map using differential algebra routines. The next step is to apply these tools to the case study EMMA. Most of the work on the field maps has already been applied to the EMMA cell. In this chapter we will present the detailed study of the beam dynamics in the magnetic field representation derived in chapter 2, using the tools contained in chapter 3.

To validate beam dynamics results obtained with dynamical maps, we chose to study the beam dynamics with another tracking code, the numerical tracking code PyZgoubi. Its main features will be presented. Both tracking methods will be applied to the case study EMMA. Thus, the EMMA FFAG cell features relevant to particle tracking will be outlined. We will compare tracking result from a hard edge simplified model of the magnets and from a detailed 3D model of the whole cell.

In the second part, single particle beam dynamics in the EMMA cell in terms of tune

per cell, time of flight and betatron motion will be developed. Results from PyZgoubi using either a hard edge model or a numerical field map will be compared with results from the dynamical map. Also we will study the difference between tracking in multiple dynamical maps with different reference energies and a single map varying the energy deviation of the tracked particle. Since dynamical maps can be useful to study non linear effect of the beam dynamics, the tune shift with amplitude will be derived by different methods, including a direct derivation from the dynamical map coefficients.

We will then focus on longitudinal dynamics. We will present the behaviour of a group of particles with an initial distribution in energy, tracked at fixed energy (no acceleration) through the cell either by applying the dynamical map or by numerical tracking with PyZgoubi; we will outline the effect of energy spread on the betatron motion measurement.

Finally we will demonstrate that the dynamical map can simulate the serpentine acceleration agreeing with an analytical model. The longitudinal and transverse distributions of a group of particles through acceleration will be studied. The effect of the rate of acceleration on the transverse distribution will be presented. It will be shown that to achieve reasonable accuracy, at least two dynamical maps with different reference energies are needed to simulate the dynamics through acceleration over the whole energy range in EMMA.

4.2 General features of the EMMA cell

The EMMA prototype aims to study the Non Scaling FFAG acceleration scheme. The dynamical behaviour of a beam in such a structure is still experimentally untested, especially its response to resonance crossing. In order to cover a wide area of dynamics, the EMMA lattice has been kept adjustable; the horizontal transverse position and strengths of both quadrupoles within each cell are degrees of freedom. Hence, it will

be possible to link a certain tune and time of flight evolution with energy with these parameters. Firstly, this is done by simulation before the commissioning of the real machine (EMMA commissioning started in July 2010). To do so, one has to model the magnetic field created by a certain configuration of magnets and track particles in this map.

The EMMA ring is composed of 42 cells. Within a cell, elements are positioned with respect to a straight line (see figure 3.5). The ring can then be seen as a 42-sided polygon. Corners are situated at the entrance of the defocussing magnet (D magnet) since bending of the electrons mainly occurs in this magnet. The rotation angle between two adjacent sides is $\theta = 2\pi/42$. Since (without acceleration) the EMMA ring is periodic, only one pair of magnets (out of 42 pairs) has to be modelled, and tracking can be done iteratively using one cell.

4.2.1 Description of the numerical tracking code : PyZgoubi

PyZgoubi is the Python interface of the Fortran tracking code Zgoubi. Zgoubi itself works with an input text file in which the sequence of beam line elements and their characteristics (written as matrix of numerical data) is contained. Each time a characteristic of the lattice is changed, a corresponding text file must be created. To make this process automatic and therefore add flexibility to the tracking code, routines are written in the Python language allowing the definition of variables. It then automatically creates the corresponding text file for Zgoubi. The tracking results from Zgoubi are also given in text files. They are processed by a python script by which results can be defined as variables and linked to plotting or optimisation routines (e.g. closed orbit seeking). The plotting routines available with Python offer a better quality of graphics than those created directly by Zgoubi.

Zgoubi uses a stepwise ray-tracing method which means that it tracks the position of a particle through a lattice element by longitudinal consecutive steps. The integra-

tion method consists in solving the Newton-Lorentz equation $m\frac{d\vec{v}}{dt} = q\vec{v} \times \vec{b}$ at each step by expressing the dynamical variables (position and velocity) as truncated Taylor expansions in the integration step ds. The numerical integration routine minimises the computing time but it does not use a purely symplectic integrator. Symplecticity is monitored in Zgoubi by built-in routines computing the symplectic error for every tracking result. It is the responsibility of the user to optimise the integration step size to achieve the desired level of symplecticity.

Originally Zgoubi was written in the early 1970's for spectrometer studies. Since the magnets were large and the magnetic field precision critical, PyZgoubi was developed to integrate the equations of motion in a field map created from magnet measurements. Therefore PyZgoubi has built-in routines handling numerical field maps provided in separated text files. This feature is crucial for the comparison with dynamical maps also derived from the integration of particle trajectories through field maps.

In addition, in PyZgoubi the magnetic field and its derivative are computed at each integration step either from an ideal analytical definition of the magnetic field in the beam line element, or by reading a numerical data table (created from OPERA, for instance). This allows us to validate an ideal analytical description of the magnets ("Hard Edge (HE) Model") against simulated field maps.

In this study, PyZgoubi has been used only with two dimensional numerical field maps, representing the field in the median plane of the magnets, being the horizontal plane (**x**,**z**) with a vertical coordinate y=0. A 2D field map gives the three components B_x (x, 0, z), B_y (x, 0, z) and B_z (x, 0, z) at each node (x, z). **B** and its derivatives at any point (x, y, z) are calculated by polynomial interpolation followed by Taylor expansions in y derived from Maxwell equations, with the possibility of enforcing symmetries.

This method may not be valid in the case of complex field configuration at the edges of the magnet. Since the dynamical maps are built with a direct 3D representation of the magnetic field, discrepancies between the two codes may occur because of the

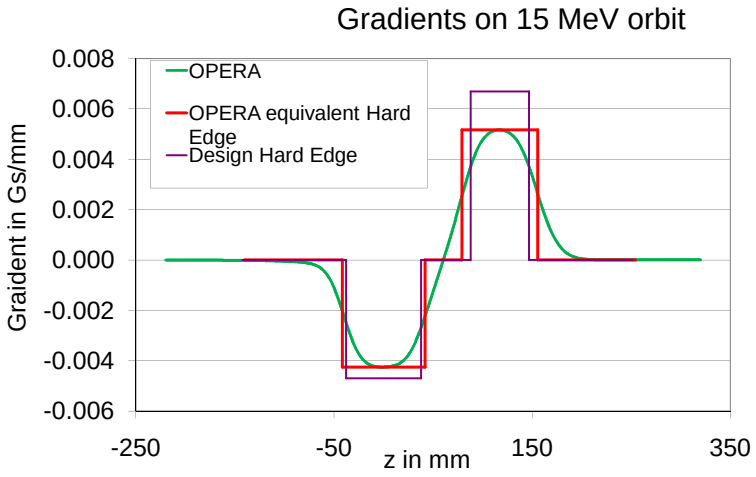

Figure 4.1: Gradient along the EMMA cell for Design Hard Edge Model and OPERA Model. The real magnetic field distribution (in green) falls off smoothly to zero. The region where the field is non-zero is wider than the actual physical length of the magnet corresponding the design hard edge model. The peak strengths of the real magnets is computed such that the integrated field over the cell equates to the design integrated gradient. One can defined the effective lengths of the magnets by plotting (in red) the hard edge equivalent model of the real magnets.

difference in these representations.

The choice of Zgoubi for the comparison with the dynamical maps simulations is also motivated by the fact that it has been benchmarked against scaling FFAGs with complex magnets and a non-scaling isochronous FFAG lattice [49, 50].

4.2.2 Hard edge model

In this section we will discuss the consequences of using a numerical field map to describe the EMMA cell in terms of geometry and rotation of the reference frame. Beam dynamics corresponding to the different approaches will be presented in the next section.

The preliminary design study of the EMMA ring has been performed with an ideal "hard edge" model of the magnets [21]. The gradient of the magnetic field is constant along the magnet length and is equal to zero elsewhere. Only the magnets' lengths and strengths are therefore necessary to characterise the lattice. Optimisation routines

useful at the design stage are fast and rather simple to write.

In reality the magnetic field varies continuously through the cell and falls off smoothly to zero outside the physical length of the magnet (see figure 4.1). Note that in several tracking codes including PyZgoubi, these "fringe" fields can be modelled using set of functions such as Enge functions [48]. These functions can be derived by fitting the measured or simulated (e.g. with OPERA) magnetic field data. Since PyZgoubi could handle directly the field map we created from finite element method (FEM) (see chapter 2), we did not investigate the use of analytical fringe fields.

Table 4.1: Description of the cell

Section	**Hard edge Design**	**Real design**
long drift in mm	210.000	217.241
D magnet in mm	75.699	65.000
short drift in mm	50.000	57.240
F magnet in mm	58.782	55.000
$\int \frac{\partial B_y}{\partial x} ds$ for D in Gs	-0.3560	-0.3558
$\int \frac{\partial B_y}{\partial x} ds$ for F in Gs	0.3940	0.3947

To design the magnet, several constraints have to be taken into account. The price of a magnet is related to the amount of material needed for the yoke and the coils. Also manufacturing costs increase with the complexity of its geometry. On the other hand the geometry must ensure a constant gradient of the magnetic field over the transverse aperture of each magnets. In EMMA the magnets are designed to achieve a field quality defined by a tolerance of 1% variation of the gradient across the vacuum chamber in each magnet aperture. Eventually magnets lengths and nominal currents must be adjusted such that the integrated gradient along the cell $\int \frac{\partial B_y}{\partial x} ds$ in real magnets and in the hard edge model are equal. Then the focusing strengths experienced by particles are expected to be reasonably close to the design values.

The magnets were built to handle larger currents than the design estimates indicated would be necessary, while keeping the required field quality. Hence, the real physical

length of the magnet can be made smaller than the design one conserving the integrated gradient. There is then more space to fit other components in the beam line. Table 4.1 presents the cell configurations for both cases and figure 4.1 shows the gradient along the EMMA cell with a hard edge model (in purple) and with an OPERA field map (in green). The actual magnetic field profile shown in figure 4.1 (in green) extends some distance outside the magnets.

PyZgoubi which will be used as a benchmarking code for the dynamical maps results, can handle both hard edge models and numerical field maps to describe a magnetic element. When tracking particles with hard edge models of the magnets, the rotation of the reference axis between consecutive cell assuming a zero field region can be performed just before the entrance of the D magnet. Since in reality the magnetic field extends outside the D magnet, when working with field map, we had to move the rotation in the long drift. As explain in section 3.3.4 of chapter 3, a correction of the particle coordinates at the exit face of a cell had to be applied to perform tracking in a realistic lattice. In the next section we will present these tracking results obtained with PyZgoubi and with dynamical maps.

4.3 Beam dynamics simulations with dynamical maps

4.3.1 Transverse beam dynamics

As explained in chapter 3, a dynamical map is valid in the vicinity of a reference axis, for particles travelling with an energy close to a chosen reference energy. Since in EMMA the energy range and the transverse excursion range are quite large, the range of validity of a dynamical map had to be tested against the EMMA FFAG beam dynamics. The first approach consisted in considering various reference energies across the whole energy range. As a second approach, we computed a dynamical map for a reference energy in the middle of the energy range (14 MeV or 15 MeV) and studied

the behaviour of particles with energy deviation δ using that single map.

4.3.1.1 Maps with various reference energies

Eleven dynamical maps are calculated around the closed orbits for reference energies from 10 MeV to 20 MeV, in steps of 1 MeV as explained in section 3.3.4 of chapter 3. The tunes (phase advances per cell) can be obtained from the eigenvalues λ of the linear part of a given map:

$$\lambda = e^{\pm 2\pi i \nu}, \tag{4.1}$$

where ν is the tune.

The zeroth-order term in the map for the fifth variable (longitudinal coordinate, z) represents the difference in path length of the closed orbit with respect to the reference trajectory.

The comparisons of these features with numerical tracking through the magnetic field map and in hard edge model with PyZgoubi are plotted in figures 4.2 and 4.3. Focusing first on the comparison between PyZgoubi with field map (red crosses) and dynamical map (blue circles) (computed from the magnetic field map), we observe a discrepancy smaller than the expected measurement precision for the vertical tune and path length. However, we obtain a larger discrepancy for the horizontal tune at low energy : 0.04 at 10 MeV and 0.02 at 11 MeV. A explanation for this discrepancy can lie in the large excursion of closed orbits for lower energies. At such large excursion, the analytical representation of magnetic field is at the limit of its validity and may therefore be slightly different from the original numerical field map used to track with PyZgoubi.

Tracking results in a hard edge model of the magnets in PyZgoubi is also presented (in green) on the plots, and indicate the impact of the fringe field : we observed a maximum discrepancy of about 0.05 at 10 MeV for the horizontal and vertical tune per

cell with respect to the tracking in field map with PyZgoubi. Hence fringe fields have more impact on the low energy closed orbits.

In figure 4.3, we observe as well a significant shift of the time of flight curve when using field maps. The minimum of the curve is shifted from 15 MeV with hard edge model (agreeing with design studies) to 17 MeV and decreased by 120 ps. PyZgoubi and dynamical maps simulations agree on this result which means that this large discrepancy is due to the difference between the hard edge representation and the more realistic field map representation of the EMMA cell. The baseline lattice was especially designed to obtained a parabola shape tof curve centred in 15 MeV. This result shows that when modelling the EMMA cell with field maps, the original baseline configuration does not ensure the desired shape for the tof curve. If the real machine measurements confirm this result (see section 5.2.3) a new baseline configuration has to be found to obtain the correct tof curve (i.e. the minimum of the curve occurs for a particular energy and tof adapted to the rf frequency of the accelerating cavities). This issue will be discussed in chapter 5.

After analysing the dynamics of the closed orbit, it is interesting to study the behaviour of particles around this closed orbit. Betatron motion has been studied by applying the dynamical maps to particles with some initial transverse offset with respect to the reference trajectory. Figure 4.4 (top) shows the horizontal phase space for reference energies from 10 MeV to 20 MeV, constructed by applying the corresponding dynamical map (in energy) for 2000 iterations to particles with 1 mm initial transverse offset. We notice that there is some non-physical growth in the amplitude over time for 10 MeV and 12 MeV: this is a consequence of a symplectic error introduced by truncation of the dynamical map to 2^{nd} order. The effect disappears if terms up to 3^{rd} order are retained (see fig. 4.4 bottom).

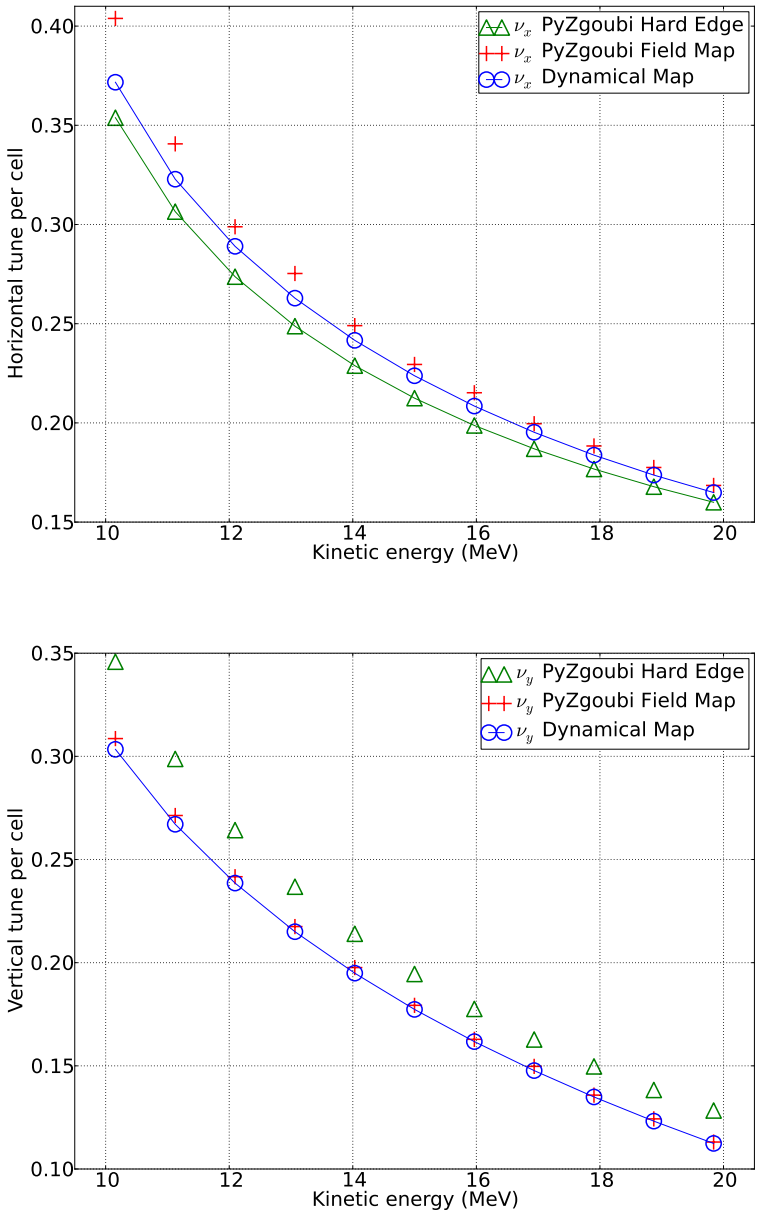

Figure 4.2: Horizontal (top) and vertical (bottom) tune versus kinetic energy computed from simulations with hard edge model and field maps. We observed a maximum discrepancy of about 0.05 at 10 MeV for the horizontal and vertical tune per cell with respect to the tracking in field map with PyZgoubi. Hence fringe fields have more impact on the low energy closed orbits.

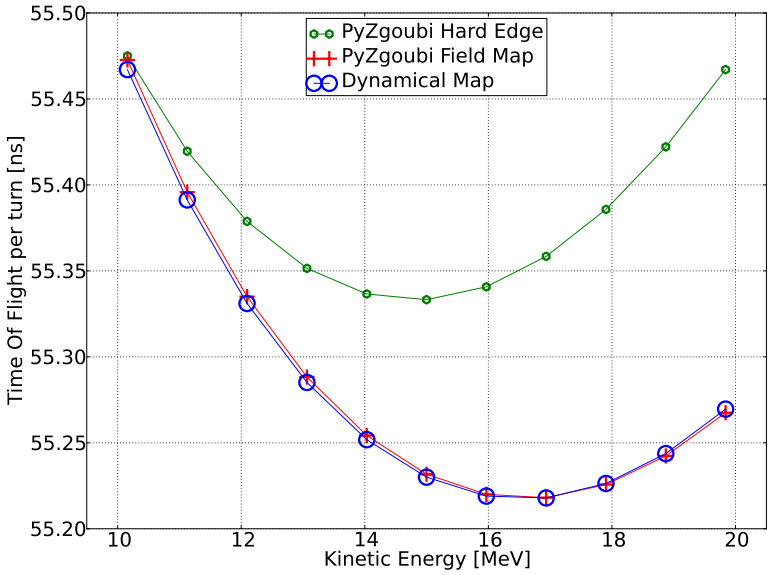

Figure 4.3: Time of Flight versus kinetic energy computed from simulations with hard edge model and field maps. We observe a significant shift of the time of flight curve. The minimum of the curve is shifted from 15 MeV with hard edge model (agreeing with design studies) to 17 MeV and decreased by 200 ns. PyZgoubi and dynamical maps simulations agree on that result which means that this large discrepancy is due to the difference between the hard edge representation and the field map representation of the EMMA cell

4.3.1.2 Maps with energy deviation

The number of dynamical maps required to model the dynamics over the full energy range in EMMA will depend on the range of validity of each map with respect to variations in the energy deviation δ. Figure 4.5 shows the horizontal tune (in blue) and the vertical tune (in red) as a function of energy obtained in two different ways: first, from different dynamical maps computed for different reference energies (circles on line); and second, from a single dynamical map at a single reference energy (14 MeV), but with different values for the energy deviation δ and for different truncation order of the map : 3 (triangles), 7 (hexagons) and 9 (crosses). We observe a large discrepancy between the two methods for low and high energy (i.e. for large energy deviation from the reference 14 MeV). The discrepancy decreases when increasing the truncation order

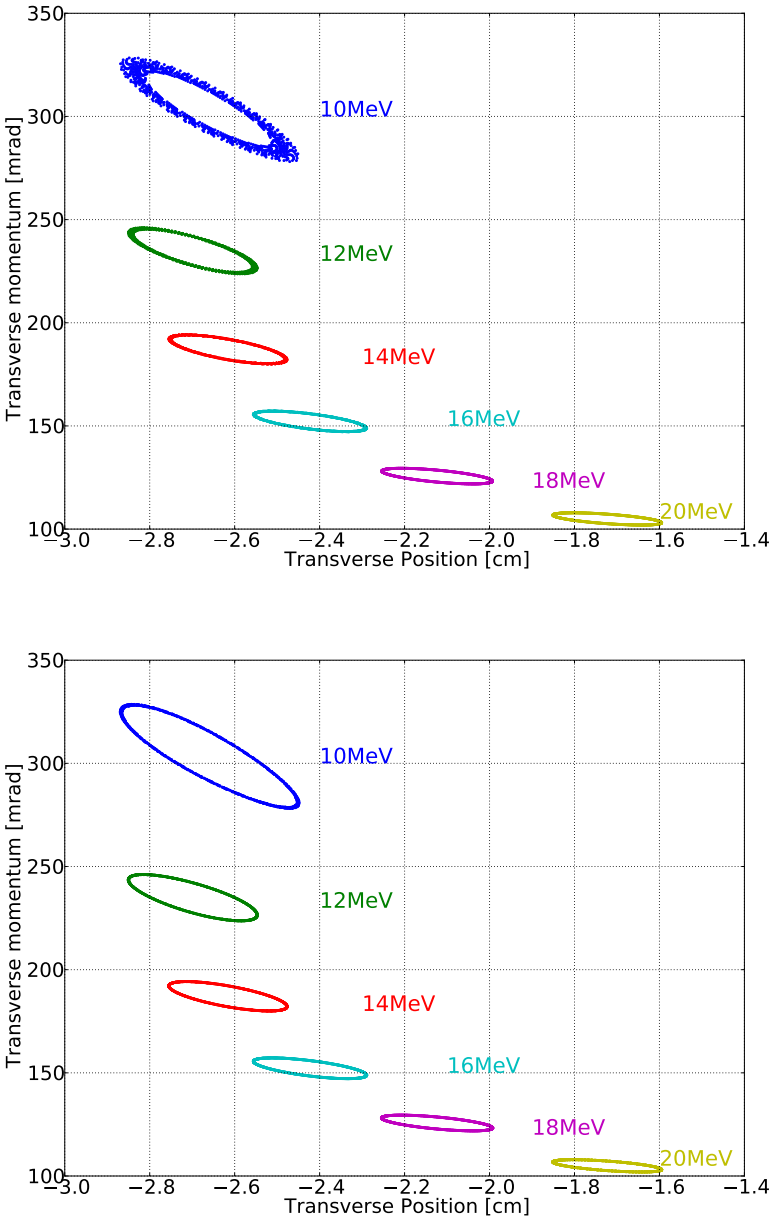

Figure 4.4: Top: Betatron motion with multiple dynamical maps order 2. We notice that there is some non-physical growth in the amplitude over time for 10 MeV and 12 MeV: this is a consequence of the truncation of the dynamical map to 2nd order. Bottom: Betatron motion with multiple dynamical maps order 3. The effect disappears if terms up to 3^{th} order are retained

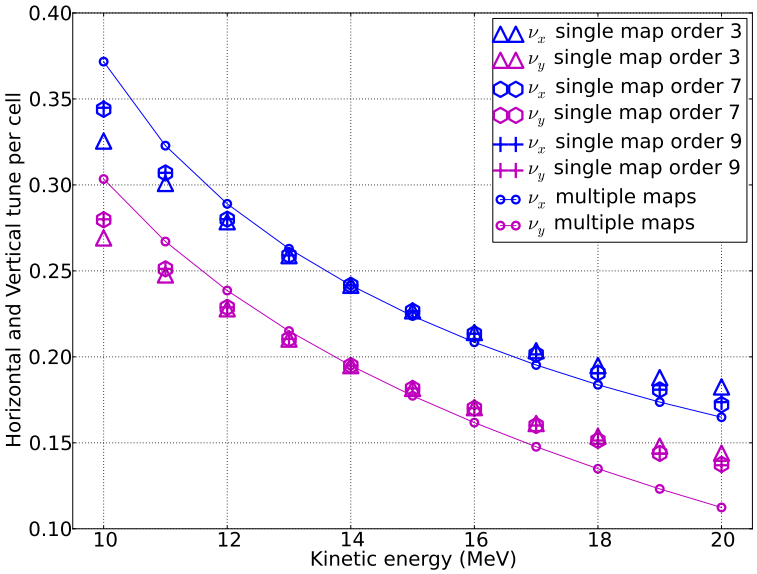

Figure 4.5: Betatron tunes computed with a set of dynamical maps at different reference energies (circles), and with a single dynamical map with different energy deviations (crosses). The agreement between the two methods is better than the expected measurement precision 0.01 for energy deviation up to ± 2 MeV (i.e 15%). This suggests that it may be necessary to use a three different maps (12.5 MeV, 15 MeV and 17.5 MeV reference energies for instance) to reproduce the transverse and longitudinal dynamics obtained with 11 dynamical maps as in section 4.3.1.1.

from 3 to 7 but no significant improvements can be seen when truncating at the 9^{th} order; this indicates that the 7^{th} is the optimal truncation order for the tune variation with energy deviation.

The expected precision of the tune measurement in EMMA is 0.01. The agreement between the two methods is within this range for energy deviation up to ∓ 2 MeV (i.e 15%). This suggests that it may be necessary to use at least three different maps (12.5 MeV, 15 MeV and 17.5 MeV reference energies for instance) to reproduce the transverse and longitudinal dynamics over the whole energy range in EMMA (obtained with 11 dynamical maps in section 4.3.1.1).

In order to simulate acceleration in EMMA, the dynamical maps should also describe accurately the variation in time of flight with energy. Figure 4.6 shows the time of

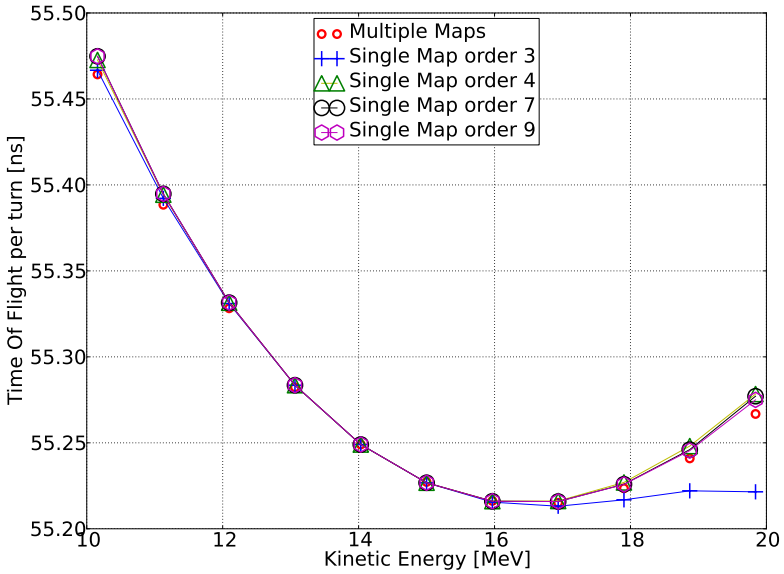

Figure 4.6: Time of flight for various energies computed with a set of dynamical maps at different reference energies (blue dots), and with a single dynamical map with different energy deviations (red circles). We see good agreement for the maps truncated at 4^{th} order

flight of the closed orbit at different energies computed in the two ways used previously for the tune (i.e. multiple maps (red circles) and single map with energy deviation with different truncation orders: 3 (crosses), 4 (triangles), 7 (black circles) and 9 (purple circles)). We observe a good agreement (within the measurement precision range of 10 ps) for the whole energy range for a dynamical map truncated at the fourth order; no significant improvement is obtained when increasing the truncation order up to 9. We conclude that a single map truncated at the fourth order can simulate the time of flight variation with energy over the whole energy range.

A last comparison between multiple maps simulation and single map with energy deviation simulations is made in terms of the betatron motion (1 mm offset) in horizontal phase space. In figure 4.7(a) we observe that for a map truncated at the 4^{th} order, the betatron motion in horizontal phase space has a strong non-physical growth in the amplitude for small energy deviation ± 1 MeV. In figure 4.7(b) this effect is reduced

by retaining terms in the map up to 7^{th} order but still noticeable for energy deviation of ± 2 MeV. A sensible behaviour in figure 4.7(c) is obtained for energy deviation of ± 2 MeV retaining terms in the map up to 9^{th} order. Computational limits in the COSY routine we used, did not allow us to investigate this effect for higher truncation order. Also, when increasing the amplitude of the betatron oscillation from 1 mm (a,b and c) to 5 mm (d), non physical growth occurs already at 16 MeV for a map truncated at the 9^{th} order. The commissioning of the machine will tell us what is a realistic betatron oscillation achievable to study the dynamics. For instance if we are able to inject a bunch 1 mm away from the closed orbit at a given energy, then simulations from a dynamical map with reference energy within ± 2 MeV of the injected energy, retaining terms up to the 9^{th} order, may show sensible agreement with experimental data.

4.3.1.3 Summary

The large range of transverse positions in an FFAG can be modelled using multiple dynamical maps with different reference energies. The phase advance per cell and the time of flight computed using a dynamical map show good agreement with the results obtained using a numerical tracking code, Zgoubi, except the horizontal tune at low energy. Accurate description of the betatron motion requires the dynamical maps to be computed to at least the 4th order, at small energy deviation. If the energy deviation is large (for example, to cover the full energy range in EMMA from 10 MeV to 20 MeV in a single dynamical map), then a map up to 9th order may be required to model the horizontal motion.

Acceleration may be included in the dynamics by making an appropriate adjustment to the energy deviation at the end of each cell (representing the effect of an RF cavity in the cell). The results presented here suggest that it may be possible to achieve a reasonable description of the dynamics using three different fixed reference energies computed up to the 9^{th} order to cover the whole energy range.

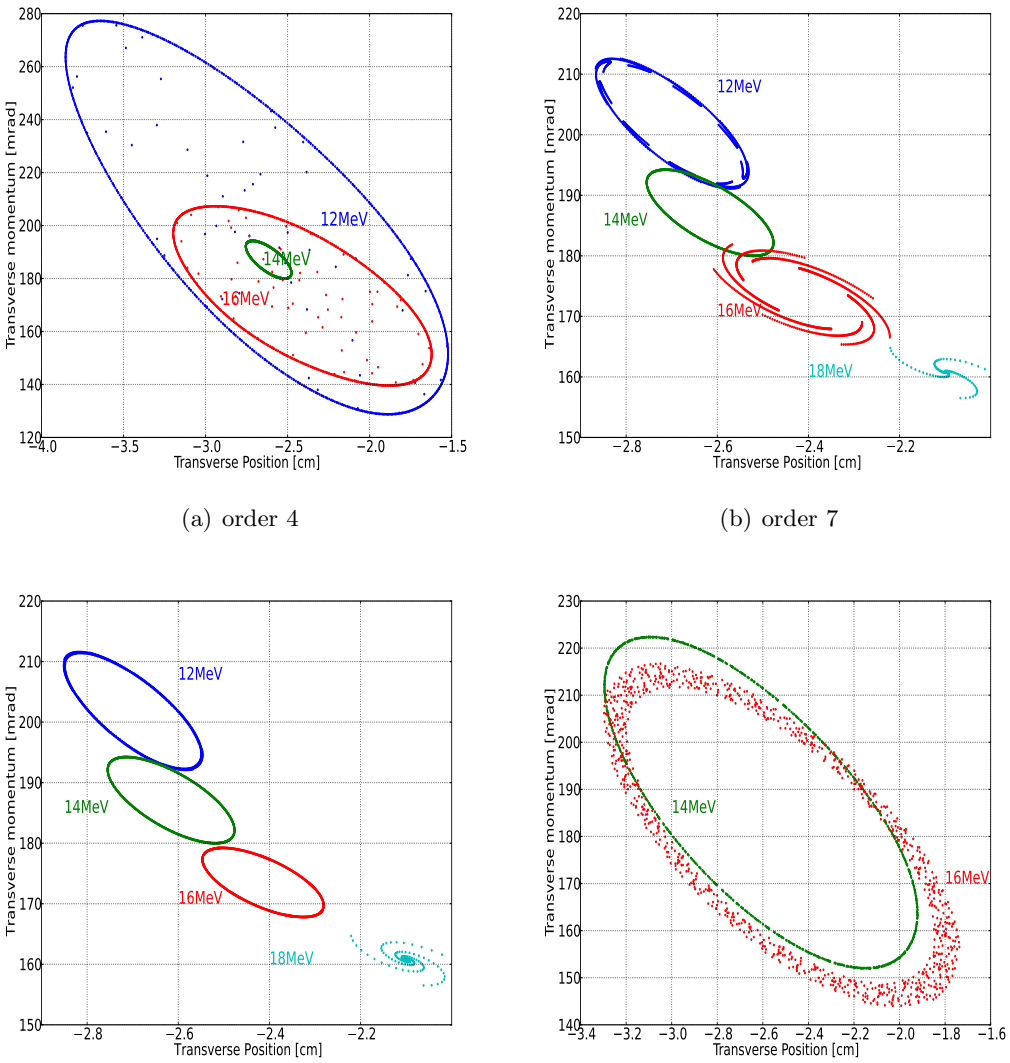

(a) order 4

(b) order 7

(c) order 9

(d) order 9, 5 mm amplitude

Figure 4.7: Betatron motion for different energy deviations, simulated with a single dynamical map up 4^{th} order (a), 7^{th} order (b) and 9^{th} order (c). We observe that for a map truncated at the 4^{th} order, the betatron motion in horizontal phase space has a strong non-physical growth in the amplitude for energy deviation ($\pm 2\,MeV$). In (b) this effect is reduced by retaining terms in the map up to 7^{th} order but still noticeable for energy deviation of ± 2 MeV. A sensible behaviour in (c) is obtained for energy deviation of ± 2 MeV retaining terms in the map up to 9^{th} order. However increasing the oscillation amplitude from 1 mm (a,b and c) to 5 mm (d) makes non physical growth appears 2 MeV energy deviation with map truncated at the 9^{th} order.

The truncation order is limited by the computing time and memory management in the routines used from COSY Infinity [47]. These routines have been used because they allow handling of differential algebra (DA) objects (see chapter 3). By writing a separate DA object code, one could optimise the computation of the dynamical maps focusing on the energy deviation variable. This variable could be truncated at an order greater than 9^{th} while the other variables truncated at lower orders.

As a result, the tracking study of acceleration would significantly be eased by handling only one map and avoiding possible discontinuities and errors occurring while swapping maps. Moreover, we will see in chapter 5 that a large number of dynamical maps (about 300) needs to be computed to simulate the various EMMA lattice configurations and find the optimum configuration for acceleration. Requiring a single dynamical map for each configuration instead of three maps reduces significantly the computing time and the inconvenience of handling a large number of files.

4.3.2 Study of a nonlinear effect : tune shift with amplitude

4.3.2.1 Introduction

Another interesting feature of dynamical maps is the fact that they contain information about nonlinear features of the beam dynamics. Nonlinear refers to order higher than one in the dynamical variables. When computing the tunes and times of flight for large energy deviations, we observed that including higher order terms in the δ variable had an influence on the results. A similar nonlinear effect may be observed in transverse dynamics. For instance, the horizontal and vertical tune are, in linear approximation, computed from the linear part of the map (see equation 4.1). However they may vary with the amplitude of the transverse motion when including terms of order higher than one in the dynamical variables (x,p_x) and (y,p_y). This variation is often referred as "tune shift with amplitude". Here the amplitude refers to the area of the ellipse traced out in transverse phase space by recording the entrance position at each turn of a

particle tracked several times though the cell at fixed energy. This ellipse is centred on the closed orbit at this energy (see figure 4.8(a)).

We have seen in chapter 3 that the set of Cartesian canonical variables (x,p_x) is linked to the set of action-angle variables (also canonical) (ϕ_x,J_x). Since the action J_x is directly linked to the amplitude of oscillation in transverse phase space, it is convenient to use action-angle variables when considering the horizontal tune shift with amplitude. Similarly (ϕ_y, J_y) are used for the vertical motion.

The relation between the two sets of canonical variables are:

$$x = \sqrt{2\beta_x J_x}\cos\phi_x \tag{4.2}$$

$$p_x = -\sqrt{\frac{2J_x}{\beta_x}}(\sin\phi_x + \alpha_x\cos\phi_x) \tag{4.3}$$

with β_x and α_x being the Twiss parameters (see chapter 3 section 3.1.3) and $\nu_x = \Delta\phi_x/2\pi$ where $\Delta\phi_x$ is the phase advance over one cell and ϕ_0 an arbitrary offset phase set to zero in the following.

Figure 4.8(a) shows the betatron ellipses traced out by particles with actions $J_1 = A_1/\pi$ and $J_2 = A_2/\pi$, with A_1 and A_2 areas of the blue and red ellipses respectively; here $J_1 < J_2$. The phase advance is related to the position of a particle around the ellipse in transverse phase space, however the shape of the ellipse varies along the beamline with the functions β_x and α_x in 4.3. The relation between the phase advance and the position in phase space is therefore not obvious. We can normalise the Cartesian coordinates such that they are expressed only in terms of the action-angle variables. To do so, we define the normalisation matrix N such that :

$$\begin{pmatrix} x_N \\ p_{xN} \end{pmatrix} = N \cdot \begin{pmatrix} x \\ p_x \end{pmatrix} = \begin{pmatrix} \sqrt{2J_x}\cos\phi_x \\ -\sqrt{2J_x}\sin\phi_x \end{pmatrix}. \tag{4.4}$$

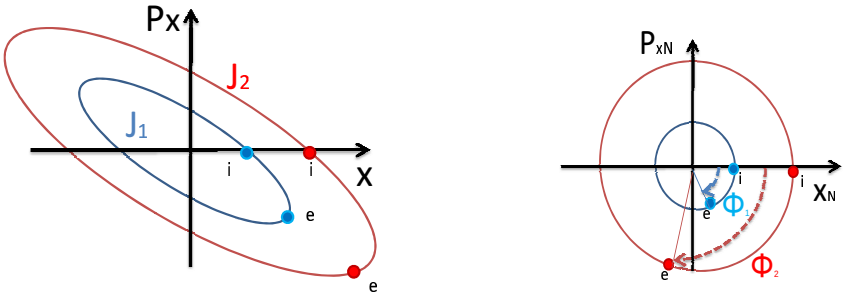

(a) (b)

Figure 4.8: (a)Schematic view of the betatron ellipse traced out in phase space by a particle going several time through the EMMA cell. The blue and red ellipses of area A_1 and A_2 respectively represent the betatron motion of two particles with different actions $J_1 = A_1/\pi$ in blue and $J_2 = A_2/\pi$ in red. Here $J_1 < J_2$. (b) Schematic view of the betatron motion in normalised variables. The ellipses in (a) are now circles with radius being equal to $\sqrt{2J_1}$ and $\sqrt{2J_2}$. The phase advance over one cell of the particle number 2 is larger than the one of particle number 1. This illustrates the variation of phase advance with the action, also called "tune shift with amplitude".

From 4.2 and 4.3 we have:

$$N = \begin{pmatrix} \frac{1}{\sqrt{\beta_x}} & 0 \\ \frac{\alpha_x}{\sqrt{\beta_x}} & \sqrt{\beta_x} \end{pmatrix} . \tag{4.5}$$

The schematic view of the tune with amplitude in the normalised transverse phase space (x_N,p_{xN}) is shown in figure 4.8(b). The betatron motion is now represented by circles with radius being equal to $\sqrt{2J_1}$ and $\sqrt{2J_2}$. Dots with subscript "i" represent the initial positions of the particles on each circle and dots with subscript "e" represent the exit positions of the particles after one cell. The phase advances per cell (or tunes) Φ_1 and Φ_2 are the angles performed by particles with action J_1 and J_2 respectively. In that case $\Phi_2 > \Phi_1$ so the tune increases with the amplitude of the action.

As explained in the introduction chapter, the phase advance (or tune) refers to oscillations of a particle around a stable orbit. These oscillations are caused by focusing and defocusing strengths. It is therefore equivalent to write that the phase advance varies with the action of a particle and that particles with different actions experience

different focusing and defocusing strengths.

Now if we imagine that in a bunch of particles, particles have different actions, therefore their oscillations around the stable orbit will be different. In practise diagnostic devices can only detect motion of a bunch of particles; since in this case the bunch oscillation is not coherent, the measurement will give little information on the betatron motion of individual particles in the beamline. This phenomenon is called decoherence and is studied in section 4.3.3.1.

In a non-scaling FFAG such as EMMA, the focusing strength experienced by particles (and therefore the tune) varies significantly with energy (i.e. large chromaticity). This has a larger effect on the decoherence than the tune shift with amplitude. Nevertheless, in a scaling FFAG, the chromaticity is kept small by using highly non-linear magnetic fields. Studying the variation of the tune with respect to the action of particles then becomes interesting; we will see in section 4.3.2.3 why dynamical maps can then be really convenient.

The aim is to evaluate the tune shift with amplitude from two different methods. The first method consists in applying the dynamical map to a set of initial coordinates of particles and then processing their exit coordinates numerically (over many turns) to find the tune shift with amplitude. This method is called Frequency Map Analysis (FMA) [51,52]. The second method is based on a direct reading of the coefficients of the dynamical map expressed in the form of a Lie factorisation [43]. The agreement between the two methods will outline the usefulness of dynamical maps since complex dynamics could (at least in principle) be extracted directly from its coefficients and therefore not require a full tracking procedure.

Also, we will compare the horizontal and vertical tune shifts with amplitude with results obtained from tracking in PyZgoubi for 19 MeV and 15 MeV particles. We will study the accuracy of the magnetic field simulations with PyZgoubi and with dynamical maps and compare with the original OPERA model. This comparison will show that

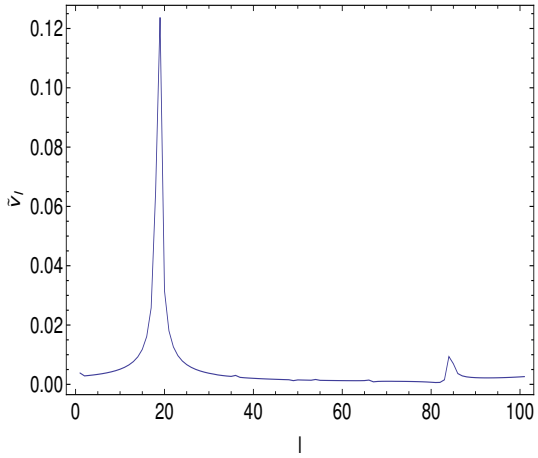

Figure 4.9: Value of the coefficients of the Fourier transform of a set of quantities v_k linked by the equation 4.6 to the positions of a particle going through the EMMA cell 100 times. A large peak occurs for l=19 from which we conclude that the phase advance of the EMMA cell is 19/100.

the nonlinear vertical dynamics seem to be more accurately simulated with dynamical maps than with PyZgoubi using a 2D field map.

4.3.2.2 Frequency map analysis

To measure the tune precisely enough to see variation with amplitude, we launch a particle in the cell and track for hundred passes. At the end of each cell, we record the exit coordinates (x_k,p_{x_k}) of the particle. We then computed the normalised coordinates (x_{N_k},p_{xN_k}) using (4.4). For the Frequency Map Analysis (FMA), we define a set of complex quantities v_k as:

$$v_k = x_{N_k} + ip_{xN_k} \tag{4.6}$$

with k ranging from 1 to the total number of cells N_c (here $N_c = 100$).

We perform a Discrete Fourier Transform (DFT) of the set of v_k by computing the quantities $\tilde{v}_l$ defined as:

$$\tilde{v}_l = \sum_{k=1...N_c} v_k \times e^{2\pi i \frac{l*k}{N_c}} \tag{4.7}$$

We obtain a spectrum plotted in figure 4.9. The tune ν_x is equal to l_{max}/N_c with

l_{max} being the index for which $\tilde{v}_l$ is maximum. Note that in a conventional DFT, l is an integer. In FMA l can take non-integer values in order to find the index l_{max} with a good precision. We applied this analysis to tracking results for particles with various actions J_x launched around the 19 MeV closed orbit. The relative horizontal and vertical tune variations with the action obtained with this method are represented by the blue crosses in figures 4.10 and 4.11 respectively. This results will be discussed in the next section when comparing with the second method using Lie factorisation.

4.3.2.3 Tune shift with amplitude extracted from Lie factorisation

In this section, we will study the effect of applying a map representing a general section of beamline, to the angle variable, representing the phase advance along the beamline.

The generator g of a Lie transformation $e^{-:g:}$ (representing for example the dynamical map for a given beamline) can conveniently be expressed as a polynomial function of the Cartesian canonical variables :

$$g = a_0 + b_0 x + b_1 p_x + c_0 x^2 + c_1 p_x^2 + c_2 x p_x + ... \tag{4.8}$$

where a_i, b_i, c_i are coefficients of the zeroth, first and second order in the dynamical variables respectively, characteristics of the beamline. The value of a function f of dynamical variables at the end of the beamline of length L can then be written:

$$f(L) = (e^{-:g:} f)_{s=0} = f(0) - (: g : f)_{s=0} + \frac{1}{2}(: g :^2 f)_{s=0} + ... \tag{4.9}$$

Note that the Lie operator acts on a variable (or a function of the dynamical variables, f), not on a value. Since we are interested in the phase advance, we can substitute the action-angle variables in the generator using 4.3. The generator g of the Lie transfor-

mation is then given by:

$$g = \sum_{l,m} \mu_{x,lm} J_x^l e^{im\phi_x} \ , \tag{4.10}$$

where μ_{lm} are coefficients characteristics of the beamline.

In (4.10) the generator contains terms mixing both action and angle variables for $m \neq 0$ (e.g. for $l = 2$ and $m = 3$: $J_x^2 \cos 3\phi_x$). To derive the tune shift with amplitude in a clear way, we are interested in expressing the generator as a function of the action J_x only. To do so, we assume that the terms dependent on the angle variable are small compared to terms depending on the action: this will be the case if the trajectory of a particle in phase space is close to an ellipse (the dependence on the angle variable would lead to a distortion of the ellipse). We average the effect of the terms dependent on the angle by averaging the generator over the angle variable ϕ_x from 0 to 2π. The generator that results from this averaging is representative of the dynamics if after many passes through the cell, the variable ϕ_x does cover the whole range from 0 to 2π. This is not the case close to a resonance where ϕ_x takes a limited range of values [53].

When averaging the generator in 4.10 for ϕ_x over 2π, it turns out that all terms containing ϕ_x cancel out and terms containing only the action remain.

$$\int_0^{2\pi} g d\phi_x = \mu_{x0} J_x + \mu_{x1} J_x^2 + \mu_{x2} J_x^3 + ... \tag{4.11}$$

We apply the definition of the Lie operator $: g :$ (see section 3.2.2 of chapter 3) for the function $g(J_x, \phi_x)$:

$$: g := \frac{\partial g}{\partial \phi_x}\frac{\partial}{\partial J_x} - \frac{\partial g}{\partial J_x}\frac{\partial}{\partial \phi_x} \tag{4.12}$$

Let us first consider the function $g_0 = \mu_{x0} J_x$ and evaluate the effect of the operator $:g_0:$ on the angle variable ϕ_x:

$$: g_0 : \phi_x = \frac{\partial \mu_{x0} J_x}{\partial \phi_x}\frac{\partial \phi_x}{\partial J_x} - \frac{\partial \mu_{x0} J_x}{\partial J_x}\frac{\partial \phi_x}{\partial \phi_x} = 0 - \mu_{x0} = -\mu_{x0} \tag{4.13}$$

Then to compute the effect of the map $e^{-:g:}$ on ϕ_x, we need to evaluate the effect of $:g_0:^2$ on the angle variable ϕ_x:

$$\begin{aligned} :g_0:^2 \phi_x &= :g_0::g_0:\phi_x \\ &= :g_0:(-\mu_{x0}) \\ &= 0 \end{aligned}$$

Similarly $:g_0:^3 =: g_0:^4 = ... = 0$ and therefore we have:

$$e^{-:\mu_{x0}J_x:}\phi_x = \phi_x + \mu_{x0}\,. \tag{4.14}$$

Let us now consider the effect of the operator $:g_1:=:\mu_{x1}J_x^2:$ on ϕ_x:

$$:g_1:\phi_x = \frac{\partial(\mu_{x1}J_x^2)}{\partial\phi_x}\frac{\partial\phi_x}{\partial J_x} - \frac{\partial(\mu_{x1}J_x^2)}{\partial J_x}\frac{\partial\phi_x}{\partial\phi_x} = 0 - 2\mu_{x1}J_x = -2\mu_{x1}J_x \tag{4.15}$$

and,

$$\begin{aligned} :g_1:^2 \phi_x &= :g_1::g_1:\phi_x \\ &= :g_1:(-2\mu_{x1}J_x) \\ &= \frac{\partial(\mu_{x1}J_x^2)}{\partial\phi_x}\frac{\partial(-2\mu_{x1}J_x)}{\partial J_x} - \frac{\partial(\mu_{x1}J_x^2)}{\partial J_x}\frac{\partial(-2\mu_{x1}J_x)}{\partial\phi_x} \\ &= 0\,. \end{aligned} \tag{4.16}$$

Similarly we have $:g_1:^3 =: g_1:^4 = ... = 0$. The process can be applied to all the terms $:g_i:=:\mu_{xi}J_x^{i+1}:$ and we obtain an expression for the effect of the map on the angle variable ϕ_x given by:

$$\phi_x(L) = (e^{-:g:}\phi_x)_{s=0} = \phi_x(0) + \mu_{x0} + \mu_{x1}J_x(0) + \frac{1}{2}\mu_{x2}J_x(0)^2 + \ldots\,. \tag{4.17}$$

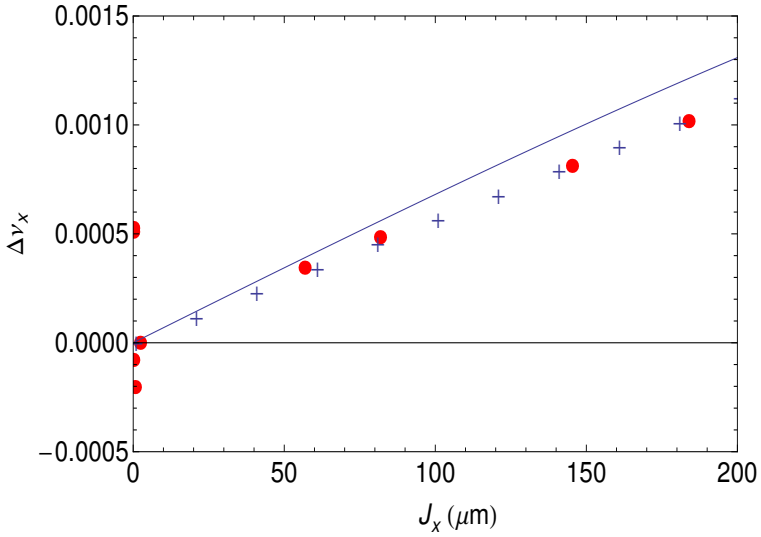

Figure 4.10: Relative variation of the horizontal tune with the horizontal action J_x. The discrepancy between the FMA of the dynamical map tracking (blue crosses) and the reading from the Lie Factorisation (blue line) is rather small : 0.0001 for J_x=60 μm and 0.0002 for $J_x = 200\,\mu$m. Red circles correspond to the result of a FMA of tracking results obtained from PyZgoubi. The agreement between PyZgoubi and dynamical map is better than 10^{-5} and gives confidence in both results. We notice also that for actions smaller than 10^{-1} the results from PyZgoubi appear not to converge. This may be due to numerical precision error when tracking particles close to the closed orbit in PyZgoubi.

The phase advance $\Delta\phi_x$ is the variation of the angle variable through the beamline ($\Delta\phi_x = \phi_x(L) - \phi_x(0)$) and is related to the tune ν_x by $\nu_x = \Delta\phi_x/2\pi$. Finally the tune for this beamline can be expressed as:

$$\nu_x = \nu_{x0} + \nu_{x1} J_x + \nu_{x2} J_x^2 + \dots , \tag{4.18}$$

where the coefficient $\nu_{x0} = \mu_{x0}/2\pi$ is the linear part of the tune, the coefficient $\nu_{x1} = \mu_{x1}/2\pi$ is the linear tune shift with amplitude and the coefficients $\nu_{xi} = \mu_{xi}/2\pi$ of the higher orders in J_x represent the higher order tune shift with amplitude. The process could be applied for the vertical transverse plane substituting the subscript x by y.

From the dynamical map in power series form computed around the 19 MeV closed orbit, we used COSY Infinity routines [47] to derive the generator of the Lie trans-

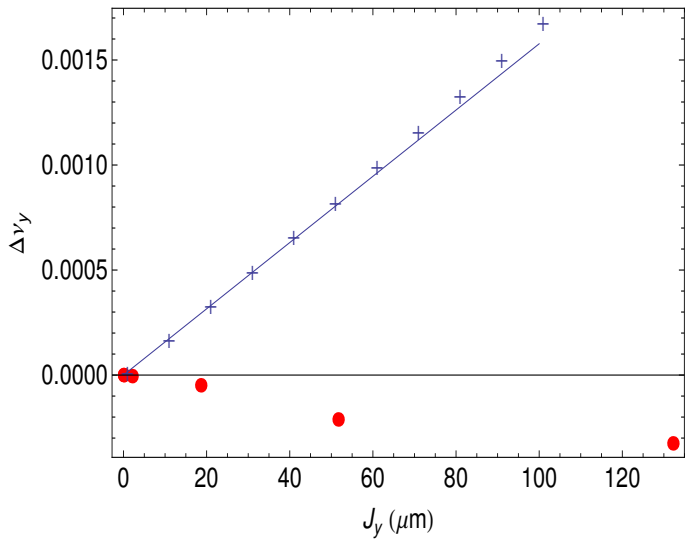

Figure 4.11: Relative variation of vertical tune with vertical action J_y. We notice a large discrepancy when comparing PyZgoubi (red circles) and dynamical map (blue crosses). The disagreement in the simulation of the vertical nonlinear effects may be explained by the difference in description of the magnetic field in the two codes. The tune shift with amplitude obtained from the Lie Factorisation (blue line) shows good agreement of better than 10^{-4} for actions smaller than $100\,\mu$m with the result of the FMA from tracking using a dynamical map.

formation expressed as in equation 4.8. COSY returns the generator in Cartesian coordinates in which we substitute the action-angle variables to identify the coefficients ν_i in expression 4.18.

In figures 4.10 and 4.11, the relative tunes variation (determined by the coefficients ν_i found using COSY infinity) $\nu_x - \nu_{x0}$ for the horizontal motion and $\nu_y - \nu_{y0}$ for the vertical motion are represented by the blue lines. The red points and the blue crosses show the result of a Frequency Map Analysis on tracking results obtained from PyZgoubi and from a dynamical map respectively.

First, we observe that the tune shift with amplitude in all cases is small (about 0.001) over a large range of variation of the action (from 0 to $200\,\mu$m). The order of magnitude of the horizontal beta-function β_x in EMMA is 1 m. Therefore from

equation 4.3, the maximum transverse coordinate equivalent to an action of 200 μm is $x_{max} = \sqrt{2\beta_x J_x} = 14\,\text{mm}$. We estimate from the early stage of the commissioning of the EMMA accelerator that a bunch of particles can be injected on the closed orbit within a precision of a few millimetres (at the location of a maximum for β_x). Therefore in reality, the amplitude of oscillation may remain smaller than 14 mm, resulting in a small tune shift with amplitude.

Regarding the horizontal motion (figure 4.10), the agreement between the FMA of the dynamical map tracking (blue crosses) and the reading from the Lie Factorisation (blue line) is rather good : the discrepancy is of order 0.0001 for J_x=60 μm and 0.0002 for $J_x = 200\,\mu$m. The agreement between PyZgoubi and dynamical map is better than 10^{-5} and gives confidence in both results. We notice also that for actions smaller than 10^{-1} the results from PyZgoubi appear not to converge. This may be due to numerical precision error when tracking particles close to the closed orbit.

In figure 4.11, the vertical tune shift with vertical action J_y obtained from the Lie Factorisation (blue line) show good agreement with the result of the FMA from tracking in dynamical map of less than 10^{-4} for action smaller than 100 μm.

We conclude that if we believe that the dynamical map describe the nonlinear effect accurately, the direct reading of the Lie Factorisation of the map gives satisfactory results in terms of horizontal and vertical tune shift with amplitude.

On the other hand, the variation of the vertical tune with amplitude shows large discrepancy when comparing PyZgoubi (red circles) and dynamical map (blue crosses). The disagreement in the simulation of the vertical nonlinear effects may be explained by the difference in the description of the magnetic field: this is discussed further in the following subsection.

4.3.2.4 Study of the discrepancy in the variation of the vertical tune with amplitude

To explore the discrepancy in vertical tune shift with amplitude between PyZgoubi and the dynamical map, we compare the magnetic field experienced by particles travelling in straight line through the cell for different vertical positions. To do so, we send particles with very high energy such that they are not deflected by the magnetic field. Their horizontal transverse position is kept zero and we vary their vertical position from 1 mm to 20 mm. The vertical motion y is affected by the horizontal component of the magnetic field B_x. We then record the horizontal component of the magnetic field B_x seen by each particle at a given longitudinal position; for this study, we chose the centre of the defocusing magnet where the field is expected to be linear. In a further study it would be interesting to perform the same study at the entrance or exit face of magnets where non-linearities in the field are expected to be stronger.

In PyZgoubi the magnetic field is derived from a 3D numerical representation of the magnetic field extrapolated from a 2D field map in the median horizontal plane. The magnetic field in dynamical maps is computed from the analytical representation of the magnetic field, expressed as a Fourier expansion, derived from the OPERA model (see chapter 2).

Results from both tracking methods are compared with the original OPERA model of the magnet. In figure 4.12, we observe that the variation of B_x with y is almost perfectly linear for PyZgoubi, OPERA and dynamical map simulations.

The tune shift with amplitude is directly related to the derivatives of B_x with respect to y. Hence we fit a polynomial function on the results obtained from the three codes, and then we identify the coefficients c_k of this polynomial function with the coefficients

of Taylor expansion of the magnetic field:

$$B_x(y) = \sum_{k=0}^{\infty} \frac{1}{k!} \frac{\partial^k B_x}{\partial y^k}\bigg|_{y=0} y^k \tag{4.19}$$

We obtain therefore

$$c_k = \frac{1}{k!} \frac{\partial^k B_x}{\partial y^k}\bigg|_{y=0} \tag{4.20}$$

In a further study, it can be proved that the tune shift with amplitude is directly related to the coefficient of order 3 (c_3) integrated along the entire cell. This coefficient is also called octupolar component of the magnetic field. Here, we restrict the study to the comparison of these coefficients obtained from fitting the magnetic field simulated from PyZgoubi, dynamical map and OPERA.

In figure 4.13, the value of the coefficients for each order are plotted in a vertical logarithmic scale. Results agree for the first order, corresponding to the quadrupolar (or gradient) component of the field $\frac{\partial B_x}{\partial y}$. However we observe a large discrepancy between PyZgoubi and the two other codes for other orders.

The coefficients of the polynomial function obtained from PyZgoubi is six orders of magnitude smaller than the dynamical map and OPERA corresponding coefficients. There is a much smaller discrepancy of less than one order of magnitude between the dynamical map and the OPERA coefficients. We conclude that dynamical maps represent more accurately the non-linearities in the magnetic field than PyZgoubi. PyZgoubi works in this study with 2D field maps in the median plane (see section 4.2.1) and uses Taylor expansion in the vertical coordinate y to reconstruct a 3D field map. This Taylor expansion becomes less accurate for increasing values of y. This may not describe accurately the variation of the fringe field or the nonlinear components of the magnetic field outside the median plane. This can explain the discrepancy in terms of nonlinear dynamics observed in figure 4.11 for the vertical tune shift with amplitude.

In addition we have studied the same comparison between tune shift with amplitude

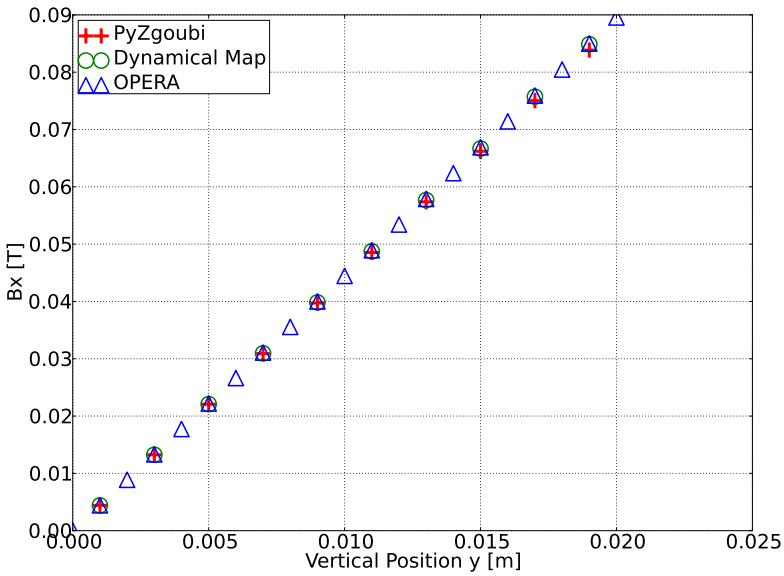

Figure 4.12: Variation of the horizontal component of the magnetic field B_x with respect to the vertical position y in the defocusing quadrupole for PyZgoubi (red crosses), dynamical map (green circles) and OPERA simulations (blue triangles). In all three cases, the variation seems to be close to linear, consistent with the fact that the field is derived in the centre of the D magnet and also consistent with the small nonlinear effect seen on the tune. The tune shift with amplitude is directly related to the derivatives of B_x with respect to y.

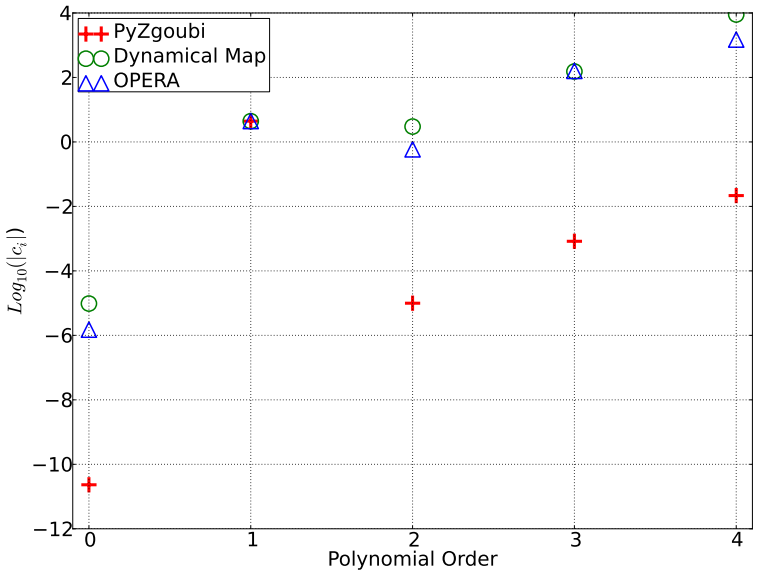

Figure 4.13: Value of the coefficients of the polynomial function fitted on the data of figure 4.12 for PyZgoubi (red crosses), dynamical map (green circles) and OPERA simulations (blue triangles). Coefficients are plotted for each order and the vertical scale is logarithmic. Results agree for the first order, corresponding to the quadrupolar (or gradient) component of the field $\frac{\partial B_x}{\partial y}$. The higher order coefficients of the polynomial function obtained from PyZgoubi are five orders of magnitude smaller than the corresponding coefficients in the case of the dynamical map and OPERA. There is a relatively small discrepancy of less than one order of magnitude between the dynamical map and the OPERA coefficients. We conclude that dynamical maps represent more accurately the non-linearities in the magnetic field than PyZgoubi. This can explain the discrepancy in terms of nonlinear dynamics observed in figure 4.11 for the vertical tune shift with amplitude.

obtained from FMA in PyZgoubi and in a dynamical map for different energies. Figure 4.14 shows the comparison for a 15 MeV reference energy. We observe a disagreement between the two tracking methods. In both cases, the tune first increases with amplitude and then decreases. However the decrease starts for action above 70 μm for the dynamical map (blue crosses) and above 200 μm for PyZgoubi (red circles). The discrepancy in tune is about 0.002 for an action of 300 μm. However this value is small and probably not measurable in the machine. A possible explanation for this difference lies in the limit of validity of the paraxial approximation made to compute the dynamical map and not used in PyZgoubi [48]. The excursion of the 15 MeV closed orbit

with respect to the reference straight line is larger than for 19 MeV for which we had good agreement (see fig.4.10). Thus the paraxial approximation at low energy limits the accuracy of simulations of the non-linearities using dynamical maps. The reference straight line of a map is located at the starting horizontal position of the closed orbit for the reference energy of the map. Instead, looking for a reference straight line that minimises the relative excursion of trajectories along the cell may overcome this problem. Also, we could validate this hypothesis by constructing a beamline with a magnet element introducing a strong tune shift with amplitude and for which an analytical solution for the beam dynamics could be derived. For instance a FODO cell also including an octupole magnet (introducing a tune shift with amplitude [53]). The analytical solution for non linear dynamics could then be compared to the tracking method for two purposes: first to validate, with non negligible non-linear effect, the derivation of nonlinear dynamics from the generator of the Lie transformation; second to verify if the discrepancy between PyZgoubi and Dynamical map for the horizontal tune shift with amplitude is caused by the paraxial approximation.

4.3.2.5 Summary and conclusions

In this section, we studied the nonlinear effect on the horizontal and vertical tune per cell in EMMA. Nonlinear effects can cause the tune value to vary with the magnitude of the action J. The aim of our study was to show that information about nonlinear dynamics could be obtained directly from the coefficients of the generator of the Lie transformation representing the map. Thus we compared the tune shift with amplitude obtained from frequency map analysis of tracking results from PyZgoubi and dynamical map, with the value for the tune shift obtained by reading directly the coefficients of the Lie operator of the dynamical map. At 19 MeV we observed a good agreement between the frequency map analysis of the horizontal motion in PyZgoubi and dynamical map. The discrepancy with the results obtained from the coefficient of the Lie operator

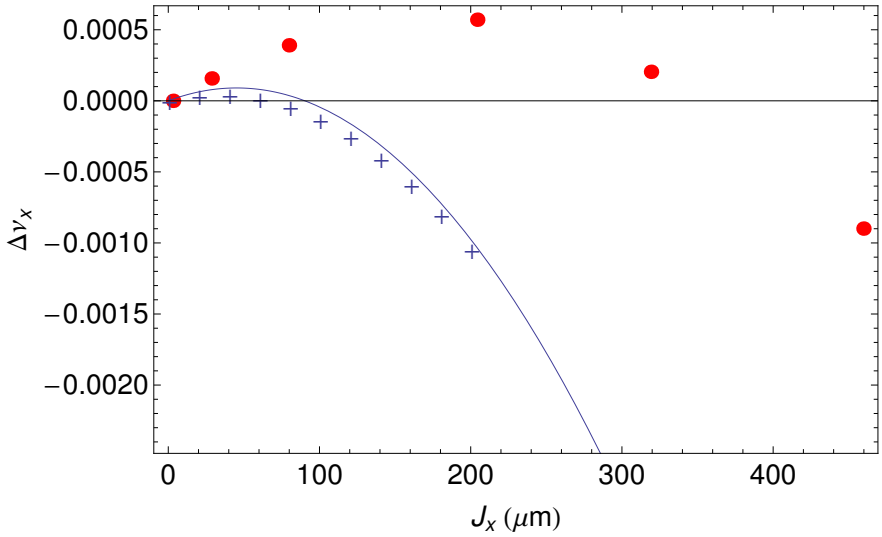

Figure 4.14: Comparison between horizontal tune shift with amplitude obtained from FMA in PyZgoubi (red circles) and dynamical map (Blue crosses) for 15 MeV reference energy. We observe a disagreement between the two tracking methods. In both cases, the tune first increases with amplitude and then decreases. However the decrease starts for action above 70 μm for the dynamical map and above 200 μm (blue crosses for dynamical maps and red circles for PyZgoubi). The discrepancy in tune is about 0.002 for an action of 300 μm. However this value is small and probably not measurable in the machine. A possible explanation for this difference lies in the limit of validity of the paraxial approximation done to computed the dynamical map and not used in PyZgoubi [48].

being smaller than measurement precision validates the reading of this nonlinear effect directly from the map. However we observed a larger disagreement in the vertical motion. By studying the variation of the horizontal component of the magnetic field along the vertical axis, we observed that PyZgoubi was not accurately simulating the nonlinear components of the magnetic field present in the OPERA model. On the other hand, the agreement between OPERA and the dynamical map descriptions of the field gives confidence in the simulation of the tune shift with amplitude with dynamical map.

We noticed also the possible limit of validity of the paraxial approximation in the dynamical map when studying this nonlinear effect for a closed orbit at 15 MeV with larger excursion from the reference axis. The horizontal tune shift with amplitude is in this case different from results obtained with PyZgoubi, which does not use the paraxial approximation. Further studies would be necessary to estimate the actual effect of the

paraxial approximation in this result. To do so, we could create a simple beamline for which the tune shift with amplitude could be derived analytically.

4.3.3 Longitudinal dynamics

4.3.3.1 Energy spread in a bunch

In this section, we will look at how particular aspects of the transverse motion of particles (or bunches of particles) depend on aspects of the longitudinal dynamics. In an accelerator such as ALICE or EMMA, particles travel by bunches. Along the beam line, Beam Position Monitors (BPMs) read the transverse position of each bunch by measuring the change in electric potential at fixed points (the BPM electrode location) as a bunch of charged particles moves past. The position read is therefore linked to the centroid of charge of the bunch and not to the position of individual particles. When trying to measure betatron oscillation, we assume that the whole bunch is coherently oscillating around a reference trajectory and that the position of the centroid of charge is significant in terms of beam dynamics.

However, in general each particle belonging to a bunch has unique values for all the dynamical variables, and the representations of the bunch in longitudinal and transverse phase spaces are not "point-like". Variation in the dynamical variables between particles appear when creating the bunch in the source and are then amplified or reduced along the beam line depending on the lattice.

We studied the effect of differences in kinetic energy between particles in a single bunch. Particles with different energies follow different trajectories and the oscillation of a bunch is not coherent anymore. At the location of a Beam Position Monitor, particles are spread around the closed orbit and the centroid of charge may be close to (or on) the closed orbit. The measurement from the BPM gives little indication of the betatron amplitudes of individual particles. Indeed particles may be close to the wall of the vacuum chamber and the centre of charge still be on the closed orbit. Simulations

must be carried out to support a proper interpretation of the BPM data.

We created a bunch of 1000 particles all having the same transverse coordinates (x_0, p_{x0}, y_0, p_{y0}) and longitudinal position z_0 with respect to the reference particle but with various energy deviations with respect to the reference energy. In that way, we studied only the effect of a longitudinal initial distribution on the transverse dynamics. The energy deviation of each particle is defined randomly following either a Gaussian or a uniform distribution. We tracked this bunch in the EMMA ring first using dynamical maps and then comparing with PyZgoubi with field maps. The position of each particle was recorded at the end of each cell. To reproduce the reading of a BPM, we computed the average of the transverse positions of all particles at each reading position.

First, we studied the effect of the distribution of energy deviations in a bunch by plotting the average transverse position of the bunch going through the EMMA lattice. For a Gaussian distribution, the energy spread is expressed in terms of σ, the standard deviation (or, for zero mean, the root mean square (rms)) value of the distribution. For a uniform distribution, the Full Width at Half Maximum (FWHM) is more relevant than the rms value. Therefore we chose the FWHM to compare the distributions. The relationship between the rms value σ and the FWHM for a Gaussian distribution is:

$$FWHM = 2\sqrt{2\ln 2}\,\sigma \tag{4.21}$$

The measured energy spread of the bunch assuming a Gaussian distribution at the end of the EMMA injector is 0.5% rms equivalent to 1.175% FWHM. We studied the effect of decoherence for bunches with reference energy of 14 MeV and FWHM of about 150 keV. In figure 4.15 we plotted the relative average horizontal transverse position of a bunch with respect to the closed orbit at the end of each cell. The zero position means that the average position of the bunch is on the closed orbit. In order to study the betatron oscillations, all particles are launched 3 mm off closed orbit with

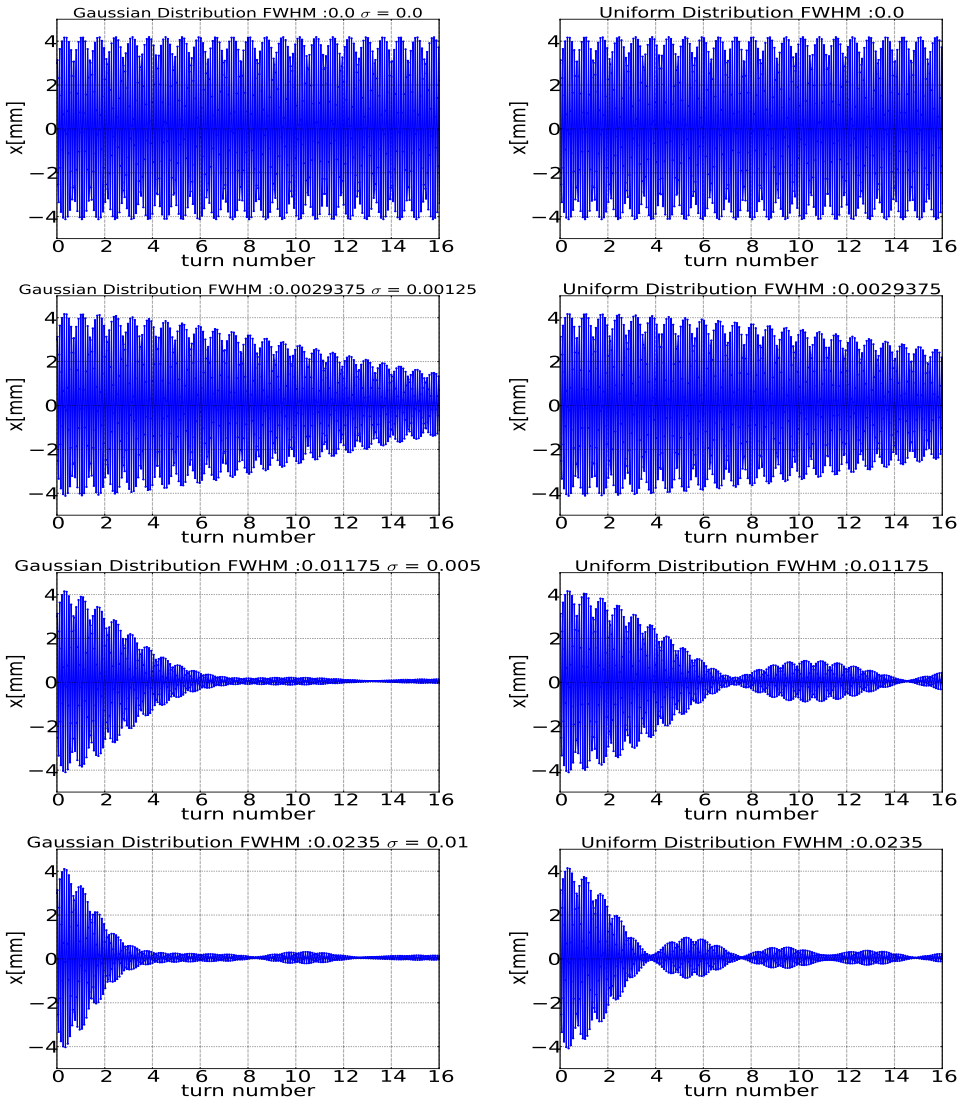

Figure 4.15: Relative average horizontal transverse position of a bunch with respect to the closed orbit at the end of each cell. The zero position means that the average position of the bunch is on the closed orbit. All particles are launched 3 mm off closed orbit with no transverse momentum at the entrance of the first cell. The four plots on the left hand side show the decoherence of a bunch with a Gaussian distribution for a FWHM equal to 0, 0.2935%, 1.175% and 2.35%. The four plots on the right hand side show the decoherence of a bunch with a uniform distribution for a FWHM equal to 0, 0.2935%, 1.175% and 2.35%. In all cases where the FWHM is > 0, we observe a damping of the betatron oscillation after a few turns. For 1.175% FWHM, the beam is mainly damped in the first 8 turns (with 42 cells per turn) for both distributions. For 2.35% FWHM, the beam is mainly damped in the first 4 turns for both distributions. However, bunches with uniform distribution seem to oscillate coherently again after the main damping. For 1.175% FWHM, the oscillation reaches an amplitude of 1 mm after 11 turns and is damped again after 14 turns. This effect is hardly visible with a Gaussian distribution.

no transverse momentum at the entrance of the first cell. The four plots on the left hand side show the decoherence of a bunch with a Gaussian distribution for a FWHM equal to 0%, 0.2935%, 1.175% and 2.35%. The four plots on the right hand side show the decoherence of a bunch with a uniform distribution for a FWHM equal to 0%, 0.2935%, 1.175% and 2.35%. In all cases (except 0%) we observe a damping of the betatron oscillation after a few turns. For 1.175% FWHM, the oscillations are almost fully damped in the first 8 turns (with 42 cells per turn) for both distributions. For 2.35% FWHM, the oscillations are almost fully damped in the first 4 turns for both distributions. However, for bunches with uniform distribution, there appears to be some recoherence after the main damping. For 1.175% FWHM, the oscillation reaches an amplitude of 1 mm after 11 turns and is damped again after 14 turns. This effect is hardly visible with a Gaussian distribution.

To understand this phenomenon we plotted in figure 4.16 the position of selected particles in the bunch in the transverse phase space (x, p_x) at several turn numbers. On the top we observe the decoherence of a bunch with Gaussian distribution for 1.175% FWHM. At turn zero (red triangle), the bunch is point like since all the particles have to same starting position (3 mm away from the closed orbit). After the first turns (green stars), all particles of the bunch are located around a similar point in phase space. Although the bunch is not anymore "point-like", the average position will be different from the centre of the ellipse (closed orbit). After 10 turns (blue crosses), particles are uniformly spread around an ellipse and the average position of the bunch is the centre of the ellipse.

On the bottom plot, for the uniform distribution after ten turns (blue crosses), particles are also spread in phase space; however in top left corner around the position (-4,20) we notice a greater density of particles than in the rest of the plot. The average position is therefore shifted away from the centre of the ellipse towards the left. The greater density seem to be caused by the superposition of particle moving round the

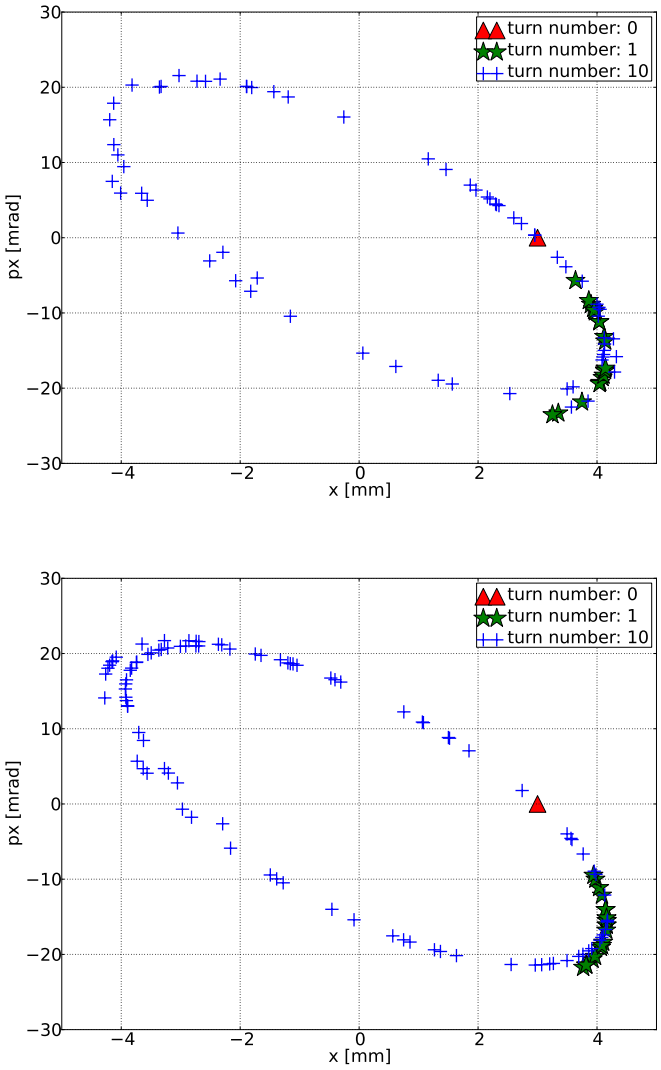

Figure 4.16: Position of each particles of the distribution in the transverse phase space (x, p_x) after a given turn numbers. Top: we observe the decoherence of a bunch with Gaussian distribution for 1.175% FWHM. At turn zero (red triangle), the bunch is point like since all the particles have to same starting position (3 mm away from the closed orbit). After the first turns (green stars), all particles of the bunch are located around a similar point in phase space. Although the bunch is not anymore "point-like", the average position will be different from the centre of the ellipse (close orbit). After 10 turns (blue crosses), particles are uniformly spread around an ellipse and the average position of the bunch is the centre of the ellipse. On the bottom plot, for the uniform distribution after ten turns (blue crosses), particles are also spread in phase space however in top left corner around the position (-4,20) we notice a greater density of particles than in the rest of the plot. The average position is therefore shifted away from the centre of the ellipse towards the left.

phase space ellipse at different rates. Since the angle moved around the ellipse depends on the energy (chromaticity), for given position around the ring particles with low energy (high betatron tune) can "catch up" with particles having high energy (low betatron tune); the centroid of charge is then shifted towards the overlap and the BPM reading of the bunch position is not the centre of the ellipse ($x \neq 0$). Their positions can either cancel each other or add up. The effect is weaker for a Gaussian distribution because the "tails" of the distribution for which the energy difference energy could be large has low particle density. The effect of recoherence on the BPM reading is therefore relatively weak.

To validate these results, we tracked a bunch with a Gaussian distribution of energy deviation for 1.175% and 2.35% FWHM in PyZgoubi using a field map of the EMMA cell. Note that the dynamical map simulations in this case turned out to be 30 time faster than the simulations in the field map with PyZgoubi. The left hand side plots in figure 4.17 results from dynamical maps and the right hand side show result from PyZgoubi. For both codes, the damping periods of 7 turns for 1.175% FWHM (top) and 4 turns for 2.35% FWHM. We observe a discrepancy in the frequency of oscillation of the envelope of the curves. The period of the envelope for PyZgoubi is of about 4 turns while it is about half a turn for the dynamical maps. This discrepancy is due to the difference of horizontal tune per cell obtained in the two codes.

The "beats" seen in the betatron motion are a consequence of the fact that we are sampling the motion at the BPMs: such beats will occur if the tune is close to a resonance (even if the motion is completely linear and regular). The fractional part of the horizontal tune per cell at 14 MeV obtained from PyZgoubi is 0.248 and from dynamical map is 0.242 therefore both are close to the $1/4^{th}$ of an integer (0.25). We created a simplistic model of the betatron oscillation ($x = \cos(2\pi\nu(42 * n))$) where n is the turn number and ν the tune value close to 0.25. Figure 4.18 shows that the frequency of the beat is related to the distance of the tune from the resonance.

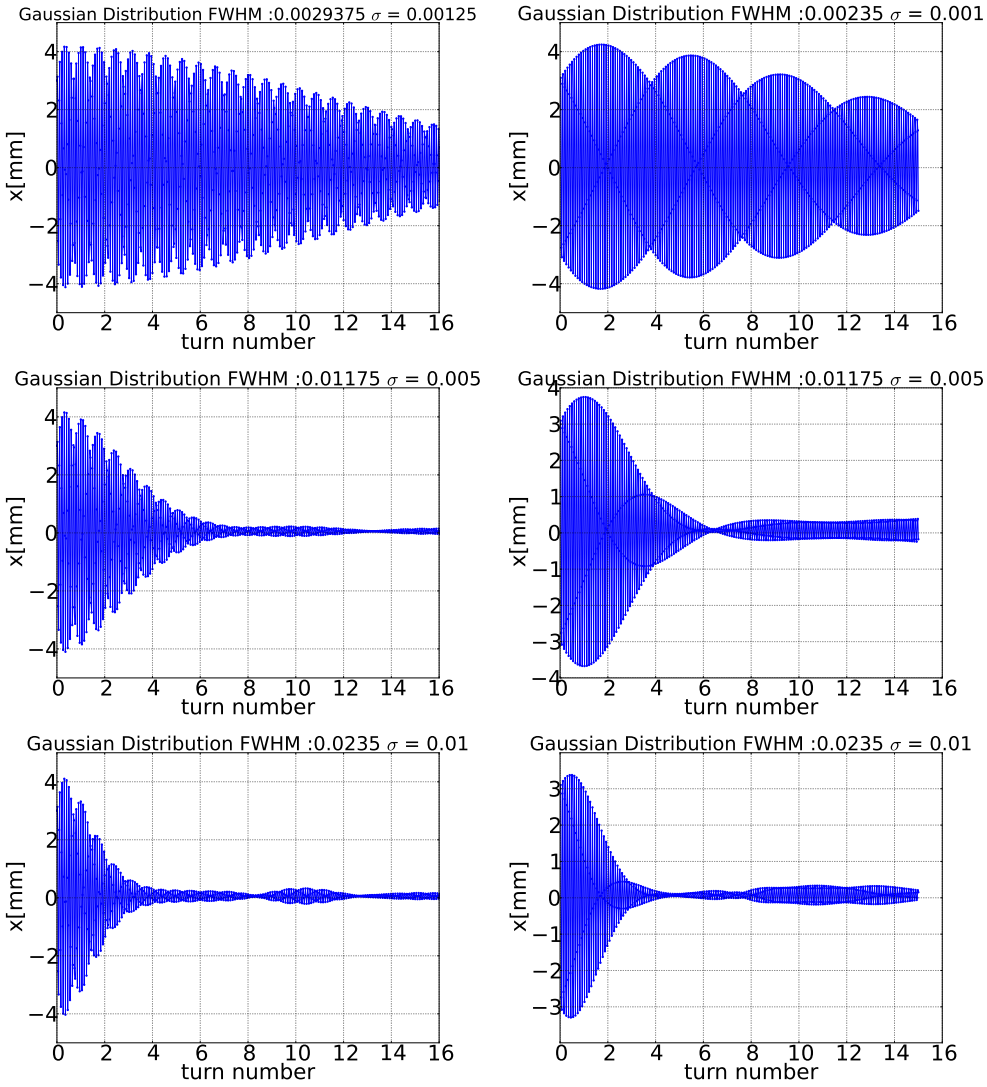

Figure 4.17: Relative average horizontal transverse position of a bunch with respect to the closed orbit at the end of each cell. The left hand side plots on figure 4.17 are result from dynamical maps and the right hand side show result from PyZgoubi. For both codes, the damping periods of 7 turns for 1.175% FWHM (top) and 4 turns for 2.35% FWHM. We observed a discrepancy in the frequency of oscillation of the envelop of the curves. The period of oscillation of the envelop for PyZgoubi is of about 4 turns whereas it is about half a turn for the dynamical maps. The frequency of the beat is related to the distance of the tune from the resonance.

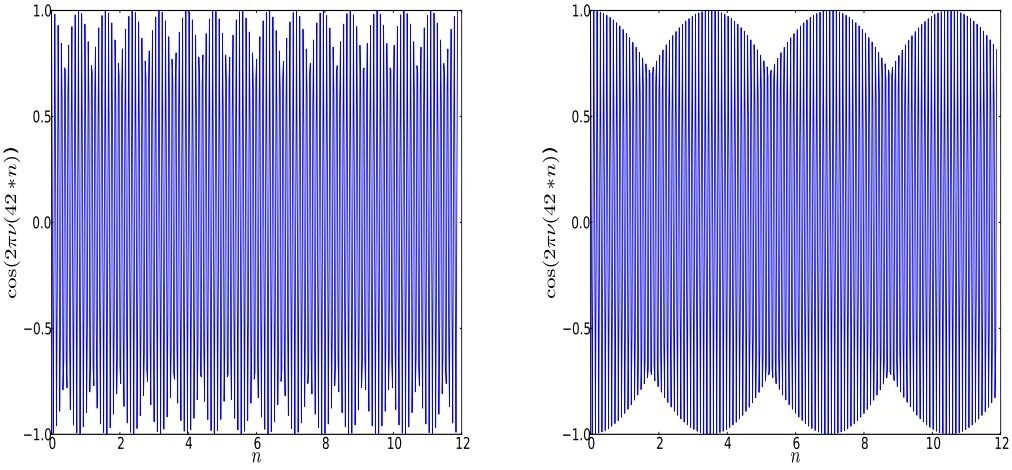

(a) $\nu = 0.242$ (b) $\nu = 0.248$

Figure 4.18: Simplistic model of the betatron oscillation ($x = \cos(2\pi\nu(42 * n))$) where n is the turn number and ν the tune value close to the $1/4^{th}$ of an integer (0.25). The frequency of the beat is related to the distance of the tune from the resonance.

We conclude that the main damping of the betatron oscillation does not strongly depend on the distribution of the energy deviations in a bunch. After a certain number of turns, the particles belonging to a bunch are spread around the betatron ellipse. The centre of charge of the bunch is then situated at the centre of the ellipse i.e. on the closed orbit but the structure of bunch is lost and the reading from the BPM gives little information on the betatron motion of particles. We observed a agreement in terms of damping period between PyZgoubi and dynamical map. The betatron oscillations of a bunch with a distribution of energy deviation with a FWHM of 1.175% (corresponding the actual measurement) is not readable after more than 7 turns. The damping period drops to less than 4 turns with a FWHM of 2.35%. The direct consequence is the decrease of amount of data available to study the transverse dynamics.

The interesting characteristics of the transverse dynamics such as tune and optical functions have to be determined by data taken within these few turns. Since tunes and optic functions are linked to the periodicity of the lattice, ideally if all the cells

in EMMA are identical, BPM measurements at the exit of the first few cells could be sufficient. However magnets are subject to alignment and strength errors and the periodicity of the lattice is then broken. An average value over several cells of the tune and optical functions is still interesting to derive but requires sufficient data to be statistically accurate. Hence the number of turns with coherent motion can be critical. Simulations have been carried out including random errors in the lattice within the tolerance expected for the real machine [28]. The data have been processed with NAFF method [55] or Model Independent Analysis [58, 59] and it has been shown [54] that the tune per cell could be derived to a precision of 0.01 in less than 1 turn for the measured energy spread at injection. The NAFF method is equivalent to frequency map analysis described in section 4.3.2.2 which compute accurately the value of the tune from a relatively small sample of tracking data.

First results from the commissioning suggest that the tune can be measured with an accuracy of about 0.01 from the BPM measurements of only 7 consecutive cells [67].

4.3.3.2 Analytical description of the acceleration in EMMA

One of the goal of EMMA is to demonstrate a new acceleration scheme. Synchrotrons use the so-called bucket acceleration which consists in synchronising the beam revolution time with the oscillations of the accelerating field in the rf cavities. The beam reaches the cavities always at the same phase of rf voltage. However this is made possible by increasing the magnet strengths as particles gain energy. The beam path remains constant during acceleration; for ultra-relativistic particles, the time of flight remains constant as well which allows the synchronisation with the rf.

In an FFAG (such as EMMA) the magnet strengths are kept constant and particles change orbits during acceleration. Therefore the time of flight varies. The beam will not be perfectly synchronised with the rf cavities. The idea is to manage to extract the beam before it reaches a cavity with negative voltage. There is therefore 180° of RF

phase available for acceleration.

The objective of this section is to show that a dynamical map can be used to model the dynamics of a particle during acceleration in an FFAG. Comparison will be made with an analytical description, to aid understanding of the relevant processes. The analytical solution has been developed by Keil and Sessler in [61]. A complete analytical derivation can also be found in [62, 63]. The general Hamiltonian for the longitudinal motion can be expressed as following [46]:

$$H = h(\frac{\eta_0\delta^2}{2} + \frac{\eta_1\delta^3}{3} + \frac{\eta_2\delta^4}{4} + ...) + \frac{2\pi h\beta_r^2 E_r}{eVN_c}[\cos(\phi_s + \phi) + \phi\sin\phi_s]\,, \tag{4.22}$$

where h is the harmonic number and δ is the energy deviation with respect to the reference energy E_r. V is the accelerating rf voltage in one of N_c cavities with synchronous phase ϕ_s. ϕ_s is measured in radian and equals zero at the zero crossing with negative gradient of the rf wave form. β_r is the speed in units of the light velocity of the reference particle. The reference particle is synchronised with the rf; hence the harmonic number, the revolution time and the rf frequency are related by $t_{rev} = h/f_{rf}$.

The origin of ϕ is at the synchronous phase ϕ_s. The coefficients η_i are the phase slip factor η_0 and its higher order terms. The phase slip factor is defined as the variation with energy of the time of flight of a particle over one revolution. Electrons in EMMA are in the ultra-relativistic regime which means that path length and time of flight evolutions with energy are equivalent. In conventional bucket acceleration, the lattice is such that the phase slip factor is mainly determined by its linear part η_0. Hence choosing arbitrarily $\phi_s = \pi$, the approximate Hamiltonian becomes:

$$H_1(\delta,\phi) = \frac{h\eta_0\delta^2}{2} - \frac{2\pi h\beta_r^2 E_r}{eVN_c}\cos(\phi)\,. \tag{4.23}$$

Figure 4.19 shows the contour plot of the Hamiltonian H_1 in 4.23 for values of the parameters arbitrarily chosen. The lines are contours of constant value of the

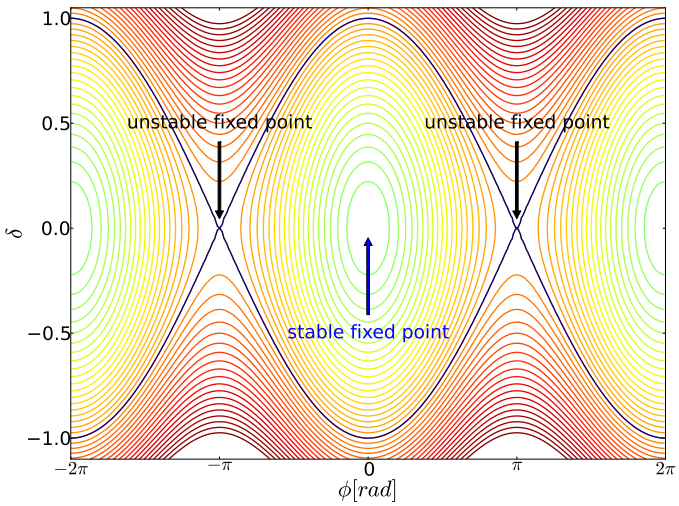

Figure 4.19: Contour plot of the Hamiltonian H_1 in 4.23 for $K_2 = 1/4$, including only the linear part of the phase slip factor η_0. Particles move along dark blue lines. The vertical axis is the scaled momentum (with 0 being the reference energy) and the horizontal axis is the relative phase ϕ. A stable fixed point is located at (0,0) whereas two unstable fixed points are located at (-π,0) and (π,0). They are linked by dark blue lines called separatrices. The largest oscillation in energy is obtained by following closed loops close to the separatrices.

Hamiltonian. We observe the so called bucket structure. If a particle is launched with a position in this diagram close to (0,0), because the Hamiltonian is an invariant of the motion, it will follow a closed loop in phase space around the point (0,0). This point is called a stable fixed point because it is at the centre of region of closed loop where the phase is kept within a finite range. On the other hand, the lines passing over the top and below the bottom of the bucket do not close on themselves. The phase of a particle following these lines will increase without limit turn after turn. The boundaries between these two different behaviours are called the separatrices and are manifested in this diagram by the two lines surrounding the bucket (one up and one down) and crossing at (-π,0) and (π,0). These points are called unstable fixed points since they are located in an area where phases drift away following the contours over and below the stable areas.

In EMMA, since the evolution of time of flight with energy is a parabola, the phase slip factor is not accurately represented by η_0 only. Hence, we cannot neglect the term in η_1 in the Hamiltonian that relates to the quadratic evolution of time of flight with energy. The Hamiltonian is then written:

$$H_2(\delta, \phi) = \frac{h\eta_0\delta^2}{2} + \frac{h\eta_1\delta^3}{3} - \frac{2\pi h\beta_r^2 E_r}{eVN_c}\cos(\phi)\,. \tag{4.24}$$

Figure 4.20(a) shows the contour plot of the Hamiltonian H_2 defined in equation 4.24 for arbitrarily chosen values for the parameters; these values were chosen such that the unstable fixed point at $\phi = 0$ occurs for $\delta = -1$. We observe new stable fixed points at (-π,-1) and (π,-1) and a new unstable fixed point at (0, -1). A "serpentine channel" is created between these various fixed points. A particle travelling on a line starting at ($-\pi$,-1.5) increases its energy until it goes over the (0,0) fixed point and then decreases its energy until $\phi = \pi$ back to the original value. This behaviour is not stable (in the sense of following a closed loop in phase space), however the stable motion is not required for acceleration.

4.3.3.3 Acceleration of a single particle in EMMA with dynamical maps

We implement acceleration in our model using dynamical maps as follows. Particles are tracked for 20 turns with a single dynamical map with reference energy E_{ref}= 14.5 MeV (to be distinguished from rf reference energy) representing a configuration of the EMMA lattice for which the time of flight variation with energy is shown in figure 4.6.

In EMMA, there is one cavity every other cell, apart from regions close to injection and extraction, which means 19 cavities in total. At the end of every other dynamical map (i.e. every other cell), the relative phase ϕ of the particle with respect to rf phase ϕ_s is computed from the path length of the trajectory. The energy deviation is then

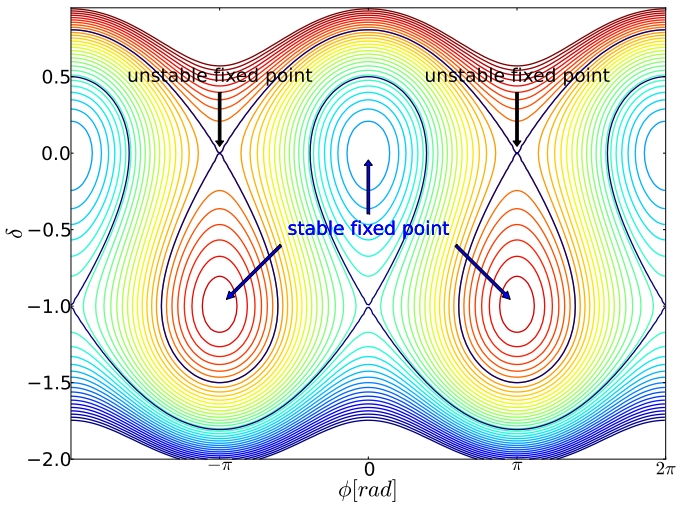

(a)

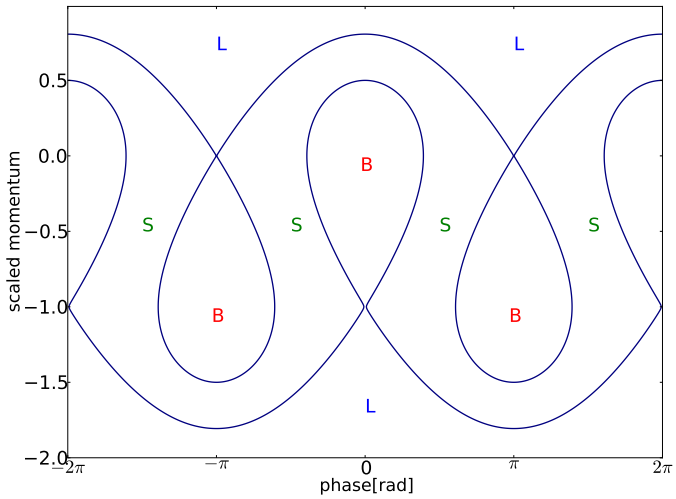

(b)

Figure 4.20: (a): Contour plot of the Hamiltonian H_2 in 4.24; the linear and quadratic part of the phase slip factor η_0 and η_1 are included. Particles move along lines. The vertical axis is the scaled momentum (with 0 being the reference momentum) and the horizontal axis is the relative phase ϕ. The largest acceleration is obtained following a contour in the region labelled S in (b). This acceleration scheme is called serpentine acceleration. (b): Blue lines are called the separatrices. They mark the boundaries between different acceleration modes."L" stands for "low acceleration"(region outside separatices). Particles following a line in this region see their phase drifting monotonically without gaining significant energy. "B" stands for bucket acceleration (region enclosed by a single separatrix). Phase and energy of particles following a closed loop in that regime will oscillate around the stable fixed point. The amount of energy gained by the particle is not optimal. "S" stands for "serpentine acceleration" (region bounded by different separatrices).

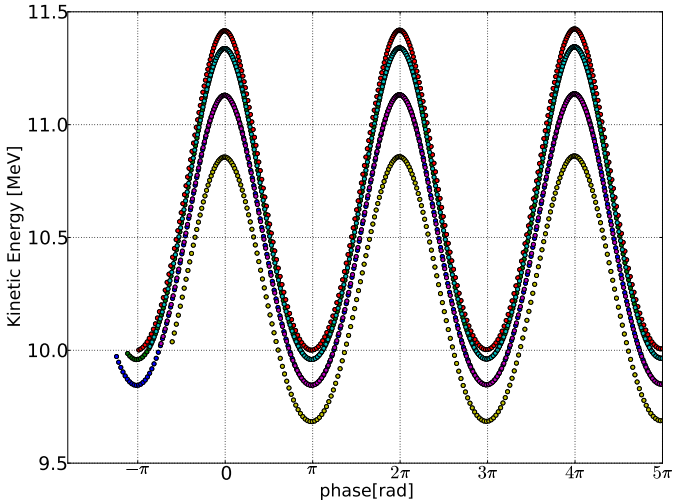

Figure 4.21: Trajectories over 20 turns in longitudinal phase space for particles injected at 10 MeV with various initial phase. The peak RF voltage sum over one turn is 0.76 MV. For all trajectories a monotonic increase of the relative phase is observed. The energy gain is only 1.5 MeV

increased according to the voltage V corresponding to the phase ϕ. The peak voltage and the frequency of the cavity are V_{rf} and f_{rf} respectively. The map for the cavity can be written as followed:

$$\delta_{new} = \delta + \frac{eV}{E_{ref}} \tag{4.25}$$

$$where\ V = V_{rf} \sin(\phi_s - \phi) \tag{4.26}$$

ϕ is related to the longitudinal position of a particle with respect to the reference particle z by $\phi = \frac{2\pi f_{rf}}{\beta c} z$.

Since we considered an infinitesimally thin cavity, the other dynamical variables are not affected. From Hamilton's equation with s being the independent variable, the

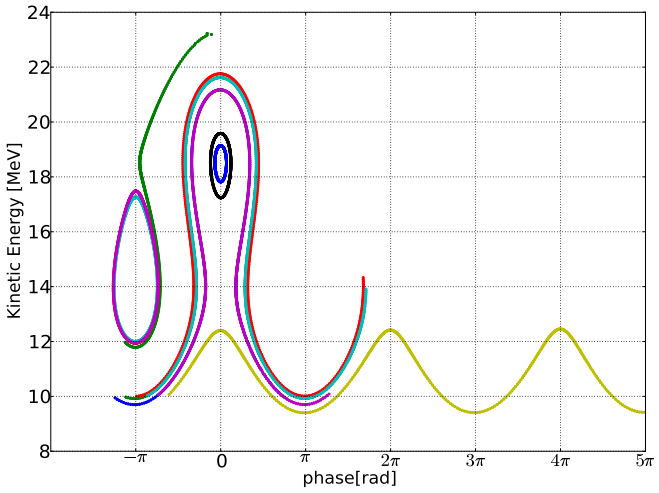

(a)

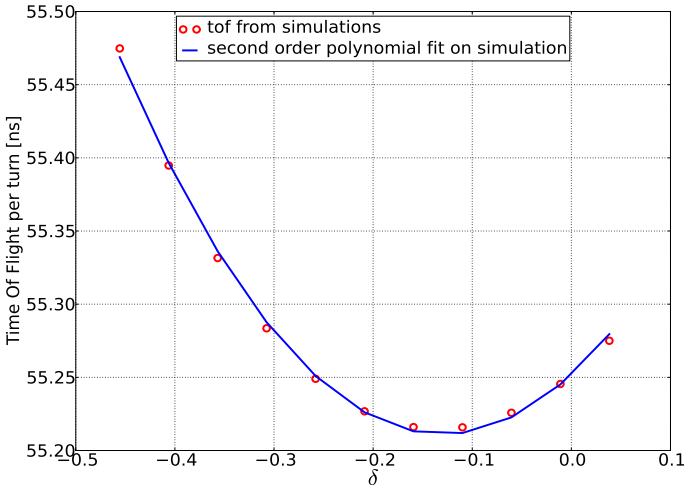

(b)

Figure 4.22: (a): Trajectories over 20 turns in longitudinal phase space for particles injected at 10 MeV with various initial phase. (b): Time of flight at various energy deviation δ (red circle) for the lattice configuration used for acceleration in (a). The reference time of flight is the time of flight at reference total energy 19.6 MeV (defined by the stable fixed point in (a)) : $t_{rev} = 55.25$ ns. Note that the time of flight at $\delta = -0.27$ is also equal to the reference time of flight. It corresponds to the other stable fixed point in (a). A second order polynomial fit is also performed and represented by a blue line. From this fit we compute $\eta_0 = 0.0114$ at the reference energy and $\eta_1 = 0.0439$.

variation in δ for a particle going through a cavity of length L can be expressed as

$$\Delta\delta = -\int_0^L \frac{\partial H}{\partial z} ds. \tag{4.27}$$

Hence, the Hamiltonian for this cavity can be written as:

$$H(z,\delta) = -\frac{eV\beta c}{2\pi f L E_{ref}} \cos(\phi_s - \frac{2\pi f}{\beta c} z)\,. \tag{4.28}$$

A 10 MeV particle is launched on the 10 MeV closed orbit found in the first section of this chapter. First we studied the acceleration in a bucket (i.e. rf voltage not large enough to create a serpentine channel). We show in figure 4.21, the energy of a single particle with respect to its relative phase. The peak RF voltage summed over one turn is 0.76 MV (or 0.76/19=40 kV per cavity). Different colours correspond to various relative phase at injection ϕ_0 of the particle. We observe that the serpentine channel is not reached by any of the initial phases from $\phi_0 = -\pi$ to $\phi_0 = \pi$. The maximum energy gain, 1.5 MeV, is therefore rather small.

When increasing the sum voltage over one turn to 1.52 MV, the serpentine acceleration is observed for particles with initial phase between $-6\pi/5$ and $-4\pi/5$ (see figure 4.22(a)). Also, we notice that particles injected at 12 MeV with $\phi_0 = 0$ and 18 MeV with $\phi_0 = \pi$ follow closed lines around stable fixed points located at (14,$-\pi$) and (19.1,0) respectively; injection at 10 MeV with $\phi_0 - 4\pi/5$ leads to a monotonic drifting of the relative phase with low energy gain; this corresponds to the area with the label 'L' in figure 4.20(b).

To compare simulated and analytical results, the numerical value of the parameters used for the simulation listed in table 4.2 are implemented in H_2 (see (4.24)) to plot the contour of the analytical Hamiltonian.

The reference total energy E_r corresponds to $y = 0$ in figure 4.20(a) for which there is a stable fixed point at $\phi = 0$. Comparing with the simulated serpentine acceleration

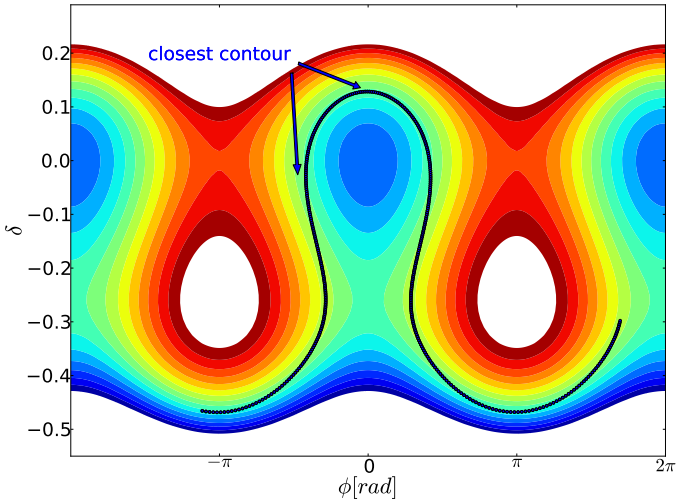

Figure 4.23: Superposition of a simulated trajectory in longitudinal phase space and analytical contour plot of the Hamiltonian defined in equation 4.24. The contours in light green matches relatively well the main features obtained from simulation: position of the stable and unstable fixed points, total energy gain from about -0.45 to 0.15, periodicity. However we observe that the analytical model is symmetric with respect to the horizontal axis at $\delta = -0.15$ whereas in the simulations, the upper part of the serpentine (for δ greater than -0.15) is not as wide as the lower part (for δ smaller than -0.15).

in figure 4.22(a), the corresponding stable fixed point occurs at kinetic energy 19.1 MeV (19.6 MeV total energy); the reference energy is the energy for which the revolution time equals the revolution time of the synchronous particle; figure 4.22(b) shows the time of flight for different value of the total energy. We read that the reference time of flight (at total energy 19.6 MeV) is 55.25 ns.

From the reference time of flight, we derived the harmonic number h, knowing that the rf frequency is 1.3 GHz: $h = t_{rev} * f_{rf} = 71.825$. Note that in the case of the serpentine acceleration scheme, the harmonic number is not necessarily an integer, as it is generally the case in a synchrotron, using bucket acceleration.

The two parameters η_0 and η_1 are given by the variation of time of flight with energy. For the simulations they are found by fitting a second order polynomial function on the time of flight evolution with energy. The result of this fit is shown in figure 4.22(b)

Table 4.2: Parameters for the Hamiltonian description of the serpentine acceleration

Parameter	Simulations
rf frequency (GHz)	1.3
rf voltage per turn $V \times N_c$ (MV)	1.52
reference total energy E_r (MeV)	19.6
reference β_r	0.9997
reference revolution time (ns)	55.25
harmonic number, $h = f_{rf} * t_{rev}$	71.825
η_0 at E_r (i.e. $\delta = 0$)	0.0114
η_1	0.0439

from which we compute $\eta_0 = 0.0114$ at 19.6 MeV and $\eta_1 = 0.0439$.

The comparison between the position in longitudinal phase space of a simulated trajectory and the analytical model of the Hamiltonian H_2 is shown in figure 4.23. The contours in light green matches relatively well the main features obtained from simulation: position of the stable and unstable fixed points, total energy gain from about -0.45 to 0.15, periodicity. However we observe that for the analytical model, the widths of the bucket around the upper stable fixed point (0,0) and the lower stable fixed point ($-\pi$,-0.25) are identical; therefore the contours in the serpentine channel are symmetrical with respect to the horizontal axis at $\delta = -0.15$ whereas in the simulation, the upper part of the serpentine (for δ greater than -0.15) is more narrow than the lower part (for δ smaller than -0.15). This could be explained in two ways: first the actual time of flight variation with energy through acceleration could be different from the time of flight computed at various fixed energies. Second, retaining higher order terms in δ in the Hamiltonian of equation 4.22 may be necessary to match the simulations.

From our study, we conclude that our simple implementation of acceleration is capable of reproducing the important characteristics of the longitudinal dynamics in EMMA.

4.3.3.4 Evolution of particle distribution through acceleration in EMMA

In this section, we will present results of tracking longitudinal and transverse distributions of particle through the EMMA lattice including the 19 accelerating cavities. We explained in section 4.3.1 of this chapter that beam dynamics at different energies could be simulated either with several dynamical maps with various reference energies or with a single map varying the energy deviation variable. The study of acceleration in EMMA is a wide subject and an entire thesis could be dedicated to it. However, in this study, we will only present some examples of simulations with dynamical maps to demonstrate the capabilities and some limitations of this technique.

First, thousand particles are tracked using 10 dynamical maps with reference energies from 10 MeV to 19 MeV increasing with 1 MeV step. A particle is tracked in a map until the energy deviation variable reaches $\pm 0.5\,MeV$. A dynamical map with different reference energy is then used. Note that the components of the momentum of a particle are normalised with respect to the reference momentum. In particular, the six dynamical variables are defined by:

$$X_1 = x; \qquad X_2 = p_x/p_0; \tag{4.29}$$

$$X_3 = y; \qquad X_4 = p_y/p_0; \tag{4.30}$$

$$X_5 = z = \frac{s}{\beta_0} - ct; \qquad X_6 = \delta = \frac{E}{p_0 c} - \frac{1}{\beta_0}; \tag{4.31}$$

where p_0, E_0 and β_0 are the momentum, total energy and velocity of the reference particle respectively. s is the independent variable and t is the time taken for a particle to travel from $s = 0$ to the position defined by s. Therefore when tracking in a new dynamical map, the final coordinates of the particles obtained from the previous map must be scaled to the new reference values. For instance let us consider a particle that travels along a given orbit. For a dynamical map with reference momentum $p_0 = \beta_0\gamma_0 m_0 c$, the longitudinal position of the particle with respect to the reference

particle is given by:

$$z_0 = \frac{s}{\beta_0} - ct_0 \,. \tag{4.32}$$

A particle travelling along the same trajectory but tracked with a dynamical map with reference momentum p_1, the longitudinal position variable becomes:

$$z_1 = \frac{s}{\beta_1} - ct_1 \,. \tag{4.33}$$

Since the particle is travelling along the same trajectory in both case, the path length given by $t\beta c$ must be the same. This gives:

$$t_1\beta_1 c = t_0\beta_0 c \,. \tag{4.34}$$

Multiplying equations 4.32 and 4.33 by β_0 and β_1 respectively, and subtracting the two expressions, we obtain:

$$\begin{aligned} \beta_1 z_1 - \beta_0 z_0 &= s - s + c(t_1\beta_1 - t_0\beta_0) \\ &= 0 \,, & (4.35) \\ \text{thus} \quad z_1 &= z_0 \frac{\beta_0}{\beta_1} \,. & (4.36) \end{aligned}$$

Similarly for p_x we have:

$$p_{x1} = p_{x0}\frac{p_0}{p_1} \,. \tag{4.37}$$

In the following, we will study the evolution of different initial distributions of particles through serpentine acceleration in EMMA. We will carry on the study of the decoherence effect started in section 4.3.3.1 by defining a purely longitudinal distribution of particles (tracing an ellipse in the (z,δ) phase space) launched on the closed orbit. Then we will study the behaviour of this distribution launched with an offset of 1 mm with respect to closed orbit and which therefore has an initial betatron amplitude.

We can then observe the effect of decoherence through acceleration.

Then we will study the evolution of a purely transverse distribution of particles through acceleration. In particular, we will look at the deformation of this distribution (initially an ellipse) when crossing resonances.

Finally we will apply dynamical maps with different orders of truncation to a group of particles with transverse and longitudinal distributions; these distributions are defined by parameters obtained from simulation of the distribution delivered by the ALICE injector [65, 66]. We will also apply different numbers of maps with various reference energies to the same group of particles. This way we will be able to determine the minimum order of truncation and the minimum number of maps necessary to simulate the dynamics for distribution, close to the real machine behaviour, through acceleration with reasonable accuracy.

Case 1 In figure 4.24 we studied the acceleration of a group of particles with a longitudinal distribution corresponding to an ellipse in longitudinal phase space defined by a full height (energy spread) of 100 keV and a full width (bunch length) of 20 ps. All the particles in the bunch have the same transverse initial position; the energy spread and the bunch length values correspond to measurements of bunch characteristics coming from the ALICE injector [64].

The position of each particle of the distribution is recorded (and plotted) after each turn in longitudinal phase space (as described in section 4.3.3.3) and transverse phase space for an accelerating voltage of 2 MV per turn (distributed over the 19 cavities around the ring) in figures 4.24(a) and 4.24(b) respectively. The initial transverse position of the particles is on the closed orbit at 10 MeV.

During acceleration through the serpentine channel, the energy spread of the distribution is multiplied by two from 100 keV at 10 MeV to 200 keV at 14 MeV (figure 4.24(a)); for large energy up to 20 MeV the distribution is tilted and the bunch length

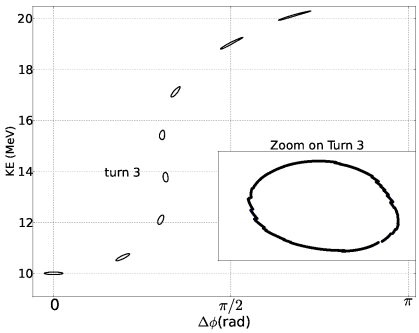

(a) Longitudinal Phase space, V=2 MV

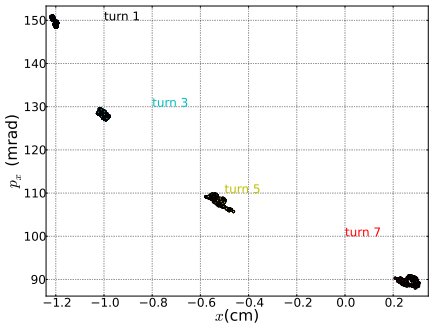

(b) Transverse Phase space, V=2 MV

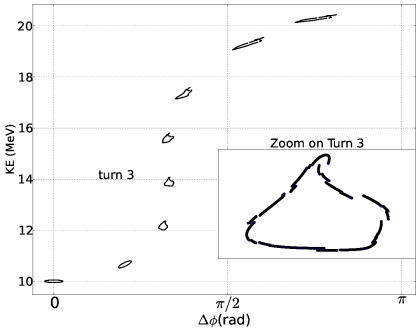

(c) Longitudinal Phase space, 1 mm offset

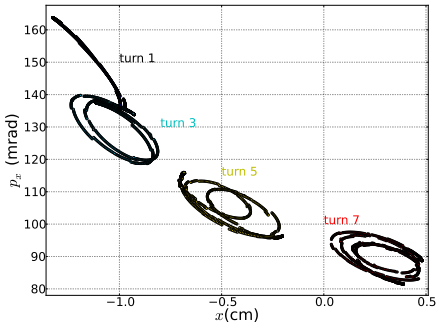

(d) Transverse Phase space, 1 mm offset

Figure 4.24: (a) Acceleration through the serpentine channel for a bunch with a longitudinal distribution corresponding to an ellipse in longitudinal phase space defined by a full height (energy spread) of 100 keV and a full width (bunch length) of 20 ps. We observe in the transverse phase space (b) an increase of the bunch width up to 1 mm for the 7^{th} turn in the horizontal transverse direction. We then introduce an offset in the initial transverse position of the bunch (1 mm offset with respect to the closed orbit at 10 MeV). In the longitudinal phase space (c), we observe a distortion of the ellipse, shown for turn 3. In the transverse phase space (d), after 3 turns, particles are spread around an ellipse and occupy about 5 mm in the transverse direction; extracting the whole bunch may be complicated in this case.

is almost twice as large as the initial one. Also we observe in the transverse phase space (figure 4.24(b)) an increase of the bunch width up to 1 mm for the 7^{th} turn in the horizontal transverse direction. Note that the initial distribution of the bunch (not represented here) is point-like in transverse phase space. The extraction scheme needs to be implemented in the tracking code to evaluate the requirement on the extracted beam to achieve reasonable extraction.

Case 2 We then introduce an offset in the initial transverse position of the bunch (1 mm offset with respect to the closed orbit at 10 MeV). We observe a distortion of the ellipse in longitudinal phase space (see figure 4.24(c)). In the transverse phase space (figure 4.24(d)), after 3 turns particles are spread around an ellipse and occupy about 5 mm in the transverse direction; extracting the whole bunch may be complicated in this case. Again, this requires more simulations work.

Case 3 Then we used the routine written to simulate the acceleration in EMMA with dynamical maps to observe the effect of resonances on the transverse distribution of a group of particles. All particles have the same initial energy (10 MeV) and the same initial longitudinal position (z=0). In the transverse phase space, the initial coordinates of the particles are chosen such that they map out the betatron motion around the closed orbit at 10 MeV; this ellipse can be seen in figure 4.4 (bottom) with the label "10 MeV". The simulated normalised emittance is $\epsilon_N = 10$ mm.mrad. We can use this ellipse as being the action J_{xN} of a single particle tracked several time in one cell. The corresponding action at 10 MeV ($\gamma_{10MeV} = 20.57$) is therefore $J_x = J_{xN}/\beta\gamma \approx 0.5$ mm.mrad. The corresponding maximum betatron amplitude in the middle of the long drift (initial longitudinal position of the dynamical map) is then $x_{max} = \sqrt{2\beta_x J_x} = 0.5$ mm where $\beta_x = 0.25$ m is the value of the horizontal beta function at this location. We observe in figure 4.4 (bottom) that the maximum transverse excursion is about 2 mm with respect to the centre of the ellipse. Hence we

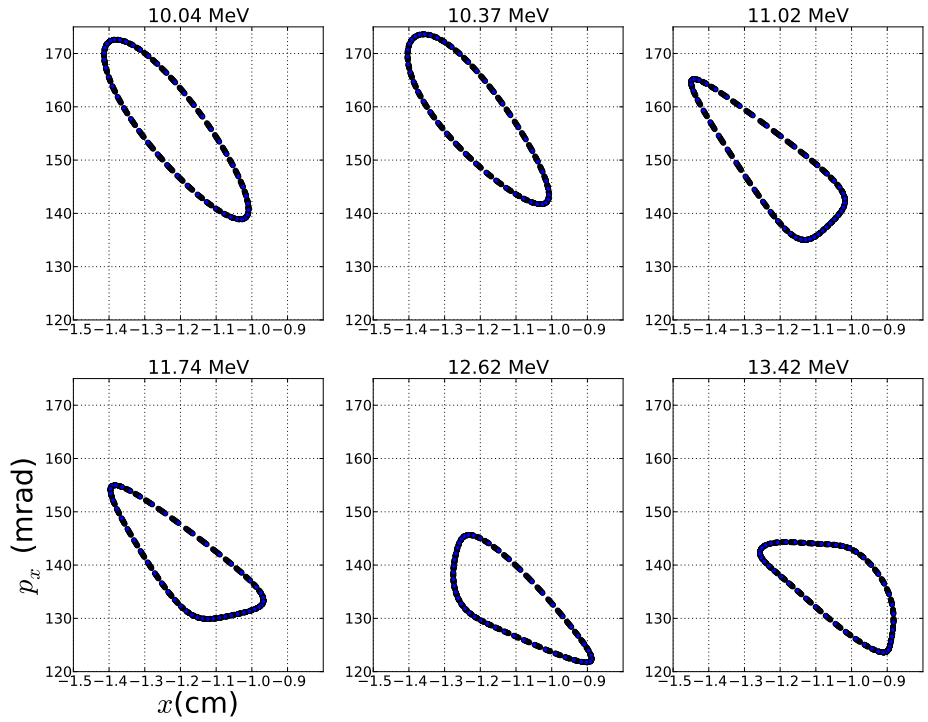

(a) Transverse distribution through acceleration

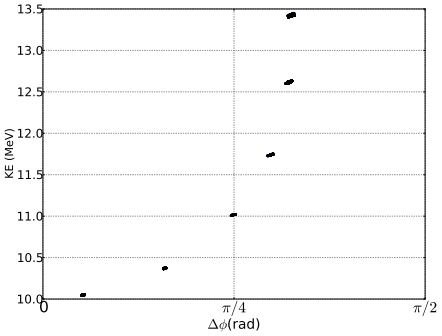

(b) Longitudinal distribution through acceleration

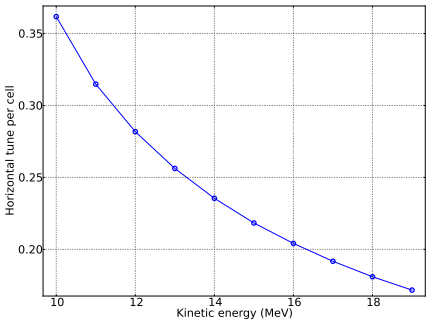

(c) Horizontal tune per cell vs. energy

Figure 4.25: (a) Evolution of the transverse distribution through acceleration for an rf voltage of 2 MV per turn. Each subplot corresponds to one group of particles represented in the longitudinal phase space in (b). Positions are recorded every 20 cells. We observe that between 10.37 MeV and 11.02 MeV, the shape of the distribution (initially an ellipse) becomes distorted, acquiring the shape of a triangle. This may indicate the effect of a third-order resonance [23]. The horizontal tune is indeed taking the value 1/3 for 10.70 MeV in (c).

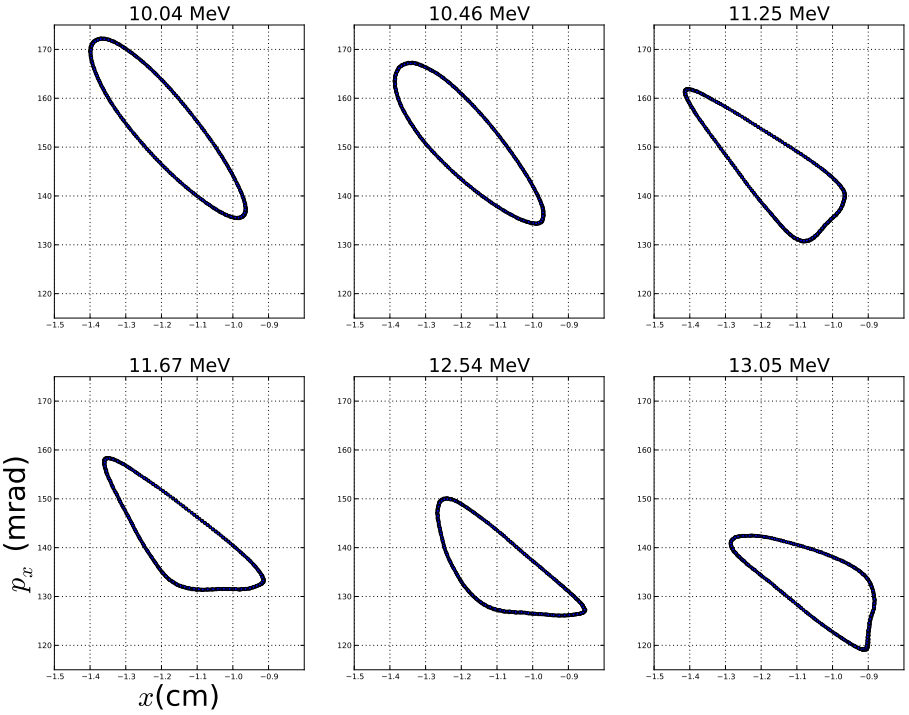

Figure 4.26: Evolution in the transverse phase space (p_x in mrad vs x in cm) of the transverse distribution through acceleration for an rf voltage of 2 MV per turn simulated with PyZgoubi. Each subplot corresponds to one group of particles whose positions are recorded every 20 cells. We observe a distortion of the shape of the distribution due to the crossing of a resonance.

are simulating a distribution with a larger action than the expected one; the effect of non-linearities and resonances should be stronger than in reality.

The position of the particles is recorded every 20 cells and the rf voltage is 2 MV per turn. Figure 4.25(a) shows the evolution of the transverse distribution through acceleration. Each subplot corresponds to one group of particles represented in the longitudinal phase space in figure 4.25(b). We observe than between 10.37 MeV and 11.02 MeV, the shape of the distribution (initially an ellipse) becomes distorted, acquiring the shape of a triangle. This may indicate the effect of a third-order resonance [23, 24].

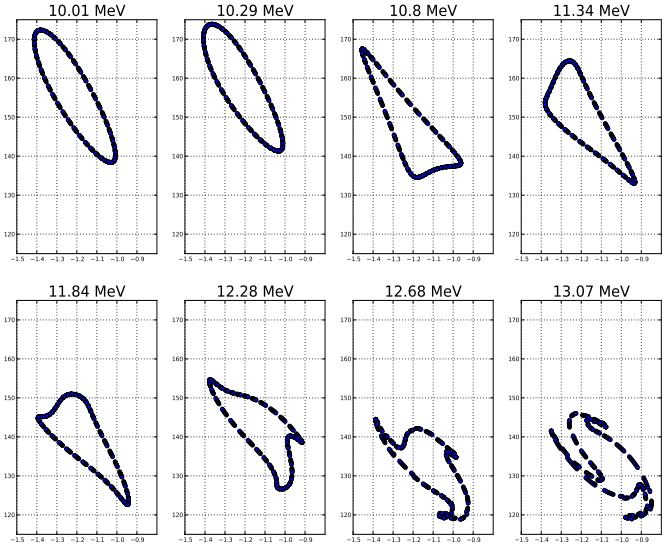

(a) Dynamical maps

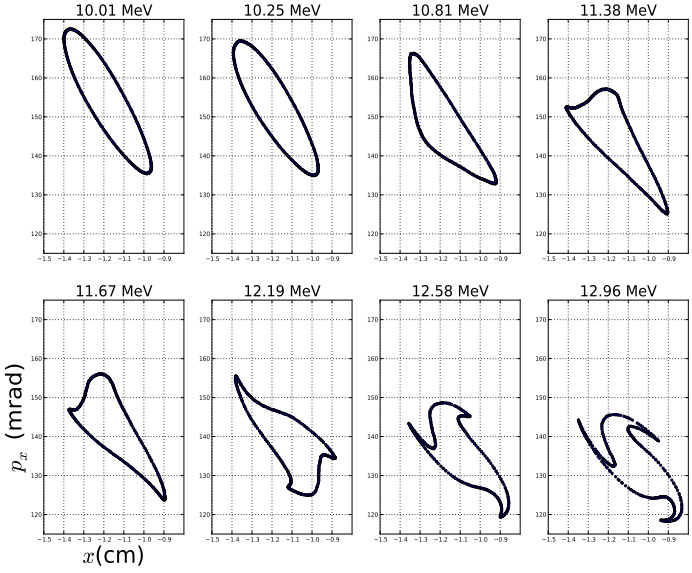

(b) PyZgoubi

Figure 4.27: Evolution in the transverse phase space (p_x in mrad vs x in cm) of the transverse distribution through acceleration for an rf voltage of 0.55 MV per turn. Each subplot corresponds to one group of particles whose positions are recorded every 40 cells. We observe a strong distortion of the shape of the distribution due to the slow crossing of resonances.

The variation of the horizontal tune with energy computed at fixed energy with 10 dynamical maps with different reference energies is shown in figure 4.25(c). Note that the lattice configuration used for acceleration has been chosen such that the time of flight evolution with energy is a parabola with its minimum at 15 MeV, since this is the nominal configuration for acceleration. Therefore the horizontal tune represented in figure 4.25(c) is different from the one in figure 4.2 in section 4.3.1.1.

The horizontal tune per cell takes the value $1/3 = 0.33$ for 10.7 MeV; this value for the tune correspond to a third order resonance. We observe that the area of the distribution does not increase significantly when crossing this resonance; this is an encouraging sign for the success of fast acceleration in the serpentine channel in a non-scaling FFAG.

To verify the results, we implemented acceleration in PyZgoubi using a field map to represent the magnets and a similar simple model for the accelerating cavities (zero length and sinusoidal rf voltage). Representation of the equivalent initial transverse distribution is shown in figure 4.26. A similar distortion of the ellipse is observed when particles gain energy. This gives confidence in the accuracy of the results obtained with dynamical map.

With a high rf voltage (2 MV per turn in this case), the distribution is crossing the resonance quickly enough not to be strongly affected. However, with a slower acceleration (rf voltage of 0.55 MeV per turn) we observe in figure 4.27(a) (position recorded every 40 cells) that the distortion of the ellipse is significantly stronger. Again the comparison for low rf voltage with PyZgoubi in figure 4.27(b) gives satisfactory results. A growth of the transverse distribution could lead to significant beam losses around the ring and could also make the extraction of particles impossible.

Case 4 We have seen in this chapter that beam simulations for various energies could be carried out applying a single dynamical map with 15 MeV reference energy. Similarly

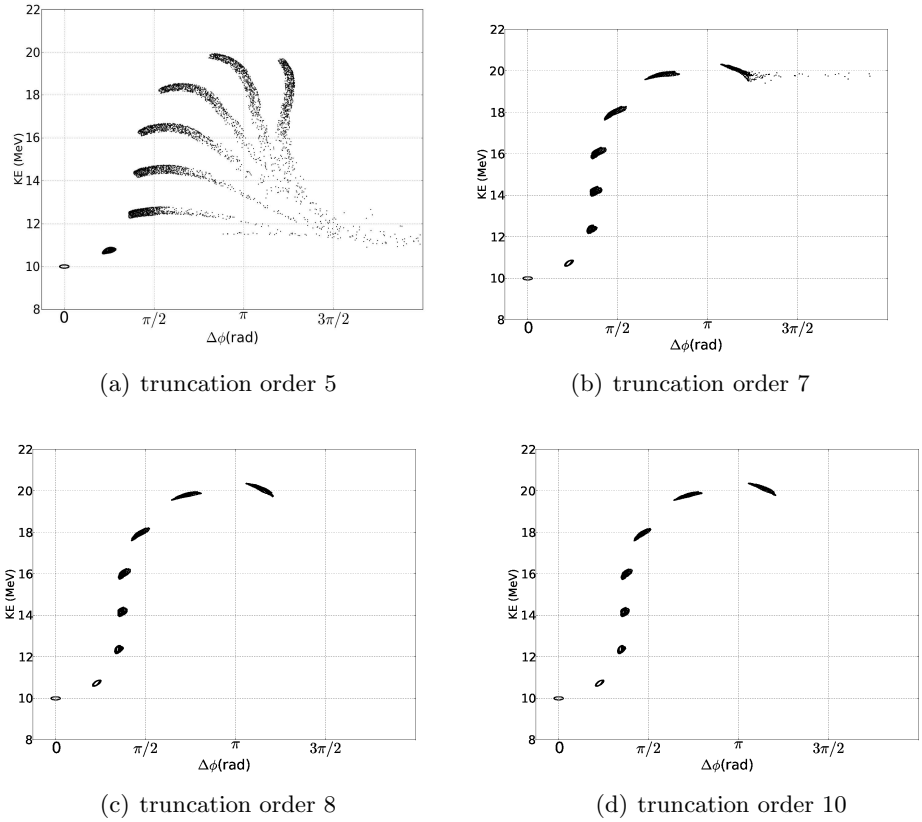

(a) truncation order 5

(b) truncation order 7

(c) truncation order 8

(d) truncation order 10

Figure 4.28: (a) to (d) show the longitudinal phase space for tracking a particle distribution with dynamical maps truncated at orders 5, 7, 8 and 10 respectively. Simulations with maps truncated at the 5^{th} (a) and 7^{th} (b) order show a significant discrepancy with the simulation with higher truncation order. Dynamics are very similar for maps truncated at the 8^{th} and 10^{th} orders; it seems than a convergence in the beam dynamics occurs after the 8^{th} order in this case.

we applied this map to a group of particles having the same longitudinal distribution as in the previous study in case 1 and 2. In the transverse phase space, the initial distribution is the same as in case 3. The rf voltage is 2 MV per turn.

Simulations are carried out with dynamical maps computed for different truncation orders. Figures 4.28 (a) to (d) show the longitudinal distribution of a group of particles tracked with dynamical maps truncated at orders 5, 7, 8 and 10 respectively. Simulations with maps truncated at the 5^{th} and 7^{th} order (see figure 4.28(a) and 4.28(b) respectively) show a significant discrepancy with the simulation with multiple maps

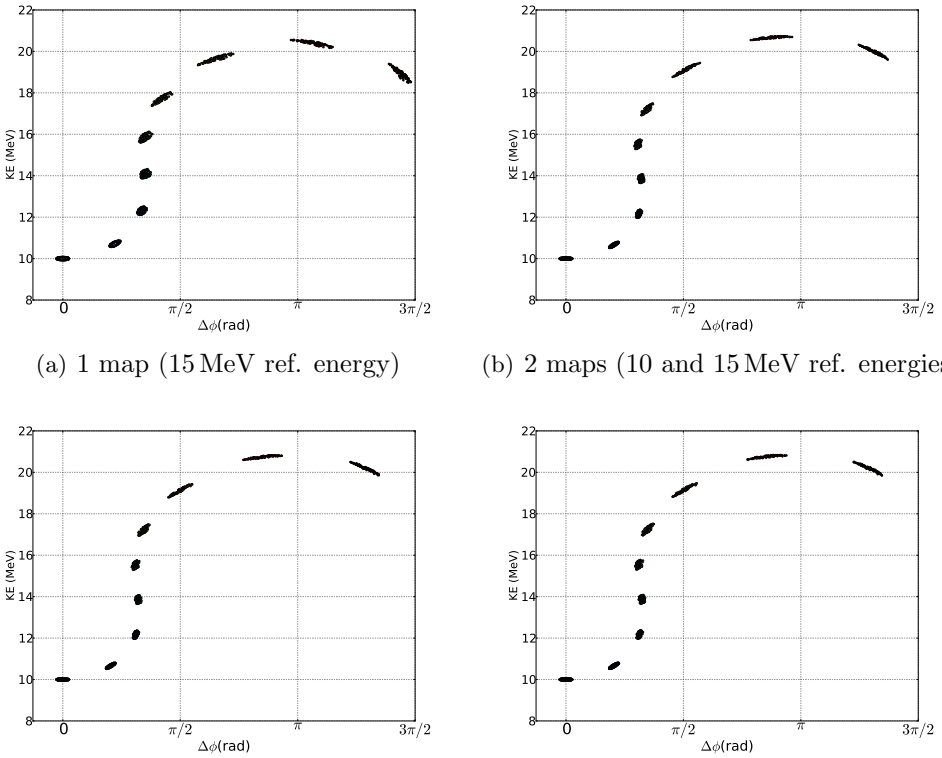

(a) 1 map (15 MeV ref. energy)

(b) 2 maps (10 and 15 MeV ref. energies)

(c) 3 maps (10, 14 and 18 MeV ref. energies)

(d) 10 maps (10 to 19 MeV with 1 MeV step ref energies)

Figure 4.29: Longitudinal phase space representation of a distribution of particle tracked through acceleration in the EMMA lattice using 1, 2, 3 and 10 dynamical maps with different reference energies. The positions in longitudinal phase space of the seventh and eighth turns for the single map simulation (a) are shifted to higher relative phases (just above π for turn 7 and about $3\pi/2$ for turn 8) compared to the three other simulations ((b), (c) and (d)) with the multiple maps cases agreeing almost perfectly (just below π for turn 7 and about $5\pi/4$ for turn 8). Turns are counted starting from turn 0 at ($\Delta\Phi$=0, 10 MeV).

(see figure 4.24(a)). For the map truncated at order 5, a fraction of the beam does not follow the serpentine channel and instead "slips" to the area of low acceleration labelled "L" in figure 4.20(b).

Dynamics are very similar for maps truncated at 8^{th} and 10^{th} orders; it seems than a convergence in the beam dynamics occurs after the 8^{th} in this case.

Case 5 It was then interesting to investigate the minimum number of maps with different reference energy that needed to be used to simulate acceleration. Figures 4.29(a) to 4.29(d) show the longitudinal distribution of a bunch tracked through acceleration in the EMMA lattice using 1, 2, 3 and 10 dynamical maps with different reference energies respectively. The corresponding transverse distributions of the bunch at the initial position and after the first, fifth and eighth turns are shown in figures 4.30(a) to 4.30(d).

The positions in longitudinal phase space of the seventh and eighth turns for the single map simulation (figure 4.29(a)) are shifted to higher relative phases (just above π for turn 7 and about $3\pi/2$ for turn 8) compared to the three other simulations with the multiple maps cases agreeing almost perfectly (just below π for turn 7 and about $5\pi/4$ for turn 8). Turns are counted starting from turn 0 at ($\Delta\Phi$=0, 10 MeV). This disagreement appears more clearly comparing the transverse distribution of the bunches through acceleration in figure 4.30. A good agreement is obtained between simulations performed with 2 maps, 3 maps and 10 maps. The 8^{th} turn is shifted towards negative values of x (centred on -0.2 cm) for the single map configuration whereas it is centred on x=0.2 cm in the case of simulations with multiple maps. This observation agrees with features in figure 4.29(a) in which the average energy of the 8^{th} turn is 19 MeV and 20.2 MeV for simulations with single map and multiple maps respectively. The position in transverse phase space of the former, with lower energy, is therefore towards the inside of the ring (i.e. negative value of x).

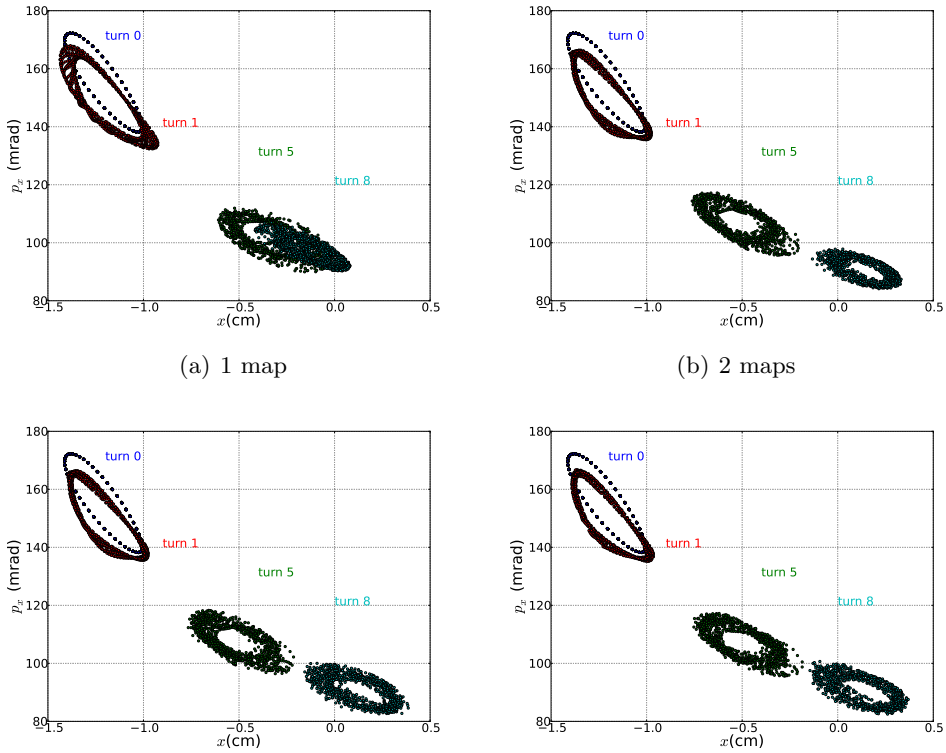

(a) 1 map

(b) 2 maps

(c) 3 maps

(d) 10 maps

Figure 4.30: Transverse phase space representation of a distribution of particle tracked through acceleration in the EMMA lattice using 1, 2, 3 and 10 dynamical maps with different reference energies. A good agreement is obtained between simulations performed with 2 maps, 3 maps and 10 maps. The 8^{th} turn is shifted towards negative values of x (centred on -0.2 cm) for the single map configuration whereas it is centred on x=0.2 cm in the case of simulations with multiple maps. This observation agrees with features in figure 4.29(a) in which the average energy of the 8^{th} turn is 19 MeV and 20.2 MeV for simulations with single map and multiple maps respectively.

The large value taken by the energy deviation variable when tracking a particle from 10 MeV to 20 MeV with a single dynamical map affects the precision of the simulations. In the present study, simulations of accelerations with two dynamical maps agree with simulations with 10 maps. Therefore only two maps may be sufficient.

Note that the 10 MeV map is always used as the starting map when using multiple maps. Thus the initial transverse distribution corresponding to the betatron ellipse at 10 MeV matches the dynamics at the initial reference energy. In the case of a single map with reference energy 15 MeV, the equivalent situation would be obtained by using the betatron ellipse at fixed energy 10 MeV defined by the energy deviation variable. However we observed in figure 4.7(c) the non physical growth at fixed energy observed for large energy deviation. Therefore we could not recreate the equivalent initial transverse distribution at 10 MeV and used the same ellipse as for the study with multiple maps (scaling up the momentum according to equation 4.37). This difference of starting condition is likely to explain the discrepancy between simulations with single map and multiple maps in this case.

Also we observed in section 4.3.1.2 for large values of the energy deviation for the horizontal and vertical tune between single map and multiple map simulations. Here again a single map may not accurate enough to simulation the acceleration of a bunch over the whole range of energy in EMMA. An interesting study would consist in looking for the minimum number of maps required to simulate accurately the nonlinear beam dynamics through acceleration.

From the design studies, cavities in EMMA had a rather simple field profile and no significant non linear effect were predicted by the model. However, in other types of FFAG, in particular in scaling FFAG where cavities must be large radially to accommodate large excursions of the particles, non linear effect may appear. It could then be required to construct a dynamical map for the cavity itself and apply it to tracked particles. Variation with time of the electromagnetic field in the cavity must also be

taken into account.

4.4 Summary and conclusions

In this chapter, we have studied the beam dynamics obtained from dynamical maps in explicit form. Firstly we presented a summary of PyZgoubi, chosen as a comparative tracking code because of its ability to handle numerical field maps and hard edge models. We presented as well the geometry features of the EMMA cell considering fringe field rather than hard edge model. Special care has been taken regarding the rotation of the reference frame, being performed in a field free region but also simulating realistically the EMMA lattice. Appropriate translation of the particle coordinates and momenta at the end of each cell respected both requirements.

In the following section, we focused on the crucial beam dynamics parameters for an FFAG, namely the tune per cell and time of flight. We compared the results obtained from PyZgoubi with Hard Edge model, from PyZgoubi with field map, and from dynamical maps. The shape of the time of flight curve changed significantly when tracking in an hard edge model or in field map; this can have an impact on the optimisation of the lattice to achieve acceleration. PyZgoubi and dynamical map results with field map show good agreement for the tof curve, however there was a discrepancy in the horizontal tune for low energies. This is likely to be due to the inaccuracy for large particle excursions of the analytical representation of the magnetic field used for dynamical map and also to the limit of validity of the paraxial approximation for large excursions of the particles.

We then studied the range of validity in energy of the dynamical maps. We compared the tune and time of flight evolution with energy either by computing a dynamical map for different reference energy or by considering the energy dependence of the dynamics in a single map. We concluded that a single dynamical map computed up to

the 4^{th} order could be used to predict the time of flight and the tune within a range of about ± 3 MeV around the 14 MeV reference energy. Furthermore, plotting betatron ellipses around closed orbits at various energies with a single map led to the conclusion that the dynamical map needs to be computed up to the 9^{th} order to keep the symplectic error to an acceptably low value over that range.

We then looked at a nonlinear feature: the tune shift with amplitude. We first used the Frequency Map Analysis (FMA) technique to process numerical tracking results from PyZgoubi and the dynamical map of the EMMA cell for a reference energy of 19 MeV. We observed for both codes that the horizontal and vertical tune shift with amplitude was small (the tune changes by less than 10^{-4} for an action of 100 μm). The two codes agreed for the horizontal tune shift with amplitude but because of a difference of representation of the 3D magnetic field in PyZgoubi we observed a large discrepancy in the vertical plane. We studied in more detail the field experienced by particle following the same trajectory in the two codes and noticed that PyZgoubi represented inaccurately the nonlinear variation of the horizontal component B_x of the magnetic field present in the OPERA model. Since the dynamical map representation of the magnetic field agreed with the OPERA model, we concluded that the vertical tune shift with amplitude obtained from dynamical map was likely to be more accurate.

We then looked at a method allowing the evaluation of the tune shift with amplitude directly from the Lie Factorisation of the dynamical map. Comparing the results with the one obtained with FMA, we concluded that the agreement was good enough to derive this nonlinear feature of the dynamics directly from the map, without performing any tracking. However, when studying the same feature for a reference energy of 15 MeV for which the closed orbit excursion with respect to the reference trajectory is large, the discrepancy between the results from PyZgoubi and the dynamical map suggested that the paraxial approximation could limit the validity of the derivation of non-linear features from the dynamical map.

The next section was dedicated to the study of longitudinal dynamics. First, we looked at coupling between the longitudinal structure of a bunch of charged particles and its transverse dynamics. We studied the average horizontal position of a bunch of particles tracked through the EMMA cell not including any acceleration feature. Particles were launched with the same transverse position and angle, 3 mm off closed orbit but with different kinetic energies. The distribution of these energies was either uniform or Gaussian centred on the 14 MeV reference energy. Particles with different energies experience different focusing (and defocusing) strengths. Therefore after a certain number of turns, particles that had the same starting transverse position, do not oscillate around the stable orbit with the same betatron frequency. In transverse phase space, particles within a given bunch are spread around the betatron ellipse. Thus the average transverse position of the bunch corresponds to the centre of the ellipse and does not characterise the oscillations of particles around the stable orbit. We observed that the decoherence period does not significantly depend on the distribution.

Decoherence periods have been assessed for bunches with various widths of energy distribution tracked in PyZgoubi and dynamical maps. Codes agree on the damping period of about 7 turns for a Full Width at Half Maximum (FWHM) of 1.175% (measured value of the energy spread at the end of the injector line) and less than 4 turns for a FWHM of 2.35%. To measure the tune and the optic functions in the EMMA ring, the periodicity of the lattice is critical. If magnet random misalignments are large, then the lattice is not periodic and more data (i.e. more turns) are necessary to measured these features accurately. In that case the damping period is critical and efficient methods to process the measured position of the bunch had to be developed (e.g. NAFF). Simulations show that less than one turn could sufficient. First results of the commissioning tend to validate this statement since a measurement of the tune per cell with an accuracy of 0.01 is obtained using BPM measurements from seven consecutive cells.

We then derived the analytical model of the acceleration in a standard accelerator. Particles follow lines of constant Hamiltonian in the longitudinal phase space. Stable trajectories are represented by closed loops and correspond to bucket acceleration. Then we derived the analytical description of the serpentine acceleration, specific to the EMMA ring. By retaining a term in the Hamiltonian of 3^{rd} order in the energy deviation, we observed that particle could be accelerated by following lines in between the stable fixed points. In that way, a large amount of kinetic energy could be gained if the particles were extracted at the optimal moment. This analytical model was then compared to tracking results from dynamical map. We conclude that our simple implementation of acceleration is capable of reproducing the important characteristics of the longitudinal dynamics in EMMA.

In the last section, we applied the accelerating voltage to a distribution of particles and studied its representation in longitudinal and transverse phase space. We observed that a group of particles starting from the same transverse coordinates but with various energies and positions with respect to the reference trajectory, had different transverse positions after being accelerated from 10 MeV to 20 MeV within 8 turns. This illustrated that longitudinal and transverse dynamics are coupled in EMMA. Also the transverse size of the distribution was significantly increased by including the effect of the betatron motion of particle through acceleration.

We then draw the conclusion that simulation of acceleration with reasonable accuracy over the whole range of energy in EMMA required at least two dynamical maps with different reference energies and truncated to the 8^{th} order. For this study, we added a non zero transverse distribution to the group of particle.

Finally we found that the distortion of the transverse distribution of particles through acceleration between 10 MeV to 11 MeV was consistent with the resonance crossing predicted by the horizontal tune variation with energy computed with fixed energy. We then clearly observed the importance of the rate of acceleration when cross-

ing resonance by observing the strong distortion of the initial ellipse for an rf voltage of 0.55 MV.

To conclude this chapter, we must assess if the objectives have been fulfilled. Firstly, using dynamical maps to simulate the beam dynamics in an FFAG accelerator was challenging in terms of range of validity of this map. Indeed from 10 MeV to 20 MeV, the dynamics of particles such as the transverse excursion and the time of flight, varied significantly. We therefore studied the validity of the dynamical map by comparing tracking results with PyZgoubi using field maps. We concluded that using dynamical maps with different reference energies would allow an accurate description of the whole range of dynamics in EMMA. Using the canonical variable related to the energy deviation in each map reduces the number of maps needed to cover the whole energy range. We also showed that longitudinal dynamics such as serpentine acceleration and decoherence, could be simulated with dynamical maps.

Secondly, our objective was to demonstrate the benefits and the drawbacks of performing tracking studies with dynamical maps with respect to other tracking methods. A possible limitation is the effect of paraxial approximation on nonlinear dynamics. For particles with large excursion with respect to the reference trajectory, we could see discrepancies with PyZgoubi results. An alternative integration technique creating a dynamical map with a non straight line reference trajectory may be appropriate (but symplecticity may be an issue). On the other hand, we observed that the 3D analytical representation of the magnetic field used to construct the dynamical maps was more appropriate to study nonlinear feature of the vertical motion.

In addition, we proved by comparing with hard edge model results, that the use of field maps to model the EMMA cell was relevant. Tracking in dynamical maps was significantly faster than tracking in field map with PyZgoubi. The main benefit (in this chapter) of the dynamical map is that having obtained the map, any particle (i.e. with any initial values for the dynamical variables) can be tracked through a cell in "one

step"; in PyZgoubi, tracking a "new" particle must be done in small steps each time.

Finally when considering all the different lattices available by moving the magnets and changing their strength, PyZgoubi seemed to be rather inconvenient; a magnetic field map has to be created for each new configuration. This will be treated in the next chapter.

5

Application of the Dynamical Maps to Experimental Procedure

5.1 Interpolation between different EMMA lattices

5.1.1 Introduction

Having studied the dynamics in a given configuration of the lattice, it is interesting to find a way to extend the use of the dynamical map approach, to allow a range of different machine configurations to be easily modelled and compared. When using a hard edge model for the magnets, it is trivial to study any lattice by directly adjusting the parameters and performing the tracking study. However, the use of a field map is of a significant improvement in the lattice description; but then a different field map is needed for each configuration. This would mean that an accurate OPERA model would have to be solved each time a new lattice is tried requiring considerable computer time. During the commissioning of the machine a real-time simulation of the effect of a change in the lattice configuration is useful.

We solved a series of OPERA models with various lattice parameters. A grid of lattice configurations (including a range of magnet strengths and positions) is then

obtained and any configuration can be studied by interpolation within this grid. Beam dynamics for a given configuration can be interpolated from the dynamical map in explicit form (power series). However the symplecticity of the map is not preserved if no specific constraints are applied to the interpolation. To overcome this issue, we developed a routine performing the interpolation from the generating functions corresponding to the "solved" configurations. These two approaches will be discussed in this section.

5.1.2 Preparation of the field maps

To compute the dynamics for various lattice configurations, we first need to create each analytical representation of the field. Our starting point in the process is the OPERA model of the magnets. In chapter 2 section 2.2.4, we have seen that the field map of the entire cell could be created by superposition of the field maps with individual magnets powered. We assume that the magnetic field (in the vacuum chamber) induced by a magnet varies proportionally to the current in its coils. In other words, we assume that there is no magnetic saturation in the magnet yokes. This assumption allows us to consider that it is equivalent to multiply the field map obtained for one magnet by a given factor and to increase the current in the magnet by the same factor. Therefore when creating the field map for a lattice configuration in which the D magnet current is 90% of nominal current and the F magnet is 103% of the nominal current, we will superpose the field map from the D magnet multiplied by a factor A_d= 0.9 and the field map from the F magnet multiplied by a factor A_f= 1.03. However, the model for one magnet powered had to be solved including the unpowered yoke of the other magnet. This means that the distance between the magnetic axes of the magnets must still be taken into account.

Hence, we create OPERA models of the EMMA cell for distances between magnetic axes varying from 20 mm to 42 mm in 2 mm steps. These models are then solved with

one magnet powered and the yoke of the other magnet unpowered. When extracting the numerical magnetic maps, we consider the positions of the magnets with respect to the design polygon. From one model with a given distance between the magnets, several lattice configuration can be extracted. For instance X_f=6 mm/X_d=34 mm and X_f=10 mm/X_d=38 mm are two different configurations extracted from the same model (X_f and X_d being the position with respect to the polygon of the F magnet and D magnet respectively).

Dynamical maps with 14 MeV reference kinetic energy were computed for 300 lattice configurations: A_f and A_d were varied from 94% to 110% in 4% steps (so 5 configurations each), X_d was varied from 32 mm to 38 mm in 2 mm steps (4 configurations)and X_f was varied from 8 mm to 12 mm in 2 mm steps (3 configurations). We thus obtained a grid of configurations with 300 nodes (5x5x4x3). This process takes about 300 minutes for dynamical maps computed up to the 5^{th} order.

For the remainder of this chapter lattice configurations will be described as quadruples such as (102, 104, 6.4, 36.2) corresponding to a configuration where the focusing (F) and defocusing (D) magnets strengths are 102% and 104% of the baseline magnet strengths value respectively; and the F and D magnetic centres are displaced by 6.4 mm and 36.2 mm with respect to the reference polygon.

5.1.3 Approach with dynamical maps in explicit form

For a given lattice configuration, a dynamical map in explicit form (truncated power series) is computed as explained in the previous chapter. Dynamical maps up to the 8^{th} order are computed for each lattice configuration described above. We obtain a 4 dimensional grid for each coefficient of the dynamical map. We attempt to construct dynamical maps for lattice configurations between the known grid points by interpolating the coefficients of the Taylor series representations of the dynamical maps. In practise each coefficient is interpolated independently. Thus there are no constraints

to enforce symplecticity (to a given order) of an interpolated map, although the map at any grid points should have a small symplectic error (arising only from truncation of the power series).

5.1.3.1 Dynamics in the interpolated dynamical map

To discuss the validity of the explicit form interpolation, we compared the beam dynamics resulting from an interpolated map with the dynamics from the directly computed map for the same lattice configuration. The expected worst case scenario for the interpolation is when the point is located far from the mesh nodes in the 4 dimensional grid. The lattice configuration (100, 100, 7, 35) has been chosen because it is located half way between two nodes in all directions and moreover it is close to the baseline lattice configuration (100, 100, 7.514, 34.048). Beam dynamics for various energies are computed in a single map by using different values for the energy deviation. As described in section 4.3.1.2 of chapter 4, this approach is satisfactory for energy deviations up to 15% when considering a map with 14 MeV reference energy computed to the 9^{th} order. If we want a more accurate description of the dynamics over the whole range of energies, a 4 dimensional grid of dynamical maps should be derived for each reference energy. As a first approach, considering the amount of computing time necessary to create all the dynamical maps, in the following we limit ourselves to a grid with a single reference energy.

In figure 5.1, we observe that the horizontal tune extracted from the coefficients of the interpolated map (eigenvalues expressed as function of the energy deviation variable) is in good agreement, to within less than 0.01, with the directly computed model. The results from these two methods regarding the vertical tune shows a slightly larger discrepancy (of the order of 0.01), of the order of the expected measurement precision.

In figure 5.1.b, for 20 MeV, the time of flight obtained from the interpolated power

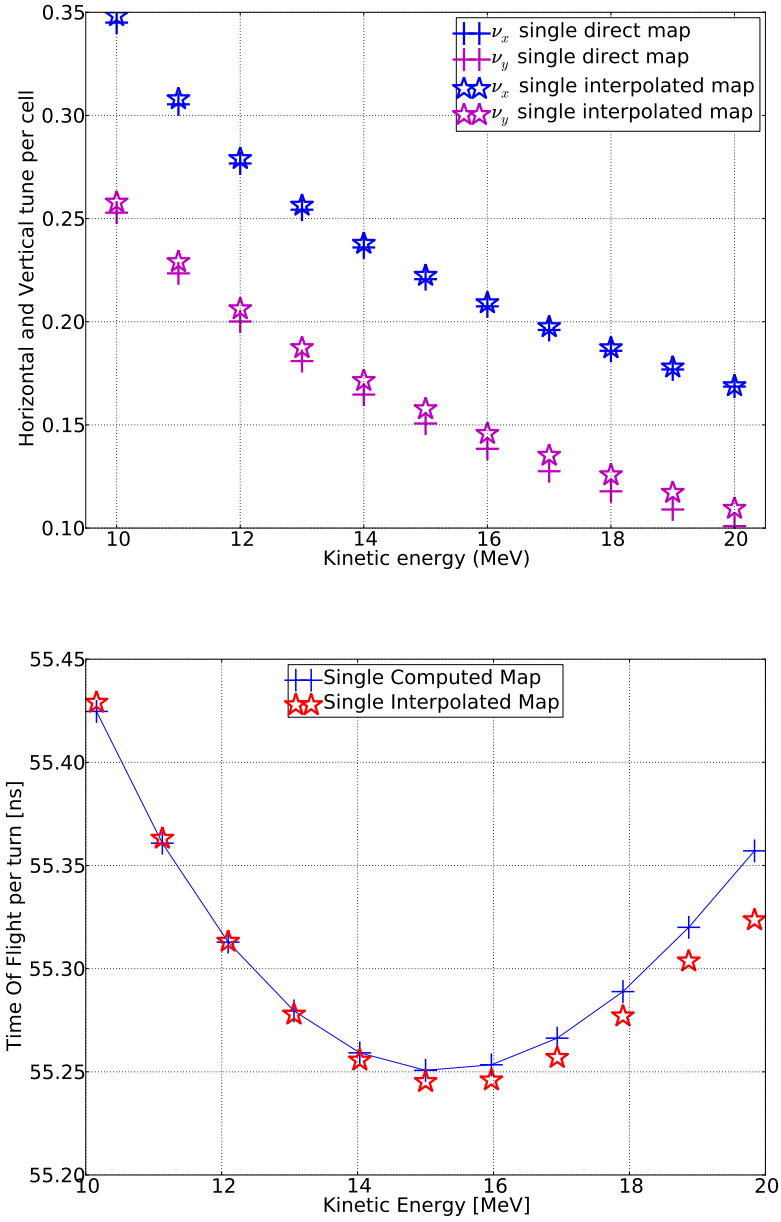

Figure 5.1: Top: Variation of horizontal (blue) and vertical (purple) tune per cell with energy. There is good agreement in the horizontal tune between the directly computed and interpolated dynamical maps in power series form. Results are obtained from dynamical maps with 14 MeV reference energy in both case. There is a discrepancy of the order of measurement precision in vertical tune. This error increases with energy. Bottom: Variation of time of flight with energy. A large discrepancy (35 ps difference at 20 MeV) between computed and interpolated solution is observed for high energy.

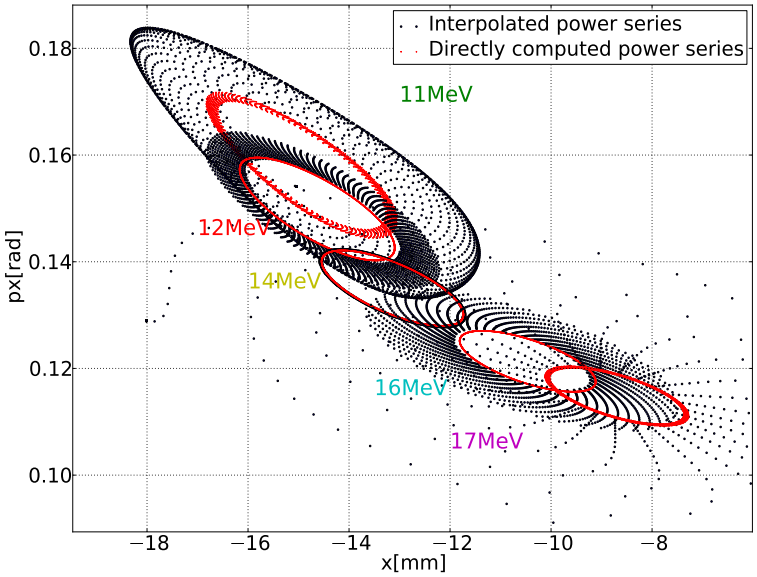

Figure 5.2: Betatron motion for various value of the energy deviation in a dynamical map of order 8 with reference energy 14 MeV compared with dynamical maps with different reference energies. A strong non symplectic behaviour is observed for non zero values of the energy deviation in the interpolated map

series is about 35 ps smaller than for the directly computed map. Since a better precision is expected for the machine measurement, we conclude that substantial errors in the power series are introduced by this interpolation method, and the results obtained from the interpolated map are not satisfactory regarding the evolution of the time of flight with energy.

In addition, the beam dynamics shows evidence of non symplectic behaviour. Figure 5.2 shows the betatron motion of particles launched off the closed orbit for various energies, similar to figure 4.7(a) in chapter 4; the reference energy is 14 MeV. We observe a good agreement between the directly computed map ellipses in red and the interpolated map tracking in blue for the reference energy 14 MeV. However, the ellipses shapes are lost for the interpolate map at 12 MeV and 16 MeV (±15% energy deviation). The position of the particles spirals out with respect to the centre of the ellipse in

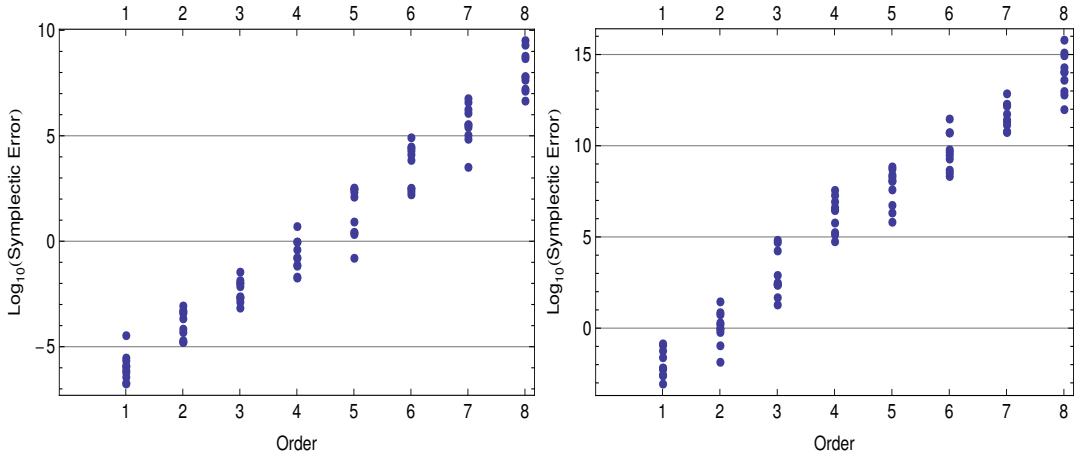

Figure 5.3: Symplectic error for a directly computed map (l.h.s) and interpolated map (r.h.s) in explicit form. Both maps are truncated at order n (≤ 9) and therefore the Jacobian can be computed to order $n-1$ (≤ 8). In both case the error grows exponentially (linearly in logarithmic scale) with the truncation order. Also, we observe that the maximum symplectic error (over all coefficients at each order) is about 5 order of magnitude higher for the interpolated map than for the computed map. This can explain the discrepancy observed in terms of time of flight and betatron motion (see fig 5.1.b and fig 5.2).

successive turns. In the case of a symplectic transformation, the action J of a particle is conserved. In one degree of freedom, the area of the phase space ellipse traced out by the particle is equal to πJ and is therefore invariant. This seems not to be the case for the interpolated map which may thus have a strong symplectic error.

It is interesting to evaluate in a more quantitative way the relative symplecticity of these two approaches (directly computed and interpolated).

5.1.3.2 Symplectic error

Symplecticity is defined in terms of the Jacobian J of the map. If we consider a transformation $\vec{X}$ acting on vector of canonical variables $\vec{x}$, the Jacobian is expressed as:

$$J_{ij} = \frac{\partial X_i}{\partial x_j} \tag{5.1}$$

with i and j varying from 1 to 6 corresponding to the six canonical variables. We notice that if a transformation is expressed as a power series truncated at order n, the Jacobian will be a polynomial of order $n-1$ (after differentiation of the map). The transformation (or map) is symplectic if:

$$J^T \cdot S \cdot J = S \tag{5.2}$$

where S is a 6×6 block-diagonal constructed from 2×2 antisymmetric matrices S_2:

$$S_2 = \begin{pmatrix} 0 & 1 \\ -1 & 0 \end{pmatrix} \tag{5.3}$$

It is possible to characterise the symplectic error in terms of the components of the matrix Δ defined as:

$$\Delta = J^T \cdot S \cdot J - S \tag{5.4}$$

For a dynamical map expressed in power series form truncated to order n, each term of the Jacobian J_{ij} in equation 5.1 is a polynomial in the canonical variables. Thus the components of the matrix $J^T \cdot S \cdot J$ are also expressed as polynomial functions. To evaluate numerically the components of the matrix Δ, we must replace the variables by some values; these values can be chosen arbitrarily. We expect the Taylor series to be valid if the coordinates x, y and z take values much smaller than 1 m, and if the momenta p_x, p_y and δ are each much smaller than 1. Therefore we can consider an "extreme" case to be one where all variables take value equal to 1.

In figure 5.3, each point corresponds to a component of the matrix Δ computed for various truncation orders for the directly computed map and the interpolated power series on the left hand side and right hand side respectively. We focus on the maximum value of this difference for each truncation order. In the case of the computed map the

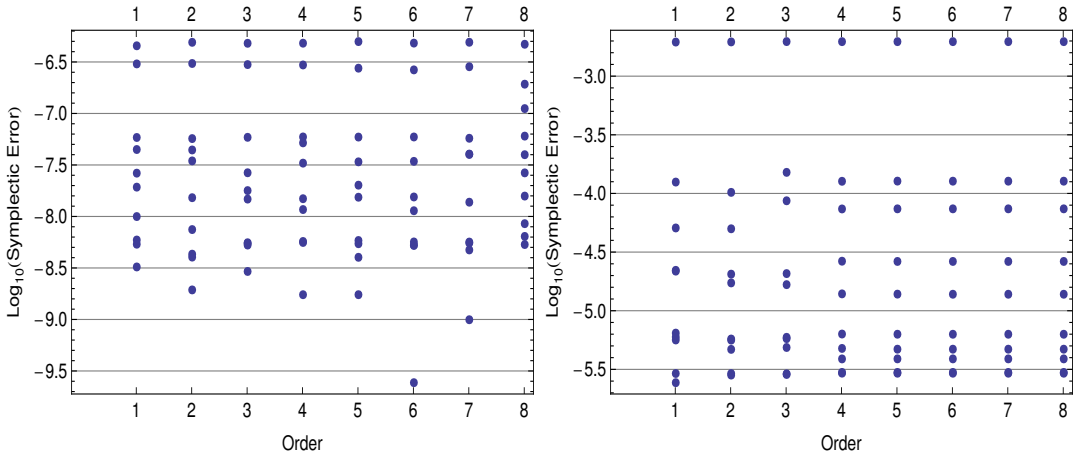

Figure 5.4: Symplectic error for computed map (l.h.s) and interpolated map (r.h.s) in explicit form. The canonical variables are set to the value 0.01 and 0.001 respectively. We observe that the symplectic error remains constant with a maximum around 10^{-6} for the computed map and 10^{-3} for the interpolated power series. The range of magnitude of the variables allowing an increase of the truncation order without losing symplecticity is reduce by a factor 10 when using an interpolated power series. In addition, the value of the symplectic error is three orders of magnitude larger for an interpolated map than for a computed map.

difference ranges from about 10^{-5} for the truncation at first order to about 10^{10} for the truncation at the 9^{th} order in the map. In the case of the interpolated map the difference ranges from about 10^{-1} for the truncation at first order to about 10^{16} for the truncation at 9^{th} order in the map. We observe in both cases an exponential growth (linear in logarithmic scale) of this difference when increasing the truncation order; however the value is consistently five orders of magnitude larger for the interpolated map.

Since the choice of the numerical value of the variable was arbitrary, the vertical axis of the two plots do not have an explicit meaning. Instead we can adjust the value given to the variables (being the same for each of the six variables) such that the symplectic error remains constant when increasing the truncation order. Figure 5.4 shows the symplectic error of the directly computed map (l.h.s) and the interpolated power series (r.h.s) when setting the six canonical variables to the value 0.01 and 0.001 respectively.

We observe that the symplectic error remains constant with a maximum around 10^{-6} for the computed map and 10^{-3} for the interpolated power series. For these ranges of values higher orders in the map appear to increase the symplectic error.

The range of magnitude of the variables allowing an increase of the truncation order without losing symplecticity is reduced by a factor 10 when using an interpolated power series. In addition, the value of the symplectic error is three orders of magnitude larger for an interpolated map than for a directly computed map. The difference in symplectic error between the directly computed map and the interpolated power series is not surprising since when interpolating the coefficients independently, no special care was taken to preserve the symplecticity. Not preserving symplecticity may partly explain the discrepancies observed in figure 5.1 and figure 5.2 in terms of tune and time of flight variation with energy and betatron motion.

Note that these values (0.01 and 0.001) are not strict upper limits for tracking simulations; the symplectic error introduced by high orders can still be considered small enough for larger values of the dynamical variables; also simulations may be accurate for a truncation order lower than 9^{th} order.

These results obtained by interpolating the dynamical map in explicit form are not fully satisfactory, because of the loss of symplecticity. It is therefore of interest to develop this process a step further to obtain a dynamical map with lower symplectic error.

5.1.4 Interpolation of generating functions

Using a COSY infinity routine, it is possible to construct a generating function (gf) that reproduces the map of order n from any dynamical map expressed in the form of a power series of order n [47,45]. A gf is not in explicit form (i.e. it cannot be used directly for particle tracking), however a map represented in the form of a gf is necessarily symplectic. It can be reconverted to a power series such that the symplectic

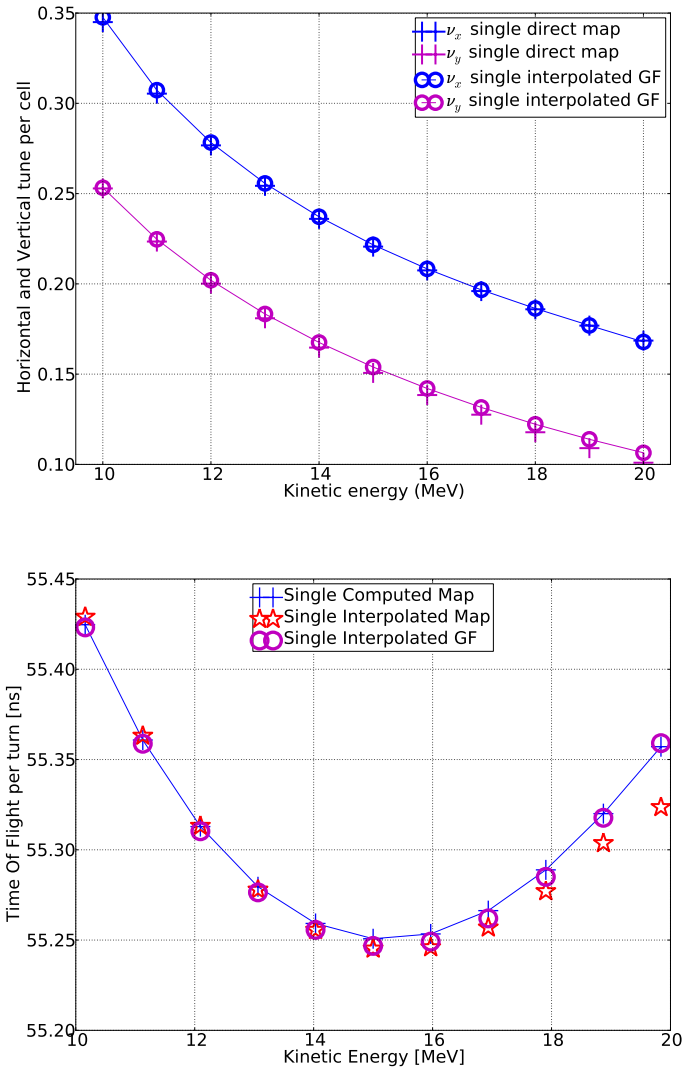

Figure 5.5: Top: horizontal (blue) and vertical (purple) tune per cell for closed orbit at various energies. The comparison between directly computed power series and power series derived from interpolated generating functions shows a better agreement than with interpolated power series, especially for the vertical tune (see fig. 5.1). A slight discrepancy is still present however it is below the measurement precision threshold of 0.1. Bottom:Variation of time of flight with energy. We observe a good agreement between the computed map and the map from interpolated generating function. The discrepancy observed previously with the interpolated power series is corrected.

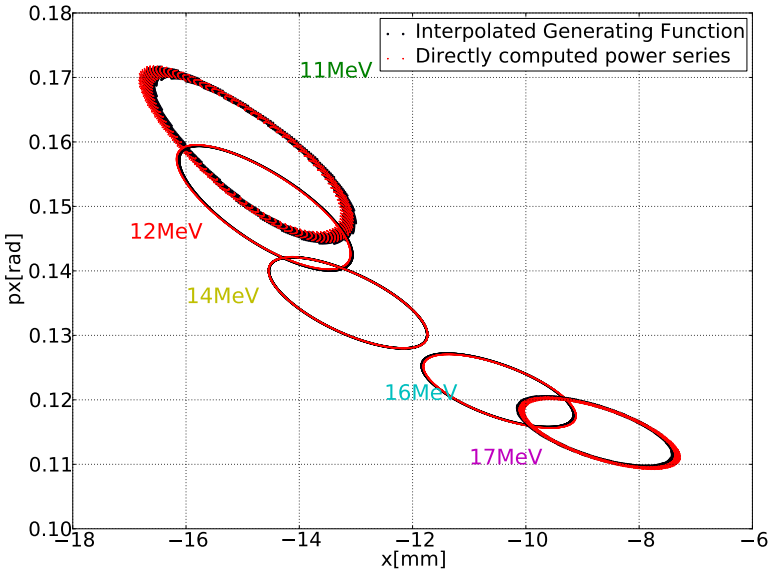

Figure 5.6: Betatron motion with multiple dynamical maps order 8 for five energy deviations with 14 MeV reference energy. For the computed map (red) and the map derived from interpolated gf (blue), effect of non symplecticity occurs for energy deviation of 3 MeV (20%). We observe that even the non symplectic behaviour is similar in both cases.

error of the final power series is smaller than the original one.

To solve the problem of symplecticity encountered in the previous section, the idea is here to interpolate the coefficients of the gf for a given lattice and compute the corresponding dynamical map in explicit form. A four dimensional grid of generating functions is created from the power series grid created previously.

5.1.4.1 Dynamics in the interpolated generating function

Figures 5.5 shows the horizontal and vertical tunes and times of flight of closed orbits for various kinetic energies obtained from a directly computed power series and from a power series derived from an interpolated generating function. The reference energy is still 14 MeV. Horizontal and vertical tunes obtained from the interpolated generating function agree more closely with the computed power series than does the interpolated

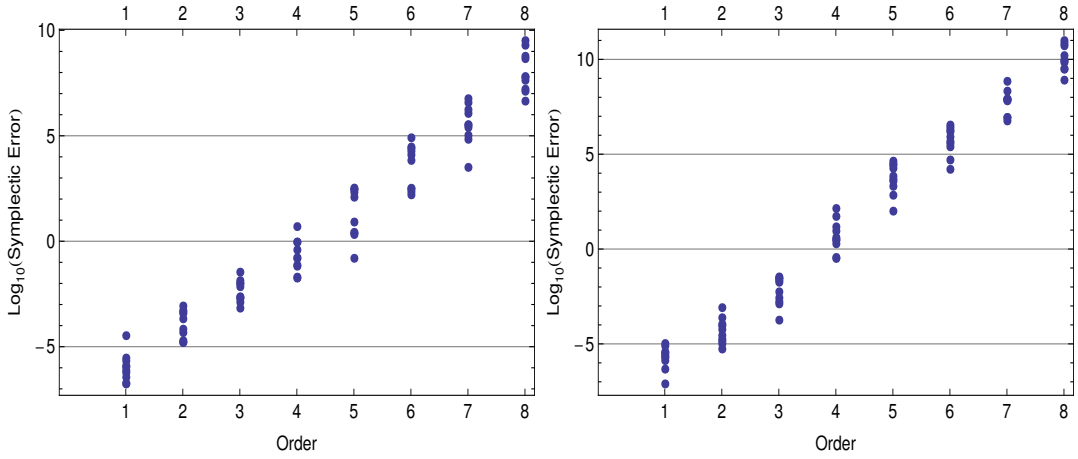

Figure 5.7: Symplectic error with respect to the order included in the calculation for computed map and map derived from interpolated generating function. The agreement between the two plots confirms the preservation of symplecticity when interpolating the lattice configuration from generating function.

power series in fig 5.1 (these points are also shown again in figure 5.5 for comparison). The discrepancy is still below the measurement precision threshold. The evolution of time of flight with energy computed from the interpolated generating function matches the direct computation for the whole range of energy.

We observe also that the transverse horizontal phase space representations of the betatron motion around reference trajectories for 11, 12, 14, 16 and 17 MeV (Fig. 5.6) agree. In both cases (computed power series and interpolated gf), non symplectic behaviour (a steady "spiralling out" of the particle in phase space) appears for energy deviations larger than 15% (2 MeV deviation from 14 MeV reference energy).

These results seem to justify the choice of interpolating the coefficients of the gf rather than those of the power series. Similarly we must evaluate the symplectic error of a map derived from an interpolated gf.

5.1.4.2 Symplectic error

As we did in section 5.1.3.2, we compute the Jacobian of the map derived from the interpolated gf using equation 5.1. We then evaluate the coefficients of the matrix Δ to

characterise the symplectic error. First the dynamical variables are set to unit values. In the results presented in figure 5.7, symplectic error in the directly computed map (l.h.s.) and in the map derived from interpolated gf (r.h.s.) have similar evolutions while increasing the truncation order. The symplectic error of the latter is 4 orders of magnitude smaller than the symplectic error in the interpolated power series (r.h.s in figure 5.3).

In addition, we evaluate the symplectic error setting the canonical variables to 0.01 for the computed map and 0.007 for the interpolated gf. We observe in figure 5.8 that in both cases maximum values for the coefficients remain close to 10^{-6} when increasing the truncation order. The value of the variables in the case of the interpolated gf being slightly smaller, we conclude that the symplecticity achieved by this method is not as good as the original computed map, however there is a significant improvement compared to the interpolated power series whose symplectic error was 10^{-3} for canonical variables set to 0.001.

5.1.4.3 Summary

In this section, we looked at the construction of a dynamical map for any chosen lattice configuration interpolating between a grid of computed dynamical map. When interpolating the coefficients of the map in explicit form (power series) we observed a discrepancy of the order of the expected measurement precision in the tune per cell evolution with energy with results from the directly computed map. A significant discrepancy appeared at high energy in the time of flight and for large energy deviation in the betatron motion. We derived a numerical evaluation of the symplectic error outlining the loss of symplecticity resulting from this method of interpolation.

We then studied the beam dynamics results obtained from a map in explicit form derived from an interpolated gf. The agreement (with directly computed map) in terms of tune and time of flight evolutions with energy and betatron motion was within the

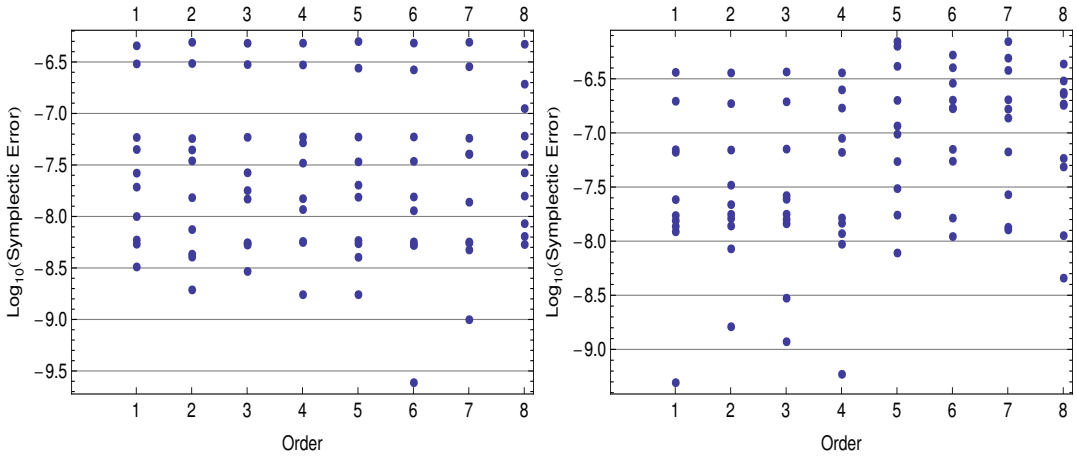

Figure 5.8: Symplectic error with respect to the order of terms included in the calculation for a directly computed map and a map derived from interpolated generating function. The agreement between the two plots confirms the preservation of symplecticity when constructing the map by interpolating between gf for known lattice configurations.

expected measurement precision. We then observed that the symplectic error of the map built by this method was of the same order of magnitude as the directly computed map.

We conclude that the interpolation of the gf is a more suitable method since it preserves symplecticity. It also reproduces more accurately the beam dynamics results of a directly computed map. The reason for such an improvement in the description of the beam dynamics may not simply lie in the decrease of the symplectic error and is an interesting issue for future further investigation.

Eventually, we will see in the next section that this technique can be useful when looking for the lattice that fulfils requirements regarding (for example) tune and time of flight. By developing a routine that finds by interpolation the lattice corresponding to a chosen set of constraints, we create a powerful tool for the commissioning of the machine both to define a suitable working point and to estimate from measurements the errors in the lattice (e.g. magnet strengths and positions).

5.2 Application to the EMMA experiment

5.2.1 Experimental setting

The beam injected into EMMA is driven from the electron gun to the EMMA ring by the ALICE accelerator. Ideally the beam could be injected into EMMA at any energy between 10 MeV and 20 MeV. However ALICE is a complex accelerator because it is used for several other experiments [64]. It has been commissioned only relatively recently and the injected beam still has limited flexibility. To ensure the stability of the beam and the reproducibility the experiment, the injector was optimised to inject the beam in EMMA with a fixed kinetic energy of 12 MeV (equivalent to fixed beam momentum of 12.511 MeV/c, c being the speed of light).

However the EMMA lattice is characterised by linear dynamics for several fixed energies (i.e. without acceleration) from 10 MeV to 20 Mev. We therefore used the fact that a decrease in the strength of the magnets is equivalent in terms of beam dynamics to an increase of the beam momentum. This can be proved by looking at the general expression of the Hamiltonian given by:

$$H = \frac{\delta}{\beta_0} - \sqrt{\left(\frac{1}{\beta_0} + \delta - \frac{q\phi}{P_0 c}\right)^2 - (p_x - a_x)^2 - (p_y - a_y)^2 - \frac{1}{\gamma_0^2 \beta_0^2}} - a_z \,, \tag{5.5}$$

where the normalised vector potential $\mathbf{a}$ is defined by:

$$\mathbf{a} = q\frac{\mathbf{A}}{P_0} \,. \tag{5.6}$$

P_0 is the reference momentum. We see here that it is equivalent for the Hamiltonian in (5.5) (i.e. for the dynamics) either to half the vector potential $\mathbf{A}$ or to multiply the reference momentum P_0 by a factor two. In practise, this equivalence is valid if the relative magnitude of the magnets multipole components remain constant when varying the current in the coils; this feature of the magnets will be evaluated experimentally

by optimising ALICE to inject at other fixed energies. Equivalent and real energies dynamics will then be compared.

To give an example, let us take the baseline lattice for which the nominal current in the magnets should be: 350 A for the defocusing magnet and 320 A for the focusing magnet. Decreasing both currents by 20% (to 280 A and 256 A respectively) is equivalent to studying the same lattice with a beam with 20% higher momentum (15 MeV/c). Hence, even if the real momentum is fixed at 12.5 MeV/c, we can study a given lattice configuration for various momentum keeping the same ratio between the magnet currents.

Note that the time of flight measured for an equivalent energy needs to be corrected by the relativistic beta factor to reflect the time of flight for real energy. For instance the relativistic factor for electrons at 12 MeV and at 16 MeV is $\beta = 0.998817$ and $\beta = 0.99952$ respectively. The time of flight t_{eq} measured with equivalent energy 16 MeV (while the real energy from the injector is 12 MeV) is related to the real time of flight at 16 MeV t_{real} by:

$$t_{real} = \frac{0.9952}{0.998817}\, t_{eq}\,. \tag{5.7}$$

The effect of this correction is shown in figure 5.9.

5.2.2 Time of flight measurement

We shall now present the measurements of the tof evolution with energy for various lattice configurations. The tof is measured using the beam position monitors (BPMs) [69], composed of four electrodes (or "buttons") located on the beam pipe; each buttons detects the change in electric potential when a bunch passes nearby, the closer is the bunch, the stronger is the change in potential. The time between two consecutive signals observed on a scope connected to one button corresponds to the revolution time of a bunch in the ring (i.e. tof for one turn)

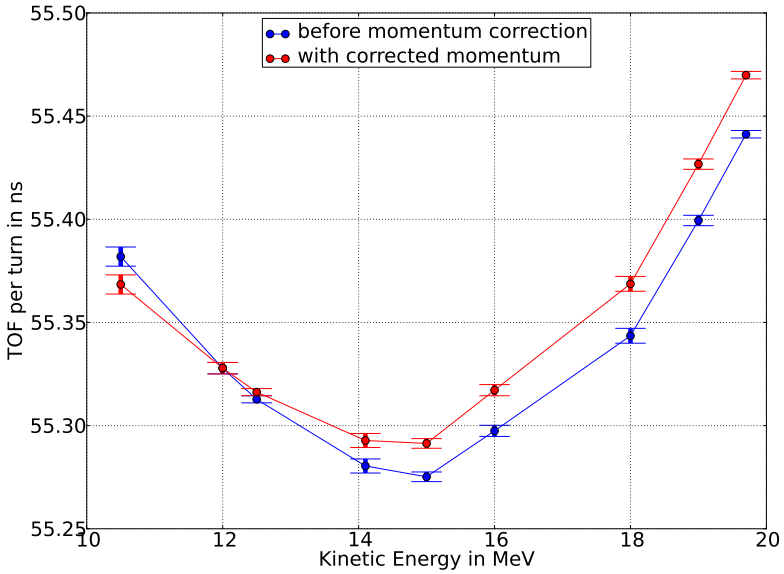

Figure 5.9: Measurements of the tof for one turn in EMMA for various equivalent momenta without correction of the real velocity (blue line) and with correction described by equation 5.7. This correction modifies the tof by up to 30 ps at high energy (20 MeV) and must therefore be taken into account when comparing simulations for real momenta and measurements for equivalent momenta.

To perform a precise tof measurement, a reliable time reference is needed. A sinusoidal clock signal (part of the low level rf system) is used as reference for the rf wave generator in the ALICE accelerating cavities [18, 19]. The rf frequency is 1.3 GHz; therefore an rf period lasts 0.77 ns. We can estimate the tof for one turn in EMMA, by counting the number of rf period for each turn of the beam; hence this clock signal can be used as reference for the tof measurements.

Figure 5.10 shows the ALICE rf signal in blue and the signal from a bpm in the ring in red. Each peak corresponds to one pass of the beam and the time between two peaks is the time of flight for one turn. The 1.3 GHz oscillations can be seen by zooming on this plot (see figure 5.10 (b) and (c)). Note that the oscillations of the blue trace between -0.08 V and 0.06 V in figure 5.10 (a) are due to electronic noises from other devices present in the accelerator room.

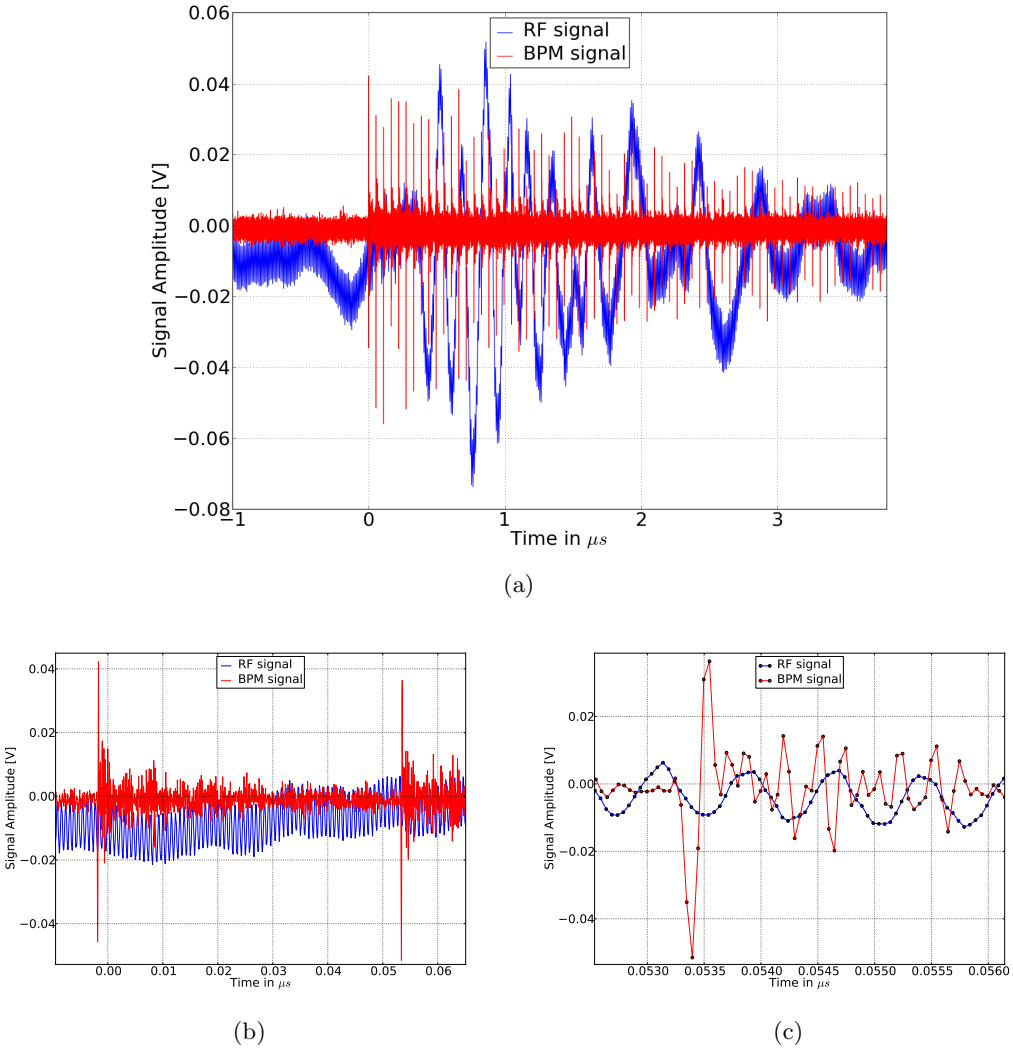

Figure 5.10: (a) Waveform exported from the oscilloscope reading signals coming from devices located in the ring. In red the raw signal from one BPM in the ring. Each vertical spike corresponds to one turn in the ring. The time difference between two spikes is therefore the time of flight for one turn. The 1.3 GHz rf signal is represented in blue. Electronic noise from other devices in the accelerator room is superposed to the sinusoidal signal at 1.3 GHz. The oscillation can be seen by zooming on this plot (b) and (c). Each period is 0.77 ns. First the tof is measured by counting the number of oscillation between two red spikes in (b). Then the position of the spike is read within one oscillation in (c).

A python routine [74] processes the numerical data extracted from the scope for these two traces and counts the number of rf oscillations (detecting the zero-crossing in the positive slope of each period), between two BPM signals. It is possible to refine this measurement evaluating the position of the BPM signal within one rf oscillation. The precision is related to the sampling speed of the scope. The scope used had a frequency of measurement of 20 GHz meaning that each rf oscillation contains 15.3 measurements which allows a precise reconstruction of the sinusoidal signal. We estimate that the zero crossing with positive slope of the signal is obtained with a precision of the order of 50 ps.

To increase the precision, we can measure the tof of particles over several turns. Without acceleration the variation of the tof, mainly due to beam losing energy through beam loading in the cavities, is negligible. The limitation in the number of turns available is the amplitude of the signal detected by the BPM decreasing due to beam loss; 20 turns are used in this case.

With 20 turns, the relative error of measurement within one rf period is divided by 20 with respect to the relative error with one turn. For instance if the time of flight of the beam for one turn is 55.35 ns, the measurement within one turn is 55.35 ns $\pm$ 0.05 ns whereas the measurement over 20 turns will be $55.35 \times 20 = 1107$ ns ± 0.05 ns since the precision is still linked to the position of the peak in the rf oscillation. The time of flight over 20 turns is then divided by 20 and the result over one turn is in the range of [1106.95/20, 1107.05/20]= [55.3475, 55.3525]. The precision of the measurement is then ± 0.0025 ns. The number of turn considered for the measurement had to be seen the same for all the measurements. Since the beam was lost in a few turns when injecting at certain equivalent energy, we had to limit the number of turn taken into account in the measurement to 10. The measurement precision was then of ± 0.005 ns.

Each measurement is made taking a snapshot of the scope signal and processing the data. Each bunch coming from the injector ALICE may has slightly different momen-

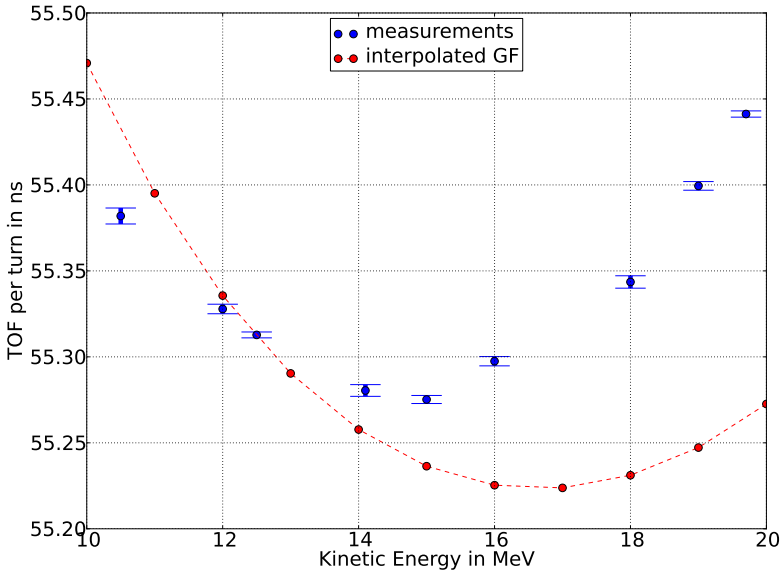

Figure 5.11: Comparison between measurements and simulations of the time of flight variation with energy for this lattice configuration. We observe that the measured lattice has a minimum time of flight of 55.275 ns at 15 MeV whereas the simulated lattice has a minimum time of flight of 55.225 ns at 17 MeV.

tum, energy spread or transverse position because of rf phase jitter or different electron gun conditions; therefore several snapshots are saved for each tof measurements. In the following section, we plotted the mean value and the standard deviation (error bar) for sets of eight measurements.

5.2.3 Comparison between measurements and simulations

Note that from the magnetic field measurements in the ring magnets, it has been found that the currents corresponding to the nominal (i.e. for the baseline lattice configuration) integrated gradients were 310.32 A for the D magnet and 262.68 A for the F magnet; hence the nominal ratio of magnet strength is 1.18. As explain in section 5.2.1, the kinetic energy of the injected beam from ALICE is fixed (12 MeV). The time of flight variation with energy is studied by decreasing the magnet strengths conserving

the same ratio between them.

In practise, we looked for a magnet strength ratio for which injection was good (many turns before the beam signal is lost on the scope) over a wide range of equivalent energies. With a magnet strength ratio of 1.12 and moving both magnets outward by 2 mm with respect to their nominal positions, we managed injection from 11 MeV equivalent to 20 MeV equivalent.

We used the generation function interpolation routine to simulate the beam dynamics of this lattice configuration. Figure 5.11 shows the comparison between measurements and simulations of the time of flight variation with energy for this lattice configuration. We observe that the measured lattice has a minimum time of flight of 55.275 ns at 15 MeV whereas the simulated lattice has a minimum time of flight of 55.225 ns at 17 MeV. We conclude from this discrepancy that the actual measured lattice contains error in magnet strengths and positioning not taken into account in the simulation, that changes the time of flight variation with energy. In other words, there appears to be some significant systematic difference between the machine and the model.

The next step consists in using the grid of lattice configurations to find which simulated lattice corresponds to the measurements. To do so we use an optimisation routine based on the interpolation method described in section 5.1 to look for a simulated lattice configuration that matches four constraints defined by the time of flight measurements at four different energies.

5.2.4 Prediction of the lattice configuration from the optimisation routine

The time of flight evolution with energy has been measured for various EMMA lattices. The aim of the section is to compare the measurements to the results obtained with an optimisation routine written in Mathematica using the simplex method [72,73,75].

5.2.4.1 Time of flight variation with magnets transverse displacement

For each lattice configuration of the grid, we use the dynamical map to compute the tof of the closed orbits from 10 MeV to 20 MeV, varying the energy deviation. In many lattice configurations, especially close to the edges of the grid, no closed orbit could be found for energies higher than 18 MeV; therefore the time of flight could only be interpolated between 10 MeV and 18 MeV.

Note that finding the closed orbits and extracting the tof for 9 energies for 300 configurations takes about 20 seconds using the dynamical maps whereas the same tasks takes more than 4 hours with numerical tracking in 300 numerical magnetic field maps with PyZgoubi. Considering only the computation of the time of flight and including the 300 minutes to compute the grid of dynamical maps, both codes seems to be equivalent in terms of computing time. However, to compute the tof for a different energy than the 9 energies already computed, it takes about half an hour (4 hours/9) with PyZgoubi and a few seconds with dynamical maps. Moreover in order to compute any other characteristic of the dynamics such as tune and dispersion, only a few tens of seconds will be needed with dynamical maps since information are already contained in the coefficients of the map, whereas another few hours would be necessary by numerical tracking in PyZgoubi.

The created grid of tof for all the lattice configurations between 10 MeV and 18 MeV is used by the optimisation routine to find the lattice that most closely matches the tof measurements from the EMMA accelerator.

Figure 5.12 shows the result of the comparison between measurements and simulations from the lattice configuration found by the optimisation routine. The measurements were performed with a magnet ratio of 1.12 and both magnets moved outward by 2 mm with respect to their nominal positions (same as section 5.2.3). The experimental lattice, referenced as E_1 is written according to the notation explained in section 5.1.2 of this chapter as: (A_f =105.6%, A_d =100%, X_f =9.51 mm, X_d =36.048 mm). From the

tof measurements (blue dots with error bars) four constraints (green triangles) are defined for the optimisation routine; the lattice S_1 found by the routine is : (94.30, 100.02, 11.56, 34.00). The time of flight for a range of energy between 10 MeV and 20 MeV is then computed for this lattice (red dashed line) from the interpolated generated function for the corresponding lattice. It shows good agreement with measurements with a maximum discrepancy of about 20 ps at 10.5 MeV. All the other measurements agree within less than 10 ps; another measurement for an energy close to 11 MeV would be useful to confirm the discrepancy.

Lattices S_1 and E_1 are then compared in terms of tune per cell. The experimental values of the tune is obtained from the orbit transverse position (given by BPMs around the ring) by the NAFF method [55]. We observe in figure 5.13(a) that there is a relatively good agreement for the horizontal tune (in red) for energies smaller than 16 MeV. The simulated vertical tune (green circles on line) is significantly larger than the measurement (green stars), especially for large energy. Note that the simulated tune is computed from a single dynamical map with a reference energy of 14 MeV which is not as accurate as the simulation with several maps with different reference energies.

Comparing this figure 5.13(a) with figure 4.2 in chapter 4, we observe that computing the tune from maps with different reference energies gives smaller values for the tune at high energy. This may explain part of the discrepancy. In order to interpolate a generating function with a different reference energy, a new grid of dynamical maps must be computed for each energy.

Instead we can solve the OPERA model for the lattice configuration found by the routine, derive the analytical representation of the magnetic field and directly compute the dynamical maps with different reference energies. The agreement between measurements and multiple computed map simulations is lower than 0.005 for the horizontal tune (see figure 5.13(b)); the simulated vertical tune is still larger than the measurement however the discrepancy is significantly reduced at high energy.

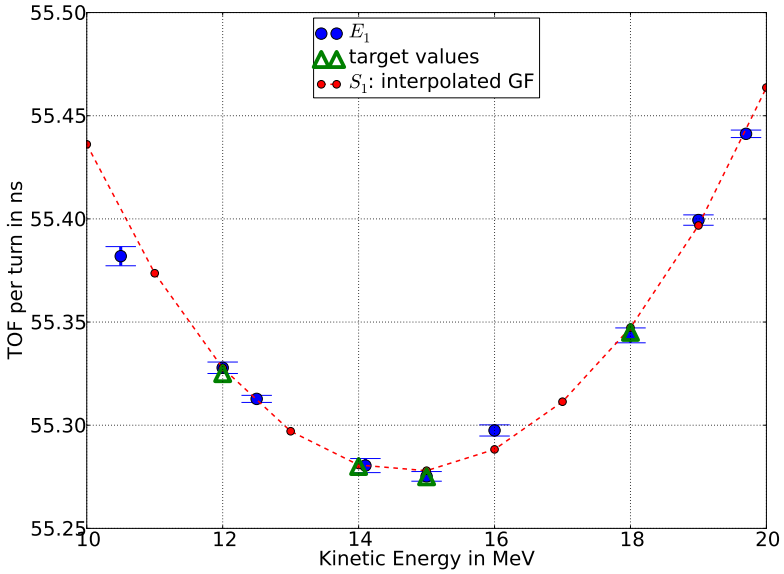

Figure 5.12: From the tof measurements (blue dots with error bars) four constraints (green triangles) are defined for the optimisation routine; the lattice S_1 found by the routine is : (94.30, 100.02, 11.56, 34.00). The time of flight for a range of energies between 10 MeV and 20 MeV is then computed for this lattice (red dashed line) from the interpolated generated function for the corresponding lattice. It shows good agreement with measurements with a maximum discrepancy of about 20 ps at 10.5 MeV.

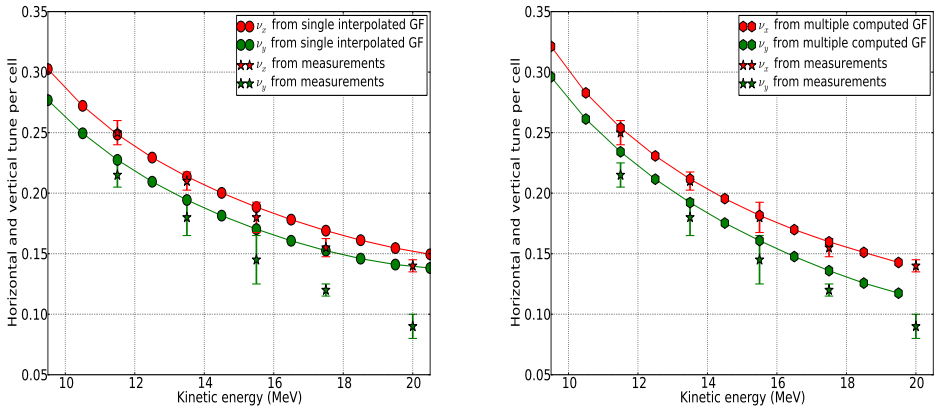

(a) (b)

Figure 5.13: (a):Lattices S_1 (circles) and E_1 (stars) are compared in terms of tune per cell. The experimental value of the tune is obtained by the NAFF method [55]. There is a relatively good agreement for the horizontal tune (in red) for energies smaller than 16 MeV. The simulated vertical tune is significantly larger than the measurement, especially for large energy. The simulated tune is computed from a single with a reference energy of 14 MeV.(b) Same as (a) but the simulation results are obtained with multiple maps with different reference energies. The discrepancy is significantly reduced, especially for the vertical tune at high energy.

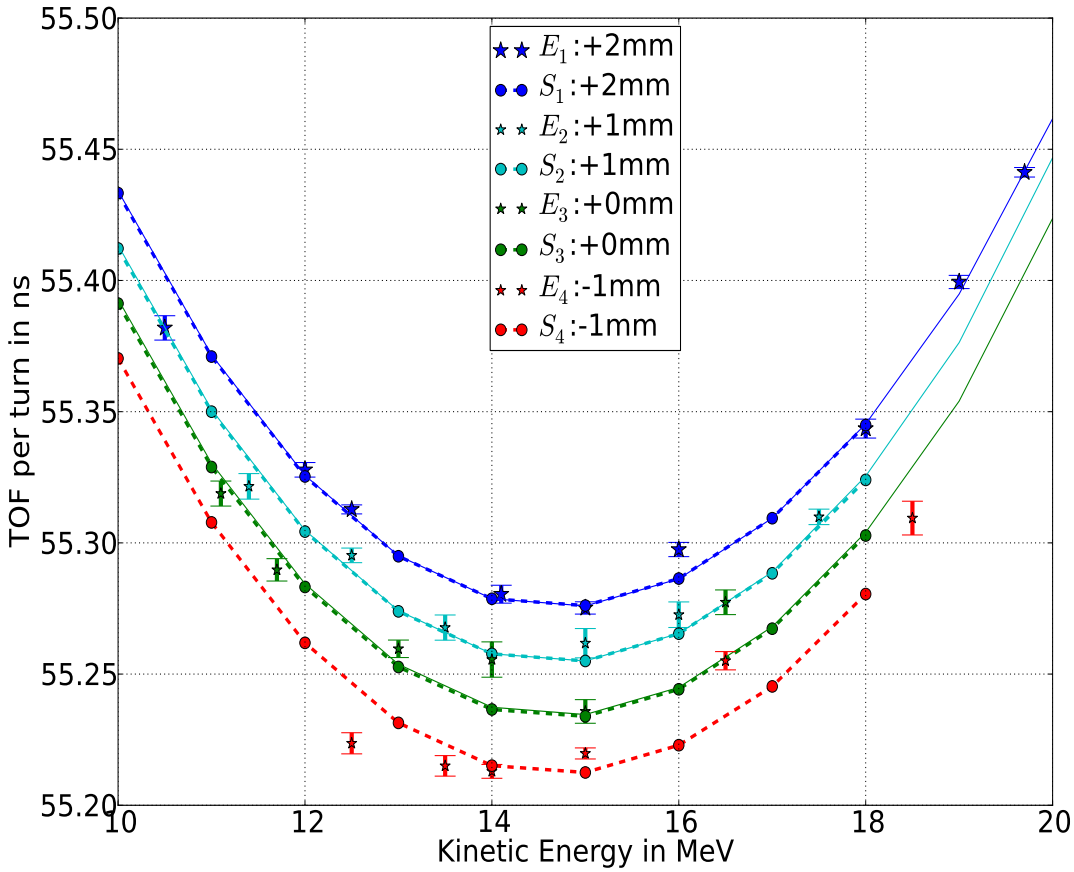

Figure 5.14: Comparing the experimental result to the simulated results, we observe that for lattices 1, 2 and 3, the agreement is within 20 ps apart from some specific measurements for which the actual kinetic energy of the beam coming from ALICE might not have been 12 MeV exactly because of rf phase jitter and electron gun instabilities. The discrepancy for the fourth lattice is larger and can be explained by the fact the configuration is outside the grid requiring an extrapolation of the data. However there is agreement on the minimum value of 55.22 ns between 14 MeV and 15 MeV; this value is important to evaluate the optimal rf frequency of the cavity to achieve acceleration.

We conclude that the lattice found by the optimisation routine to match the measurement agrees also with the measurements of the horizontal tune at various energies. This is a interesting result since it gives confidence in the use of the optimisation routine not only to characterise longitudinal dynamics but also to investigate the transverse dynamics such as resonance crossing.

However, there is a large discrepancy for the vertical tune per cell. This can be explained by the fact that when varying slightly the target values in the optimisation routine, lattices different from S_1 that still match relatively well the time of flight variation with energy, could be found. This is especially true if the time of flight mainly depends on the magnet position; the magnet strengths could then be adjusted to agree with the tune measurement while still matching the tof constraints. In other words a new constraint on the value of the vertical tune at high energy could be implemented in the routine. The new lattice found would correspond better to the experimental lattice. This is a possible topic for a further study.

The simulation lattice S_1 that matches the tof measurements does not correspond to the experimental lattice E_1. Although simulations and measurements do not agree in absolute terms, it is interesting to compare the response to changes in the lattice predicted by the model with the response to changes measured in the machine. To do so, we measured the time of flight for various energies for three transverse positions of both magnets: both moved 1 mm outward (lattice E_2, +1 mm offset), both in nominal position (lattice E_3, 0 mm offset) and 1 mm inward (lattice E_4, -1 mm offset); the magnet strengths are kept constant; for instance the lattice E_2 is (105.6, 100, 8.51, 35.048). The tof measurements for these lattices are represented by stars with error bars in figure 5.14. We then apply the corresponding moves of the magnets to the lattice S_1 and obtain the lattices S_2, S_3 and S_4; for instance lattice S_2 is (94.30, 100.02, 10.56, 33.00). For each corresponding position of the magnets, the experimental and simulated results are plotted in the same colour.

For these simulated lattices, the tof at different energies is calculated in two different ways. The dots on the dashed line are values interpolated directly from the tof grid, hence limited to 18 MeV. The continuous line is obtained by interpolating the generating function for the corresponding lattice from the dynamical map grid. The lattice S_4 is found to be outside the grid ($X_d < 32$) and while the tof could be extrapolated, the generating function could not be derived. For the three other configurations, the generating functions agree perfectly with the interpolated tof.

We observe that for lattices 1, 2 and 3, the agreement between measurement and simulation is within 20 ps apart from some specific measurements for which the actual kinetic energy of the beam coming from ALICE might not have been 12 MeV exactly because of ALICE rf phase jitter and electron gun instabilities. The discrepancy for the fourth lattice is larger and can be explained by the fact the configuration is outside the grid, hence the simulated data were extrapolated. However there is agreement on the minimum value of 55.22 ns between 14 MeV and 15 MeV; this value is important to evaluate the optimal rf frequency of the cavity to achieve acceleration.

We can then conclude that simulations could be used to predict the effect on the time of flight when moving both magnets by the same amount. This prediction could be used to optimise acceleration. The next steps would be to measure the tof for magnets moved further outwards and also for magnets moved independently; the range of validity of the optimisation process could be then characterised more precisely.

Finally, the tune per cell measurements are obtained from the transverse position of the beam in each cell. At that stage of the commissioning, the transverse position of the orbit was measured by directly connecting the BPM signal to a four input channel scope in the control room; measuring the orbit around the entire ring required therefore a significant time (cabling and averaging) and it was not done for the other experimental lattices described here. In a near future, all the BPMs will be connected to an EPICS interface [70,71] and hence the measurement of orbit position and tunes

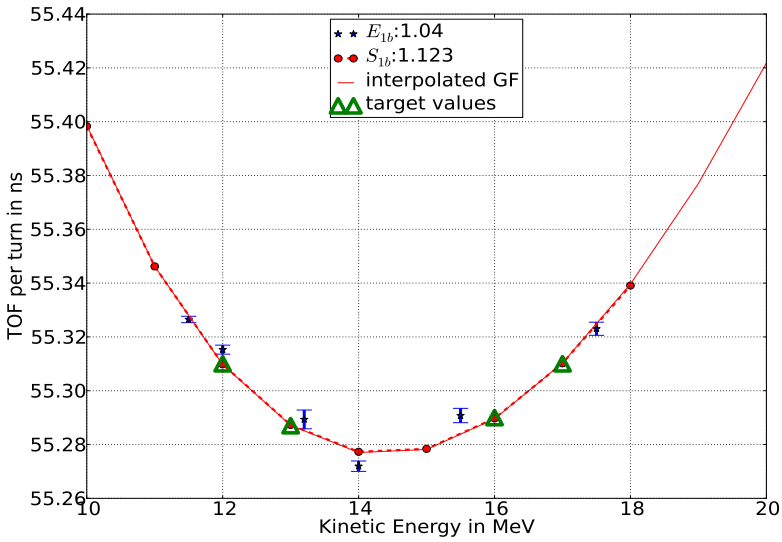

Figure 5.15: The initial measured lattice, E_{1b} is: (112.68, 100.00, 7.51, 34.048) represented by the blue stars with error bars; the corresponding magnet ratio is $A_d/A_f = 1.04$. The corresponding simulated lattice S_{1b} (red dashed line) matching the four targets values (purple dashed line) is: (98.9, 94, 9.97, 33.50). The magnet ratio for this lattice is 1.123. Here again the simulated lattice does not correspond to the actual lattice. Also, the dynamics obtained from the generating function interpolated for this configuration (green line) agree perfectly with the interpolated tof.

will be instantaneous. A more rigorous and complete evaluation of the optimisation routine will then be made more feasible.

5.2.4.2 Time of flight variation with change in magnets strengths

Measurements have also been carried out for lattices with different magnet strengths without moving the magnets. The initial measured lattice, E_{1b} is: (112.68, 100.00, 7.51, 34.05) represented by the blue stars with error bars in figure 5.15; the corresponding magnet ratio is $A_d/A_f = 1.04$. The simulated lattice S_{1b} matching the four targets values (green triangles) is: (98.90, 94.00, 9.97, 33.50) and is represented by the red dashed line; the simulations from its interpolated gf (red line) also shows good agreement with the measurements. the magnet ratio for this lattice is 1.123. Here again the simulated

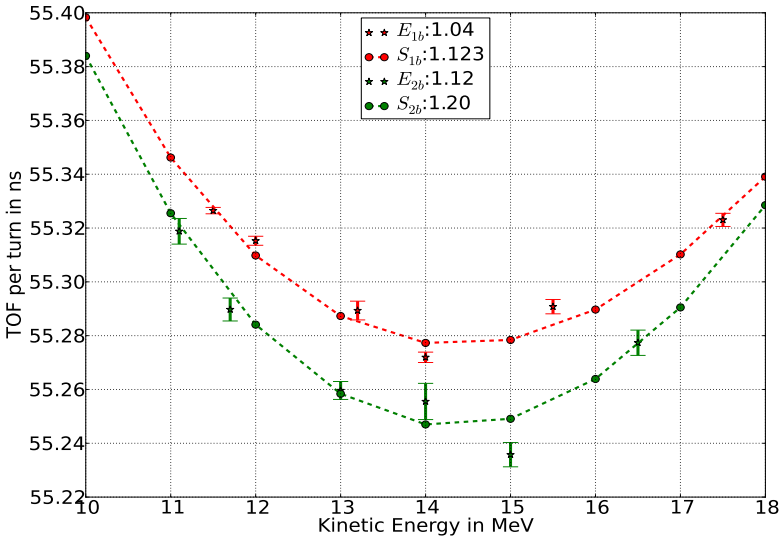

Figure 5.16: comparison of the response to a change in the magnet strength ratio predicted by the model with the response of the machine to the same change in magnet strength ratio. The tof measurements and the simulation results are represented by stars with error bars and dashed line respectively. The discrepancy between the tof for various energies between the lattices E_{2b} and S_{2b} (green) reaches 15 ps at 15 MeV/c. However, the measurement performed at that point seems to be out of the trend of the other tof measurements for this lattice. The agreement is within less than 10 ps for the other data points.

lattice S_{1b} does not correspond to the actual lattice E_{1b}.

To study the relative agreement between experimental and simulated results when varying the magnet strength ratio A_d/A_f, we measured the time of flight for various energies for another magnet ratio of 1.12 corresponding the lattice E_{2b} is: (105.40, 100.00, 7.51, 34.05). Note that the strength of the D magnet is kept constant. Figure 5.16 shows the comparison of the response to a change in the magnet strength ratio predicted by the model with the response of the machine to the same change in magnet strength ratio. The tof measurements are represented by stars with error bars. From a ratio of 1.04 to 1.12 the relative change is of 7.6%. We apply the same relative change to the lattice S_{1b} (red) conserving the strength of the D magnet and obtain the lattice S_{2b} (green) with ratio 1.20 : (91.90, 94.00, 9.97, 33.50). Note that the gf could not be derived because the lattice configuration was outside the grid but the tof for energies between 10 MeV and 18 MeV could be extrapolated from the grid of tof for known lattice configurations.

The discrepancy between the tof for various energies between the lattices E_{2b} and S_{2b} reaches 15 ps at 15 MeV/c. However the measurement performed at that point seems to be out of the trend of the other tof measurements for this lattice. Extending this study to other magnet strength ratio would be necessary before drawing firm conclusions on the stability of the optimisation process. At this stage of the study, this result is very encouraging and validates the use of the dynamical maps to predict linear beam dynamics in FFAG accelerators.

The success of the acceleration in EMMA depends largely on the chosen lattice configuration. The accelerating system can be optimised for a given variation of the time of flight with energy. However, some features of the rf system are limited in range (e.g. frequency, voltage) and it is instead necessary to adapt the lattice to the rf capabilities. Also, since crossing resonances through acceleration may destroy the beam, setting the lattice to avoid the most destructive resonances is crucial. We saw that this

routine can give an estimate of the changes needed in the lattice parameters to optimise the lattice. More experimental data in the following months of the commissioning will help refining this process and also define its limitations.

5.3 Summary and conclusions

In the first section of this chapter the objective was to predict the beam dynamics in any configuration of the lattice by constructing dynamical maps by interpolation between known configurations forming a grid.

First we observed that the interpolation of the coefficients of the Taylor series representation of the dynamical map introduced a large symplectic error in the beam dynamics. We then showed that interpolating the coefficients of the generating function preserved the symplecticity of the interpolated solution and gave better agreement with the directly computed solution for the tune, time of flight and betatron motion.

In the second part of this chapter, we applied these results to compare time of flight measurements obtained from the EMMA commissioning and simulations. The tof is measured with a precision of 15 ps by counting the number of rf periods between consecutive turns detected by a BPM and then evaluating the exact arrival time within one rf period. Therefore agreement between different tracking codes within 15 ps is satisfactory at that stage of the commissioning (more precise measurement techniques may be developed later).

The tof at different energies obtained from the interpolated generating function for the experimental lattice had large discrepancy with the measurements. We concluded that the experimental lattice and the simulated lattice were not equivalent. The origin of the disagreement is not clear at present.

An optimisation routine identified the simulated configuration of the lattice that matches the time of flight measurements. The tune per cell variation with energy de-

rived from the interpolated generating function showed large discrepancies with the measurements especially at high energy for the vertical tune per cell. The discrepancy was decreased by computing dynamical maps with various reference energies. The agreement was within 0.005 for the horizontal tune per cell. This confirms the conclusions of chapter 4 stating that a single dynamical map may not be sufficient to simulate accurately the dynamics over the whole range of energy in EMMA.

In addition, a constraint on the vertical tune should be added to the routine to obtain a lattice that agrees with the experimental results for the time of flight and for linear transverse beam dynamics.

It was then shown that the effect predicted from simulation on the time of flight of moving both magnets horizontally inward and outward by a few millimetres agreed within 15 ps with the experimental measurements for the corresponding move. Also simulations could predict the effect on the time of flight of a change in magnet strength ratio. The agreement in terms of vertical and horizontal tunes could not be verified because of the lack of orbit position measurements.

These results partly validate the simulations of linear beam dynamics in FFAG with dynamical maps. They show that the work carried out to construct the optimisation routine is relevant since it agrees within reasonable tolerances with the experimental data. An improvement would be to understand why the lattice found from simulation is different from the experimental lattice. However the ability to predict the effects of changes in the lattice configuration (magnet strengths and positions) is already useful for the optimisation of the lattice to achieve acceleration. This must be studied more widely for arbitrary changes in the four parameters of the lattice configuration. More experimental data obtained in the next months of the commissioning will certainly allow for an improvement of this technique.

6

Discussion

The objective of this last chapter is to discuss, after having presented the whole study, the initial aims and objectives defined in the introduction chapter. We will recall each aim and briefly sum up the part of the study relevant to the related objectives. We will then discuss whether the aims were achieved and potentially define additional objectives for a further completion.

6.1 Aim 1: Obtain an accurate 3D representation of a magnetic element.

Since in many cases of particle accelerator, the 3D geometry of the magnets is too complex to solve Maxwell's equations exactly, a numerical solver is required. We used the 3D OPERA model of the EMMA cell created for the design of the machine and obtained a numerical solution of the magnetic field by finite element method. We evaluated the minimum mesh density such that an increase of this density would affect the first order beam dynamics (tune and time of flight) by an amount smaller than the measurement precision in the machine. It would be interesting to study the effect of the mesh density on nonlinear dynamics. The nonlinear effects in the case study EMMA

may be too weak to draw clear conclusions on that study and another case study, such as complex magnets in scaling FFAGs, would be more relevant.

We constructed the field representation of the entire cell by superposing the field from each magnet. An important result was the fact that the presence of the unpowered yoke when solving each magnet separately had a significant effect on the dynamics; beam dynamics codes using simple hard edge model for the magnets (and therefore not taking into account neither edge effect of the magnets nor the interferences between magnets) are not as accurate as codes using detailed 3D field maps. Some discrepancies in the magnetic field could be observed between the field map for the entire cell and the superposition of maps; however their effect on linear beam dynamics seemed negligible. Nevertheless in order to model the FFAG EMMA ring with higher precision, the OPERA model should be compared to a detailed three dimensional map measured in the ring magnets. We considered at that stage of the study that the representation was accurate enough.

In order to construct a dynamical map, differential algebra objects were used as variables for the symplectic integration through the magnetic field of the beamline. The magnetic field also needed to be expressed in analytical form. An analytical representation of the magnetic field in the form of Fourier series in cylindrical coordinates was derived by fitting a set of coefficients on the numerical values of the field interpolated on a reference cylinder from the field map obtained from OPERA; the residual of the fit increases exponentially outside this cylinder. Then the set of coefficients was transformed to Cartesian coordinates more adapted to beam dynamics studies. The residual of the fit was kept smaller than a few Gauss within the reference cylinder and the tune and time of flight obtained from tracking in the original field map and in the fitted representation differed by a smaller amount than the measurement precision for trajectories contained in the reference cylinder; however several cylinders are then needed to cover the whole aperture when a large cylinder is limited by the magnets

poles.

In the case of accelerators like EMMA with large horizontal excursion of the particles, instead of covering the aperture with several cylinders, other sets of functions such as Mathieu's function fitting on a cylinder with elliptical base may be more appropriate; the conversion to Cartesian coordinates can then be rather cumbersome and hence the most practical solution could be to include this basis of functions in elliptical cylindrical coordinates directly in the integrator script.

6.2 Aim 2: Derive the equations of motion of a particle in a general magnetic element to obtain a dynamical map.

Solving the equations of motion for a particle moving in a magnetic field is a very common problem which we chose to solve such that we obtained a symplectic solution expressed in the form of a dynamical map.

The first objective was therefore to derive the equations of motions such that a symplectic solution could be computed. Since Hamiltonian systems are intrinsically symplectic, we chose the Hamiltonian formalism for the expression of the dynamics. We derived the accelerator Hamiltonian for a straight reference trajectory. Unfortunately, systems described by this Hamiltonian in general do not have exact solution in closed form. Making the paraxial approximation, we could expand this Hamiltonian in a sum of integrable terms and find approximate solutions in closed form for multipole magnets. The next objective was to extend this result to a general magnetic field and use it to build a symplectic integrator.

6.2 Aim 2: Derive the equations of motion of a particle in a general magnetic element to obtain a dynamical map.

Using a technique developed by Wu et al, the Lie transformation and its properties allowed us to express the dynamics in a general magnetic field as the concatenation of integrable maps. We obtained a symplectic explicit integrator of the second order (paraxial approximation) in the step size. The effect of the paraxial approximation is crucial in the case study of an FFAG where trajectories can have large excursion with respect to the reference trajectory.

From the symplectic integrator, the map could be expressed algebraically in closed form. We used a differential algebra (DA) code to construct the Taylor series representing the dynamics in a given magnetic element described by an analytical representation of the magnetic field. The dynamical map in this form provides a convenient, compact and efficient description of the particle motion; and may also, by inspection of the map, provide useful information directly on the impact the magnetic component may have on the beam dynamics in an accelerator. However the integrated solution in the form of Taylor series contains a very large number of terms which in practice the computing routine needs to truncate at a given order. The effect of the truncation on the symplecticity can be quantified through the Jacobian of the map. It is important to note that the symplectic error comes from the limited numerical precision, regardless of the integration step size. This is a fundamentally different approach to standard Runge-Kutta integrator that only reaches symplecticity as it becomes more accurate by decreasing the step size.

This technique has been mathematically developed further by Wu et al. and also by Berz and Makino to construct a explicit symplectic integrator of higher order not making the paraxial approximation. A study of the dynamics in the FFAG EMMA with this integrator would give a deeper understanding of the effect of the paraxial approximation in our simulation results (corresponding to the following aim of the study). Also developing the symplectic integrator for a curvilinear reference trajectory

may improve the accuracy of the simulation in an FFAG where trajectories can be significantly curved.

6.3 Aim 3: Study the validity of the beam dynamics simulations of FFAG accelerators with dynamical maps.

We then aimed at studying the validity of the beam dynamics simulations of FFAG accelerators with dynamical maps. Although it was hoped that use of dynamical maps would offer some benefits for simulation studies (compared to purely numerical techniques) the main motivation of the present study was to assess the limitations of this technique for FFAGs. A stronger motivation for applying dynamical maps to this type of accelerator is that in general in FFAGs the dynamics are non linear. For instance scaling FFAG magnetic fields are highly non linear. Dynamical maps could therefore be an interesting tool for such machines because of their ability to provide an insight into the dynamics not provided by purely numerical tracking techniques. However as a first stage for this new type of study, we tested our technique on a more linear case: the linear non scaling FFAG EMMA.

Among all the codes that had been used to simulate beam dynamics in this accelerator, we decided to compare dynamical maps results with PyZgoubi since it could track particles in numerical field maps provided by an OPERA model and also in simple hard edge model of a magnet. The agreement between codes was considered to be satisfactory if the discrepancy was smaller than the expected measurement precision for the data (i.e. 10 ps for the time of flight and 0.01 for the tune per cell).

First we looked at the disagreement between simulations with hard edge model and with field maps. We found significant differences for the time of flight for different fixed energies. Therefore, simulations with field maps may be required to model accurately

the beam dynamics in EMMA. For instance, tracking in field maps indicated that the time of flight was smaller than the design one derived with tracking through hard edge representations of the magnets. This implied that the frequency of the cavities had to be increased or that the magnets had to be moved outwards to increased the path length of the particles to optimise the lattice for acceleration.

Then we observed a discrepancy in the tune per cell at various energies from simulations with dynamical maps and with PyZgoubi using numerical field representation. This discrepancy was significant only for low energies for which the excursion of the closed orbit with respect to the dynamical map reference trajectory was large. This suggests that the paraxial approximation may not be valid in that case, since PyZgoubi did not make this approximation.

We then studied the accuracy of the beam dynamics simulation with dynamical maps when varying the energy deviation. The time of flight could be predicted for the whole energy range with a single map truncated to the 4^{th} order. However, even retaining terms up to 9^{th} order in the map did not allow an accurate computation of the horizontal and vertical tune for energy deviation larger than 15%. We concluded that three maps with different reference energies are required to simulate accurately the linear dynamics over the full range in energy in EMMA.

After studying the linear dynamics in EMMA, we focused on nonlinear effects that can cause the tune value to vary with the value of the betatron action. We computed the tune shift with amplitude obtained from frequency map analysis of tracking results from PyZgoubi and dynamical map, and compared this result with the value for the tune shift obtained by reading directly the coefficients of the generator of the Lie transformation representing the dynamical map.

The discrepancy with the results obtained from the coefficients of the Lie generator was smaller than measurement precision; this validates the reading of this nonlinear

effect directly from the map. However we observed a larger disagreement in the vertical motion.

PyZgoubi was not accurately simulating the nonlinear components of the magnetic field present in the OPERA model; whereas the agreement of the tune shift estimated from the OPERA and the 3D analytical form (used to construct the dynamical map) descriptions of the field gives confidence in the simulation of the vertical tune shift with amplitude with dynamical map.

Finally, another objective raised from this study: we made the assumption that the discrepancy between PyZgoubi and the dynamical maps simulations could result from the paraxial approximation made to construct the dynamical map. To validate this assumption, we need to simulate a beamline for which the tune shift with amplitude could be derived analytically. We could then draw a conclusion on the effect of large values of the variables on the accuracy of the simulations.

The last objective was dedicated to the study of the longitudinal dynamics in EMMA. First we observed that a group of particles with an initial longitudinal distribution (either Gaussian or uniform) rapidly lost its coherent transverse motion when tracked for several turns in the ring at fixed energy. For an initial distribution chosen according to experimental measurements, we observed that simulations with dynamical maps and PyZgoubi predicted a complete decoherence (when BPM readings corresponds to the stable orbit) of the betatron oscillations within 7 turns (for a distribution with energy spread being 1.175% FWHM).

Furthermore, we included a simple model of acceleration in the simulations with dynamical maps. First, we showed that dynamical maps were capable of simulating fast acceleration in the case of EMMA (serpentine acceleration) predicted by the analytical model. Although one dynamical map was sufficient to model the time of flight over the full energy range, this study showed two dynamical maps with different reference energy

and truncated to order 8, may be required to reproduce the evolution of a distribution (similar to the measured distribution in longitudinal phase space at injection in EMMA) through acceleration from 10 MeV to 20 MeV. Transverse distributions with different values for the horizontal action of particles should be studied to verify if the simulations with two maps are still accurate. Note that the estimation regarding the computation of the tune for various value of the energy deviation was that three maps would be necessary.

Eventually simulations with PyZgoubi and dynamical maps of the distortion of a transverse distribution passing through a third order resonance during acceleration with 2 MV per turn in the cavities showed good agreement. No significant growth of the transverse size of the distribution occurred, giving confidence in the capability of a non-scaling FFAG to accelerate a beam without losses in a serpentine channel. We could also observe in both codes, a larger distortion of the initial ellipse shape for lower rate of acceleration (i.e. decreasing the rf voltage to 0.55 MV per turn).

From this chapter we can conclude that dynamical maps are capable of simulating basic transverse and longitudinal beam dynamics in a non-scaling FFAG. A deeper study of the capability of dynamical maps to simulate dynamics in FFAG can be carried out in three ways:

1. Construct a dynamical map for beamline with strongly non-linear elements in which the beam dynamics can be solved analytically. The effect of the paraxial approximation could then more easily be investigated.

2. Apply the technique to a different machine, in particular a scaling FFAG in which non linear effects are expected to be larger.

3. Compare the simulations to experimental data from EMMA. Although this task was partially tackled in the last chapter, a better knowledge of the machine will allow more precise evaluation of the different simulation techniques.

6.4 Aim 4: Make use of dynamical maps to analyse the experimental results.

To achieve the last aim of this study, we had to define a task for which the technique that we had developed would be useful. The fact that experimental data started to be available from the commissioning of the machine helped to define this task.

The starting observation was that the actual experimental lattice was not precisely known. A fit on the measurements would in principle allow us to derive the corresponding simulated lattice. The development of a model that accurately predicts the behaviour of the real machine would be of great value in tuning and operating the accelerator. However we believed that the hard edge model would not be as accurate as the analytical representation of the field that we had derived. The task would then be to find the simulated lattice with dynamical map that matches the experimental data.

The first objective was to predict the beam dynamics in any configuration of the EMMA lattice. This was achieved by interpolating the dynamical map between known configurations forming a grid. We observed that interpolating the coefficients of the Taylor series introduced a significant symplectic error that was largely decreased when interpolating the coefficients of the generating function. We observed also that using an interpolated generating function, the beam dynamics agreed better with the results from directly computed map for the given configuration.

We then had to decide which experimental data would be the most appropriate to be measured and then fitted. Since the measurement of the transverse position of the beam at that stage of the commissioning was cumbersome, measurements of the tune were not easily available. However the measurement of the time of flight was relatively straightforward. Since the EMMA lattice was defined by four parameters (strengths and positions of the two magnets), we chose the four constraints on the fit to be the

measured time of flight at four momenta.

We found that the simulated lattice obtained from the optimisation routine by fitting the time of flight measurements did not correspond very closely to the configuration of the experimental lattice. However we noticed that the simulated vertical tune also did not agree with the measurements; it is therefore likely there are several lattice configurations matching the time of flight measurements but having different variation of the tune with energy. Measured tune values should be included as constraints in the optimisation routine to avoid the degeneracy of the result.

Despite this disagreement, we showed that the response in terms of time of flight to changes in the lattice parameters predicted by the model agreed (within measurement precision) with the response to changes measured in the machine. The changes applied to the lattice were: first, a move of both magnets transversely, and second, a variation of the ratio of the magnet strengths. This should be generalised to the prediction of the beam dynamics for any change in the four parameters of the lattice. This procedure could then stand as a powerful tool in order to set the machine in the optimal configuration for serpentine acceleration or for a particular resonance crossing.

6.5 Conclusions

The technique presented in this study consists in the application of three independent tasks: firstly deriving an accurate analytical representation of any magnetic field configuration; secondly making use of an integrator that preserves an important characteristic of Hamiltonian system (in particular the symplecticity); and thirdly performing particle tracking using differential algebra and creating a dynamical map in the form of a power series of the dynamical variables or in the form of generating functions.

The case study for this procedure was chosen to be the non-scaling FFAG accelerator EMMA for four main reasons:

- the particular design of the magnets in which the magnetic field at the entrance and exit faces may have a strong influence on the dynamics. This can be significant in the modelling of the lattice for simulations.
- The flexibility of the lattice with its four degrees of freedom, which requires also the flexibility of a code simulating dynamics in EMMA.
- The large excursion of particle trajectories with respect to a given straight reference trajectory, suggesting the approximation made on the small variation of variable may not apply for FFAGs.
- The fact that the commissioning of the machine, being the first ever built non scaling FFAG, was occurring on site; this therefore offered access to the expertise of the physicists working on this project and also allowed us to take and process the first experimental data.

There are close links between the three tasks involved in the analysis and these four motivations. First, the complicated design of the magnets required a precise understanding of the properties of the magnetic field and the analytical representation was a convenient form for the rest of the study. The first task and the first motivation are closely related.

The need for a symplectic integrator does not appear really relevant at first sight since symplecticity is more often an issue occurring in a lattice where thousands of turns are performed by the particles. However the link is here two-fold: first, since it is the first time that such a machine with non conventional beam dynamics is built, no particle tracking codes have been benchmarked against this kind of simulations. Therefore in order not to be "walking blindly" in the study of the machine, it is useful to be able to confirm that tracking results respect theoretical constraints. Symplecticity is a convenient constraint, since it imposes a number of conserved quantities, that can be easily evaluated. The significance of the symplectic constraint confirmed when we

obtained more accurate results for the interpolation of the generating function than for the interpolation of the power series. Second, the symplectic integrator we used required the paraxial approximation; trajectories with large excursions in FFAGs stood therefore as a crucial test for this technique and EMMA was particularly interesting since experimental data allowed a benchmarking of the integrator.

Finally the use of dynamical maps was very convenient to predict the beam dynamics in any configuration of the EMMA lattice using a precise 3D representation of the magnetic field. We saw that dynamical maps contain a large amount of information in a compact format. This is a crucial feature for optimisation routines and a powerful tool for the commissioning of the machine.

An important aspect that was not tackled in this study was the relevance of this process for beam dynamics with strong non linearities in scaling FFAGs. However the satisfactory agreement shown in this study between dynamical maps and numerical methods, and the understanding obtained of the benefits and limitations of the application of dynamical maps to non-scaling FFAGs, provide an important foundation for a more detailed study of the stronger non-linear effects expected in scaling FFAGs.

Appendix A

Transformation of Fourier series coefficients from cylindrical to Cartesian coordinates

The aim of this section is to derive a relation between the a_{mn} and c_{mn} coefficients for even value of m. We start with the expressions for the azimuthal component and vertical component of the magnetic field:

$$B_y = \sum_{m,n} c_{mn} \sin(mk_x x) \cosh(k_y y) \sin(nk_z z) \tag{A.1}$$

$$B_\phi = \sum_{m,n} a_{mn} \frac{m}{nk_z\rho} I_m(nk_z\rho) \cos(m\phi) \sin(nk_z z)\,. \tag{A.2}$$

Since the field in one representation must equal the field in the other representation at all points in space, and both fields are entirely determined by the coefficients, we can choose any particular point in space to carry out the study. If we can find the coefficients a_{mn} by considering the fields at that particular point, then we have solved the problem.

Let us choose the point:

$$x = \rho, \;\; y = 0, \;\; z = \pi/(2nk_z)\,. \tag{A.3}$$

For $y = 0$, i.e in the median plane, the relation between the transverse magnetic field components in cylindrical and Cartesian bases are given by:

$$B_y = B_\phi \;\text{ and }\; B_x = B_\rho \tag{A.4}$$

At that location in space, only considering even values for m, expressions (A.1) and (A.2) become:

$$B_\phi = \sum_{m,n} a_{mn} \frac{m}{nk_z\rho} I_m(nk_z\rho)\,, \tag{A.5}$$

$$B_y = \sum_{m,n} c_{mn} \sin(mk_x\rho)\,. \tag{A.6}$$

Then,

$$\sum_{m,n} a_{mn} \frac{m}{nk_z\rho} I_m(nk_z\rho) = \sum_{m,n} c_{mn} \sin(mk_x\rho) \tag{A.7}$$

Let us assume that a function f exists such that:

$$c_{mn} = f_{mm'} a_{m'n} \tag{A.8}$$

Our goal is to find the components $f_{mm'}$, which will allow us to transform from the cylindrical to the Cartesian basis. Substituting equation (A.8) into (A.7) gives:

$$\sum_{mn} a_{mn} \frac{m}{nk_z\rho} I_m(nk_z\rho) = \sum_{m,n,m'} f_{mm'} a_{m'n} \sin(mk_x\rho) \tag{A.9}$$

This equation is satisfied (a sufficient but not necessary condition) if each term in

the summation over n on one side is the same as the corresponding term on the right hand side. Then, we can simply drop the summation over n:

$$\sum_m a_{mn} \frac{m}{nk_z\rho} I_m(nk_z\rho) = \sum_{mm'} f_{mm'} a_{m'n} \sin(mk_x\rho) \tag{A.10}$$

Now we make use of the series expansions for the derivative of the modified Bessel function:

$$I_m(\rho) = \sum_{l=0}^{\infty} \frac{1}{l!m+l!} (\frac{\rho}{2})^{(2l+m)} \tag{A.11}$$

and for the sine function:

$$\sin(mk_x\rho) = \sum_{l=0}^{\infty} (-1)^l \frac{(mk_x\rho)^{2l+1}}{2l+1!} \tag{A.12}$$

Substituting equations (A.12) and (A.11) into (A.10) gives:

$$\sum_{m,l} a_{mn} \frac{m}{l!m+l!} \frac{(nk_z\rho)^{2l+m-1}}{2^{2l+m}} = \sum_{m,m',l} f_{mm'} a_{m'n} (-1)^l \frac{(mk_x\rho)^{2l+1}}{2l+1!} \tag{A.13}$$

Equation (A.13) must be true for all values of ρ. Therefore, the coefficients of equal powers of ρ on either side must be equal. Let us consider the coefficients of $2l'+1$. On the right hand side, this is simply the term in the summation over l with:$l = l'$. On the left hand side, with is the term in the summation over l with:

$$2l + m - 1 = 2l' + 1 ... thus ... l = l' + 1 - \frac{m}{2} \tag{A.14}$$

Hence, comparing coefficients of powers of ρ gives:

$$\sum_m a_{mn} \frac{m}{(l' + 1 - \frac{m}{2})!(l' + \frac{m}{2} + 1)!} \frac{(nk_z)^{2l'+1}}{2^{2l'+2}} = \sum_{m,m'} f_{mm'} a_{m'n} (-1)^l \frac{{mk_x}^{2l'+1}}{2l'+1!} \tag{A.15}$$

Let us interchange the labels m and m' on the right hand side:

$$\sum_m a_{mn} \frac{m}{(l'+1-\frac{m}{2})!(l'+\frac{m}{2}+1)!} \frac{(nk_z)^{2l'+1}}{2^{2l'+2}} = \sum_{m',m} f_{m'm} a_{mn} (-1)^l \frac{m' {k_x}^{2l'+1}}{2l'+1!} \quad \text{(A.16)}$$

As before we can equate corresponding terms in the summation; in this case, we take the summation over m:

$$\frac{m}{(l'+1-\frac{m}{2})!(l'+\frac{m}{2}+1)!} \frac{(nk_z)^{2l'+1}}{2^{2l'+2}} = \sum_{m'} f_{m'm} (-1)^{l'} \frac{(m'k_x)^{2l'+1}}{(2l'+1)!} \quad \text{(A.17)}$$

Since there is no summation over l, this becomes:

$$m \frac{(2l'+1!)(-1)^{l'}}{(l'+1-\frac{m}{2})!(l'+\frac{m}{2}+1)!} \frac{(nk_z)^{2l'+1}}{2^{2l'+2}} = \sum_{m'} f_{m'm} (m'k_x)^{2l'+1} \quad \text{(A.18)}$$

Now we observe we can write this in matrix form as:

$$\mathbf{v}_{lm} = \sum_{m'} \mathbf{k}_{lm'} f_{m'm} \quad \text{(A.19)}$$

where we define the matrix $\mathbf{v}$ with components:

$$\mathbf{v}^{(n)}_{l'm} = m \frac{(-1)^{l'}(2l'+1)!}{(l'+1-\frac{m}{2})!(l'+\frac{m}{2}+1)!} \frac{(nk_z)^{2l'+1}}{2^{2l'+2}} \quad \text{(A.20)}$$

and the matrix $\mathbf{k}$ with components:

$$k_{l'm'} = (m'k_x)^{2l'+1} \quad \text{(A.21)}$$

Formally, the matrices have an infinite number of components; however, we can reduce them to finite-sized square matrices by making appropriate truncations in l', m

and m'. We can then solve equation A.21 for the required components $f_{mm'}$:

$$f_{mm'} = \sum_{l'} \mathbf{k}^{-1}_{ml'} v_{l'm'} \tag{A.22}$$

We calculated in a similar way the transformation for odd values of m choosing $x = 0$, $y = \rho$ and $z = \pi/(2nk_z)$ as reference point where the relation between the component of the magnetic field in cylindrical and Cartesian bases are:

$$B_y = B_\rho \text{ and } B_x = B_\phi \tag{A.23}$$

At that new location in space, considering only odd values of m, we have:

$$B_\rho = \sum_{m,n} a_{mn} I'_m(nk_z\rho)(-1)^{\frac{m-1}{2}} , \tag{A.24}$$

$$B_y = \sum_{m,n} c_{mn} \cosh(k_{y,mn}\rho) . \tag{A.25}$$

Eventually we obtain the components $g^{(n)}_{mm'}$ of the g function given by:

$$g^{(n)}_{mm'} = \sum_{l'} k^{-1}_{ml'} v^{(n)}_{l'm'} , \tag{A.26}$$

where the coefficient of the matrix $\mathbf{v}^{odd}$ are given by:

$$v^{(n)}_{l'm} = (-1)^{\frac{m-1}{2}} \frac{(2l'+1)!(nk_z)^{2l'}}{2^{2l'+1}(l' - \frac{m-1}{2})!(l' + \frac{m+1}{2})!} \tag{A.27}$$

and the matrix $\mathbf{k}$ with components:

$$k^{(n)}_{l'm'} = (m'^2 k_x^2 + n^2 k_z^2)^{l'} \tag{A.28}$$

Using equations (A.8), (A.22) and (A.26) one can transform the multipole expansion

of the magnetic field from cylindrical to Cartesian basis. The analytical representation in Cartesian coordinate of the magnetic field can then be compared to the original numerical field data.

Appendix B

Generating functions

Generating functions are a very useful tool to represent a canonical transformation. Any canonical transformation and therefore any symplectic map can be represented by at least one generating function. However the dynamical map expressed in form of a generating function is implicit. There are four generally used generating function:

$$F_1 = F_1(q_i, q_f, t)\,,\ F_2 = F_2(q_i, p_f, t)\,,\ F_3 = F_3(p_i, q_f, t)\,,\ F_4 = F_4(p_i, p_f, t) \tag{B.1}$$

where q_i are the old coordinates and q_f are the new coordinates. p_i and p_f are their respective conjugate momenta. These generating functions generate a canonical transformation in which the old and new variables are related by:

$$p_i = \frac{\partial F_1}{\partial q_i} \quad p_f = -\frac{\partial F_1}{\partial q_f} \tag{B.2}$$

$$p_i = \frac{\partial F_2}{\partial q_i} \quad q_f = \frac{\partial F_2}{\partial p_f} \tag{B.3}$$

$$q_i = -\frac{\partial F_3}{\partial p_i} \quad p_f = -\frac{\partial F_3}{\partial q_f} \tag{B.4}$$

$$q_i = -\frac{\partial F_4}{\partial p_i} \quad q_f = \frac{\partial F_4}{\partial p_f} \tag{B.5}$$

and in all cases the new Hamiltonian K with z as independent variable is given by:

$$K = H + \frac{\partial F_n}{\partial z}\,, \tag{B.6}$$

We observe that F_1, generating function of the first kind, is a function of the old coordinates and the new coordinates, whereas the other generating functions of other kind mix up old and new canonical variables. Note that since the action-angle variables (ϕ_x,J_x) are obtained from the Cartesian variables (x,p_x) by a canonical transformation, then we can construct a generating function mixing the pairs of variable:

$$F_1(x,\phi_x) = -\frac{x^2}{2\beta_x}(\tan\phi_x + \alpha_x) \tag{B.7}$$

We can verify the validity of the function by computing p_x and J_x recalling that:

$$\begin{aligned} x &= \sqrt{2\beta_x J_x}\cos\phi_x\,, & \text{(B.8)}\\ p_x &= -\sqrt{\frac{2J_x}{\beta_x}}(\sin\phi_x + \alpha_x\cos\phi_x)\,. & \text{(B.9)} \end{aligned}$$

In other word:

$$\begin{aligned} \tan\phi_x &= -\alpha_x - \beta_x\frac{p_x}{x}\,, & \text{(B.10)}\\ 2J_x &= \gamma_x x^2 + 2\alpha_x x p_x + \beta_x p_x^2\,. & \text{(B.11)} \end{aligned}$$

Using the generating function, J_x is given by:

$$\begin{aligned} J_x &= \frac{\partial F_1}{\partial\phi_x}\\ &= \frac{x^2}{2\beta_x\cos^2\phi_x} \end{aligned} \tag{B.12}$$

From B.12 we have:

$$x^2 = 2\beta_x J_x \cos^2 \phi_x \,, \tag{B.13}$$

which is equivalent to B.8.

For p_x:

$$\begin{aligned} p_x &= \frac{\partial F_1}{\partial x} \\ &= -\frac{x}{\beta_x}(\tan \phi_x + \alpha_x) \end{aligned} \tag{B.14}$$

Expression B.10 is derived straightforwardly from B.14.

This gives a brief example of how generating functions can be used. Their full derivation and construction are explained in more details in [41, 44].

Appendix C

Symplectic Integrator in COSY routine

In this appendix, we will give an overview of the script of the explicit symplectic integrator. This script uses routine from COSY infinity [47]. It includes general functions such that input/output functions (READ/WRITE), sinusoidal functions (COS/SIN/SINH /COSH) and some basic mathematical operations (ABS/SQRT). Moreover it includes function that can handle Differential Algebra (DA) objects. The DA objects are created by "DAINI" which sets also the order of truncation and the number of dynamical variables involved. Finally two functions "FIT" and "POLVAL" are used to find the closed orbit at a given energy. "POLVAL" applies a dynamical map in Taylor model form to a set of numerical initial coordinates. The "FIT" procedure uses recursively "POLVAL" in order to find the transverse initial coordinates that are unchanged when applying the map. These coordinates are the coordinate of the closed orbit.

C.1 Potential Vector

The potential vector, defined as a DA object (and therefore takes the form of a Taylor series) is computed at each integration step. The position of the particle in space (x,y,z) is defined by the variables ($X(1)$,$X(3)$,$X7$). The potential vector has a different expression whether the index m of the transverse multipole is even or odd. The parity of m is tested by the function "MOD(m,2)".

Let us remember that the symplectic integrator (see C.6 in this appendix) include the Lie transformation $e^{:I_y:}$ that acts on the dynamical variables as follow:

$$e^{:I_y:}p_x = p_x - \int_0^y \frac{\partial}{\partial x} a_y(x, y', s)dy' \,, \tag{C.1}$$

$$e^{:I_y:}p_y = p_y - a_y \,, \tag{C.2}$$

$$e^{:I_y:}\delta = \delta \,. \tag{C.3}$$

For the variables "AY" and "IADY" corresponding to a_y and $\int \frac{\partial}{\partial x} a_y dy$ in C.1 and C.2.

```
PROCEDURE AYFIELD;
LOOP J 1 NMODES;
      MKX  := CMN(J,1)*KX;
      NKZ  := CMN(J,2)*KZ;
      KY   := SQRT(MKX*MKX + NKZ*NKZ);
      C    := CMN(J,3);
      EVEN:= MOD(CMN(J,1),2);
      IF EVEN=1;
    AY  := AY   + C*SIN(MKX*X(1))*COS(NKZ*X7)*SINH(KY*X(3))*NKZ/MKX/KY;
    IADY := IADY + C*COS(MKX*X(1))*COS(NKZ*X7)*(COSH(KY*X(3)) - 1.0)*NKZ/KY/KY;
      ELSEIF 1=1;
    AY  := AY   - C*COS(MKX*X(1))*COS(NKZ*X7)*SINH(KY*X(3))*NKZ/MKX/KY;
    IADY := IADY + C*SIN(MKX*X(1))*COS(NKZ*X7)*(COSH(KY*X(3)) - 1.0)*NKZ/KY/KY;
```

```
      ENDIF;
ENDLOOP;
ENDPROCEDURE;
```

Similarly for the Lie transformation $e^{:H_3:}$, we compute $\frac{\partial}{\partial x}a_s$ and $\frac{\partial}{\partial y}a_s$:

```
PROCEDURE ASFIELD;
LOOP J 1 NMODES;
      IF EVEN=1;
  ASDX := ASDX - C*COS(MKX*X(1))*SIN(NKZ*X7)*COSH(KY*X(3));
  ASDY := ASDY - C*SIN(MKX*X(1))*SIN(NKZ*X7)*SINH(KY*X(3))*KY/MKX;
      ELSEIF (1=1);
  ASDX := ASDX - C*SIN(MKX*X(1))*SIN(NKZ*X7)*COSH(KY*X(3));
  ASDY := ASDY + C*COS(MKX*X(1))*SIN(NKZ*X7)*SINH(KY*X(3))*KY/MKX;
      ENDIF;
ENDLOOP;
ENDPROCEDURE;
```

C.2 Integrator

In this section, we will present the code performing the symplectic integration. First let us recall the expression of the symplectic integrator derived in section 3.2.3.3 in chapter 3. The dynamical map $\mathcal{M}(\Delta\sigma)$ of a beamline can be expressed as follows:

$$\mathcal{M}(\Delta\sigma) = e^{-\Delta\sigma:H_1+H_2+H_3:}, \tag{C.4}$$

$$\mathcal{M}(\Delta\sigma) \approx e^{-\frac{\Delta\sigma}{2}:H_1+H_3:}e^{-\Delta\sigma:H_2:}e^{-\frac{\Delta\sigma}{2}:H_1+H_3:}, \tag{C.5}$$

$$\mathcal{M}(\Delta\sigma) \approx e^{-\frac{\Delta\sigma}{4}:H_1:}e^{-\frac{\Delta\sigma}{2}:H_3:}e^{-\frac{\Delta\sigma}{4}:H_1:}e^{-\Delta\sigma:H_2:}e^{-\frac{\Delta\sigma}{4}:H_1:}e^{-\frac{\Delta\sigma}{2}:H_3:}e^{-\frac{\Delta\sigma}{4}:H_1:}, \tag{C.6}$$

where:

$$e^{-\Delta\sigma:H_2:} = e^{:I_y:}e^{-\Delta\sigma:\tilde{H}_2:}e^{-:I_y:}, \tag{C.7}$$

and :

$$H_1 = -\left(\frac{1}{\beta_0}+\delta\right)+\frac{1}{2\gamma_0^2\beta_0^2}\left(\frac{1}{\beta_0}+\delta\right)^{-1}+\frac{\delta}{\beta_0}+\frac{(p_x-a_x)^2}{2(\frac{1}{\beta_0}+\delta)}+p_s \quad \text{(C.8)}$$

$$\tilde{H}_2 = \frac{(p_y-a_y)^2}{2(\frac{1}{\beta_0}+\delta)} \quad \text{(C.9)}$$

$$H_3 = -a_s\,. \quad \text{(C.10)}$$

The corresponding code using COSY routine to handle DA object is:

```
PROCEDURE STEPX Z;
DP   := 1/( 1/BETA0 + X(6) );
DD   := 1/BETA0 - 1 - DP*DP/2/BETA0/BETA0/GAMMA0/GAMMA0;
```

Here, we defined $DP$and DD corresponding to terms in H_1.

```
X(1) := X(1) + X(2)*DP*DL/4;
X(5) := X(5) + (DD - X(2)*X(2)*DP*DP/2 )*DL/4;
```

The corresponding operations are: $e^{-\frac{\Delta\sigma}{4}:H_1:}x$, $e^{-\frac{\Delta\sigma}{4}:H_1:}z$.

```
X7   := Z + DL/4;
ASFIELD;
X(2) := X(2) - ASDX*DL/2;
X(4) := X(4) - ASDY*DL/2;
X(1) := X(1) + X(2)*DP*DL/4;
X(5) := X(5) + (DD - X(2)*X(2)*DP*DP/2 )*DL/4;
```

The corresponding operations are: $e^{-\frac{\Delta\sigma}{2}:H_3:}p_x$, $e^{-\frac{\Delta\sigma}{2}:H_3:}p_y$, $e^{-\frac{\Delta\sigma}{4}:H_1:}x$, $e^{-\frac{\Delta\sigma}{4}:H_1:}z$.

```
X7   := X7 + DL/4;
AYFIELD;
X(2) := X(2) + IADY;
```

```
X(4) := X(4) + AY;
X(3) := X(3) + X(4)*DP*DL;
X(5) := X(5) - X(4)*X(4)*DP*DP*DL/2;
```

We here had to call the function AYFIELD in order to perform the operations: $e^{-\frac{\Delta\sigma}{4}:I_y:}p_x$, $e^{-\frac{\Delta\sigma}{4}:I_y:}p_y$, $e^{-\Delta\sigma:H_2:}y$, $e^{-\Delta\sigma:H_2:}z$.

```
AYFIELD;
X(2) := X(2) - IADY;
X(4) := X(4) - AY;
X(1) := X(1) + X(2)*DP*DL/4;
X(5) := X(5) + (DD - X(2)*X(2)*DP*DP/2 )*DL/4;
```

since $e^{-\Delta\sigma:H_2:}$ had an effect on $X(3)$ and $X(5)$, AYFIELD is called again before applying: $e^{-\frac{\Delta\sigma}{4}:-I_y:}p_x$, $e^{-\frac{\Delta\sigma}{4}:-I_y:}p_y$, $e^{-\frac{\Delta\sigma}{4}:H_1:}x$, $e^{-\frac{\Delta\sigma}{4}:H_1:}z$.

```
X7   := X7 + DL/4;
ASFIELD;
X(2) := X(2) - ASDX*DL/2;
X(4) := X(4) - ASDY*DL/2;
X(1) := X(1) + X(2)*DP*DL/4;
X(5) := X(5) + (DD - X(2)*X(2)*DP*DP/2 )*DL/4;
X7   := X7 + DL/4;
ENDPROCEDURE;
```

And finally: $e^{-\frac{\Delta\sigma}{4}:H_3:}p_x$, $e^{-\frac{\Delta\sigma}{4}:H_3:}p_y$, $e^{-\frac{\Delta\sigma}{4}:H_1:}x$, $e^{-\frac{\Delta\sigma}{4}:H_1:}z$

This whole sequence is performed at every integration step

C.3 Rotation

In the absence of a magnetic field, the equations relating the canonical variables after rotation (written with subscript "new") to those before rotation were taken from 41

and are expressed as followed:

$$x^{new} = \frac{x}{\cos\theta(1 - \frac{p_x \tan\theta}{p_z})} \tag{C.11}$$

$$p_x^{new} = p_x \cos\theta + p_z \sin\theta \tag{C.12}$$

$$y^{new} = y + \frac{p_y \ x \ \tan\theta}{p_z(1 - \frac{p_x \tan\theta}{p_z})} \tag{C.13}$$

$$p_y^{new} = p_y \tag{C.14}$$

$$l^{new} = l + \frac{(1+\delta) \ x \tan\theta}{p_z(1 - \frac{p_x \tan\theta}{p_z})} \tag{C.15}$$

$$\text{where } p_z = \sqrt{(1+\delta)^2 - p_x^2 - p_y^2} \tag{C.16}$$

which corresponds to the script:

```
PZ:=sqrt((1+X(6))*(1+X(6))-X(4)*X(4)-X(2)*X(2));

X(5):=X(5)-(1+X(6))*X(1)*tan(T)/(PZ*(1-X(2)*tan(T)/PZ));

X(3):=X(3)+X(4)*X(1)*tan(T)/(PZ*(1-X(2)*tan(T)/PZ));

X(1):=X(1)/(cos(T)*(1-X(2)*tan(T)/PZ));

X(2):=X(2)*cos(T)+sin(T)*PZ;

X(4):=X(4);

X(6):=X(6);

X(1):=X(1)+XS;

X(5):=X(5)+ZS;
```

Bibliography

Bibliography

[1] ILC Reference Design Report (2008). http://www.linearcollider.org/cms/?pid=1000025 1

[2] M. Battaglia, A. de Roeck, J.R. Ellis (CERN), D. Schulte, "Physics at the CLIC Multi-TeV Linear Collider : report of the CLIC Physics Working Group", *CERN report hep-ph/0412251, CERN-2004-005.* 1

[3] European Synchrotron Radiation Source. http://www.esrf.eu 1

[4] DIAMOND Light Source: http://www.diamond.ac.uk/Home/Publications.html 1

[5] J. Murphy, C. Pellegrini, "Introduction to Free-electron Lasers", *in Laser Handbook, Vol.6 Free Electrons Lasers, Ch.1, North Holland (1990).* 1

[6] Spallation Neutron Source: http://neutrons.ornl.gov/facilities/SNS 2

[7] M. Seidel, P.A. Schmelzbach, "Upgrade of the PSI cyclotron facility to 1.8 MW", *Proceedings of Eighteenth International Conference on Cyclotrons and Their Applications 2007* 2

[8] E.M. McMillan, "Particle Accelerators, in Experimental Nuclear Physics", *III, 639-786 (1959)* 3

[9] M. K. Craddock and K. R. Symon, "Cyclotrons and fixed-field alternating-gradient accelerators," *Rev. Accel. Sci. Tech.* **1**, *65 (2008).* 3

[10] K.R. Symon,"Fixed field alternating gradient accelerators," *Phys. Rev. 98, 1152 (1955); D.W. Kerst et al., ibid. 1153;* 3

[11] M. Aiba et al., *Proceedings EPAC 00* 3

[12] Y. Mori, M. Aiba, "Scaling FFAG accelerator", *ICFA Beam Dynamics Newsletter 43 (2007) 27-37.* 4, 76

[13] C. Prior, JS. Berg, M. Meddahi, Y. Mori, "The International Design Study for a Neutrino Factory", *Proceedings of EPAC 08* 3

[14] M. Tanigaki *et al.*, "Present status of FFAG accelerators in KURRI for ADS study," *Proceedings of EPAC 06.* 4

[15] http://www.conform.ac.uk/ 6

[16] http://www.basroc.org.uk/ 6

[17] K. Peach et al., "PAMELA Overview: Design Goals and Principles", *Proceedings of PAC 09.* 6, 78

[18] A. Wheelhouse et al. ,"Operational experience of the superconducting rf system on ALICE at Daresbury Laboratory", *Proceedings of IPAC 10.* 225

[19] A. Moss et al., "The EMMA LLRF systen and its synchronisation with ALICE", *Proceedings of IPAC 10.* 225

[20] R. Edgecock et al., "EMMA - the world's first non-scaling FFAG," *Proceedings of EPAC 08.* 6

[21] J. S. Berg, "The EMMA main ring lattice," *Nucl. Instrum. Meth. A* **596**, *276 (2008).* 9, 12, 13, 16, 17, 132, 141

[22] D.W. Kerst, *Phys. Rev., 60 (1941) 47.* 13

[23] S. Machida, "Resonance crossing and dynamic aperture in nonscaling fixed field alternating gradient accelerators," *Phys. Rev. ST Accel. Beams* **11**, *094003 (2008).* 16, 193, 194

[24] D. Robin, C. Steier, J. Safranek, W. Decking, Enhanced performance of the ALS through periodicity restoration of the lattice, *Proceedings of EPAC 00.* 194

[25] OPERA magnet modelling software,Vector Field OPERA 3D, http://www.vectorfield.com/. 17, 24

[26] Tesla Engineering, http://www.tesla.co.uk. 26, 27

[27] C. Johnson, Numerical Solution of Partial Differential Equations by the Finite Element Method, *Cambridge University Press, 1987.* 31

[28] B. Shepherd, 'EMMA Magnet Design', *CONFORM report, conform-mag-rpt-0001 and conform-mag-rpt-0002 (2007).* 27, 39, 45, 178

[29] N. Marks and B. Shepherd, "Development and adjustment of the EMMA quadrupoles," *Proceedings of EPAC 08.* 24

[30] J.D. Jackson, "Classical Electrodynamics," *3rd ed. 1998* . 51

[31] H. Goldstein, "Classical Mechanics," *Addison-Wesley (2nd edition, 1980).* 90, 105

[32] K. Wille, "The Physics of Particle Accelerators, An Introduction", *Oxford University Press, 2000, ISBN: 19 850549 3.* 15, 58

[33] M. Abramowitz and I.A. Stegun (Eds.)., "Mathieu Functions." *Ch. 20 in Handbook of Mathematical Functions with Formulas, Graphs, and Mathematical Tables, 9th printing. New York: Dover, pp. 721-746, 1972.* 78

[34] M. Venturini, A. Wolski and A. Dragt, "Wigglers and Single-Particle Dynamics in the NLC Damping Rings," *Proceedings of PAC 03.* 53

[35] A. Wolski, M. Venturini, S. Marks, "Dynamic aperture study for the NLC main damping rings", *Proceedings of EPAC 04.* 53

[36] H. Witte , T. Yokoi, S. Sheehy, J. Cobb, K. Peach ,"PAMELA magnets - Design and performances",*Proceedings of PAC 09.* 79

[37] E. Forest, "Beam Dynamics: A New Attitude and Framework," *Taylor and Francis (1998), p173.* 105

[38] E. Forest, "Beam Dynamics: A New Attitude and Framework," *Taylor and Francis (1998), p94.* 112

[39] Y.K. Wu, E. Forest, D.S. Robin, "Explicit symplectic integrator for s-dependent static magnetic field," *Phys. Rev. E 68, 046502 (2003).* 19, 114, 115

[40] E.W. Weisstein, "Lie Algebra." From MathWorld–A Wolfram Web Resource. http://mathworld.wolfram.com/LieAlgebra.html 116

[41] E. Forest, "Beam Dynamics: A New Attitude and Framework," *Taylor and Francis (1998).* 90, 125, 262, 267

[42] H. Yoshida, "Construction of higher order symplectic integrators" *Phys. Lett A 150, 262 (1990).* 113

[43] A. J. Dragt, E. Forest, "Computation of nonlinear behavior of Hamiltonian systems using lie algebraic methods", *J. Math. Phys. 24 (12) (1983) 2734-2744.* 156

[44] A.J. Dragt, "Lie Methods for Nonlinear Dynamics with Applications to Accelerator Physics," (2009). 262

[45] M. Berz, "Modern Map Methods in Particle Beam Physics," *Academic Press, 1999, ISBN 0-12-014750-5 chapter 4.* 217

[46] A.W. Chao and M. Tigner (editors), "Handbook of Accelerator Physics and Engineering". *3rd edition World Scientific, 1999.* 179

[47] COSY Infinity, `http://bt.pa.msu.edu/index_cosy.htm`. 119, 153, 161, 217, 263

[48] F. Méot, S.Valero, "Zgoubi users' guide", *CEA DSM DAPNIA/SEA-97-13 (1997).* 17, 142, 167, 169

[49] F. Lemuet, F. Méot, "Developments in the ray-tracing code Zgoubi for 6-D multiturn tracking in FFAG rings", *Nuclear Instruments and Methods in Physics Research A 547 (2005) 638-651.* 141

[50] F. Méot, "Beam dynamics simulations in FFAGs: the ray-tracing code Zgoubi", *BD-Newsletter 43, C.R.Prior & W.Chou Eds. (Aug.2007) 47-54.* 141

[51] J. Laskar, "Introduction to Frequency Map Analysis in Proceedings of NATO Advanced institute", *SAgaro, June 1995, C. Simó, ed. (1999)* 156

[52] L. Yang , C. Steier,"Experimental Frequency Map Analysis Using Multiple BPMs", *Proceedings of PAC 09.* 156

[53] A. Chao: Lecture Notes on Special Topics in Accelerator Physics, SLAC-PUB 9574, Ch. 9. Lie Algebra Techniques for non-linear dynamics, http://www.slac.stanford.edu/~achao/LieAlgebra.pdf 159, 168

[54] Comparison of tune measurement methods (NAFF and Least Square Method) was presented at a EMMA collaboration meeting by Scott Berg. 178

[55] R. Bartolini et al.,"Precise Determination of the Betatron Tune," *Proceedings of EPAC 96*. 178, 231, 233

[56] S. Tygier, D. Kelliher, "PyZgoubi interface to Zgoubi," http://sourceforge.net/projects/pyzgoubi/. 17, 119

[57] Python programming language; http://python.org/ 54

[58] Y. Giboudot, I. Kirkman, A. Wolski, "Tune measurement in non-scaling FFAG EMMA with model independent analysis," *Proceedings of IPAC 10*. 178

[59] J. Irwin, C.X. Wang, Y. Yan, et. al., "Model-Independent Beam Dynamics Analysis," *Phys. Rev. Lett. 82, 1684 (1999)*. 178

[60] Y. Giboudot, A. Khan, R. Edgecock, A. Wolski, "Particle tracking studies using dynamical map created from finite element solution of the EMMA cell,"*Proceedings of PAC 09*.

[61] E. Keil, A.M. Sessler, "Muon acceleration in FFAG rings", *Nuclear Instruments and Methods in Physics Research A 538 (2005) 159-177*. 179

[62] C. Johnstone, S. Koscielniak, "Mechanisms for nonlinear acceleration in FFAGs with fixed RF", *Nuclear Instruments and Methods in Physics Research A 523 (2004) 25-49*. 179

[63] K.Y. Ng, "Quasi-isochronous buckets in storage rings," *Nuclear Instruments and Methods in Physics Research A 404 (1998) 199.* 179

[64] Y. Saveliev, et al., "Recent developments on ALICE (accelerators and lasers in combined experiments) at Daresbury Laboratory,"*Proceedings of IPAC 10* 190, 223

[65] R.T.P. DÁrcy. et al., "Modelling of the EMMA ns-FFAG Injection Line using GPT," *Proceedings of IPAC 10* 190

[66] S. Machida, D. Kelliher, J.S. Berg, S. Koscielniak, "Collective Effects in the EMMA Non-scaling FFAG," *Proceedings of EPAC 08* 190

[67] S.L. Smith, "First commissioning results from the non-scaling FFAG accelerator, EMMA," *Proceedings of CYCLOTRONS 2010.* 178

[68] Y.Giboudot,F.Méot, "Optical matching of EMMA cell parameters using field map sets," *Proceedings of PAC 09* 17

[69] A. Kalinin, R. Smith, and P. A. McIntosh, "Diagnostic System Commissioning of the EMMA NS-FFAG Facility at Daresbury Laboratory", *Proceedings of IPAC 10* 224

[70] EPICS Experimental Physics and Industrial Control System, http://www.aps.anl.gov/epics/ 236

[71] J.S. Berg, Y. Giboudot, D. J. Kelliher, S. Machida, F. Méot , B. Shepherd, S. Tygier, "Recent developments on the EMMA on-line commissioning software", *Proceedings of IPAC 10* 236

[72] Mathematica script written by J.Jomes and adapted by Y.Giboudot to the processing of experimental results from EMMA. 229

[73] http://www.wolfram.com/ 229

[74] Routine written by S.Machida that process the data collected by the scope and output the time of flight. 227

[75] Thomas H. Cormen, Charles E. Leiserson, Ronald L. Rivest, and Clifford Stein. Introduction to Algorithms, Second Edition. MIT Press and McGraw-Hill, 2001. ISBN 0-262-03293-7. Section 29.3: The simplex algorithm, pp. 790-804. 229